Méthodes de conception et de commande de systèmes robotiques prenant en compte la consommation d'énergie et améliorant leur comportement

Yaodong Lu

To cite this version:

Yaodong Lu. Méthodes de conception et de commande de systèmes robotiques prenant en compte la consommation d'énergie et améliorant leur comportement. Robotique [cs.RO]. INSA de Rennes, 2024. Français. NNT : 2024ISAR0004 . tel-04779948

HAL Id: tel-04779948
https://theses.hal.science/tel-04779948v1

Submitted on 13 Nov 2024

COLLEGE DOCTORAL BRETAGNE
SCIENCES POUR L'INGENIEUR

INSA INSTITUT NATIONAL DES SCIENCES APPLIQUÉES RENNES

THÈSE DE DOCTORAT DE

L'INSTITUT NATIONAL DES
SCIENCES APPLIQUÉES DE RENNES

ÉCOLE DOCTORALE N° 647
Sciences pour l'Ingénieur
Spécialité : *« Robotique - Mécanique »*

Par

Yaodong LU

« Methods for design and control of robotic systems considering energy consumption and improving their behavior »

Thèse présentée et soutenue à Rennes , le 15/03/2024
Unité de recherche : LS2N
Thèse N° : « 24ISAR 03 / D24 - 03 »

Rapporteurs avant soutenance :

Erika OTTAVIANO	Associate Professor at University of Cassino, Italy
Amine Med LARIBI	Maître de Conférences, HDR, Université de Poitiers

Composition du Jury :

Président :	Emmanuel DELALEAU	Professeur des Universités, ENIB, Brest
Examinateurs :	Damien CHABLAT	Directeur de Recherche CNRS, LS2N, Nantes
	Erika OTTAVIANO	Associate Professor at University of Cassino, Italy
	Natalie SMITH-GUERIN	Maître de Conférences, HDR, Université Bretagne Sud, IUT Lorient
	Amine Med LARIBI	Maître de Conférences, HDR, Université de Poitiers
Dir. de thèse :	Vigen ARAKELIAN	Professeur des Universités, INSA de Rennes

Invité :

Yannick AOUSTIN	Professeur des Universités, LS2N, Université de Nantes

RÉSUMÉ

Cette thèse traite de méthodes de conception et de commande des systèmes robotiques en tenant compte de la consommation d'énergie et de l'amélioration de leur comportement. La prise en compte des défis environnementaux urgents, en particulier le changement climatique, est devenue une priorité mondiale au 21e siècle. La communauté de l'ingénierie, en particulier dans le domaine du génie mécanique, joue un rôle prépondérant dans le développement de technologies innovantes visant à réduire l'impact environnemental de la production et de la consommation d'énergie. Ainsi, il est nécessaire de prendre en compte la consommation d'énergie des systèmes robotiques lors de leur phase de conception. Dans cette thèse, différentes méthodes sont développées pour l'évaluation et l'amélioration de l'efficacité énergétique afin de répondre aux exigences des divers systèmes robotiques.

La revue critique présentée dans le premier chapitre est divisée en trois sections en raison de la nature des problèmes examinés : la modélisation de la force de frottement de systèmes mécaniques, le découplage dynamique dans les manipulateurs de robots et les principes de conception d'exosquelettes robotiques portables pour les membres supérieurs.

Le chapitre 2 traite du développement d'une nouvelle solution pour l'analyse des forces, y compris le frottement de Coulomb dans les articulations mécaniques d'un mécanisme à maillons multiples ou d'un mécanisme à boucles multiples. Cette approche est très pratique pour les ingénieurs et offre des perspectives précieuses sur la consommation d'énergie dans la conception des mécanismes. Il est largement reconnu que l'utilisation du frottement de Coulomb pour déterminer une solution exacte aux équations d'équilibre d'un mécanisme entraînera des systèmes d'équations non linéaires. Avec l'abondance des outils informatiques disponibles aujourd'hui, les tâches de ce type, en particulier les calculs numériques, ne présentent pas de difficultés particulières. Cependant, de nouvelles méthodes approximatives analytiquement traitables restent précieuses en tant que moyen simple pour résoudre le problème.

Dans la première section du Chapitre 2, les équations d'équilibre considérant le frottement de Coulomb sont établies pour un mécanisme à quatre barres en se basant sur le concept du cercle de frottement. On peut observer que l'inclusion du frottement de Coulomb dans les équations d'équilibre les transforme en un système d'équations non

linéaires. Dans la deuxième section, une méthode existante bien connue est brièvement décrite pour déterminer les réactions aux articulations mécaniques, en tenant compte du frottement sans avoir besoin de résoudre un système d'équations non linéaires. L'efficacité de cette méthode a été démontrée en l'appliquant avec succès à une classe spécifique de mécanismes de disjoncteur. Cependant, avec les retours des utilisateurs, il est facile de se tromper lors d'une utilisation pratique. Ainsi, dans la section suivante, une nouvelle méthode similaire mais plus simple, plus claire et plus rapide pour résoudre ce problème est développée, en se basant sur la méthode babylonienne. La méthode babylonienne est une méthode efficace pour approximer les racines carrées, ce qui peut être utilisé pour linéariser les termes non linéaires dans les équations d'équilibre. La stabilité de l'approximation sera assurée dans les applications. Ainsi, pour démontrer l'efficacité de la méthode proposée, des simulations numériques ont été réalisées pour approximer les réactions aux articulations du mécanisme et la perte d'énergie du mécanisme à quatre barres, ainsi que des manipulateurs parallèles 5R et 3RRR. Les résultats obtenus montrent la grande précision d'approximation de la méthode proposée.

Le chapitre 3 aborde la minimisation du couple et l'amélioration des performances de contrôle des manipulateurs série spatiaux. La dynamique du manipulateur robotique est connue pour être fortement non linéaire et couplée, ce qui entraîne une performance de commande plus faible à des vitesses élevées. La dynamique complexe résulte de l'inertie variable et des interactions entre les différentes articulations, et la dynamique non linéaire couplée du manipulateur robotique augmente la charge computationnelle, voire la consommation d'énergie dans le processus de contrôle. Étant donné qu'il est difficile de trouver une stratégie simple et efficace pour contrôler les manipulateurs robotiques en raison de la présence de non-linéarités et d'erreurs de modèle, le découplage dynamique est adopté pour simplifier la dynamique des manipulateurs série spatiaux par le biais de modifications mécaniques. Le système découplé obtenu permet non seulement une génération de mouvement efficace pour minimiser le couple, mais facilite également la conception du régulateur. Au sein de ce système découplé, l'utilisation de régulateurs avec des structures simplifiées contribue à une précision de suivi accrue et à une réduction de la consommation d'énergie dans le processus de contrôle.

Dans la première section de Chapitre 3, le découplage dynamique est réalisé par la redistribution de masse et le déplacement des actionneurs dans les manipulateurs série spatiaux. Le modèle dynamique non linéaire et couplé des manipulateurs série spatiaux est simplifié en un modèle linéaire à double intégrateur pour chaque actionneur. En ce qui concerne la minimisation du couple dans les manipulateurs robotiques, il existe deux approches différentes. En mode statique, cela est facilement résolu par la technique de compensation de la gravité. Cependant, en mode dynamique, résoudre ce problème par des modifications mécaniques est assez difficile, c'est pourquoi la génération de mouvement efficace est considérée. Sur la base du système dynamique simplifié, la minimisation du couple peut être réalisée en diminuant les accélérations angulaires maximales des liaisons du robot. À cette fin, un profil bang-bang est appliqué. Les simulations numériques démontrent la réduction des couples d'entrée maximum dans les manipulateurs découplés dynamiquement.

Cependant, certaines erreurs imprévisibles liées aux paramètres de conception ne peuvent être évitées dans le processus de fabrication ou d'assemblage, entraînant un découplage dynamique incomplet. En raison du découplage incomplet, les couples d'entrée peuvent s'écarter des valeurs de référence, entraînant potentiellement une consommation d'énergie supplémentaire. Par conséquent, la méthode d'analyse de sensibilité globale est appliquée pour déterminer les paramètres les plus influents sur les couples d'entrée des manipulateurs découplés. Dans la dernière section de ce chapitre, pour suivre le profil de mouvement souhaité, les régulateurs linéaires classiques sont utilisés pour stabiliser asymptotiquement le système découplé et réduire leur consommation d'énergie. En cas d'incertitudes liées aux paramètres et de perturbations externes inconnues, il est proposé d'utiliser des régulateurs robustes avec des structures simples pour commander les systèmes de manipulateurs découplés. Les simulations numériques démontrent l'amélioration de l'efficacité énergétique et des performances de commande des manipulateurs découplés dynamiquement.

Le chapitre 4 présente la conception et l'étude d'un exosquelette destiné à l'assistance au transport de charges. Bien que les exosquelettes rigides présentent une performance élevée pour fournir des forces et des couples importants, ils ont plusieurs inconvénients. Le poids important et l'inertie des exosquelettes rigides affectent la transparence mécanique. Les exosquelettes flexibles, appelés "exosuits", ont suscité beaucoup d'intérêt de la part des chercheurs. Ils sont généralement constitués de composants flexibles tels que des câbles et des pièces de tissu, qui sont généralement plus légers et consomment moins d'énergie. Cependant, une attention limitée a été accordée à la pression excessive exercée par les câbles sur les tissus mous et le squelette humain, entraînant un inconfort, voire des blessures. Étant donné que l'exosquelette doit être porté par l'utilisateur pendant une longue période pour des besoins industriels, il est également nécessaire de prendre en compte leur performance en termes d'efficacité énergétique lors de la phase de conception.

Dans les première et deuxième sections du Chapitre 4, le concept de conception et la modélisation du système de l'exosquelette sont présentés. Contrairement aux exosquelettes rigides, l'exosquelette proposé se distingue par son utilisation minimale d'éléments rigides, entraînant des forces d'inertie plus faibles et une transparence mécanique améliorée. Dans la conception proposée, des câbles sont utilisés pour reproduire la fonctionnalité des muscles humains, la tension des câbles agissant comme l'équivalent de la force de contraction musculaire. Des moteurs à courant continu exercent des forces sur les câbles, soulevant progressivement le bras de la personne à la position désirée. Ensuite, ces câbles transmettent des forces au membre supérieur de l'utilisateur à travers des bracelets de bras. Il convient de noter que les forces exercées par les câbles pour la compensation de la gravité génèrent des forces d'interaction sur le corps humain, nécessitant une prise en compte lors de la phase de conception. Ainsi, dans la troisième section, un cadre d'optimisation multi-objectifs a été développé pour améliorer les conditions de confort humain et l'efficacité énergétique. Comparé aux études existantes, la recherche proposée prend en compte un grand nombre de critères de performance de l'exosquelette. Le cadre d'optimisation peut également distinguer et hiérarchiser les objectifs définis. Des simulations numériques ont été réalisées pour démontrer l'efficacité de la conception proposée de l'exosquelette. De plus, les paramètres les plus influents sur le confort humain sont identifiés dans la conception de l'exosquelette, fournissant des perspectives précieuses pour la conception de l'exosquelette.

Le chapitre 5 se concentre sur une phase expérimentale visant à valider la conception optimisée de l'exosquelette avec une consommation d'énergie réduite. Malgré les résultats prometteurs des simulations numériques dans la section précédente, la validation de ces améliorations par l'expérience réelle est essentielle. Un membre supérieur de mannequin-démonstrateur est fabriqué dans le laboratoire LS2N. Une étape d'expérimentation a été conçue, comprenant trois phases principales : l'optimisation pour le membre supérieur du mannequin-démonstrateur, la sélection des composants électroniques et l'analyse des résultats expérimentaux.

Initialement, le cadre d'optimisation proposé est appliqué pour identifier l'arrangement optimal des points d'ancrage et d'attache. Ensuite, divers composants électroniques utilisés dans l'expérimentation sont sélectionnés et présentés. Ils comprennent le schéma électronique et la boucle de contrôle de l'expérimentation. Dans la troisième section, les résultats de l'expérimentation sont présentés et analysés, démontrant la haute efficacité énergétique de la conception optimisée de l'exosquelette.

La thèse se conclut par des annexes qui révèlent en détail les objectifs et les finalités déclarés de l'étude.

ABSTRACT

This thesis deals with the methods for design and control of robotic systems considering energy consumption and improving their behavior. Addressing urgent environmental challenges, particularly climate change, has become a global priority in the 21st century. The engineering community, especially in the field of mechanical engineering and robotics, is taking a leading role in developing innovative technologies aimed at reducing the environmental impact of energy production and consumption. Thus, it is necessary to take into account the energy consumption of the robotic systems during their design phase. In this thesis, various methods are developed for energy consumption assessment and improvement of diverse robotic systems.

The critical review given in the first chapter is divided into three sections due to the nature of the examined problems: modelling of friction force in mechanical systems, dynamic decoupling in robot manipulators and design principles in upper-limb wearable robotic exoskeleton.

Chapter 2 deals with the development of a new solution to force analysis including Coulomb friction in mechanism joints of multilink or multiloop mechanism, which is very practical for engineers to employ and provides valuable insights of energy loss in mechanism design. It is widely acknowledged that if Coulomb friction is used in determining an exact solution to the equilibrium equations for a mechanism, then it will involve nonlinear systems of equations. With the abundance of computer tools now available, tasks of this kind, especially numerical computations, are not particularly challenging. However, new analytically tractable approximate methods are still valuable as a straightforward way of solving the problem.

In the first section of the chapter 2, the equilibrium equations considering the Coulomb friction are established for 4-bar mechanism based on the friction circle concept. It could be observed that the inclusion of Coulomb friction in the equilibrium equations transforms them into a system of nonlinear equations. In the second section, a well-known existing method is briefly described for determining the reactions at mechanical joints, accounting for friction without need to solve a system of nonlinear equations. The effectiveness of this method has been demonstrated by applying it successfully to a specific class of circuit-

breaker mechanisms. However, along with user feedback, it is easy to go wrong with their method in practical use. Thus, in the next section, a new similar method but simpler, clearer and quicker for solving this problem is developed, based on the Babylonian method. The Babylonian method is an efficient method for approximating the square roots, which can be used for linearizing the nonlinear terms in the equilibrium equations. The stability of the approximation is ensured in applications. Hence, to demonstrate the effectiveness of the proposed method, numerical simulations have been conducted for approximating the reactions of mechanism joints and energy loss of the four-bar linkage, 5R and 3RRR parallel manipulators. The obtained results show the high approximation accuracy of the proposed method.

Chapter 3 deals with the torque minimization and control performance improvement of spatial serial manipulators. The robot manipulator dynamics is known to be highly nonlinear and coupled, leading to poorer control performance at high speeds. The complex dynamics is the result of varying inertia and interactions between the different joints, and the nonlinear coupled dynamics of robot manipulator increases the computational burden or even the energy consumption in the control process. Since it is challenging to find a simple and effective strategy for controlling robot manipulators due to the presence of model nonlinearities and errors, dynamic decoupling is adopted for simplifying the dynamics of spatial serial manipulators through mechanical modifications. The obtained decoupled system not only enables efficient motion generation to achieve torque minimization but also facilitates the controller design. Within this decoupled system, the use of controllers with simplified structures contributes to enhanced tracking accuracy and reduced energy consumption in the control process.

In the first section of the chapter 3, the dynamic decoupling is achieved via mass redistribution and actuator relocation in spatial serial manipulators. The nonlinear and coupled dynamics of spatial serial manipulators is simplified as a linear double integrator model for each actuator. With regard to torque minimization in robot manipulators, there are two different approaches. In static mode, it is easily solved by gravity compensation technique. However, in dynamic mode, solving this problem by means of mechanical modifications is quite difficult, therefore the efficient motion generation is considered. Based on the linear and decoupled dynamic system, the torque minimization is carried out by diminishing the maximum angular accelerations of robot links. For this propose, bang-bang profile is applied. The numerical simulations have demonstrated the reduction of the maximum input torques in dynamically decoupled manipulators via bang-bang motion profile.

However, some unpredictable errors of design parameters cannot be avoided in fabrication or assembling process, leading to incomplete dynamic decoupling. Owing to the incomplete decoupling, input torques deviate from the reference values, potentially resulting in additional energy consumption. Hence, the global sensitivity analysis method is applied to determine the most influential parameters to the input torques of the decoupled manipulators. In the last section of this chapter, to track the desired motion profile, the classical linear controllers are employed to stabilize the decoupled system asymptotically and reduce their energy consumption. In the case of parameter uncertainties and unknown external disturbances, it is proposed to use the robust controllers with simple structures for controlling the decoupled manipulator systems. The numerical simulations have demonstrated the improved energy efficiency and control performance of dynamically decoupled manipulators.

Chapter 4 presents the design and study of an exosuit for load-carriage assistance. Although the rigid exoskeletons show high performance for providing large forces and torques but they have several drawbacks. Large weight and inertia of rigid exoskeletons affect the mechanical transparency. The flexible exoskeletons, known as the "exosuits", have attracted a great deal of interest from researchers. They are usually made up of flexible components such as cables and pieces of fabric, which are typically lighter and consume less energy. However, limited attention has been devoted to the excessive pressure exerted by cables on soft tissues and skeleton of the human, leading to discomfort or even injuries. Since exosuit should be worn by user over long time for industrial needs, it is also required to consider their energy efficiency performance during the design phase.

In the first and second section of the chapter 4, the design concept and system modelling of the exosuit are presented. In contrast to rigid exoskeletons, the proposed exosuit is distinguished by its minimal use of rigid elements, leading to lower inertia forces and enhanced mechanical transparency. In the proposed design, cables are employed to replicate the functionality of human muscles, with cable tension acting as the equivalent of muscle contraction force. DC motors exert forces on the cables, steadily lifting the person's arm to the desired position. Then, these cables transmit forces to the user's upper limb through arm bracelets. It should be noted that the forces exerted by the cables for gravity compensation generate interaction forces on the human body, necessitating consideration during the design phase. Thus, in the third section, a multi-objective optimization framework has been developed for enhancing the human comfort conditions and energy efficiency. Compared to the existing studies, the proposed research takes into account a large number of exosuit performance criteria. The optimization framework is capable of distinguishing and prioritizing the defined objectives. The numerical simulations have been conducted for demonstrating the effectiveness of the proposed exosuit design. Additionally, the most influential parameters to the human comfort are identified in the exosuit design, providing valuable insights in the design phase.

Chapter 5 focuses on an experimental phase aimed at validating the optimized exosuit design with reduced energy consumption. Despite promising results from the numerical simulations in the chapter 4, the validation of these improvements through real-world experiments is essential. A demonstrator-mannequin upper-limb is fabricated in the laboratory LS2N. An experimentation step has been designed, comprising three main steps : Optimization for the demonstrator-mannequin upper-limb, selection of the electronic components and analysis of experimental results.

Initially, the proposed optimization framework is applied for identifying the optimal arrangement of anchor and attachment points. Next, various electronic components used in experimentation are selected and presented. They consist the electronic diagram and control loop of experimentation. In the third section, the results of the experimentation are presented and analyzed, demonstrating the high energy efficiency of the optimized exosuit design.

The thesis concludes with insights that thoroughly unveil the stated purposes and objectives of the study.

ACKNOWLEDGEMENT

Before starting my Ph.D. dissertation, I would like to say some words to the people who have supported and encouraged me during the 42-month study.

First of all, I would like to express my sincere gratitude to my supervisor Prof. Vigen ARAKELIAN for his continuous support and valuable advice during my Ph.D. studies. When I met difficulties in the research, he always encouraged me and gave me some useful suggestions based on his tremendous experience in robotics and mechanism design. Furthermore, his gentleness and patience are qualities I aspire to learn from throughout my life.

This work has been supported by China Council Scholarship (CSC) and INSA de Rennes. I would like to thank CSC for the financial support and the opportunity of doing a thesis in France.

Moreover, I would like to express my gratitude to the people and collaborators who helped me a lot for my Ph.D. researches. Thanks to the members of the individual monitoring committee (CSI) of my thesis, Prof. Yannick AOUSTIN and Emmanuel DELALEAU. During my three years of Ph.D. study, I have received valuable suggestions and inspirations from them. And I also thanks to Frédéric Marie for his help for the experiments of exosuit system.

I would also like to thank the other Ph.D. students in our research group MECAPROCE (Jing, Léo). At the beginning of my Ph.D. thesis, they gave me a lot of useful advice of being a qualified Ph.D. student and we established a strong friendship during our life.

Finally, I would like to express my sincere gratitude to my mother Xin XU and my father Xiaofeng LU. In the past three years, they always supported me and believed me that I could succeed in defending my Ph.D. thesis.

TABLE OF CONTENTS

Résumé **3**

Abstract **9**

Acknowledgement **13**

List of figures **23**

List of tables **25**

1 Literature review and current challenges **27**

1.1 Modelling of friction force in mechanical systems 28
1.1.1 Static friction model 29
1.1.2 Dynamic friction model 33
1.2 Dynamic decoupling in robot manipulators 35
1.2.1 Dynamic decoupling via mass redistribution 37
1.2.2 Dynamic decoupling via actuator relocation 41
1.2.3 Dynamic decoupling via adding auxiliary links 43
1.3 Design principles in upper-limb wearable robotic exoskeletons 46
1.3.1 Applications of robotic exoskeleton in upper-limb assistance 46
1.3.2 Rigid exoskeletons for upper-limb power assistance 48
1.3.3 "Exosuit" — the soft upper-limb exoskeletons 50
1.4 Thesis outline 54

2 Estimation of energy loss in mechanical systems due to the friction: a new solution to force analysis including Coulomb friction **57**

2.1 Force analysis including Coulomb friction in mechanism joints 58
2.1.1 Equilibrium equations considering the Coulomb friction 58
2.1.2 Solution based on linearizing approximations 61
2.2 Proposed solution based on the Babylonian method 62
2.2.1 Babylonian method for square-root approximation 62

2.2.2 Babylonian method in force analysis including Coulomb friction . . 64
2.2.3 Stability analysis of the Babylonian method 69
2.3 Illustrative examples and numerical simulations 70
2.3.1 Four-bar linkage 70
2.3.2 5R parallel manipulator 74
2.3.3 3RRR parallel manipulator 81
2.4 Summary 90

3 Torque minimization and control performance improvement of dynamically decoupled spatial serial manipulators 91
3.1 Decoupled dynamics of the spatial serial manipulators 92
3.1.1 Decoupled dynamics of 2R spatial serial manipulator 93
3.1.2 Decoupled dynamics of 3R spatial serial manipulator 95
3.2 Optimal motion generation in dynamically decoupled manipulators 98
3.2.1 Bang-bang motion profile for input torque minimization 98
3.2.2 Numerical simulations of 2R spatial serial manipulator 100
3.2.3 Numerical simulations of 3R spatial serial manipulator 101
3.3 Error sensitivity analysis in dynamically decoupled manipulators 103
3.3.1 Sensitivity analysis criterion 103
3.3.2 Local and global sensitivity analysis method 104
3.3.3 Sensitivity analysis of 2R spatial serial manipulator 106
3.3.4 Sensitivity analysis of 3R spatial serial manipulator 106
3.4 Control performance improvement in dynamically decoupled manipulators 108
3.4.1 Control performance indices 108
3.4.2 Lead compensation performance 109
3.4.3 Linear quadratic regulator performance 113
3.4.4 Parameter uncertainty and external disturbance 115
3.4.5 Model-reference adaptive control performance 117
3.4.6 Modified twisting controller performance 119
3.4.7 Modified twisting observer performance 122
3.5 Summary 125

4 Optimal design of an exosuit for load carriage based on human comfort conditions and energy efficiency 127
4.1 Design concept of robotic suit for load carriage 128

4.1.1 Functionality of cables in exosuit 128
4.1.2 Robotic suit operation 129
4.2 Cable-driving wearable robot modeling 130
4.2.1 Cable-tension force analysis 132
4.2.2 Optimization goals and design constraints 136
4.3 Multi-objective optimization algorithm and development 140
4.3.1 Inverse-PageRank-PSO 140
4.3.2 Development for multi-objective optimization 142
4.4 Numerical simulations and sensitivity analysis 144
4.4.1 Optimization results and analysis 144
4.4.2 Sensitivity analysis of design parameters 152
4.5 Summary 156

5 Validation through experimentation of the optimized exosuit design with reduced energy consumption 157
5.1 Numerical simulation with demonstrator-mannequin upper-limb 158
5.1.1 Parameters of the demonstrator-mannequin upper-limb 158
5.1.2 Numerical simulation results and analysis 159
5.2 Experimental equipements 161
5.2.1 DC Gear motor selection 161
5.2.2 Arduino Mega controller 163
5.2.3 L298N motor driver 163
5.2.4 INA219 current sensor 165
5.2.5 MPU6050 IMU sensor 166
5.3 Electronic diagram 168
5.4 Experimentation and results 169
5.5 Summary 172

Conclusion 173

Bibliography 176

Appendix A 193

List of publications 195

LIST OF FIGURES

1.1 Fuel energy dissipation in passenger cars (60 km/h), provided by [12]. . . . 29
1.2 Coulomb's law. 30
1.3 Coulomb's law with linear function [20]. 30
1.4 Threlfall friction model [21]. 31
1.5 Ambrósio friction model [22]. 31
1.6 Coulomb's law considering Stribeck effect [27]. 32
1.7 Coulomb's law with linear function [14]. 32
1.8 Model proposed by Brown and McPhee [29]. 32
1.9 Physical interpretation of LuGre model [14]. 34
1.10 "Design for control" methodology [59]. 36
1.11 A manipulator arm with open kinematic chain [61]. 38
1.12 Joints of manipulator [61]. 38
1.13 Manipulator with two orthogonal joint axes [61]. 40
1.14 Two kinds of 2-DOF manipulators with decoupled and configuration-invariant inertia matrix [61]. 40
1.15 3-DOF manipulators with configuration-invariant inertia matrix [61]. . . . 40
1.16 General structure of 2-DOF manipulator. 41
1.17 2-DOF manipulator structure with actuator relocation [62]. 41
1.18 Prototype with actuation relocation [62]. 42
1.19 Remote actuation via cable transmission system [63]. 42
1.20 A 2-DOF decoupled manipulator with adaptive balanced mechanism proposed in [66]. 43
1.21 A decoupled 2-DOF planar serial manipulator proposed in [67]. 44
1.22 A decoupled 3-DOF spatial serial manipulator proposed in [67]. 44
1.23 A 2-DOF decoupled manipulator with Scott-Russell mechanism [69]. 45
1.24 Power-assist exoskeleton for physically weak persons [77]. 47
1.25 Muscle suit for static holding [78]. 47
1.26 FORTIS [83]. 48
1.27 Hybrid exoskeleton [84]. 48

1.28 Cinemaker [89]. 49
1.29 Exoskeleton with additional mechanism [91]. 49
1.30 MAXFAS [94]. 50
1.31 STRONGARM [95]. 50
1.32 Exosuit for assisting stroke survivors [96]. 52
1.33 Exosuit for heavy load carriage [95]. 52
1.34 Areas to be avoided in upper-limb exosuit design [93]. 53

2.1 Planar four-bar linkage. 59
2.2 Geometric approximation path of the Babylonian method. 64
2.3 Coulomb friction approximation with the Babylonian method. 64
2.4 Forces due to the friction determined from linear equations (2.28)-(2.33). . 71
2.5 Approximation stability analysis of four-bar linkage. 71
2.6 Joint reaction forces of the four-bar linkage. 73
2.7 Input torque of the four-bar linkage. 74
2.8 5R parallel manipulator. 74
2.9 Forces due to the friction determined from linear equations (2.57)-(2.62). . 77
2.10 Approximation stability analysis of 5R parallel manipulator. 78
2.11 Joint reaction forces of the 5R parallel manipulator 79
2.12 Input torques of the 5R parallel manipulator 80
2.13 3RRR parallel manipulator. 81
2.14 Forces due to the friction determined from linear equations (2.69)-(2.80). . 86
2.15 Stability criterion verification for the 3RRR parallel manipulator. 87
2.16 Reaction forces at the actuating joints of the 3RRR parallel manipulator. . 88
2.17 Input torques of the 3RRR parallel manipulator. 89

3.1 2R spatial serial manipulator. 93
3.2 3R spatial serial manipulator (KR 16R1610). 95
3.3 Initial structure. 96
3.4 With relocated actuators. 96
3.5 "Bang-bang" profile used for motion generation in dynamically decoupled spatial serial manipulators. 99
3.6 Decoupled 2R manipulator's input torque magnitude for two studied cases (Case 1: fifth order polynomial profile; Case 2: bang-bang profile). 100

3.7 Decoupled 3R manipulator's input torque magnitude for two studied cases (Case 1: fifth order polynomial profile; Case 2: bang-bang profile). 102
3.8 Input torques of 2R spatial serial manipulator with incomplete dynamic decoupling (5 % error in I_{x_2}). 104
3.9 Frequency domain response with 70° phase lead compensator. 110
3.10 Trajectory tracking of lead compensator in the decoupled 2R spatial serial manipulator. 111
3.11 Torque generation of lead compensator in the decoupled 2R spatial serial manipulator. 111
3.12 Trajectory tracking of lead compensator in the decoupled 3R spatial serial manipulator. 111
3.13 Torque generation of lead compensator in the decoupled 3R spatial serial manipulator. 111
3.14 Trajectory tracking of LQR in the decoupled 2R manipulator. 114
3.15 Torque generation of LQR in the decoupled 2R manipulator. 114
3.16 Trajectory tracking of LQR in the decoupled 3R manipulator. 115
3.17 Torque generation of LQR in the decoupled 3R manipulator. 115
3.18 Joint friction curve. 116
3.19 Trajectory tracking of MRAC in the decoupled 2R manipulator. 118
3.20 Torque generation of MRAC in the decoupled 2R manipulator. 118
3.21 Trajectory tracking of MRAC in the decoupled 3R manipulator. 118
3.22 Torque generation of MRAC in the decoupled 3R manipulator. 118
3.23 Trajectory tracking of modified twisting controller in the decoupled 2R manipulator. 120
3.24 Torque generation of modified twisting controller in the decoupled 2R manipulator. 120
3.25 Trajectory tracking of modified twisting controller in the decoupled 3R manipulator. 121
3.26 Torque generation of modified twisting controller in the decoupled 3R manipulator. 121
3.27 Difference between the actuator torque and the ideal torque in the decoupled 2R manipulator. 121
3.28 Difference between the actuator torque and the ideal torque in the decoupled 3R manipulator. 121

3.29 Trajectory tracking with modified twisting observer in the decoupled 2R manipulator. . . . 123
3.30 Torque generation with modified twisting observer in the decoupled 2R manipulator. . . . 123
3.31 Trajectory tracking with modified twisting observer in the decoupled 3R manipulator. . . . 124
3.32 Torque generation with modified twisting observer in the decoupled 3R manipulator. . . . 124
3.33 Joint velocity estimation in the decoupled 2R manipulator. . . . 124
3.34 Joint velocity estimation in the decoupled 3R manipulator. . . . 124

4.1 OpenSim model: Arm26 [133] 128
4.2 A human body wearing the proposed exosuit for load carriage. . . . 129
4.3 Modeling of an exosuit with four cables. . . . 131
4.4 Human upper-limb carrying load in the sagittal plane. . . . 131
4.5 Human upper-limb carrying load in the transversal plane. . . . 131
4.6 Sagittal plane, the assisted arm with the exosuit (cable 4 passes through the attachment points on the right shoulder, see Fig 4.3). . . . 137
4.7 Attachment points of cuffs at arm. . . . 137
4.8 Attachment points of cuffs at forearm. . . . 137
4.9 Diagram of multi-objective optimization process. . . . 144
4.10 End-effector positions before (left) and after (right) optimization. Brown dots are feasible, while black dots are infeasible. . . . 146
4.11 Movement of particles during the searching process. . . . 147
4.12 Non-dominated solutions found by multi-objective I-PR-PSO. . . . 147
4.13 $\mathcal{O}_1$ and $\mathcal{O}_2$ of sixteen non-dominated solutions found by multi-objective I-PR-PSO. . . . 147
4.14 $\mathcal{O}_3$ of sixteen non-dominated solutions found by multi-objective I-PR-PSO. 148
4.15 Cuffs at arm with solution IV. . . . 149
4.16 Cuffs at forearm with solution IV. . . . 149
4.17 Forces exerted on the shoulder by 4 cables with solution IV. . . . 149
4.18 Forces exerted on the upper limb by 4 cables with solution IV. . . . 149
4.19 Important forces exerted on shoulder and upper limb (magenta dots). . . . 150
4.20 Feasible workspace of the solution obtained by *fmincon* (brown dots). . . . 150
4.21 F_1 in workspace. . . . 151

4.22 F_2 in workspace. 151
4.23 F_3 in workspace. 151
4.24 F_4 in workspace. 151
4.25 Forces exerted on the shoulder with a 5 kg load. 152
4.26 Forces exerted on the upper limb with a 5 kg load. 152
4.27 Sensitivity analysis stages. 153
4.28 Feature importance to $\mathcal{O}_1$. 154
4.29 Feature importance to $\mathcal{O}_2$. 155

5.1 Demonstrator-mannequin fabricated in LS2N. 158
5.2 Demonstrator-mannequin upper-limb with cable transmission system. . . . 159
5.3 Non-dominated solutions found by multi-objective I-PR-PSO. 160
5.4 Couzet DC gear motor. 161
5.5 Couzet DC gear motor [155]. 162
5.6 Torque-speed relationship [155]. 162
5.7 Arduino Mega controller [156]. 163
5.8 L298N motor driver [156]. 163
5.9 H-bridge circuit [157]. 164
5.10 INA219 current sensor [156]. 165
5.11 MPU6050 [156]. 166
5.12 Yaw, roll and pitch angles of MPU6050. 167
5.13 Electronic diagram and components in the experimentation [156]. 168
5.14 Optimal solution IX. 169
5.15 Non-dominated solution VII. 169
5.16 Control loop in experimentation. 169
5.17 Upper-arm position measured by MPU6050 in the control process. 170
5.18 Forearm position measured by MPU6050 in the control process. 170
5.19 Current measured with optimal solution IX in the control process. 170
5.20 Current measured with solution VII in the control process. 170
5.21 Mannequin upper-limb with cable transmission system. 193

LIST OF TABLES

2.1 Numerical approximation to $\sqrt{2}$ using the Babylonian method with $x_0 = 6$. 63
2.2 Direction change of relative angular velocity in four-bar linkage 71
2.3 Approximation of energy loss due to friction in the 5R parallel manipulator 80
2.4 Energy loss due to friction in the 3RRR parallel manipulator. 89

3.1 Length and mass parameters of the industrial robot KR 16R1610 [124]. . . 101
3.2 Sobol indices of the decoupled 2R spatial serial manipulator. 106
3.3 Sobol indices of the decoupled 3R spatial serial manipulator. 107
3.4 Results of different phase lead angles in the decoupled 2R spatial serial manipulator. 112
3.5 Results of different phase lead angles in the decoupled 3R spatial serial manipulator. 112
3.6 Results of two controllers in the presence of parameter uncertainty. 119
3.7 Results of different controllers in the presence of joint friction. 122

4.1 Modified Denavit Hartenberg parameters of human arm 130
4.2 Range of the exosuit design parameters. 145
4.3 Sixteen non-dominated solutions found by multi-objective I-PR-PSO. . . . 148

5.1 Parameters of mannequin upper-limb. 159
5.2 Performance of the non-dominated solutions found. 160
5.3 Parameters of Couzet gear motor 828690 [155]. 161
5.4 Switch control in the H-bridge. 165
5.5 Average energy loss power. 171

CHAPTER 1

LITERATURE REVIEW AND CURRENT CHALLENGES

1.1 Modelling of friction force in mechanical systems ... 28
1.2 Dynamic decoupling in robot manipulators ... 35
1.3 Design principles in upper-limb wearable robotic exoskeletons ... 46
1.4 Thesis outline ... 54

In the first chapter of the thesis, the critical review of the design technologies considering energy consumption and the other behavior of robotic systems is given. For instance, friction estimation methods are used for evaluating the energy consumption of mechanical systems during their design phase. Dynamic decoupling techniques applied in robot manipulators not only simplify their nonlinear dynamics but also improve the control performance. In the design of upper-limb exoskeleton robots, the exoskeletons fabricated with soft materials are much lighter and consume less energy than rigid ones. They are also featured with higher mechanical transparency.

Thus, this chapter is divided into three sections with respect to the nature of the examined problem: modelling of friction force in mechanical systems, dynamic decoupling in robot manipulators and design principles in upper-limb exoskeleton robots.

The known solutions are summarized through the suggested critical review and some of their drawbacks are disclosed.

1.1 Modelling of friction force in mechanical systems

Energy efficiency, reliability and durability are three important criteria indicated by [1], which should be considered in the design phase of mechanical systems. Due to the poor performance of these criteria, energy dissipation and failure of components take place in mechanical systems, leading to economic loss or even severe safety accidents. These criteria rely on the dynamic performance of the designed system and thereby force analysis is necessary to be carried out for estimating the interacting force of mechanical components. In force analysis, friction force in mechanical system has been considered as the major cause of low energy efficiency, poor reliability and durability of mechanical systems [2].

Friction is a complex and nonlinear phenomenon, which occurs at the interface of components (prismatic and revolute joints) in relative motion. Consequently, the mechanical components wear and their kinetic energies are dissipated. Besides, other effects associated with friction like self-excited vibration and noise occur in mechanical system, which could have a long-term impact on reliability and functionality of mechanical system. Furthermore, friction is another obstacle to the precise control, which can cause 50% tracking error in some heavy industrial manipulators [3] (especially at low velocities). According to [4], “Friction is the nemesis of precision control”. To overcome the difficulty, various compensation technologies based on friction modelling are applied for counteracting friction effects in mechanical system or in control scheme [5]–[10]. As mentioned above, friction can not only deteriorate mechanical components’ life but also control system performance. For a mechanical system or control system, the absence of consideration about friction is a “fatal flaw”.

From an economic perspective, in the Jost report [11], it was stated that a sizable of the GDP of a nation was invested for alleviating friction ramification in mechanical systems. For instance, friction in automobile engine increases CO2 emission due to low energy efficiency. As low CO2 emission is an attractive point to the customers which is related directly to fuel consumption, every automotive manufacturer attempts to improve their engine efficiency. The friction power loss of the engine corresponds to 25–30 g of CO2/km, with a corresponding fuel consumption of roughly 0.9 L/100 km [2]. As indicated in [12], 33 % of the fuel energy dissipation in passenger car is due to the friction, as shown in Fig. 1.1.

Thus, it is required a large attention to this phenomenon when designing mechanical

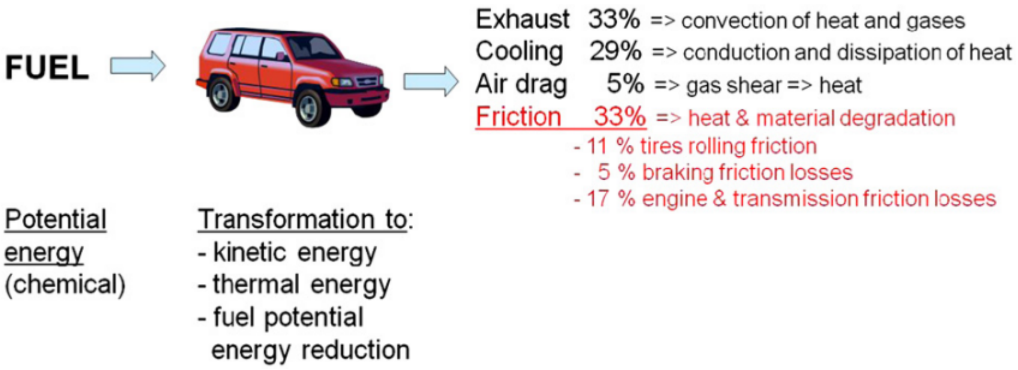

Figure 1.1 – Fuel energy dissipation in passenger cars (60 km/h), provided by [12].

systems. Hence, to evaluate the energy loss due to friction, the force analysis including friction in mechanical system is indispensable. Various friction models are developed in [13]–[17], in which some of the most important phenomena related to friction are considered, like static friction, stick-slip, Stribeck effect, viscous friction, friction lag, pre-sliding displacement and break-away force. Friction is paramount in the study of robot manipulators, significantly influencing the assessment of their performance and energy consumption. Typically, most of the researchers divided the friction force models into two main groups, the static models and the dynamic models. A review of these friction models is presented as the following.

1.1.1 Static friction model

Static friction model is widely used in the simulations of multibody mechanical systems. They only describe the steady-state behavior of friction force–relative velocity relation, which makes them easy to implement in the numerical simulations.

As early as the 18th century, Charles-Augustin de Coulomb (1736 – 1806) postulated a simple law specifying that friction force always opposes to the relative motion between two contacting surfaces, and its magnitude is proportional to the normal contact force [18]:

$$\mathbf{F}_f = \begin{cases} F_C \operatorname{sign}(\mathbf{v}_{\mathrm{T}}) \\ \min\left(\left\|\mathbf{F}_e\right\|, F_C\right) \operatorname{sign}(\mathbf{F}_e) \end{cases} \tag{1.1}$$

where,

$$F_C = \mu_k \left\|\mathbf{F}^{\mathrm{N}}\right\| \tag{1.2}$$

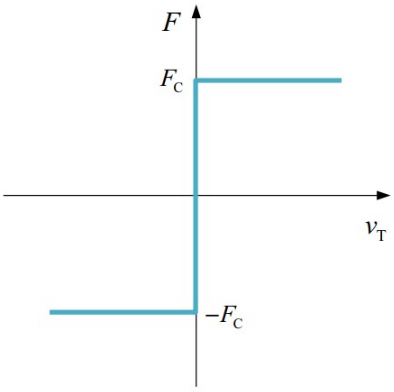

Figure 1.2 – Coulomb's law.

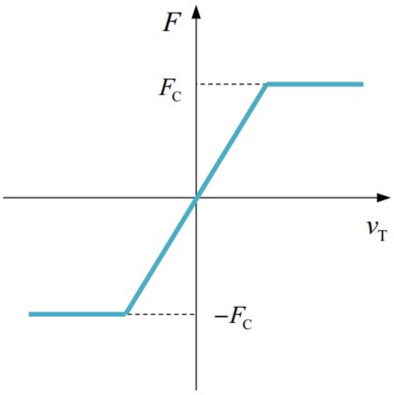

Figure 1.3 – Coulomb's law with linear function [20].

In which $\mathbf{F}^{\mathrm{N}}$ is the normal contact force, μ_k denotes the kinetic coefficient of friction, F_C represents the magnitude of Coulomb friction, and $\mathbf{v}_{\mathrm{T}}$ denotes the relative tangential velocity of the contacting surfaces ($\|\mathbf{v}_{\mathrm{T}}\| \neq 0$). $\mathbf{F}_e$ denotes the external tangential force. The direction of the friction force depends on the relative velocity, which is defined by:

$$\operatorname{sign}(\mathbf{v}_{\mathrm{T}}) = \begin{cases} \dfrac{\mathbf{v}_{\mathrm{T}}}{\|\mathbf{v}_{\mathrm{T}}\|} & \text{if } \|\mathbf{v}_{\mathrm{T}}\| \neq 0 \\ \mathbf{0} & \text{if } \|\mathbf{v}_{\mathrm{T}}\| = 0 \end{cases} \tag{1.3}$$

It should be admitted that Coulomb's law is extensively employed in mechanical system modeling due to its simplicity, as illustrated in Fig. 1.2. It requires only one input parameter, i.e., the kinetic coefficient of friction μ_k, and proves to be a suitable choice for most of the dynamic systems where friction does not play a main role. Nevertheless, it possesses limitations when it comes to accurately describing diverse friction phenomena, including the Stribeck effect, pre-sliding displacement, stiction, viscous effects, and more. In order to address this issue, researchers have proposed various modified Coulomb friction models [14], [19].

Firstly, the discontinuity at null velocity in Coulomb's law presents the problem in numerical simulations. In [20]–[22], several researchers proposed different approaches to deal with the friction discontinuity. As shown in Figs. 1.3-1.5, the original function in the neighborhood of zero velocity is replaced by a smoother or alternative one. In these approaches, the degree of smoothness is defined by an extra tolerance parameters. These models are capable of providing numerical stability in simulations. However, they do not take other friction phenomena into account.

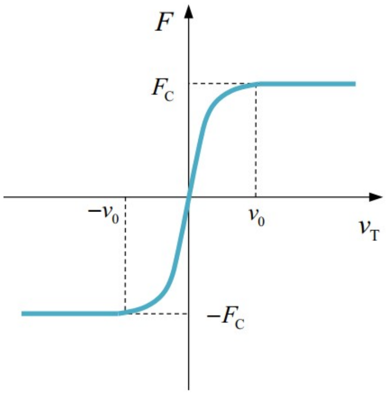

Figure 1.4 – Threlfall friction model [21].

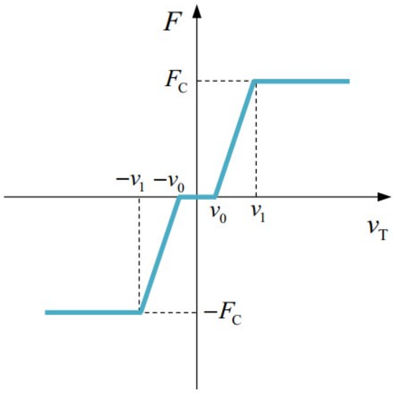

Figure 1.5 – Ambrósio friction model [22].

As examples, key phenomena includes the viscous friction, Stribeck effect, and stiction. Stiction refers to a phenomenon where friction at zero velocity exceeds kinetic friction. Concerning the Stribeck effect, it signifies a continuous transition from static to kinetic friction. Viscous friction implies that the magnitude of friction force is related to the relative velocity. In order to model these friction phenomena, several studies proposed various models in [7], [23]–[27], in which the most utilized is presented as follows [27]:

$$\mathbf{F}_f = \left(F_C + (F_S - F_C) \mathrm{e}^{-\left(\frac{\|\mathbf{v}_{\mathrm{T}}\|}{v_S}\right)^{\delta_\sigma}} \right) \operatorname{sign}(\mathbf{v}_{\mathrm{T}}) + F_v \mathbf{v}_{\mathrm{T}} \tag{1.4}$$

where,

$$F_S = \mu_s \left\| \mathbf{F}^{\mathrm{N}} \right\| \tag{1.5}$$

in which μ_s denotes the static coefficient of friction and F_S is the magnitude of static friction. v_S denotes the Stribeck velocity and δ_σ is a factor that relies on the geometry of the contacting surfaces, often considered to be equal to 2 [19]. F_v is the magnitude of viscous friction. This friction model takes into account the Coulomb, viscous, stiction and Stribeck friction effects. Fig. 1.6 presents an example of the model with dry friction, neglecting the viscous effect. It can be seen that the discontinuity at zero velocity may lead to numerical issues in dynamic simulations. In the literature, several studies develop various approaches to prevent the numerical stability [28]–[30]. Figs. 1.7 and 1.8 show two examples of them, whose original function is replaced by a smoother one.

While static friction models have undergone continuous modification and improvement over time, certain limitations remain significant. For instance, due to mathematical constraints, static models are unable to capture the dynamic behavior inherent in frictional

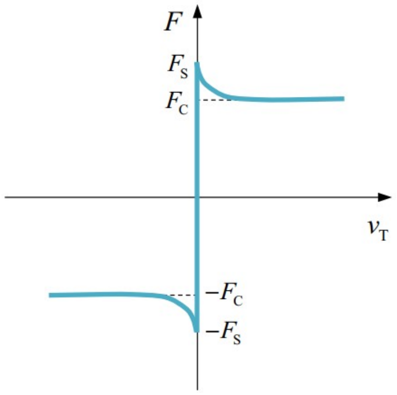

Figure 1.6 – Coulomb's law considering Stribeck effect [27].

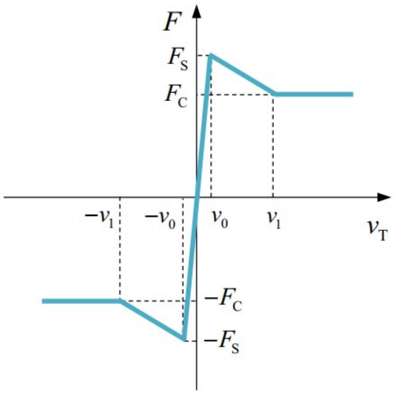

Figure 1.7 – Coulomb's law with linear function [14].

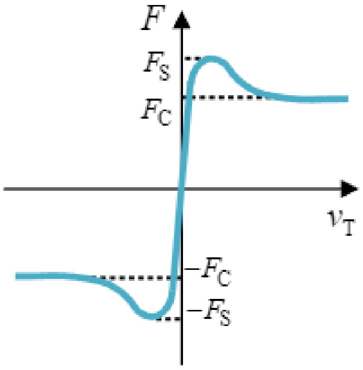

Figure 1.8 – Model proposed by Brown and McPhee [29].

interactions, including pre-sliding displacement and frictional lag. Therefore, the need for more advanced friction models is crucial to enhance precision by accounting for the historical context of frictional interactions.

1.1.2 Dynamic friction model

The dynamic friction force models are more complex than the static models because they require the inclusion of additional friction phenomena on the contact modeling related to the properties of surfaces, the contact pressure, the nature and quality of lubricant and many other contingencies [4], [31]–[34]. From a mathematical perspective, an additional state variable $\mathbf{z}$ is employed, representing the average bristle deflection that characterizes the behavior of surface asperities in contact interactions. During the sticking phase, the bristles exhibit spring-like behavior.

In the history of development, various dynamic models were proposed [14] and let us review the most commonly utilized ones. The Dahl friction model [35], [36], is the earliest one introduced to model the friction behavior of ball bearings. The mathematical expression is given as follows:

$$\mathbf{F}_f = \sigma_0 \mathbf{z} \tag{1.6}$$

where σ_0 denotes the bristle stiffness, and the behavior of $\mathbf{z}$ is modeled by the following differential equation:

$$\frac{\mathbf{dz}}{\mathrm{d}t} = \left(1 - \frac{\sigma_0}{F_C}\mathbf{z} \cdot \mathrm{sign}(\mathbf{v}_\mathrm{T})\right)\mathbf{v}_\mathrm{T} \tag{1.7}$$

The introduction of the additional state variable $\mathbf{z}$ not only eliminates the discontinuity at zero velocity but also considers the pre-sliding displacement through the differential equation. However, a limitation of the Dahl model is the lack of consideration in stiction and the Stribeck effect.

To address this issue, various models have been developed to describe additional friction phenomena. Among these, the LuGre model was proposed by Canudas de Wit et *al.* [37] and is widely considered to be the most accepted in the scientific community. The model not only retains the advantages of dynamic friction models for capturing dynamic behaviors like friction lag and pre-sliding displacement, but it also includes the Stribeck and stiction effects. These phenomena present the dynamic characteristics of frictional effects. Pre-sliding displacement is characterized by a slight motion in the elastic range when the applied force is lower than the break-away force, and frictional lag refers to the delay in the change of friction force in relation to velocity.

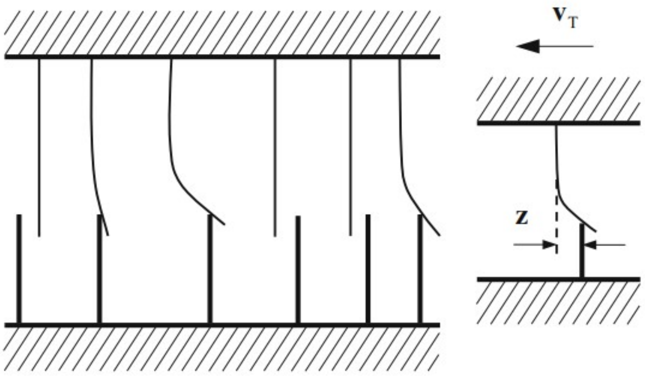

Figure 1.9 – Physical interpretation of LuGre model [14].

Similar to the Dahl model, the LuGre model also utilizes an internal state variable to characterize the average bristle deflection, as shown in Fig. 1.9. At the microscopic level, surfaces exhibit significant irregularities, resulting in contact at a number of asperities. It can be visualized that two rigid bodies make contact through elastic bristles. Application of a tangential force causes the bristles to deflect like springs, which increases the friction force. When the force exceeds a critical threshold, certain bristles deflect so much and they will slip. The mathematical expression is provided as follows:

$$\frac{\mathbf{dz}}{\mathrm{d}t} = \left(1 - \frac{\sigma_0}{G(\mathbf{v}_\mathrm{T})}\mathbf{z} \cdot \mathrm{sign}(\mathbf{v}_\mathrm{T})\right)\mathbf{v}_\mathrm{T} \tag{1.8}$$

$$\mathbf{F}_f = \sigma_0 \mathbf{z} + \sigma_1 \frac{\mathbf{dz}}{\mathrm{d}t}\mathrm{d}t + \sigma_2 \mathbf{v}_\mathrm{T} \tag{1.9}$$

where σ_1 represents the bristle damping, σ_2 denotes the viscous friction coefficient and $G(\mathbf{v}_\mathrm{T})$ is an arbitrary function for modelling the Stribeck curve, which could be defined as:

$$G(\mathbf{v}_\mathrm{T}) = F_C + (F_S - F_C)\mathrm{e}^{-\left(\frac{\|\mathbf{v}_\mathrm{T}\|}{v_S}\right)^{\delta_\sigma}} \tag{1.10}$$

The Dahl model and LuGre model are two typical models in the group of dynamic friction models. Compared to the static friction models, the dynamic models have the ability of capturing more characteristics of frictional behavior. However, there is no such thing as a free lunch. The application of dynamic friction models often leads to heavy computational burden in numerical simulations. Not only for the dynamic model, even with the Coulomb friction model (Eq. (1.1)), when the mechanical system consists of a series of interconnected linkages, it gives rise to numerous nonlinear calculation problems.

Current challenges: Despite the multitude of friction models and various methods for their calculation, incorporating friction into the design equations of mechanical systems proves to be a complex task. Consequently, there is a continued relevance for the development of new approximate methods that provide reasonably accurate calculated values. This is especially crucial for swiftly estimating energy consumption in robotic systems. Hence, there is consistently significance in the development of effective approximation tools for force analysis including friction in mechanical systems.

1.2 Dynamic decoupling in robot manipulators

The second key section in the literature review focuses on dynamic decoupling in robotic systems. In recent years, industrial robots have been widely utilized for high-precision tasks [38]. They are designed for diverse tasks such as painting, welding, manufacturing, and assembly, emphasizing the need for accuracy, speed, and versatile manipulation. In response to this demand, robot control is a critical element for robot manufacturers, and a great deal of development work was carried out to enhance the performance of robot manipulators, reduce their cost and introduce new functionalities. In terms of controller design, robustness, tracking accuracy, energy consumption and computational burden are essential factors that should be taken into consideration [39]–[46]. However, the inherent nonlinearity and coupling in robot manipulator dynamics are well-known challenges that can lead to a degradation in control performance at high speeds [47], [48]. The complex dynamics of robot manipulator results from varying inertia and interactions between the different joints. Furthermore, the nonlinear coupled dynamics of robot manipulator contributes to increased energy consumption and computational burden of the controller [47]. To address this challenge, various nonlinear control strategies have been developed, such as feedback linearization [49].

Widely adopted for controlling nonlinear systems, feedback linearization is a tool that effectively cancels the nonlinearities in robot dynamics [50], [51]. Through this approach, the closed-loop system can be transformed into a nominally linear form, facilitating the application of linear control techniques in controller design. However, it should be noted that feedback linearization requires an accurate model and high sampling rate for successful implementation [52]. Additionally, the computational burden resulting from nonlinear and coupled terms cannot be avoided with complex robot structures in feedback control [53], [54].

For example, computed torque (CT) control is a well-known control law that combines a proportional-derivative (PD) term and the feedback dynamic compensation term calculated from the actual velocity and desired acceleration signals [55]. CT control provides a wide range of advantages in control process, such as high tracking accuracy, low energy consumption, and more compliant control. However, an important limitation of CT control is the requirement for accurate analytical dynamic models to generate compensation torque, which cannot always be obtained due to modeling errors and unknown disturbances [56]. Inaccurate models lead to low tracking performance with CT controller, and the computational burden also becomes significant when controlling a robot manipulator with complex structure.

Due to the inherent nonlinearity in robot manipulator dynamics, designing an efficient controller becomes a challenging task. Some researchers suggest removing the complex inertia terms in the controller, as they are considered negligible at low speeds [57], [58]. However, at high motion speeds, the errors in the model resulting from this approach become significant and may likely impact the stability, leading to loss of effectiveness in tracking performance.

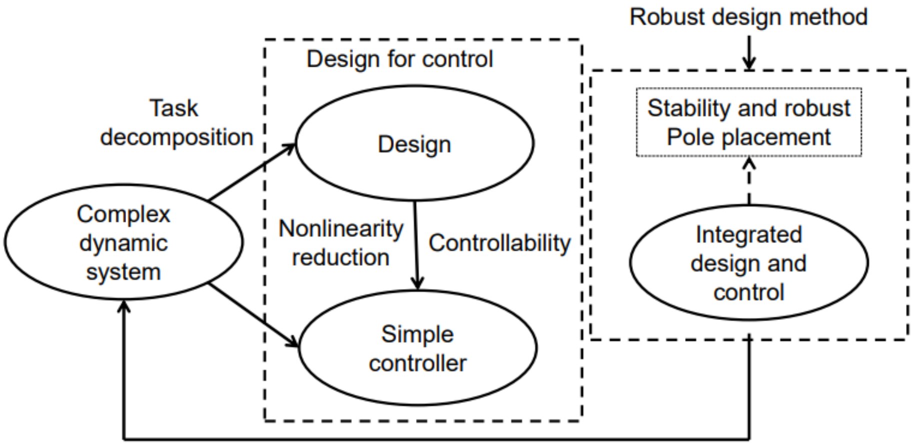

Figure 1.10 – "Design for control" methodology [59].

As described above, it is challenging to find a simple and effective strategy for controlling robot manipulators due to the presence of model nonlinearities and errors. To resolve this problem, a mechatronic design methodology known as Design For Control (DFC) was proposed by [60]. The method indicates that the performance of the mechatronic system relies not only on the controller design but also on the design of its mechanical structure. It has also been indicated in [59] that the controller design is usually considered subsequent to mechanical design, but an appropriate mechanical structure design can yield a simplified dynamic model and thereby facilitates the controller design process, as shown in Fig. 1.10. Through dynamic decoupling, a simplified dynamic system is achieved, enabling the utilization of effective and straightforward control techniques rather than complex nonlinear ones. In general, there are three ways to create dynamically decoupled manipulators through mechanical modifications: i) via mass redistribution; ii) via actuator relocation; iii) via the addition of auxiliary links. Let us review these principal dynamic decoupling techniques.

1.2.1 Dynamic decoupling via mass redistribution

Generally, the mass properties and the kinematic structure determine the dynamics of a manipulator. An improved redistribution of mass and modification of the arm structure could simplify the manipulator dynamics [61]. Let us review the necessary properties of mass distribution to reach this goal.

Let θ_i and τ_i, be the joint displacement and torque of the i-th joint, respectively, then the equation of motion of the manipulator is given by:

$$\tau_i = H_{ii}\ddot{\theta}_i + \sum_{j \neq i} H_{ij}\ddot{\theta}_j + \sum_j \sum_k \left(\frac{\partial H_{ij}}{\partial \theta_k} - \frac{1}{2}\frac{\partial H_{jk}}{\partial \theta_i} \right) \dot{\theta}_j \dot{\theta}_k + \tau_{gi} \tag{1.11}$$

where H_{ij} denotes the $i-j$ element of the manipulator inertia matrix, and τ_{gi} is the torque applied on the i-th joint due to gravity. The first term on the right side of this equation represents the inertia torque generated by the acceleration of the i-th joint. The second term is the interactive inertia torque caused by the accelerations of the other joints, which is linearly proportional to acceleration. The third term accounts for the nonlinear velocity torques arising from the Coriolis and centrifugal effects. Considering the inertia matrix that reduces to a diagonal matrix for an arbitrary arm configuration, then the second term in equation mentioned above vanishes and no interactive torques appear. The equation of motion is reduced to:

$$\tau_i = H_{ii}\ddot{\theta}_i + \sum_k \left(\frac{\partial H_{ii}}{\partial \theta_k}\dot{\theta}_j \dot{\theta}_k - \frac{1}{2}\frac{\partial H_{kk}}{\partial \theta_k}\dot{\theta}_k^2 \right) + \tau_{gi} \tag{1.12}$$

It is important to observe that the quantity of terms in this equation is considerably smaller compared to the original number of nonlinear velocity torques. This reduction

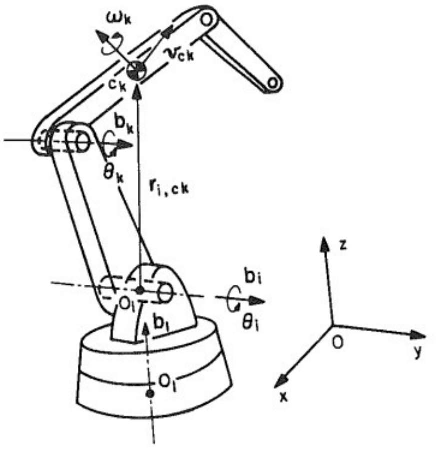

Figure 1.11 – A manipulator arm with open kinematic chain [61].

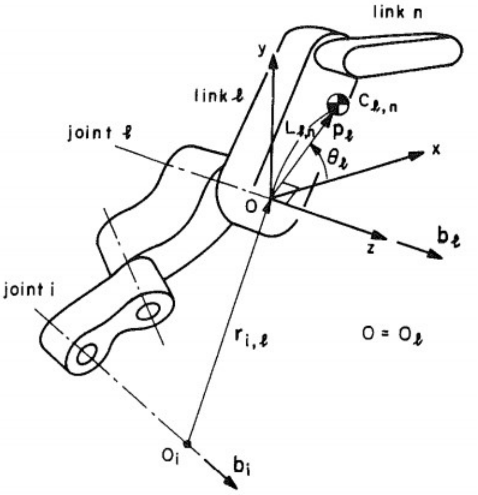

Figure 1.12 – Joints of manipulator [61].

results from the fact that all off-diagonal elements for $\theta_1, ..., \theta_n$ are zero. The consequence of this is a significant simplification in the computational complexity associated with the calculation of nonlinear torques.

Then, considering that the inertia matrix in this case does not vary from an arbitrary arm configuration, the third term in first equation vanishes and the equation of motion reduces to

$$\tau_i = H_{ii}\ddot{\theta}_i + \tau_{gi} \tag{1.13}$$

The system is completely decoupled and linearized, except the gravity term. Thus, the system can be treated as single-input, single-output systems with constant parameters. In order to eliminate the coupling and nonlinear torques, the inertia matrix must be diagonalized and made invariant for all the arm configurations. Then, let us review the necessary and sufficient conditions for an open-kinematic-chain manipulator arm to possess a decoupled and configuration-invariant inertia matrix.

As shown in Figs. 1.11-1.12, a manipulator arm is considered to be an open kinematic chain comprising revolute joints. The joints are sequentially numbered from 1 to n. The connection between joints i and $i+1$ defines link i. The axis direction of joint i is indicated by a unit vector $\mathbf{b}_i$, while the rotation of link i is represented by θ_i, denoting the angle of rotation around the unit vector. The centroid of link k is marked as point c_k in the figure, with the velocity vector of the centroid designated as $\mathbf{v}_{c_k}$, and the angular velocity vector as ω_k. Assuming m_k and $\mathbf{I}_k$ represent the mass and inertia tensor of link k with reference to the inertial reference frame, the total kinetic energy of links from 1 to n can be expressed as:

$$K = \sum_{k=1}^{n} \frac{1}{2}(m_k \mathbf{v}_{c_k}^{\top} \mathbf{v}_{c_k} + \omega_k^{\top} \mathbf{I}_k \omega_k) \tag{1.14}$$

where the angular velocity ω_k is given as:

$$\omega_k = \sum_{i=1}^{k} \mathbf{b}_i \dot{\theta}_i \tag{1.15}$$

To illustrate the linear velocity of the centroid c_k, the position vector $\mathbf{r}_{i,c_k}$ is employed, which connects an arbitrary point on the i-th joint axis to the centroid c_k.

$$\mathbf{v}_{i,c_k} = \sum_{i=1}^{k} \mathbf{b}_i \dot{\theta}_i \times \mathbf{r}_{i,c_k} \tag{1.16}$$

Substituting equation 1.16 and 1.15 into equation 1.14 yields:

$$K = \frac{1}{2} \sum_{i=1}^{n} \sum_{j=1}^{n} H_{ij} \dot{\theta}_i \dot{\theta}_j \tag{1.17}$$

where H_{ij} is the $i - j$ element of the $n \times n$ manipulator inertia matrix given by:

$$H_{ij} = \sum_{k=max[i,j]}^{n} \Big[m_k (\mathbf{b}_i^{\top} \mathbf{b}_j \cdot \mathbf{r}_{i,c_k}^{\top} \mathbf{r}_{j,c_k} - \mathbf{b}_j^{\top} \mathbf{r}_{i,c_k} \cdot \mathbf{b}_i^{\top} \mathbf{r}_{j,c_k}) + \mathbf{b}_i^{\top} \mathbf{I}_k \mathbf{b}_j \Big] \tag{1.18}$$

Thus, all the elements of inertia matrix are expressed with the parameters of manipulator. In order to make the inertia matrix diagonalized and invariant, several propositions have been indicated in [61].

- For manipulator arms with an open-kinematic-chain structure, the inertia matrix cannot be decoupled unless the joint axes are orthogonal to each other. When $\mathbf{b}_i^{\top} \mathbf{b}_l = 0$, namely the two joint axes are orthogonal, as shown in Fig. 1.13.
- The necessary and sufficient conditions for an open-kinematic-chain manipulator arm to possess a decoupled and configuration-invariant inertia matrix are related to the mass properties.

Based on these dynamic decoupling conditions, various examples were developed in literature. Youcef-Toumi and Asada proposed two kinds of 2-DOF serial manipulators with decoupled and configuration-invariant torques [61] (Fig. 1.14). Their two joint axes

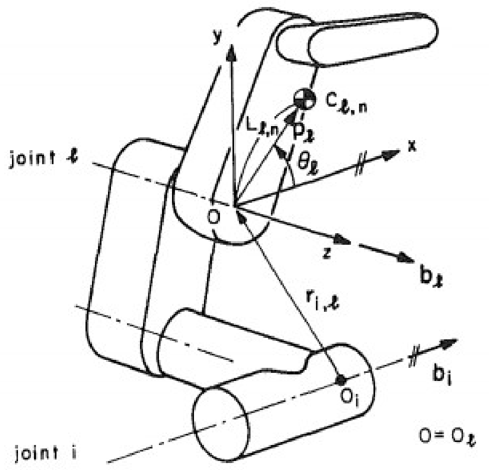

Figure 1.13 – Manipulator with two orthogonal joint axes [61].

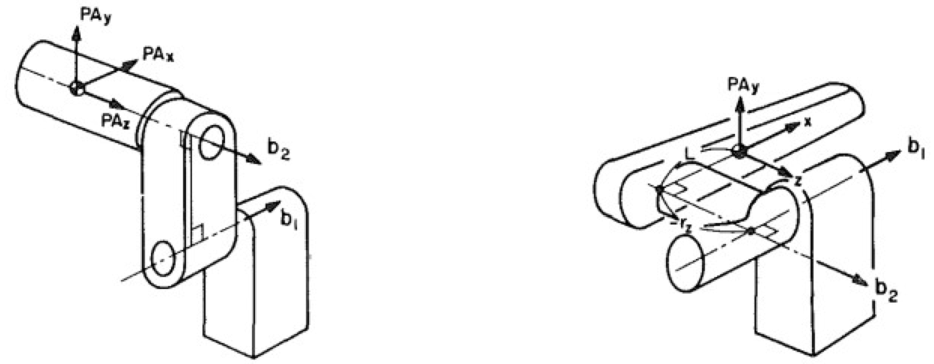

Figure 1.14 – Two kinds of 2-DOF manipulators with decoupled and configuration-invariant inertia matrix [61].

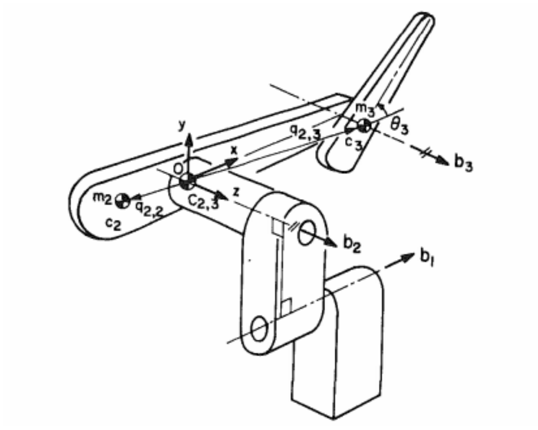

Figure 1.15 – 3-DOF manipulators with configuration-invariant inertia matrix [61].

are orthogonal and different mass property conditions should be satisfied for ensuring a decoupled and configuration-invariant inertial matrix (see detail in [61]).

It has also been found in [61] that the dynamic decoupling conditions via mass redistribution cannot be achieved in the serial manipulators with more than 2-DOF. However, for reducing the nonlinear velocity torques in Eq. (1.11), it is possible to achieve the configuration invariance of the inertia matrix through mass redistribution in these manipulators. For example, as shown in Fig. 1.15, the mass centers of last two links in 3-DOF manipulators should be located at $\mathbf{b}_2$ and $\mathbf{b}_3$ respectively. Besides, the inertia matrix of the last two links must satisfy several quite complex mass property conditions, which is not practical in applications. For decoupling, it could be also noted that the mass redistribution technique is applied to serial manipulators in which the axes of joints are not parallel. In the case of parallel axes, such an approach cannot be used for achieving a dynamic decoupling.

1.2.2 Dynamic decoupling via actuator relocation

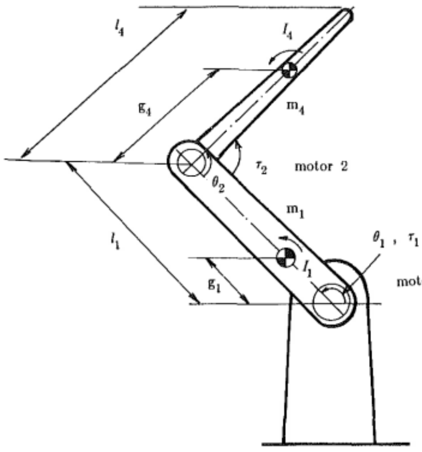

Figure 1.16 – General structure of 2-DOF manipulator.

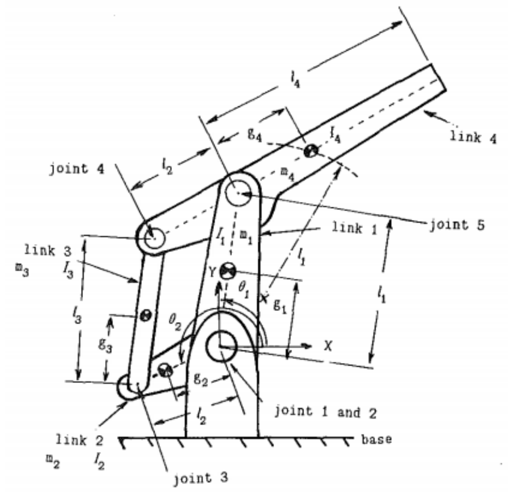

Figure 1.17 – 2-DOF manipulator structure with actuator relocation [62].

As discussed in the previous section, there are some drawbacks associated with dynamic decoupling via mass redistribution in open chain mechanisms. For instance, while it is possible to decouple an arm inertia matrix for spatial 2-DOF systems, the same approach is not practical for planar mechanisms due to the nature of inertial matrix. This limitation arises from the parallel configuration of joint axes in planar mechanism, making it difficult to achieve decoupling through only the mass redistribution. Applying mass redistribution alone is insufficient for the decoupling of manipulators with more than 3-DOF. Faced with these limitations, actuator relocation stands out as a possible solution. This involves mounting actuators remotely instead of directly at the joints of the open kinematic chain.

The general configuration of the 2-DOF planar manipulator is depicted in Fig. 1.16. In this arrangement, the lower link is actuated by a motor fixed on the base, while the upper link is driven by a motor located at the extremity of the lower link. The weight of the second motor imposes a load on the first motor, and additionally, the reaction torque of the second motor affects the first motor. Notably, when the second motor accelerates in the clockwise direction, it induces a counter-clockwise torque on the first motor, and vice versa. Consequently, these two motors exhibit significant interactions.

Asada and Youcef-Toumi proposed the first 2-DOF planar manipulator structure with actuator relocation [62]. Two motors fixed on the base drive the two input links and cause a two-dimensional motion at the tip of the arm, as shown in Fig. 1.17. The weight of one motor is not a load on the other. The distance between the two motors is zero and the two pairs of opposite links are parallel. Besides, the interactive inertia torques are eliminated through the modification of the mass ratio or the mass center distance ratio of link 3 and link 4. Thus, the inertia matrix is invariant and completely decoupled. A prototype was fabricated in Fig. 1.18, which demonstrated the effectiveness of the actuator relocation in dynamic decoupling and also the control performance improvement due to its simplified dynamics.

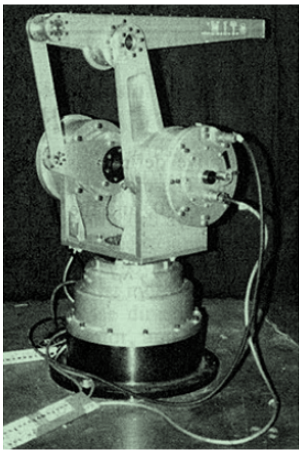

Figure 1.18 – Prototype with actuation relocation [62].

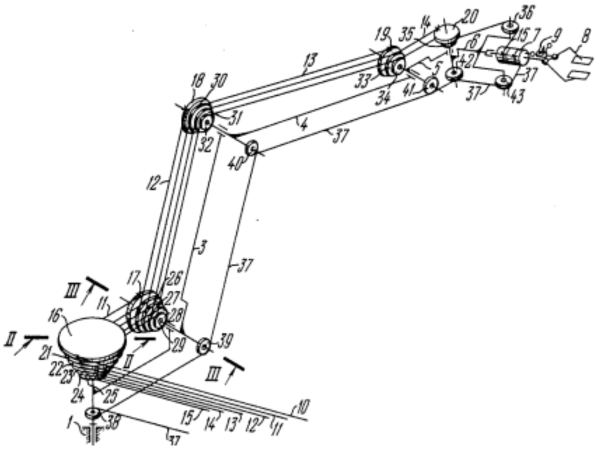

Figure 1.19 – Remote actuation via cable transmission system [63].

As shown in Fig. 1.19, to achieve the actuator relocation, the transmission mechanism consisting of cables or belts is often utilized and it is capable of reducing the total weight of the decoupled manipulator. However, a review [64] has shown that the remote-actuation design concept is not optimal from the point of view of precise reproduction of the end-effector tasks, because it accumulates all errors due to intermediate transmissions. It is evidently much better to connect actuators directly to the links than to use transmission mechanisms. The clearance, flexibility, manufacturing and assembly errors of the added transmission mechanisms have a negative impact on the robot's precision.

1.2.3 Dynamic decoupling via adding auxiliary links

The linearization of the dynamic equations and their decoupling by adding auxiliary links has been developed in [65]–[68]. In this case, the added complementary links allow the optimal redistribution of kinetic and potential energies, which leads to the linearization and decoupling of the dynamic equations. The determination of the parameters of the added links is based on eliminating coefficients of nonlinear terms in the manipulator's kinetic and potential energy equations, especially the off-diagonal parameters in the inertial matrix.

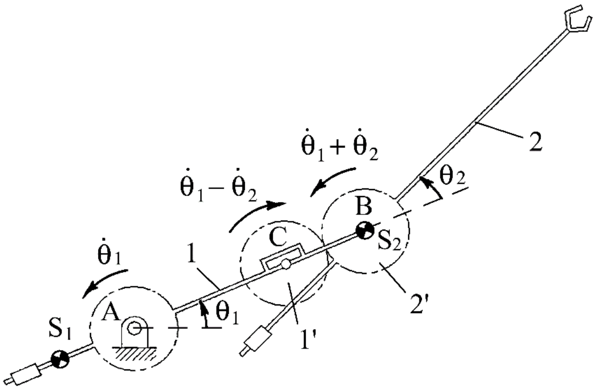

Figure 1.20 – A 2-DOF decoupled manipulator with adaptive balanced mechanism proposed in [66].

Coelho *et al.* [66] has claimed that its design methodology proposed is the first time for achieving dynamic decoupling, in which the adaptive balancing technique is applied by adding the auxiliary links. As shown in Fig. 1.20, to eliminate the terms due to cross inertia in Eq. (1.11), a rotor is mounted on the link 1 by a revolute joint. This rotor is also geared to link 2 and rotates in opposite direction. Although the mass of the rotor remains unchanged, its mass of inertia can be altered through moving the radial position of the compensation inertias connected to it by prismatic joints. By appropriately selecting the values and positions of the compensating inertias, it is possible to cancel out terms arising from cross inertia. As a result, the dynamic equations of the 2-DOF manipulator are decoupled (more detail in [66]).

The dynamic decoupling proposed by [66] is innovative, but the main drawback is leading the unavoidable increase of the total mass of the manipulator. The added elements are mounted at the end of each link. To resolve the problem, a solution has been proposed in [67], which permits the dynamic decoupling of the serial manipulators with a relative small increase in the total mass of the moving links.

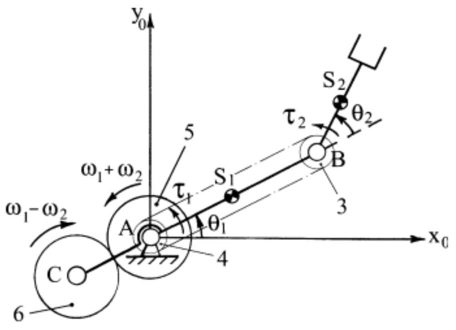

Figure 1.21 – A decoupled 2-DOF planar serial manipulator proposed in [67].

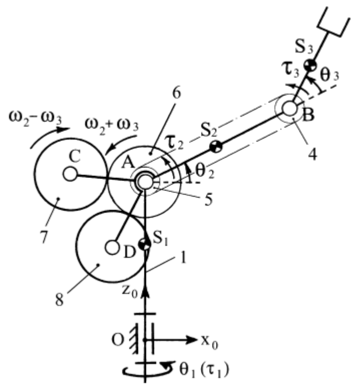

Figure 1.22 – A decoupled 3-DOF spatial serial manipulator proposed in [67].

As shown in Fig. 1.21, to achieve the dynamic decoupling in 2-DOF planar manipulator, the addition elements are added: two counter rotating links 5 and 6 are mounted on actuated element 1 and linked kinematically with second actuated element 2 through a belt transmission. In the case of the 3-DOF spatial serial manipulator (Fig. 1.22), two rotating gears 7 and 8 are mounted on the second link of the manipulator and coupled with gear 6 linked with third link through a belt transmission.

In contrast to the dynamic decoupling achieved through actuator relocation, the utilization of motors mounted directly at the joints of the link offers the advantage of reduced error accumulation attributed to belt transmission clearances and elasticity. In comparison to the design in [66], where two gears are affixed to the frame or extension of link 1, this approach significantly decreases the overall masses of the decoupled manipulator's

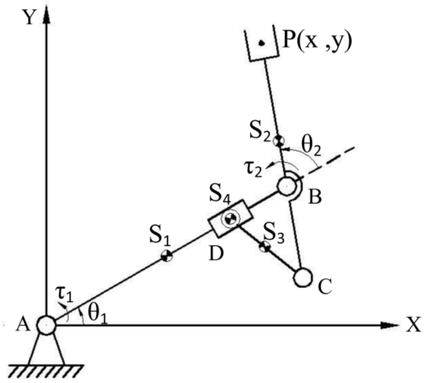

Figure 1.23 – A 2-DOF decoupled manipulator with Scott-Russell mechanism [69].

links. Nonetheless, a noteworthy limitation of this design is the occurrence of shocks and noise between the teeth due to the connection of gears to the oscillating links.

In [69], the dynamic decoupling of the planar manipulator involves connecting to initial structure a two-link group forming a Scott-Russell mechanism. Fig. 1.23 shows such a robot arm, which consists of two principal links AB, BP and a sub-group with links BC and CD. The movements of this manipulator are planar motions which are perpendicular to the vertical plane, and therefore not subjected to gravitational forces. The slider D can slide freely along the link AB, and it's connected with link CD by revolute joint D. Thus, the added sub-group with links BC, CD and the slider forms with link BP of the original structure a Scott-Russell mechanism. The Scott-Russell mechanism [70] has been invited to generate a theoretically linear motion by using a linkage form with three portions of the links all equal, and a rolling or sliding connection.

The motion of links in the Scott-Russell mechanism combined with optimal redistribution of masses allows the cancellation of the coefficients of nonlinear terms in the manipulator's kinetic and potential energy equations. Then, by using the optimal control design, the dynamic decoupling due to the changing payload is achieved. It becomes relatively easy because in the modified structure of the manipulator with two-link group the coupling and the nonlinearity has been cancelled. However, due to the addition elements added in the manipulator, the decoupling condition is usually achieved by modifying a number of manipulator parameters.

The study [71] provided a tolerance analysis of the 2-DOF decoupled manipulator with Scott-Russell mechanism. It showed that, in the presence of parameter uncertainties, the tracking accuracy of this manipulator was higher than the ones decoupled by feedback linearization and the coupled manipulator. According to their results, the tracking accuracy is more sensitive to the length variables and the mass parameters. However,the parameter errors also lead to incomplete dynamic decoupling and their influences on the input torques are not taken into account. Furthermore, the used statistic method did not consider the interactive effects of the parameter errors.

Current challenges: The literature review uncovers different dynamic decoupling methods. However, a promising opportunity lies in creating methods that blend the diverse approaches mentioned above. Importantly, after dynamic decoupling, the equations of motion shift to linearity with respect to accelerations for each degree of freedom. This paves the way for the development of techniques aimed at minimizing the maximum values of input torques.

1.3 Design principles in upper-limb wearable robotic exoskeletons

1.3.1 Applications of robotic exoskeleton in upper-limb assistance

In the last decade, exoskeleton robots have become one of the potential solutions for assisting the patients with locomotor disability or amplifying physical strength of workers in industrial field [72], [73]. Locomotor disability is the most frequently reported type of disability. It is defined as a person's inability to perform the activities of daily living (ADLs) associated with moving oneself and objects from one place to another, and results from musculoskeletal or nervous system disorders. According to a report published by the World Health Organization (WHO) [74], stroke is a leading cause of acquired disability in adults. In 2030, nearly 23 million people will suffer from stroke, which will lead to 8 million stroke deaths if secular trends continue. One-third of surviving patients from stroke do not regain their limb motor function completely. Aging of population will also aggravate the situation and increase the number of people with locomotor disabilities. As reported in [75], in France, one Frenchman by three will be aged 60 years older in 2050, who will be more likely to suffer from the locomotor disabilities. Thus, faced with these hard situations, the WHO has recommended a number measures to enable people with disabilities to participate more fully in social activities and decision-making. The WHO has also encouraged more scientific research into disability to improve the situation.

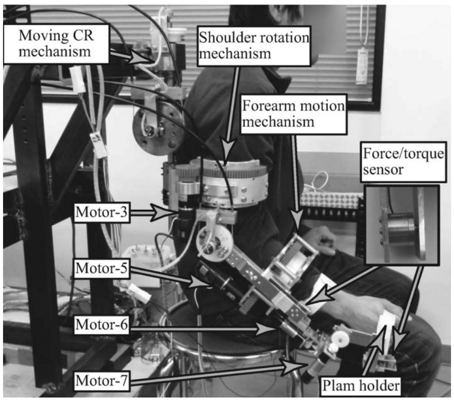

Figure 1.24 – Power-assist exoskeleton for physically weak persons [77].

Figure 1.25 – Muscle suit for static holding [78].

Assistive devices have been considered as one of the potential solutions to help the patients with locomotor disabilities participate in more daily activities by amplifying their basic limb strength. To compensate for loss of use of lower limbs, the use of a wheelchair is considered as an efficient solution for the comfort and mobility of patients. According to Janssen et al. [76], upper-limb assistance for every task is more challenging, such as bringing hands to mouth and shifting while seated. Although a robot manipulator with a robotic hand as effector could help the patients achieve their daily tasks, an upper-limb exoskeleton is more appropriate as the daily tasks could be achieved with their own dexterity. For instance, a power-assist exoskeleton robot has been developed in [77] to assist physically weak persons such as elderly, disabled, or injured person in self-rehabilitation or daily-life motions (shown in Fig. 1.24). But the kinematics of the human hand is quite complex and its behavior is quite impossible to reproduce. One important advantage of exoskeleton for upper-limb is to maintain the functionality of the human hand.

Besides, in industrial field, workers have become the patients suffering from work-related musculoskeletal disorders (WMSDs). Franco and Fussetti [79] suggest Bernardino Ramazzini's early observation of the link between musculoskeletal disorders and ergonomic factors from the jobs requiring heavy muscular performance, such as porters and wood-workers. The results in [80] show that some ergonomic factors, such as physical overload, compulsive working postures and repetitions are the risk factors of developing the WMSDs. Physical overload causes the fatigue and even injury of muscles like the bicep, anterior deltoid, spinal extensor etc. It is also found that the workers experience WMSDs,

Figure 1.26 – FORTIS [83].

Figure 1.27 – Hybrid exoskeleton [84].

notably impacting the body parts with high local stiffness muscles such as shoulder, neck and upper limb [81], [82]. To reduce the risk of WMSDs, the efficacy of exoskeleton robots has been proved in terms of physical load reduction provided [72]. For example, a muscle suit developed in [78] assists the worker in vertical lifting (shown in Fig. 1.25). For static holding above the head, it could bring a reduction in muscle activity for the biceps brachii by 30% to 70%.

The field of exoskeleton robots can be categorized into two groups: rigid exoskeletons and soft exoskeletons, distinguished by their material composition. In the subsequent sections, their design principles will be reviewed.

1.3.2 Rigid exoskeletons for upper-limb power assistance

It is clear that there is a growing demand of assistive exoskeleton robots for patients with upper-limb impairment. Many researchers have conducted their research in the field of wearable assistive robots and several upper-limb exoskeletons, consisting of mainly of linkages and rigid frames, have been designed for purposes ranging from physical assistance for patients [77], [85]–[87] to physical strength amplification of workers [84], [88]–[90].

In factories, prolonged use of hand tools like drills and welding guns can lead to physical exhaustion, muscle fatigue, and injuries. Lockheed Martin's FORTIS exoskeleton (Fig. 1.26) addresses this issue by enabling operators to effortlessly handle heavy tools, enhancing strength and endurance [83]. Weighing under 12.3 kg, FORTIS redistributes the weight of tools to the ground through joints at hips, knees, and ankles. A key advantage is its actuator-free design, allowing use in diverse environments, from factories to fieldwork.

Figure 1.28 – Cinemaker [89].

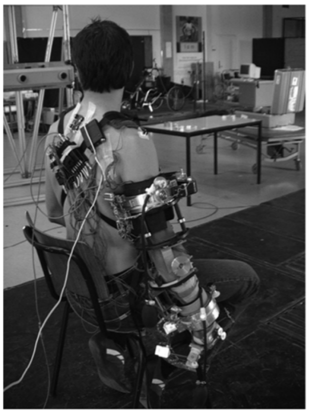

Figure 1.29 – Exoskeleton with additional mechanism [91].

The wearable device moves with the operator's natural motions during activities like standing, bending, leaning, or kneeling.

Recently, Gull *et al.* have proposed a design of hybrid exoskeleton for load-lifting assistance [84], which is built with a passive shoulder joint and an active elbow joint (Fig. 1.27). The passive shoulder joint is designed on the basis of a commercially available exoskeleton called Skelex 360, which is developed to counterbalance the gravity torque and assist users in performing overhead industrial tasks and various upper arm elevation activities. For this purpose, two flat extension springs are inserted on the backside to store potential energy when lowering the upper arm. In the hybrid exoskeleton arm, the elbow joint is actuated by a custom-made integrated driving unit capable of delivering a maximum torque of 50 Nm. The exoskeleton in this study provides passive support to the human shoulder joint and actively assists forearm movements by delivering varying levels of assistive torque.

A French company, EXHAUSS, offers a variety of exoskeletons, each specifically devised to alleviate and safeguard operators encountering diverse challenges associated with the manipulation and transportation of loads or tools [89]. In the Cinemaker design (Fig. 1.28), springs are incorporated for gravity balancing when carrying loads. The Cinemaker exoskeleton features six degrees of freedom (6-DOFs), ensuring that users can securely hold loads in various postures.

It should be admitted that rigid exoskeletons show high performance for providing large forces and torques but they have several drawbacks. Large weight and inertia of rigid exoskeletons affect the mechanical transparency. The mechanical transparency is the ability of exoskeleton robot to compensate its own weight and inertia in the case of load carrying and not to apply unwanted forces on the human body [92]. Compensation technique may be one solution to this problem. For instance, the exoskeleton designed by EXAUSS company uses spring for gravity balancing. However, the additional mechanism is heavy and not easy to handle [89]. Besides, the difference in mobility between a human joint and that of rigid exoskeleton occurs when the exoskeleton structures are oversimplified. For example, it is not sufficient to model the human shoulder joint as a spherical joint with 3-DOF, which considers only the motions of glenohumeral joint. In fact, the location of glenohumeral joint is affected by the movement of the shoulder girdle. Without taking this feature into account, excessive interaction force will be exerted on human due to the non-coincidence of joint axes [93]. To solve the problem, an additional mechanism is usually designed in rigid exoskeletons to accommodate the human body movement. Schiele and Van Der Helm [91] have proposed a kinematic design, which is capable of covering the entire workspace of the human arm, including shoulder and shoulder girdle (Fig. 1.29). However, in addition to these problems, the inertia of the exoskeleton should not be overlooked. This additional inertia makes movement of the exoskeleton-human combination more difficult.

1.3.3 "Exosuit" — the soft upper-limb exoskeletons

Avoiding the drawbacks of rigid exoskeletons, the exoskeletons with flexible structure, named “exosuits” have aroused great research interest. As opposed to the exoskeletons with rigid frames, those fabricated with soft material such as fabrics and cables are typically lighter and consume less energy. Additionally, since there are no rigid joints or frames exist in exosuits, there is few problem relating to the misalignment, contributing to enhanced human comfort and mechanical transparency.

Figure 1.30 – MAXFAS [94].

Figure 1.31 – STRONGARM [95].

The MAXFAS (Mechatronic Arm Exoskeleton for Firearm Aim Stabilization, Fig.

1.30) developed by U.S. Army Research Laboratory researchers [94] is designed to detect and mitigate arm tremors during shooting. It features three carbon fiber braces: one on the forearm and two on the upper arm. Six cables control 5-DOF, terminating at the braces with motors mounted on a fixed frame. MAXFAS, with its cable-driven and carbon fiber design, adds minimal arm weight. Unlike passive aids, it allows natural voluntary arm motion due to its control algorithm and lack of rigid joints at the shoulder and elbow. Tested with mostly inexperienced shooters, MAXFAS significantly improved shooting performance and reduced arm tremors. However, its fixed motors limit mobility.

Another assistive device proposed by STRONGARM (Fig. 1.31) utilizes a rigid frame and cable winding system for handling heavy objects. Worn on the user's body, the rigid frame connects to the user's fingers via cables. To lift a load, users stretch their arms to the load. As the load is lifted, pressure between the load and hands activates the cable locking mechanism, preventing cable unwinding. However, the finger is not a suitable body part for the application of important cable tension force. Imposing a heavy load may result in safety and comfort issues.

In [96], Mao and Agrawal have proposed a design of cable-driven exosuit for assisting and training arm movements of stroke survivors (Fig. 1.32). The exosuit also consists of rigid frames with a cable winding system. The feature like low inertia is desirable for rehabilitation. Due to the nature of cable driven systems, only pulling forces on the cables are allowed. Some postures in workspace of cable-driven exosuit may not be available. An optimization framework was proposed to enlarge the workspace of cable-driven arm exoskeleton. However, the force exerted on user was not considered in the design of exosuit, leading to human comfort problems. Moreover, the nonlinear programming method (NLP) used in their optimization is not suitable for the exosuit design with numerous design parameters, which may converge to the local optimum.

The design of an upper-limb exosuit to assist users in carrying heavy loads has been proposed by Zhang and Arakelian [95], as illustrated in Fig. 1.33. To enable the soft exosuit to adapt to various postures during load reaching, lifting, and cable locking, a cable winding and locking mechanism has been designed. No motors and control system are comprised in the suit of which the size and mass may limit the mobility when wearing the suit. They considered the forces exerted on human body in their design. An advanced optimization algorithm was adopted to minimize the forces exerted on shoulder. In addition, to evaluate the performance of the developed exosuit in a more realistic environment and validate the simulation results, a mannequin test bench has been fabricated

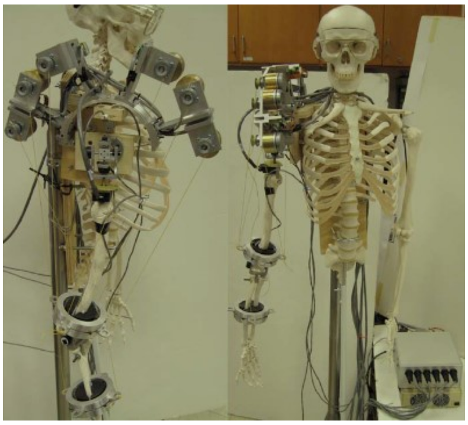

Figure 1.32 – Exosuit for assisting stroke survivors [96].

Figure 1.33 – Exosuit for heavy load carriage [95].

and tested. The test results showed that with the help of the exoskeleton, the mannequin device could hold different weights of loads steadily in different postures.

In the study on the exosuit proposed in [96], the emphasis was placed on optimizing the feasible workspace of cable tension force, which is crucial for cable actuation mechanisms. However, they did not consider the forces exerted on the user during the design phase, leading to user discomfort. The application of loads to the skeleton by upper-limb exosuit may produce excessive contact pressure, which will reduce the level of safety and comfort. Pressure magnitude and pressure distribution are related to comfort and safety. To ensure the user safety, the pressure magnitude should be lower than ischemic level (estimated at 30 mmHg), at which the capillary vessels are unable to conduct blood [97]. Another thing should be noted that not all parts of the body are suitable for transmitting loads to the skeleton. It is recommended to leave a clear space around joints and to avoid areas with surface vessels or nerves, such as medical epicondyle and lateral epicondyle of upper limb [93]. The superficial skin to the epicondyles generally has a higher density of surface vasculature and nerves versus other regions of the body [98]. For example, the ulnar nerve passes through medial epicondyle of upper limb and transmits electrical signals to muscles in the forearm and hand. Two basic strategies exist for managing a load: concentrating the load over a small area with high pressure tolerance or distributing the load as large an area as possible. The latter could prevent the pain and injury but the comfort is not guaranteed. Goonetilleke and Eng [99] have indicated that the distribution of pressure over a large area may be less comfortable for human than concentrating the pressure over a small area on the human body.

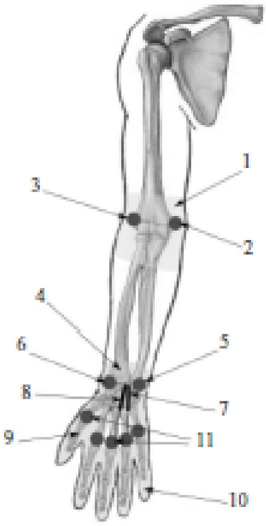

Figure 1.34 – Areas to be avoided in upper-limb exosuit design [93].

In [95] and [100], the study was devoted to an exosuit for the upper-limbs. A great attention was paid to the force exerted on the shoulder, corresponding to applying external loads over a small area with high tolerance. However, in these studies, not much attention was paid to the distribution and magnitude of the external load exerted on the soft tissues. The soft tissues transfer an important load to the skeleton and the tangential force between mechanical supports and human skin, which leads to discomfort or injury [101]. Mechanical supports should not be attached to the vulnerable area or to the upper-limb joint movement area. The joint movement area is the region surrounding the joint and the attachment points near this area could influence the range of motion. The vulnerable area is characterized by bony prominences, surface vessels or nerves, and lymphatic regions such as the axilla and groin, where the important forces applied increase the likelihood of injuries. In an upper-limb exosuit design, it should be avoided applying forces in these areas, as shown in Fig. 1.34: (1) elbow movement area; (2) medial epicondyle; (3) lateral epicondyle; (4) wrist movement area; (5) radial styloid process; (6) ulnar styloid process; (7) Guyon tunnel; (8) carpal tunnel; (9) thumb movement area; (10) finger movement area; (11) metacarpal heads.

Current challenges: As revealed above, the flexible elements hold significant promise. Nevertheless, there remains a need for deeper exploration into mitigating their energy consumption and enhancing operational behavior to effectively alleviate loads on the human body.

1.4 Thesis outline

The subsequent chapters address the following issues:

- Chapter 2 develops a novel approximate solution for determining joint reactions and energy loss in mechanical systems, considering the influence of Coulomb friction. It is widely recognized that obtaining an exact solution for the equilibrium equations of a mechanism with Coulomb friction entails solving nonlinear systems of equations. With the abundance of computer tools available today, this task is not particularly challenging, especially when it comes to numerical computations. However, the relevance of developing new analytically tractable approximate methods that provide a straightforward resolution to this problem remains pertinent. Several studies have been conducted in this area to find simple solutions to the problem. Nonetheless, the approach presented in this chapter is, in our opinion, the simplest among the existing methodologies. To demonstrate the effectiveness of the proposed method, numerical simulations will be carried out in different mechanisms and robot manipulators.

- Chapter 3 introduces the dynamic decoupling technique in spatial serial manipulators, resulting in torque minimization and control performance improvement. The dynamics of robot manipulator is known to be highly nonlinear and coupled, which can lead to high computational burden or even additional energy consumption in control process. Thus, the decoupling techniques such as mass redistribution and actuator relocation are introduced in spatial serial manipulators for achieving a linear and decoupled dynamic system. Next, an efficient motion profile is applied for reducing the input torques of decoupled manipulators. In spatial serial manipulators, it should be noted that their design parameters are implicated in the decoupling process and the parameter errors may lead to incomplete dynamic decoupling. To identify the influential design parameters during the decoupling process, a comprehensive global sensitivity analysis is conducted. Then, due to the simplified dynamic system of decoupled manipulators, various straightforward controllers are employed for enhancing the control performance, including tracking accuracy and energy efficiency. Numerical simulations demonstrate the performance enhancement in spatial serial manipulators.

- Chapter 4 presents a design of an exosuit for upper-limb power assistance. Since there are no rigid frames and links in the exosuits, they are much lighter and have less misalignment problems than the rigid exoskeletons. However, excessive pressure exerted by cables on soft tissues and skeleton of the human leads to discomfort or even injuries. This chapter discusses the improvement of these aspects in exosuit design. A cable transmission system is incorporated into the exosuit system for gravitational compensation. Then, a multi-criteria optimization approach, based on swarm intelligence, is developed and employed for reducing the uncomfortable forces applied on the user in the exosuit design. Furthermore, the energy consumption is also taken into account in the design phase. Compared to the existing studies, a larger number of exosuit performance criteria are taken into account. In addition, it is proposed an advanced optimization framework that enables efficient optimization processes by distinguishing and prioritizing different objectives in a nonlinear exosuit model, which is to our knowledge the first instance in the literature. Another important contribution of this work is the identification of two design parameters that have the strongest positive influence on optimization criteria, providing valuable information during the design phase.

- Chapter 5 introduces an experimental step aimed at validating the exosuit design with reduced energy consumption. Firstly, the proposed optimization framework is applied to enhance the energy efficiency of the demonstrator-mannequin upper-limb. This involves determining the optimal arrangement of attachment and anchor points. Subsequently, various electronic components are incorporated to form a feedback control loop and the measurement of energy loss power is conducted for both optimal and non-optimal exosuit designs. The experimentation conclusively illustrates that the optimal exosuit design can be used for load carriage applications, resulting in a substantial reduction of energy consumption.

Chapter 2

ESTIMATION OF ENERGY LOSS IN MECHANICAL SYSTEMS DUE TO THE FRICTION: A NEW SOLUTION TO FORCE ANALYSIS INCLUDING COULOMB FRICTION

2.1 Force analysis including Coulomb friction in mechanism joints 58
2.2 Proposed solution based on the Babylonian method 62
2.3 Illustrative examples and numerical simulations 70
2.4 Summary 90

Friction exists in most mechanical systems, and it has a major influence on their energy efficiency performance and durability. Understanding and identifying friction in mechanisms is valuable for comprehending wear processes and determining effective ways to influence them. Static friction models have found extensive application in the modeling of mechanical systems due to their simplicity and the small number of parameters to be identified. This chapter describes a clear and extremely simple approach for determining the reactions of joints in mechanical systems, which involves the influence of Coulomb friction. It allows one to find an approximate solution that is quite close to the exact solution, offering valuable insights into the energy consumption of robotic systems.

This chapter is organized as follows: The first section presents the force analysis considering Coulomb friction in mechanism joints. The second section introduces a new approximation technique based on the Babylonian method. The third section provides illustrative examples, including three different types of mechanisms, to demonstrate the effectiveness of the proposed method. Finally, the last section discusses the conclusions and perspectives.

2.1 Force analysis including Coulomb friction in mechanism joints

As discussed in Chapter 1, the consequences brought out by friction are serious and special attention should be paid to this phenomenon when designing mechanical systems. Two main categories of friction model (static and dynamic models) were reviewed previously. The selection of friction models is a trade-off between accuracy and computational efficiency [16]. However, the study of [19] has indicated that a static friction model like Coulomb friction is a suitable choice for most of the dynamic systems where friction does not play a main role. For instance, in many engineering problems, the friction is often treated as Coulomb friction due to its simplicity, which is the most well-known static model and indicates that the direction of friction is opposite to the relative motion between two surfaces and the magnitude is always proportional to the normal contact force. Though Coulomb friction model has been criticized for its discontinuity at zero velocity [17], [102], it is widely applicated in design of mechanical system because of its simplicity and low computational burden [103]–[105]. To deal with the zero discontinuity, different approaches, like introducing a smooth function, are employed, which is not included in the plan of this work [106].

This chapter introduces a novel approach to force analysis including Coulomb friction in the mechanical joints of multilink or multiloop mechanisms, which is very practical for engineers to employ and provides valuable insights of energy consumption and loss in mechanism design. Nowadays, although the solution of many nonlinear calculation problems including force analysis could be obtained with the help of computer software, it is always desirable and meaningful to develop the simplest algorithm to accelerate the design process, which can be employed without complex computer program.

2.1.1 Equilibrium equations considering the Coulomb friction

As reviewed in Chapter 1, the Coulomb friction between the surfaces of two sliding objects can be expressed as follows [18]:

$$\mathbf{F}_f = F_C \, \mathrm{sign}\left(\mathbf{v}_{\mathrm{T}}\right) \tag{2.1}$$

where,

$$F_C = \mu_k \left\| \mathbf{F}^{\mathrm{N}} \right\| \tag{2.2}$$

In which $\mathbf{F}^{\mathrm{N}}$ is the normal contact force, μ_k denotes the kinetic coefficient of friction, F_C represents the magnitude of Coulomb friction, and $\mathbf{v}_{\mathrm{T}}$ denotes the relative tangential velocity of the contacting surfaces ($\|\mathbf{v}_{\mathrm{T}}\| \neq 0$).

Analyzing the force of mechanical systems with ideal joints, i.e. joints without clearances, deformations or friction, involves equilibrium equations that are linear and can be easily solved. However, the inclusion of Coulomb friction in the equilibrium equations transforms them into a system of nonlinear equations. The proposed method enables precise determination of reactions at mechanical joints, accounting for friction, with no need to solve a system of nonlinear equations.

The advantages of the proposed method are clearly demonstrated with an example where it is applied to a planar four-bar linkage. The equilibrium equations using Coulomb friction are first described, followed by the approach of Professor Sadler and his co-researchers [107] in terms of its linearization, then the proposed solution is discussed. A comparative numerical analysis using an illustrative example is also provided to assess the effectiveness of the method.

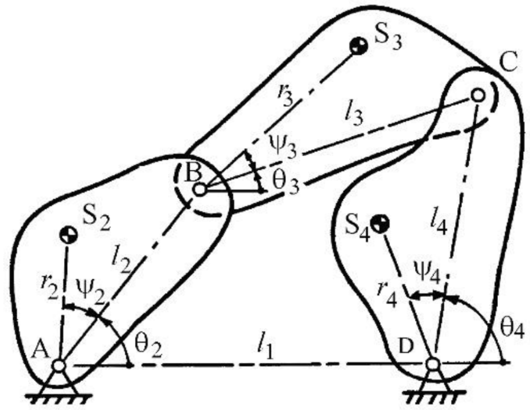

Figure 2.1 – Planar four-bar linkage.

Each link of the planar four-bar mechanism (Fig. 2.1) is defined by a length l_i between two joints, a length r_i, and an angle ψ_i, which determine the position of the center of mass. F_{ij} is the reaction force exerted by link i to link j. The solution can be obtained by considering combinations of links that are statically determined, such as 3 and 4, and solving the equation system (2.3)-(2.8) for the six unknown forces F_{23x}, F_{23y}, F_{43x}, F_{43y},

F_{14x}, and F_{14y}:

$$F_{23x} + F_{43x} = -F_{3x} \tag{2.3}$$

$$F_{23y} + F_{43y} = -F_{3y} \tag{2.4}$$

$$\begin{aligned}
&M_3 - F_{3x} r_3 \sin(\theta_3 + \psi_3) + F_{3y} r_3 \cos(\theta_3 + \psi_3) - F_{43x} l_3 \sin\theta_3 + F_{43y} l_3 \cos\theta_3 \\
&- e_{23} u_{23} \cos\theta_{23}^{\mu} \operatorname{sign}(\mathbf{v}_{32}) \left(\sqrt{(F_{23x})^2 + (F_{23y})^2}\right) \\
&- e_{43} u_{43} \cos\theta_{43}^{\mu} \operatorname{sign}(\mathbf{v}_{34}) \left(\sqrt{(F_{43x})^2 + (F_{43y})^2}\right) = 0
\end{aligned} \tag{2.5}$$

$$F_{14x} + F_{34x} = -F_{4x} \tag{2.6}$$

$$F_{14y} + F_{34y} = -F_{4y} \tag{2.7}$$

$$\begin{aligned}
&M_4 - F_{4x} r_4 \sin(\theta_4 + \psi_4) + F_{4y} r_4 \cos(\theta_4 + \psi_4) - F_{34x} l_4 \sin\theta_4 + F_{34y} l_4 \cos\theta_4 \\
&- e_{34} u_{34} \cos\theta_{34}^{\mu} \operatorname{sign}(\mathbf{v}_{43}) \left(\sqrt{(F_{34x})^2 + (F_{34y})^2}\right) \\
&- e_{14} u_{14} \cos\theta_{14}^{\mu} \operatorname{sign}(\mathbf{v}_{41}) \left(\sqrt{(F_{14x})^2 + (F_{14y})^2}\right) = 0
\end{aligned} \tag{2.8}$$

where, $F_{ijx} = -F_{jix}$, $F_{ijy} = -F_{jiy}$, $\operatorname{sign}(\mathbf{v}_{\mathrm{ij}}) = -\operatorname{sign}(\mathbf{v}_{\mathrm{ji}})$ (i = 1, 2, 3, 4; j = 2, 3, 4), $\theta_{ij}^{\mu} = \tan(F_{ij}^{T}/F_{ij}^{N})$. Note that F_{ij}^{N} is the normal components of the reaction forces and F_{ij}^{T} tangent to the contact surfaces developed by the Coulomb sliding, i.e. $F_{ij}^{T} = \mu_{ij} F_{ij}^{N}$, the coefficients of friction $\mu_{ij} = \mu_{ji}$ and the nominal bearing sizes $e_{ij} = e_{ji}$, as well as the forces F_i having the components F_{ix}, F_{iy} and the torques M_i are known and include all external and inertia loads.

A system of nonlinear equations with six unknown reactions in joints is thereby obtained, the equations for which can be solved by numerical methods for discrete positions of the mechanism [108]. Note that a similar set of nonlinear equations also emerges when the equilibrium equations for the input link 2 are presented. However, as mentioned above, it is much more desirable to find an easier solution, which is close to being exact.

2.1.2 Solution based on linearizing approximations

Before presenting the proposed method, a solution proposed by Imam, Skreiner and Sadler is briefly described [109]. This is one of the most successful linearization methods for avoiding systems of nonlinear equations.

In [109], the authors take into account that when $\theta_{ij}^{\mu} \leq 0.2$, then $\cos\theta_{ij}^{\mu} \geq 0.981$, i.e., $\cos\theta_{ij}^{\mu} \approx 1$. As a result, this simplification has minimal impact on the overall results. Thus, the friction torques from Eqs. (2.5) and (2.8) can be expressed as follows:

$$\mu_{23}e_{23}\,\mathrm{sign}(\mathbf{v}_{32})\left(\sqrt{(F_{23x})^2+(F_{23y})^2}\right)=\mu_{23}e_{23}\,\mathrm{sign}(\mathbf{v}_{32})\left(F_{23x}\cos\theta_{23}+F_{23y}\sin\theta_{23}\right) \tag{2.9}$$

$$\mu_{34}e_{34}\,\mathrm{sign}(\mathbf{v}_{43})\left(\sqrt{(F_{34x})^2+(F_{34y})^2}\right)=\mu_{34}e_{34}\,\mathrm{sign}(\mathbf{v}_{43})\left(F_{34x}\cos\theta_{34}+F_{34y}\sin\theta_{34}\right) \tag{2.10}$$

$$\mu_{14}e_{14}\,\mathrm{sign}(\mathbf{v}_{41})\left(\sqrt{(F_{14x})^2+(F_{14y})^2}\right)=\mu_{14}e_{14}\,\mathrm{sign}(\mathbf{v}_{41})\left(F_{14x}\cos\theta_{14}+F_{14y}\sin\theta_{14}\right) \tag{2.11}$$

where,

$$\theta_{ij}^{\mu}=\tan^{-1}\left(\frac{F_{ijy}}{F_{ijx}}\right) \tag{2.12}$$

However, since the correct θ_{23}, θ_{34}, and θ_{14} are not known, it is assumed that these angles do not change substantially from the case where $\mu = 0$ to the case where $\mu \neq 0$. This means that the cosine and sine values of these angles in the presence of friction are assumed to be almost the same as in the frictionless case.

The following steps are simple and clear. To solve the problem without taking into account friction, i.e. $\mu = 0$, the angles θ_{23}^0, θ_{34}^0, and θ_{14}^0 must be determined and included in Eqs. (2.9)-(2.11). By formulating a system of linear equations, it is then a straightforward task to determine the unknown reactions in the joints. The effectiveness of this method has been demonstrated by applying it successfully to a specific class of circuit-breaker mechanisms.

The method merits serious consideration as it provides a simple and clear solution to the problem at hand. By employing a systematic approach and using linear equations, it significantly reduces the complexity of determining unknown reactions in the joints, which not only streamlines the process but also enhances the overall effectiveness of solving similar problems in various engineering domains. Our observations, along with user feedback, however, have also shown that it is easy to go wrong when replacing angles θ_{23} by θ_{23}^0, θ_{34} by θ_{34}^0, and θ_{14} by θ_{14}^0, since the periodicity of the cosine and sine functions and the counter-direction of the reactions $F_{ij} = -F_{ji}$ must also be taken into account. In this regard, a new method similar to the one above but simpler, clearer, and quicker for solving this problem is developed.

2.2 Proposed solution based on the Babylonian method

2.2.1 Babylonian method for square-root approximation

To address the estimation of Coulomb friction force, let us first recall an ancient mathematical problem: how could we compute the square root $\sqrt{k}$ of a given number k. In the seventeenth century, one of the important concepts Newton-Raphson method (NRM) was employed for computing the solutions of nonlinear equations, which is a famous and widely used iterative method [110]. However, the ancient Babylonians solved this problem 3500 years ago. There exists an example drawn from old Babylonian problems involves calculating the length of the diagonal of a gate with a given height h and breadth b. The Babylonian method provides an approximation for this diagonal length, which is given by:

$$\sqrt{h^2 + b^2} \approx h + \frac{b^2}{2h} \tag{2.13}$$

Using the expression above, the ancient Babylonians were able to obtain a very close value for the length of the diagonal of a gate. However, the Babylonians did not describe their mathematical procedures in algorithmic form. Instead, they often presented multiple examples to illustrate their methods. It was the Greek mathematician Heron of Alexandria who first reformulated the Babylonian method into a general abstract form [111], which is also known as "Heron's method". In his view, the Babylonian method could be considered as an iterative process. An arbitrary positive number x_0 is first chosen as the starting point, and then the following iterated map is applied:

$$x_{i+1} = \frac{1}{2} \cdot \left(x_i + \frac{k}{x_i} \right), \; i = 1, 2, ..., n \tag{2.14}$$

where k is the radicand and x_i is the successive numerical approximation for the square root of k. n denotes the iteration number. For a clearer illustration, let us consider an example of computing the square root of 2 with this method, where $k = 2$ and x_0 is chosen as 6. Tab. 2.1 presents an example of the approximation process through the Babylonina method.

Table 2.1 – Numerical approximation to $\sqrt{2}$ using the Babylonian method with $x_0 = 6$.

i	x_i	i	x_i
0	6.000000000000000	5	1.414214157630182
1	3.166666666666667	6	1.414213562373220
2	1.899122807017544	7	1.414213562373095
3	1.476120294963737	8	1.414213562373095
4	1.415511709804956	9	1.414213562373095

From Tab. 2.1, it can be observed that after six iterations, the approximation has converged to the exact numerical value of $\sqrt{2}$, with a precision of 16 significant digits. Now, let us reconsider the equation (2.13). Indeed, the equation (2.13) represents the approximation by setting the value of x_i as h and applying Eq. (2.14). It can be seen that the approximation x_{i+1} corresponds to the expression used by the Babylonians (2.13) , with $k = h^2 + b^2$:

$$x_{i+1} = \frac{1}{2} \cdot \left(h + \frac{h^2 + b^2}{h} \right) = h + \frac{b^2}{2h} \tag{2.15}$$

To enhance the intuitive comprehension of the iterative approximation process, Fig. 2.2 shows the schematic geometric trajectory employed by the Babylonian method. In the figure, a quadratic function $f(x) = x^2 - k$ is defined, where the x-intercept is $\sqrt{k}$ and the y-intercept is $-k$. To estimate the square root of k, we start with point x_i and calculate the arithmetic mean between x_i and the auxiliary point A_i. The value of A_i is determined by the equation of the auxiliary straight line B_iC, which intersects the axis x at the auxiliary point A_i. The average of x_i and A_i yields the next point x_{i+1}. These steps are repeatedly iteratively. It is assumed that the root lies between two points, and

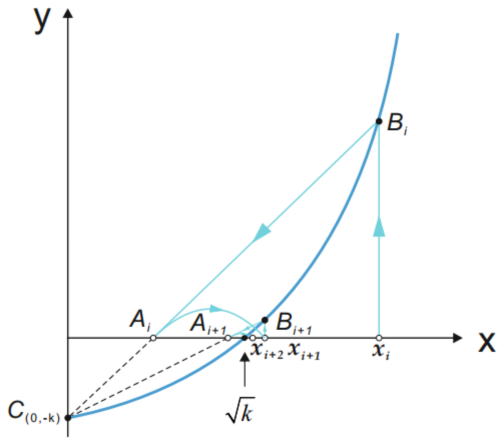

Figure 2.2 – Geometric approximation path of the Babylonian method.

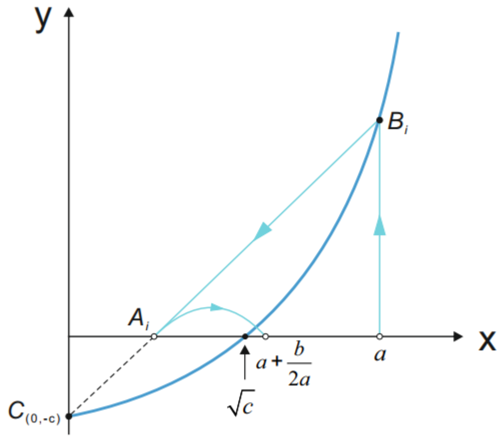

Figure 2.3 – Coulomb friction approximation with the Babylonian method.

by calculating the arithmetic mean between these two points, the root is approached progressively. The stability of convergence has been proved in [112].

2.2.2 Babylonian method in force analysis including Coulomb friction

The Babylonian method involves repeated iterations to approximate the actual square root of a number. The general idea is to start with an initial estimated value a of the square root of c, and calculate a new estimate a' using the formula:

$$a' = \frac{1}{2}(a + \frac{c}{a}) \tag{2.16}$$

The calculation is then repeated, replacing a with a', until the estimates converge to the desired precision. Note, however, that if c and a^2 are sufficiently close, a single iteration is sufficient. This is illustrated through the stability analysis in Section 2.2.3.

The reaction force between links i and j can now be determined as a sum of the reaction force without friction and the force due to friction:

$$F_{ijx} = F^0_{ijx} + \delta F_{ijx} \tag{2.17}$$

$$F_{ijy} = F^0_{ijy} + \delta F_{ijy} \tag{2.18}$$

where, F^0_{ijx} and F^0_{ijy} are the reaction forces in the revolute joints calculated without friction; F_{jix} and F_{jiy} are the reaction forces in the revolute joints with friction; δF_{ijx} and δF_{ijy} are the forces due to friction. Thus, the square of reaction force is given by:

$$F^2_{ijx} + F^2_{ijy} = \left(F^0_{ijx} + \delta F_{ijx}\right)^2 + \left(F^0_{ijy} + \delta F_{ijy}\right)^2 \tag{2.19}$$

By expanding the expression (2.19), it can be obtained as:

$$F^2_{ijx} + F^2_{ijy} = \left(F^0_{ijx}\right)^2 + \left(F^0_{ijy}\right)^2 + 2F^0_{ijx}\delta F_{jix} + \delta F^2_{ijx} + 2F^0_{ijy}\delta F_{ijy} + \delta F^2_{ijy} \tag{2.20}$$

Since the values of the reaction force in the connection with or without friction are very close, it can be considered that $\delta F^2_{ijx} \approx 0$ and $\delta F^2_{ijy} \approx 0$. The final equation can therefore be expressed as follows:

$$F^2_{ijx} + F^2_{ijy} = \left(F^0_{ijx}\right)^2 + \left(F^0_{ijy}\right)^2 + 2F^0_{ijx}\delta F_{ijx} + 2F^0_{ijy}\delta F_{jiy} \tag{2.21}$$

which can be restated as follows:

$$c = a^2 + b \tag{2.22}$$

with

$$c = F^2_{ijx} + F^2_{ijy} \tag{2.23}$$

$$a = \sqrt{\left(F^0_{ijx}\right)^2 + \left(F^0_{ijy}\right)^2} \tag{2.24}$$

$$b = 2\left(F^0_{ijx}\delta F_{ijx} + F^0_{ijy}\delta F_{jiy}\right) \tag{2.25}$$

Using the Babylonian method (see Eq. (2.16)), the following expression can be found:

$$a' = \sqrt{c} = \frac{1}{2}\left(a + \frac{c}{a}\right) = \frac{1}{2}a + \frac{(a^2 + b)}{2a} = a + \frac{b}{2a} \tag{2.26}$$

Thus,

$$F_{ij} = \sqrt{F_{ijx}^2 + F_{ijy}^2} = \sqrt{\left(F_{ijx}^0\right)^2 + \left(F_{ijy}^0\right)^2} + \frac{F_{ijx}^0 \delta F_{ijx} + F_{ijy}^0 \delta F_{ijy}}{\sqrt{\left(F_{ijx}^0\right)^2 + \left(F_{ijy}^0\right)^2}} \tag{2.27}$$

Given that c and a^2 have nearly identical values, a single iteration is sufficient. Fig. 2.3 presents intuitively the geometric path of approximation process by the Babylonian method. Thus, incorporating the above-mentioned modifications, Eqs. (2.3)-(2.8) can be presented as follows:

$$F_{23x}^0 + F_{43x}^0 + \delta F_{23x} + \delta F_{43x} = -F_{3x} \tag{2.28}$$

$$F_{23y}^0 + F_{43y}^0 + \delta F_{23y} + \delta F_{43y} = -F_{3y} \tag{2.29}$$

$$\begin{aligned} &M_3 - F_{3x} r_3 \sin(\theta_3 + \psi_3) + F_{3y} r_3 \cos(\theta_3 + \psi_3) - F_{43x} l_3 \sin\theta_3 + F_{43y} l_3 \cos\theta_3 \\ &- \mu_{23} e_{23} \operatorname{sign}(\mathbf{v}_{32}) \left(\sqrt{(F_{23x}^0)^2 + \left(F_{23y}^0\right)^2} + \frac{F_{23x}^0 \delta F_{23x} + F_{23y}^0 \delta F_{23y}}{\sqrt{(F_{23x}^0)^2 + \left(F_{23y}^0\right)^2}} \right) \\ &- \mu_{43} e_{43} \operatorname{sign}(\mathbf{v}_{34}) \left(\sqrt{(F_{43x}^0)^2 + \left(F_{43y}^0\right)^2} + \frac{F_{43x}^0 \delta F_{43x} + F_{43y}^0 \delta F_{43y}}{\sqrt{(F_{43x}^0)^2 + \left(F_{43y}^0\right)^2}} \right) = 0 \end{aligned} \tag{2.30}$$

$$F_{14x}^0 + F_{34x}^0 + \delta F_{14x} + \delta F_{34x} = -F_{4x} \tag{2.31}$$

$$F_{14y}^0 + F_{34y}^0 + \delta F_{14y} + \delta F_{34y} = -F_{4y} \tag{2.32}$$

$$\begin{aligned}
&M_4 - F_{4x} r_4 \sin(\theta_4 + \psi_4) + F_{4y} r_4 \cos(\theta_4 + \psi_4) - F_{34x} l_4 \sin\theta_4 + F_{34y} l_4 \cos\theta_4 \\
&- \mu_{34} e_{34} \operatorname{sign}(\mathbf{v}_{43}) \left(\sqrt{(F^0_{34x})^2 + \left(F^0_{34y}\right)^2} + \frac{F^0_{34x}\delta F_{34x} + F^0_{34y}\delta F_{34y}}{\sqrt{(F^0_{34x})^2 + \left(F^0_{34y}\right)^2}} \right) \\
&- \mu_{14} e_{14} \operatorname{sign}(\mathbf{v}_{41}) \left(\sqrt{(F^0_{14x})^2 + \left(F^0_{14y}\right)^2} + \frac{F^0_{14x}\delta F_{14x} + F^0_{14y}\delta F_{14y}}{\sqrt{(F^0_{14x})^2 + \left(F^0_{14y}\right)^2}} \right) = 0 \qquad (2.33)
\end{aligned}$$

Therefore, considering the given values of F^0_{ijx} and F^0_{ijy}, as well as $F_{ijx} = -F_{jix}$, $F_{ijy} = -F_{jiy}$, a system of linear equations (2.28) - (2.33) with six unknowns δF_{14x}, δF_{14y}, δF_{23x}, δF_{23y}, δF_{34x}, δF_{34y} is obtained. To obtain the desired unknowns, first, the linear equations (2.30) and (2.33) could be rewritten as follows:

$$C_1 \delta F_{34x} + C_2 \delta F_{34y} + C_3 \delta F_{23x} + C_4 \delta F_{23y} = K_1 \qquad (2.34)$$

$$C_5 \delta F_{34x} + C_6 \delta F_{34y} + C_7 \delta F_{14x} + C_8 \delta F_{14y} = K_2 \qquad (2.35)$$

where,

$$C_1 = l_3 \sin\theta_3 + \frac{\mu_{34} e_{34} \operatorname{sign}(\mathbf{v}_{43}) F^0_{34x}}{\sqrt{(F^0_{34x})^2 + (F^0_{34y})^2}} \qquad (2.36)$$

$$C_2 = -l_3 \cos\theta_3 + \frac{\mu_{34} e_{34} \operatorname{sign}(\mathbf{v}_{43}) F^0_{34y}}{\sqrt{(F^0_{34x})^2 + (F^0_{34y})^2}} \qquad (2.37)$$

$$C_3 = -\frac{\mu_{23} e_{23} \operatorname{sign}(\mathbf{v}_{32}) F^0_{23x}}{\sqrt{(F^0_{23x})^2 + (F^0_{23y})^2}} \qquad (2.38)$$

$$C_4 = -\frac{\mu_{23} e_{23} \operatorname{sign}(\mathbf{v}_{32}) F^0_{23y}}{\sqrt{(F^0_{23x})^2 + (F^0_{23y})^2}} \qquad (2.39)$$

$$K_1 = \\ -M_3 + F_{3x} r_3 \sin(\theta_3 + \psi_3) - F_{3y} r_3 \cos(\theta_3 + \psi_3) - F^0_{34x} l_3 \sin\theta_3 + F^0_{34y} l_3 \cos\theta_3 \\ + \mu_{23} e_{23} \operatorname{sign}(\mathbf{v}_{32}) \sqrt{(F^0_{23x})^2 + (F^0_{23y})^2} - \mu_{34} e_{34} \operatorname{sign}(\mathbf{v}_{43}) \sqrt{(F^0_{34x})^2 + (F^0_{34y})^2} \tag{2.40}$$

$$C_5 = -l_4 \sin\theta_4 - \frac{\mu_{34} e_{34} \operatorname{sign}(\mathbf{v}_{43}) F^0_{34x}}{\sqrt{(F^0_{34x})^2 + (F^0_{34y})^2}} \tag{2.41}$$

$$C_6 = l_4 \cos\theta_4 - \frac{\mu_{34} e_{34} \operatorname{sign}(\mathbf{v}_{43}) F^0_{34y}}{\sqrt{(F^0_{34x})^2 + (F^0_{34y})^2}} \tag{2.42}$$

$$C_7 = -\frac{\mu_{14} e_{14} \operatorname{sign}(\mathbf{v}_{41}) F^0_{14x}}{\sqrt{(F^0_{14x})^2 + (F^0_{14y})^2}} \tag{2.43}$$

$$C_8 = -\frac{\mu_{14} e_{14} \operatorname{sign}(\mathbf{v}_{41}) F^0_{14y}}{\sqrt{(F^0_{14x})^2 + (F^0_{14y})^2}} \tag{2.44}$$

$$K_2 = \\ -M_4 + F_{4x} r_4 \sin(\theta_4 + \psi_4) - F_{4y} r_4 \cos(\theta_4 + \psi_4) + F^0_{34x} l_4 \sin\theta_4 - F^0_{34y} l_4 \cos\theta_4 \\ + \mu_{14} e_{14} \operatorname{sign}(\mathbf{v}_{41}) \sqrt{(F^0_{14x})^2 + (F^0_{14y})^2} + \mu_{34} e_{34} \operatorname{sign}(\mathbf{v}_{43}) \sqrt{(F^0_{34x})^2 + (F^0_{34y})^2} \tag{2.45}$$

The next step involves expressing δF_{23x}, δF_{23y}, δF_{14x}, and δF_{14y} in terms of δF_{34x} and δF_{34y} using the expressions (2.28), (2.29), (2.31) and (2.32). These expressions can then be substituted into Eqs. (2.34)-(2.35), from which the unknowns δF_{34x} and δF_{34y} will be determined:

$$\delta F_{34x} = -\frac{C_2 K_2 - C_6 K_1 - C_2 C_7 \delta F_{14x} - C_2 C_8 \delta F_{14y} + C_3 C_6 \delta F_{23x} + C_4 C_6 \delta F_{23y}}{C_1 C_6 - C_2 C_5} \tag{2.46}$$

$$\delta F_{34y} = \frac{C_1 K_2 - C_5 K_1 - C_1 C_7 \delta F_{14x} - C_1 C_8 \delta F_{14y} + C_3 C_5 \delta F_{23x} + C_4 C_5 \delta F_{23y}}{C_1 C_6 - C_2 C_5} \tag{2.47}$$

Then, the remaining unknowns will be determined as follows:

$$\delta F_{23x} = -F_{3x} - F^0_{23x} + F^0_{34x} + \delta F_{34x} \tag{2.48}$$

$$\delta F_{23y} = -F_{3y} - F^0_{23y} + F^0_{34y} + \delta F_{34y} \tag{2.49}$$

$$\delta F_{14x} = -F_{4x} - F^0_{14x} - F^0_{34x} - \delta F_{34x} \tag{2.50}$$

$$\delta F_{14y} = -F_{4y} - F^0_{14y} - F^0_{34y} - \delta F_{34y} \tag{2.51}$$

Thus, the reaction forces in all the joints could be determined by using Eqs. (2.17)-(2.18) and the input torque of four-bar linkage is expressed as follows:

$$\begin{aligned}\tau_2 &= -F_{23x} l_2 \sin\theta_2 + F_{23y} l_2 \cos\theta_2 + F_{2x} r_2 \sin(\theta_2 + \psi_2) - F_{2y} r_2 \cos(\theta_2 + \psi_2)\\ &- \mu_{23} e_{23} \operatorname{sign}(\mathbf{v}_{32}) \sqrt{(F_{23x})^2 + (F_{23y})^2} + \mu_{12} e_{12} \operatorname{sign}(\mathbf{v}_{21}) \sqrt{(F_{12x})^2 + (F_{12y})^2} - M_2\end{aligned} \tag{2.52}$$

In comparison with the well-known solution described in Section 2.1.2 , the method proposed in this chapter is significantly simpler to apply and eliminates the ambiguities associated with angle determination, as mentioned above.

2.2.3 Stability analysis of the Babylonian method

In Section 2.2.2, it is assumed that a^2 and c are close and one iteration is therefore sufficient. When the Babylonian method is used, this condition must be verified by a stability analysis. The derivative of Eq. (2.26), the stability criterion, can be analyzed as follows:

$$f'(a) = -\frac{c - a^2}{2a^2} = -\frac{b}{2a^2} \ , \tag{2.53}$$

$$f'(a^*) = 0, \ if \ a^* = \sqrt{c} \tag{2.54}$$

It can be implied from Eqs. (2.53)-(2.54) that approximation stability is related to the derivative $f'(a)$. Since the approximated value a' is close to the exact value $\sqrt{c}$, the velocity of convergence $f'(a)$ tends towards zero and gives a small value in the approximation process [112]. As mentioned in [113], the general condition for stability in the fixed points of any one-dimensional map should be ensured:

$$|f'(a)| < 1 \tag{2.55}$$

By resolving the inequality, a suitable value a reduces the approximation error to zero, suggesting that the approximated value a' is closer to the exact value c than a. In the numerical simulations of Section 2.3, approximation stability is verified for the Babylonian approximation method.

2.3 Illustrative examples and numerical simulations

To evaluate the effectiveness of the proposed method, as well as to illustrate its application in different mechanisms, numerical simulations were carried out for a four-bar linkage, as well as 5R and 3RRR parallel manipulators, using ADAMS and MATLAB®. The approximation accuracy and stability in these mechanisms has also been verified in this section.

2.3.1 Four-bar linkage

The parameters of the four-bar linkage were defined as follows: the lengths of the links: $l_1 = 0.3$ m; $l_2 = 0.1$ m; $l_3 = 0.27$ m; $l_4 = 0.27$ m; the masses of the links: $m_2 = 1$ kg; $m_3 = 2$ kg; $m_4 = 2$ kg; the axial moments of inertial: $I_{S_2} = 8.33 \times 10^{-4}$ kgm^2; $I_{S_3} = 1.2 \times 10^{-2}$ kgm^2; $I_{S_4} = 1.2 \times 10^{-2}$ kgm^2; the locations of the mass centers: $r_2 = 0.05$ m; $r_3 = 0.135$ m; $r_4 = 0.135$ m; $\psi_2 = \psi_3 = \psi_4 = 0°$; the radius of bearings: $e_{ij} = 0.02$ m; the coefficient of friction in mechanism joints: $\mu_{ij} = 0.2$; the external and inertial moments applied to the links: $M_2 = 0$ Nm; $M_3 = 0$ Nm; $M_4 = -10$ Nm; the input angular velocity: $\dot{\theta}_2 = 0.01745$ s^{-1}; the operating range of mechanism: $\theta_2 \in [0, 2\pi]$. With the linear equilibrium equations 2.28-2.33 obtained by the Babylonian method, the forces due to friction δF_{14x}, δF_{14y}, δF_{23x}, δF_{23y}, δF_{34x}, δF_{34y}, δF_{12x}, δF_{12y} were then solved efficiently, as illustrated in Fig. 2.4.

Table 2.2 – Direction change of relative angular velocity in four-bar linkage

Relative angular angle	sign($\mathbf{v}_{32}$)	sign($\mathbf{v}_{43}$)	sign($\mathbf{v}_{41}$)
$0° \leq \theta_2 \leq 46°$	-1	1	-1
$46° < \theta_2 \leq 180°$	-1	1	1
$180° < \theta_2 \leq 243°$	-1	-1	1
$243° < \theta_2 \leq 360°$	-1	-1	-1

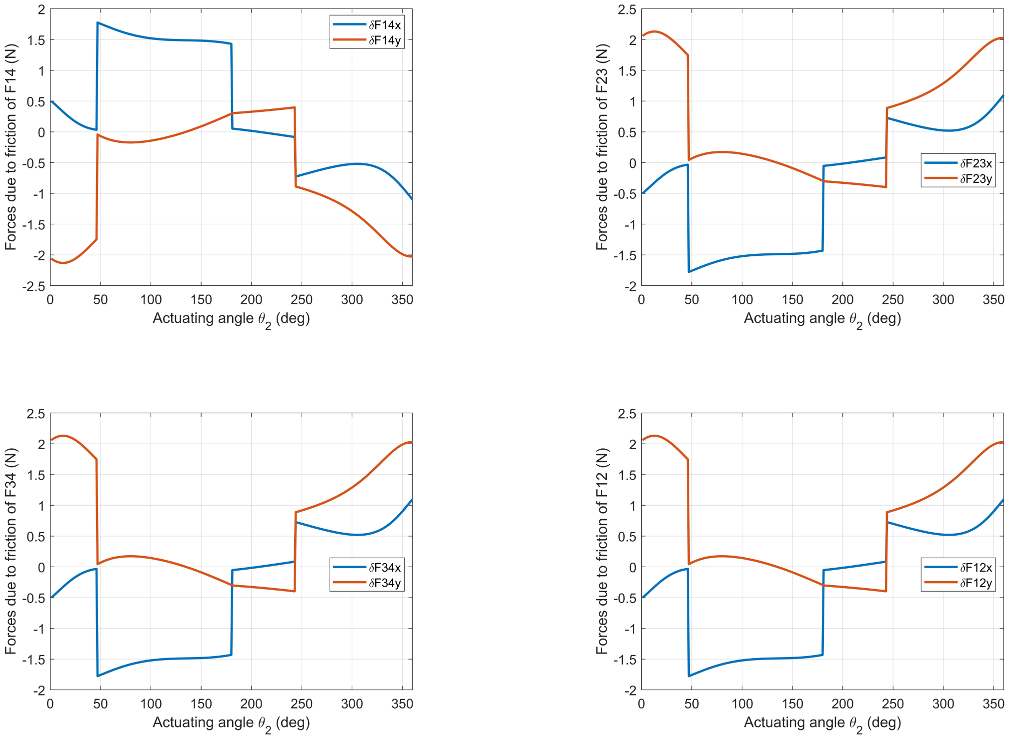

Figure 2.4 – Forces due to the friction determined from linear equations (2.28)-(2.33).

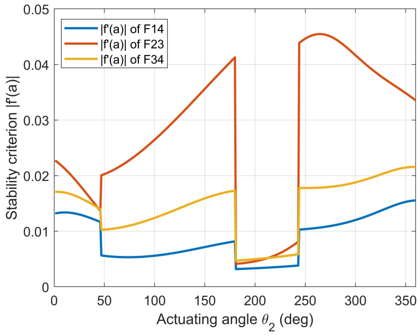

Figure 2.5 – Approximation stability analysis of four-bar linkage.

An advantage of the Babylonian method lies in its ability to provide insights into the reaction forces due to friction in mechanical design. Fig. 2.4 presents the magnitude of forces due to friction but also includes the abrupt changes at the discontinuity points. The discontinuous configurations result from the direction change of the relative angular velocity in the revolute joints of four-bar linkage. The direction of the relative angular velocity for all configurations is shown in Tab. 2.2.

Before resolving the reaction forces and input torque, let us verify the approximation stability using the criterion (2.53). It can be observed in Fig. 2.5 that the derivative $|f'(a)| < 1$ and the maximum value is less than 5×10^{-2}, which implies that the Babylonian method is capable of providing an approximated value close to the exact reaction force, by using the forces due to friction solved from the linear equations. Thus, the reaction forces in mechanism joints were then calculated using Eqs. (2.17)-(2.18), as illustrated in Fig. 2.6.

Note that the maximum error arising in the joint reactions where friction forces are disregarded does not exceed 11.42%. To assess the precision of the proposed method, the absolute error relative to the exact solution was calculated. However, this absolute value does not provide a qualitative assessment of the effectiveness of the method. To assess how closely it aligns with the exact solution, the discrepancies between the values obtained using the exact method and those using the proposed method were normalized by comparing them to the differences between the values determined using the exact method and those obtained through frictionless calculations, i.e.

$$\textbf{Approximation error} = \left| \frac{F_{ij}^{exact} - F_{ij}^{approx}}{F_{ij}^{exact} - F_{ij}^{frictionless}} \right| \cdot 100\% \tag{2.56}$$

The proximity of the proposed method to the exact solution can therefore be quantified in percentage terms. For a clearer illustration, see the depiction of reaction forces F_{14x} for $\theta_2 = 150°$ in Fig. 2.6. The approximation error here is 0.035%. This is the error between the exact and proposed methods with respect to the reaction due to friction force.

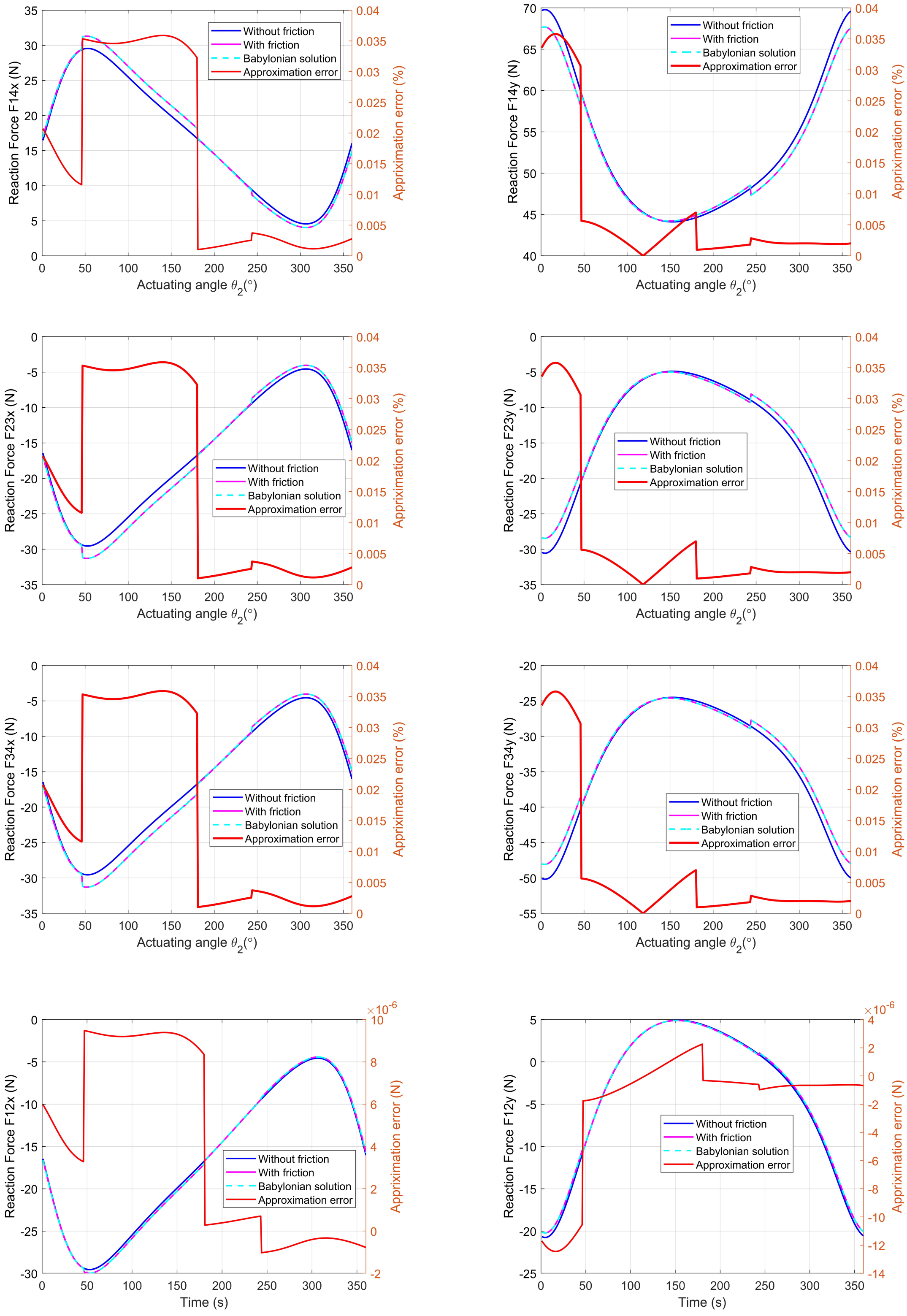

Figure 2.6 – Joint reaction forces of the four-bar linkage.

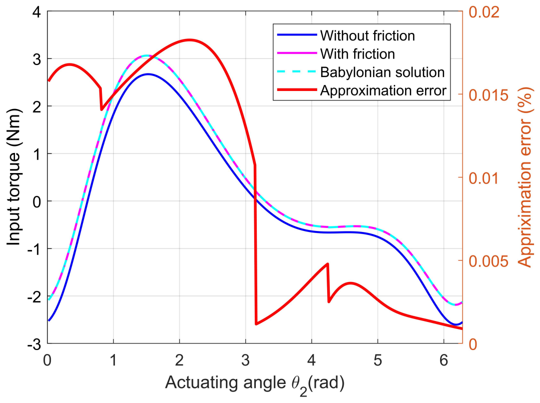

Figure 2.7 – Input torque of the four-bar linkage.

For all the reaction forces in the four-bar linkage, the approximation error calculated with Eq. (2.56) is below 0.036%, demonstrating high approximation accuracy. Then, the input torque of four-bar linkage was resolved and shown in Fig. 2.7, in which the approximation error is below 0.018%. The input energy, including Coulomb friction, was then calculated to be 8.18 J. It can also be observed from Fig. 2.7 that the friction in the four-bar linkage joints results in elevated input torque and increased energy consumption, which should be taken into account during the design phase.

2.3.2 5R parallel manipulator

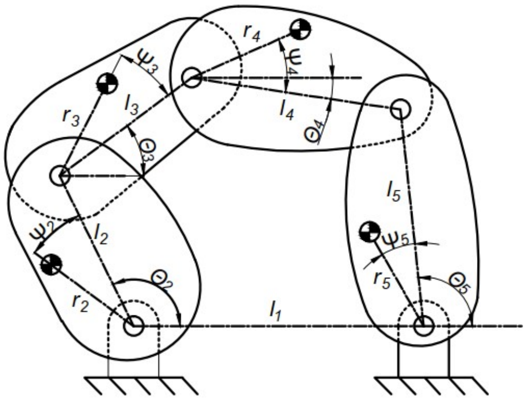

Figure 2.8 – 5R parallel manipulator.

Let us consider another application of the proposed method in a 5R parallel manipulator, as illustrated in Fig. 2.8. It comprises five linkages arranged in the vertical plane.

The gravitational force and friction need to be compensated by the actuators. In this mechanism, θ_i $(i = 1, 2, 3, 4, 5)$ represents the relative positions between the connected linkages. The parameters l_i and r_i, ψ_i $(i = 1, 2, 3, 4, 5)$ correspond to the length and the positions of mass center for each linkage, respectively. Additionally, l_1 represents the distance between the joints of the two actuating linkages fixed on the ground. For solving the unknown reaction forces in the joints of 5R parallel manipulator, six linear equilibrium equations are established as follows:

$$F^0_{23x} + F^0_{43x} + \delta F_{23x} + \delta F_{43x} = -F_{3x} \tag{2.57}$$

$$F^0_{23y} + F^0_{43y} + \delta F_{23y} + \delta F_{43y} = -F_{3y} \tag{2.58}$$

$$\begin{aligned} &M_3 - F_{3x} r_3 \sin(\theta_3 + \psi_3) + F_{3y} r_3 \cos(\theta_3 + \psi_3) - F_{43x} l_3 \sin\theta_3 + F_{43y} l_3 \cos\theta_3 \\ &- e_{23} u_{23} \operatorname{sign}(\mathbf{v}_{32}) \left(\sqrt{\left(F^0_{23x}\right)^2 + \left(F^0_{23y}\right)^2} + \frac{F^0_{23x}\delta F_{23x} + F^0_{23y}\delta F_{23y}}{\sqrt{\left(F^0_{23x}\right)^2 + \left(F^0_{23y}\right)^2}} \right) \\ &- e_{43} u_{43} \operatorname{sign}(\mathbf{v}_{34}) \left(\sqrt{\left(F^0_{43x}\right)^2 + \left(F^0_{43y}\right)^2} + \frac{F^0_{43x}\delta F_{43x} + F^0_{43y}\delta F_{43y}}{\sqrt{\left(F^0_{43x}\right)^2 + \left(F^0_{43y}\right)^2}} \right) = 0 \end{aligned} \tag{2.59}$$

$$F^0_{34x} + F^0_{54x} + \delta F_{34x} + \delta F_{54x} = -F_{4x} \tag{2.60}$$

$$F^0_{34y} + F^0_{54y} + \delta F_{34y} + \delta F_{54y} = -F_{4y} \tag{2.61}$$

$$\begin{aligned} &M_4 - F_{4x} r_4 \sin(\theta_4 + \psi_4) + F_{4y} r_4 \cos(\theta_4 + \psi_4) - F_{54x} l_4 \sin\theta_4 + F_{54y} l_4 \cos\theta_4 \\ &- e_{34} u_{34} \operatorname{sign}(\mathbf{v}_{43}) \left(\sqrt{\left(F^0_{34x}\right)^2 + \left(F^0_{34y}\right)^2} + \frac{F^0_{34x}\delta F_{34x} + F^0_{34y}\delta F_{34y}}{\sqrt{\left(F^0_{34x}\right)^2 + \left(F^0_{34y}\right)^2}} \right) \\ &- e_{54} u_{54} \operatorname{sign}(\mathbf{v}_{45}) \left(\sqrt{\left(F^0_{54x}\right)^2 + \left(F^0_{54y}\right)^2} + \frac{F^0_{54x}\delta F_{54x} + F^0_{54y}\delta F_{54y}}{\sqrt{\left(F^0_{54x}\right)^2 + \left(F^0_{54y}\right)^2}} \right) = 0 \end{aligned} \tag{2.62}$$

Thus, the forces due to friction δF_{23}, δF_{34}, and δF_{54} are considered as unknowns and a closed-form solution could be obtained. The forces due to friction applied by the frame are expressed as follows:

$$\delta F_{12x} = -F_{2x} + F^0_{23x} - F^0_{12x} + \delta F_{23x} \tag{2.63}$$

$$\delta F_{12y} = -F_{2y} + F^0_{23y} - F^0_{12y} + \delta F_{23y} \tag{2.64}$$

$$\delta F_{15x} = -F_{5x} + F^0_{54x} - F^0_{15x} + \delta F_{54x} \tag{2.65}$$

$$\delta F_{15y} = -F_{5y} + F^0_{54y} - F^0_{15y} + \delta F_{54y} \tag{2.66}$$

Subsequently, the reaction forces can be calculated in all the joints of 5R parallel manipulator using Eqs. (2.17)-(2.18). The input torques of 5R parallel manipulator are given as follows:

$$\begin{aligned}\tau_2 = & -F_{23x} l_2 \sin\theta_2 + F_{23y} l_2 \cos\theta_2 + F_{2x} r_2 \sin(\theta_2 + \psi_2) - F_{2y} r_2 \cos(\theta_2 + \psi_2) \\ & - u_{23} e_{23} \mathrm{sign}(\mathbf{v}_{32}) \sqrt{(F_{23x})^2 + (F_{23y})^2} + u_{12} e_{12} \mathrm{sign}(\mathbf{v}_{21}) \sqrt{(F_{12x})^2 + (F_{12y})^2} - M_2\end{aligned} \tag{2.67}$$

$$\begin{aligned}\tau_5 = & F_{15x} l_5 \sin\theta_5 - F_{15y} l_5 \cos\theta_5 + F_{5x} r_5 \sin(\theta_5 + \psi_5) - F_{5y} r_5 \cos(\theta_5 + \psi_5) \\ & - u_{54} e_{54} \mathrm{sign}(\mathbf{v}_{45}) \sqrt{(F_{54x})^2 + (F_{54y})^2} + u_{15} e_{15} \mathrm{sign}(\mathbf{v}_{51}) \sqrt{(F_{15x})^2 + (F_{15y})^2} - M_5\end{aligned} \tag{2.68}$$

The numerical simulations were conducted and the parameters of the 5R parallel manipulator were defined as follows: the lengths of the links: $l_1 = l_2 = l_3 = l_4 = l_5 = 0.2$ m; the masses of the links: $m_2 = m_3 = m_4 = m_5 = 1$ kg; the axial moments of inertial: $I_{S_2} = I_{S_3} = I_{S_4} = I_{S_5} = 2.33 \times 10^{-4}$ kgm^2; the locations of the mass centers: $r_2 = r_3 = r_4 = r_5 = 0.1$ m; $\psi_2 = \psi_3 = \psi_4 = \psi_5 = 0°$; the radius of bearings: $e_{ij} = 0.02$ m; the coefficient of friction in mechanism joints: $\mu_{ij} = 0.2$; the resistant moments applied to the links: $M_2 = M_3 = M_4 = 0$ Nm; $M_5 = -5$ Nm; the input angular velocity: $\dot{\theta}_1 = \dot{\theta}_2 = 0.01745$ s^{-1}; the operating range of mechanism: $\theta_1 \in [36°, 56°]$ and $\theta_2 \in [0°, 20°]$. Let us firstly resolve the linear equations (2.57)-(2.62) to obtain the forces due to friction in mechanism joints, as shown in Fig. 2.9.

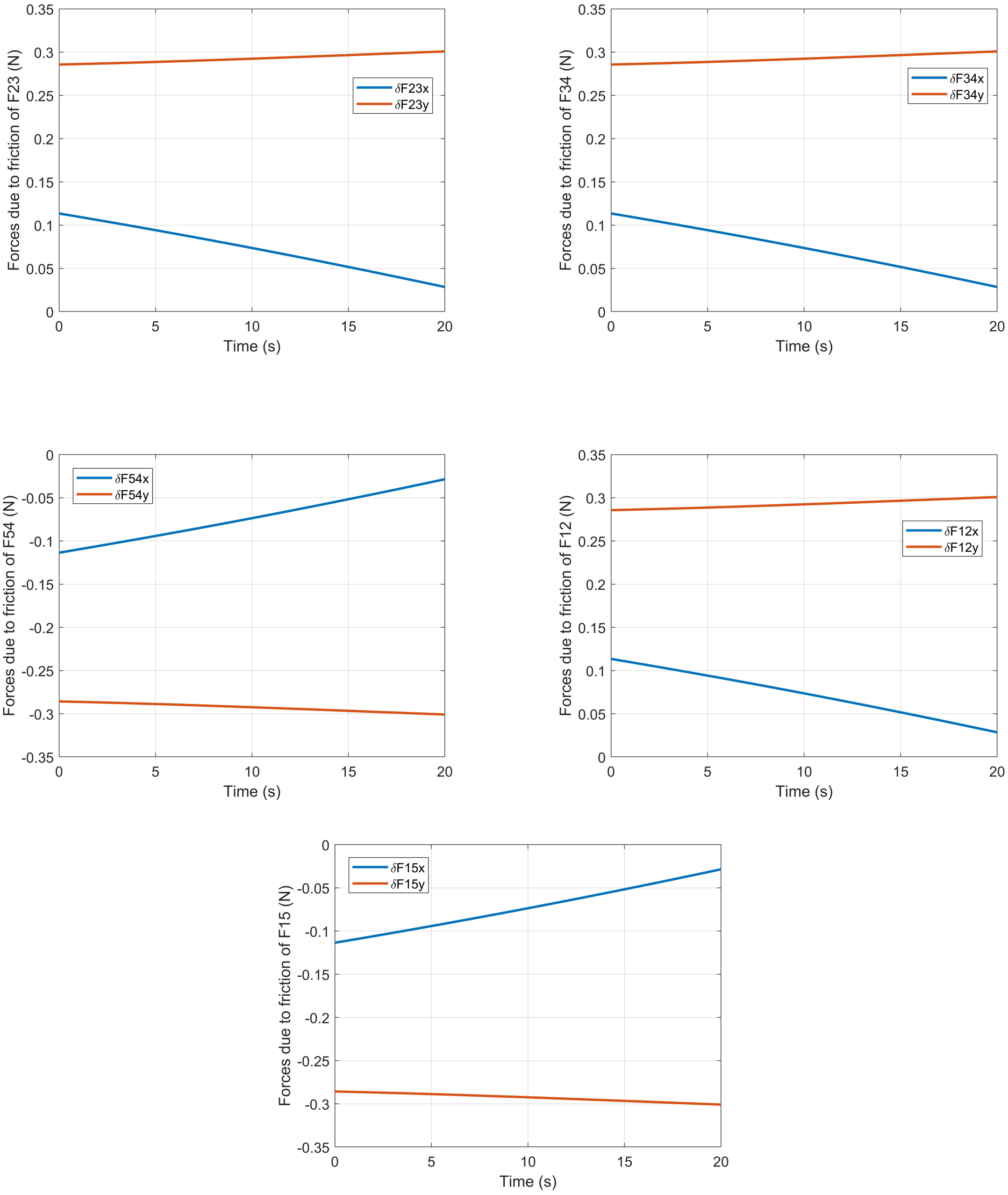

Figure 2.9 – Forces due to the friction determined from linear equations (2.57)-(2.62).

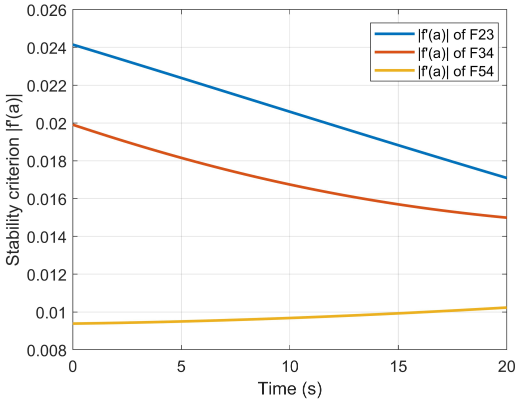

Figure 2.10 – Approximation stability analysis of 5R parallel manipulator.

As illustrated in Fig. 2.10, the derivative $|f'(a)| < 1$ and the maximum value is less than 2.5×10^{-2}. Thus, the approximation stability has been ensured in 5R parallel manipulator. Then, the reaction forces in mechanism joints were solved using Eqs. (2.17)-(2.18). They are presented as the following Fig. 2.11.

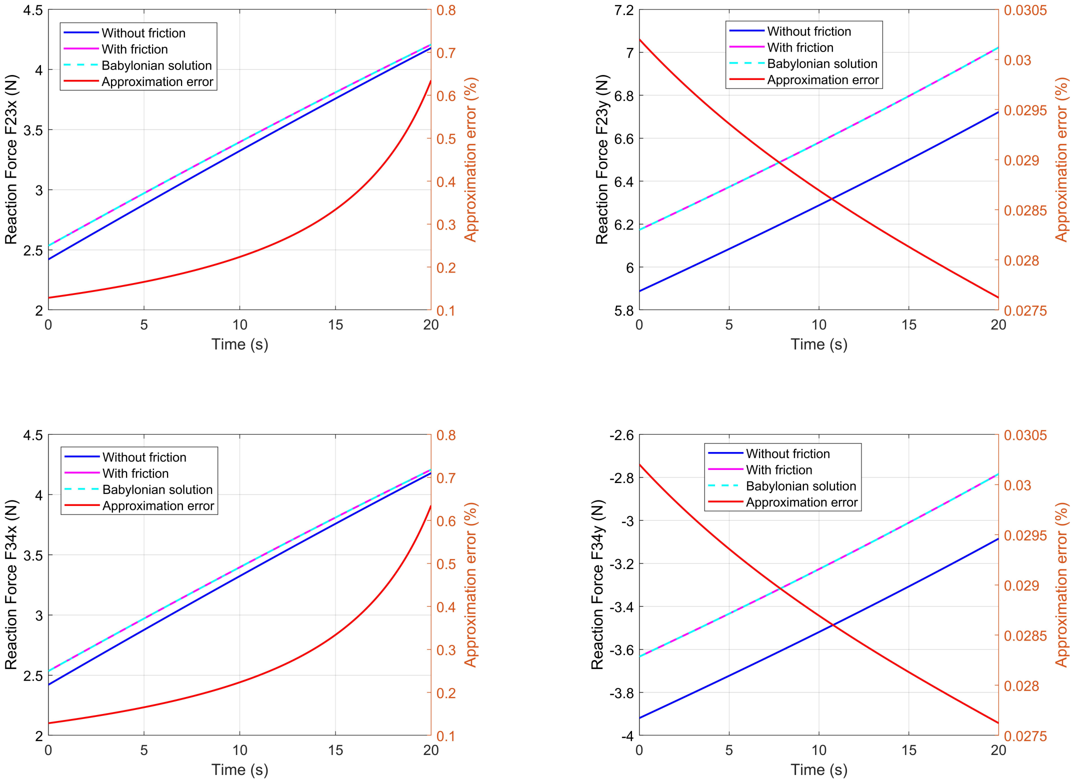

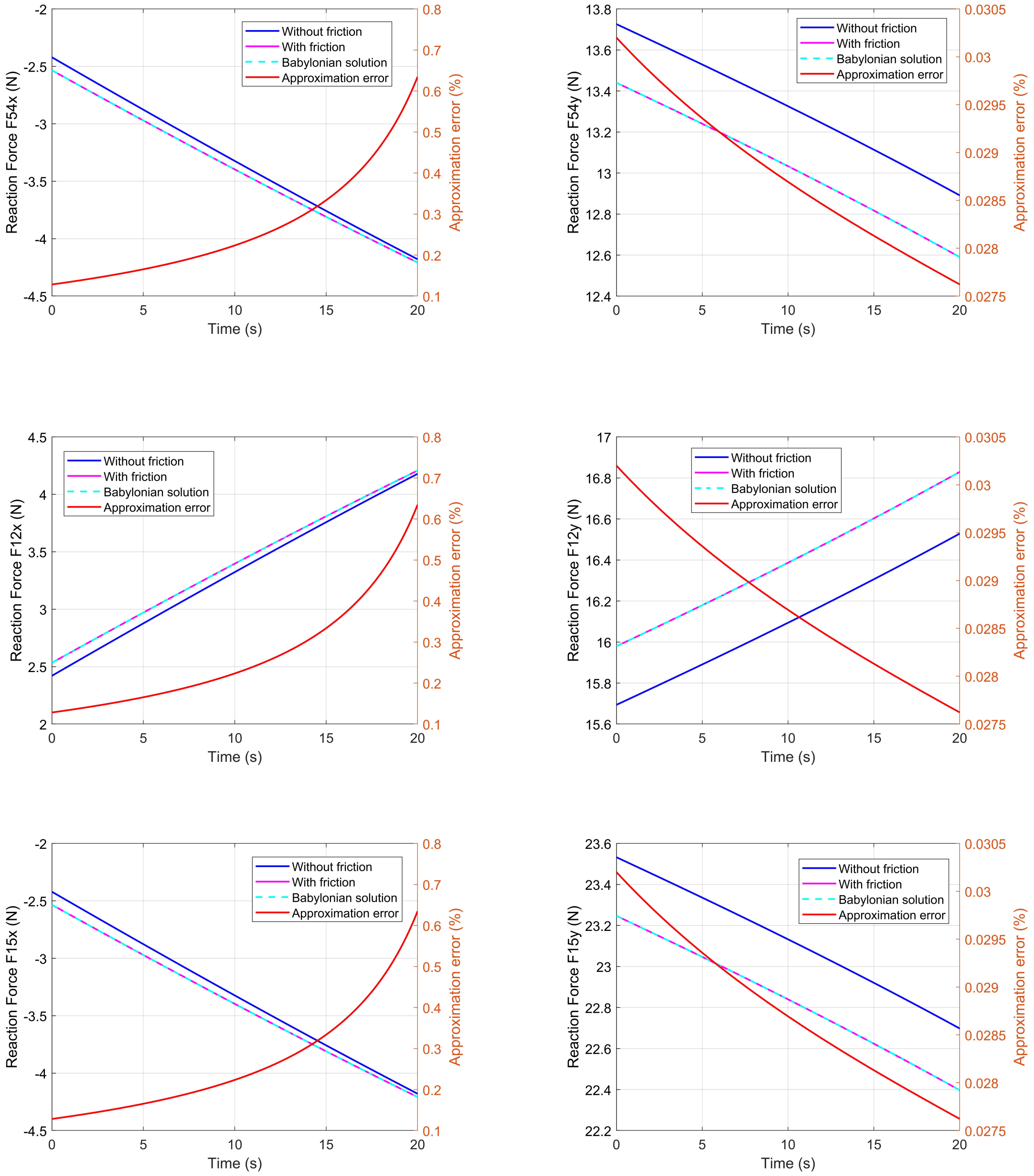

Figure 2.11 – Joint reaction forces of the 5R parallel manipulator

.

It could be observed that the solution in frictional case is deviated from the frictionless case. The solution approximated by the Babylonian method aligns closely to the exact solution, in which the maximum approximation error is inferior to 0.64%. Thus, the precision of approximation has been ensured and the input torques of the 5R parallel manipulator could then be calculated from Eqs. (2.67)-(2.68), as shown in Fig. 2.12

The maximum approximation error for input torques is less than 0.033%. As indicated in Tab. 2.3, the maximum approximation error for energy loss in two motors is below 0.032%. Additionally, Tab. 2.3 highlights a 10.48% increase in energy consumption due to friction in motor 1 , emphasizing the need for consideration in the design of 5R parallel manipulator.

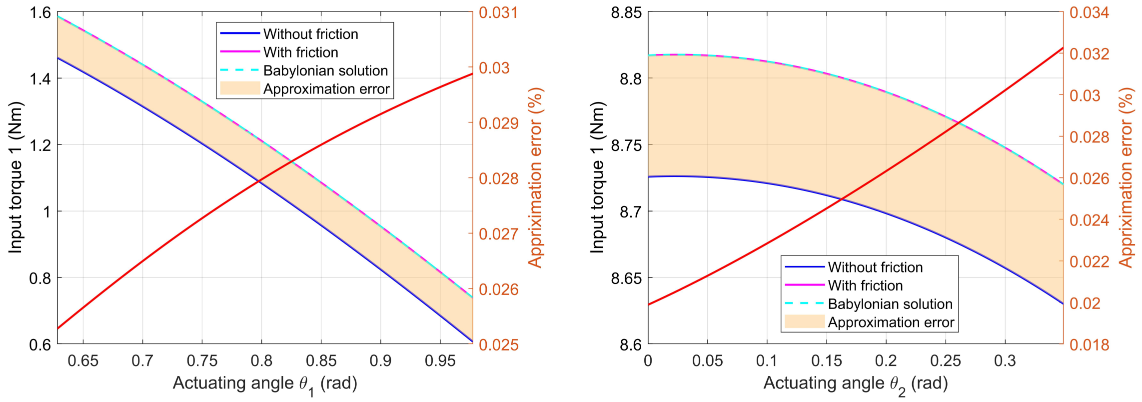

Figure 2.12 – Input torques of the 5R parallel manipulator

.

Table 2.3 – Approximation of energy loss due to friction in the 5R parallel manipulator

	Motor 1	Motor 2
Energy consumption of motors (J)	0.42	3.07
Energy loss due to friction (J)	0.044	0.032
Energy loss due to friction (%)	10.48	1.04
Approximation error for energy loss (%)	0.028	0.032

2.3.3 3RRR parallel manipulator

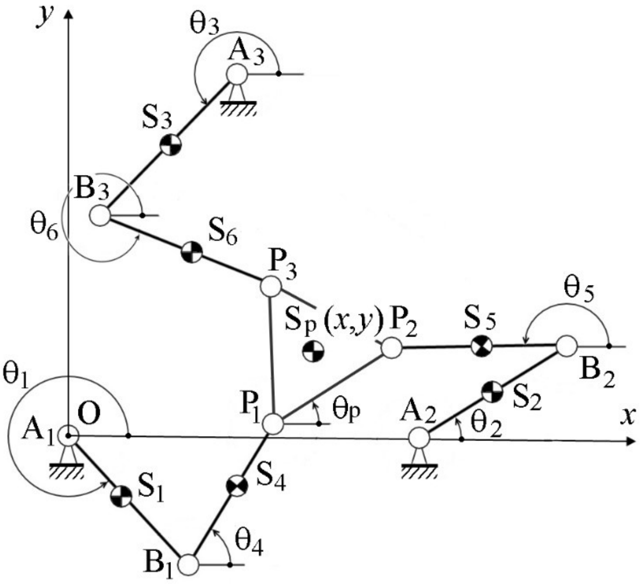

Figure 2.13 – 3RRR parallel manipulator.

Moreover, let us consider an application of the Babylonian method in 3RRR parallel manipulator, in which the equilibrium equations are more complicated and involve more unknowns. As an illustrative example, the planar 3RRR parallel manipulator is considered (Fig. 2.13). The moving platform of the manipulator is connected to its legs by three revolute joints P_i $(i = 1,\ 2,\ 3)$.

Each leg comprises two links connected by revolute joints B_i (for $i = 1,\ 2,\ 3$), and they are mounted on the frame, denoted as 0, by revolute joints A_i (for $i = 1,\ 2,\ 3$). The input parameters of such a manipulator are defined by the joint angles θ_i (for $i = 1,\ 2,\ 3$), and the output parameters by the pose of the moving platform, i.e., its orientation θ_P and the position of one point of the moving platform, for example, the center of mass of the moving platform S_P with parameters x and y.

Note that all axes of revolute joints are parallel; i.e. this is a mechanical system in which all points of the links describe paths located in parallel planes.

The lengths of the links and the positions of their centers of mass are denoted as follows: $l_1 = l_{A_1B_1}$; $l_2 = l_{A_2B_2}$; $l_3 = l_{A_3B_3}$; $l_4 = l_{B_1P_1}$; $l_5 = l_{B_2P_2}$; $l_6 = l_{B_3P_3}$; $r_1 = l_{A_1S_1}$; $r_2 = l_{A_2S_2}$; $r_3 = l_{A_3S_3}$; $r_4 = l_{B_1S_4}$; $r_5 = l_{B_2S_5}$; $r_6 = l_{B_3S_6}$. The platform is defined by the following parameters: $d_1 = l_{P_1P_2}$, $d_2 = l_{P_1P_3}$, $\psi_d = \angle P_3P_1P_2$. The disposition of the center of mass of the platform is described by the parameters: $\psi_P = \angle PP_1P_2$ and $r_P = l_{P_1S_P}$. The angles θ_i (for $i = 4, 5, 6$) define the orientations of the corresponding links (see Fig. 2.13).

To formulate the equilibrium equations for the 3RRR parallel manipulator, it was broken down into Assur groups, i.e. kinematic chains with zero degrees of mobility. These groups can be added or subtracted from a mechanism without altering its original number of degrees of freedom [114]. The first structural group was thus obtained, comprising links 4, 5, 6 and the platform. The equilibrium equations accounting for the friction forces in the joints of the mechanism are then established (see Eq. (2.27)) for the platform:

$$F^0_{4Px} + F^0_{5Px} + F^0_{6Px} + \delta F_{4Px} + \delta F_{5Px} + \delta F_{6Px} = -F_{Px} \tag{2.69}$$

$$F^0_{4Py} + F^0_{5Py} + F^0_{6Py} + \delta F_{4Py} + \delta F_{5Py} + \delta F_{6Py} = -F_{Py} \tag{2.70}$$

$$\begin{aligned}
&M_P - F_{Px} r_P \sin(\theta_P + \psi_P) + F_{Py} r_P \cos(\theta_P + \psi_P) - F_{5Px} d_1 \sin\theta_P + F_{5Py} d_1 \cos\theta_P \\
&- F_{6Px} d_2 \sin\left(\theta_P + \psi_d\right) + F_{6Py} d_2 \cos\left(\theta_P + \psi_d\right) \\
&- \mu_{4P} e_{4P}\, \mathrm{sign}(\mathbf{v}_{\mathrm{P4}}) \left(\sqrt{\left(F^0_{4Px}\right)^2 + \left(F^0_{4Py}\right)^2} + \frac{F^0_{4Px}\delta F_{4Px} + F^0_{4Py}\delta F_{4Py}}{\sqrt{\left(F^0_{4Px}\right)^2 + \left(F^0_{4Py}\right)^2}} \right) \\
&- \mu_{5P} e_{5P}\, \mathrm{sign}(\mathbf{v}_{\mathrm{P5}}) \left(\sqrt{\left(F^0_{5Px}\right)^2 + \left(F^0_{5Py}\right)^2} + \frac{F^0_{5Px}\delta F_{5Px} + F^0_{5Py}\delta F_{5Py}}{\sqrt{\left(F^0_{5Px}\right)^2 + \left(F^0_{5Py}\right)^2}} \right) \\
&- \mu_{6P} e_{6P}\, \mathrm{sign}(\mathbf{v}_{\mathrm{P6}}) \left(\sqrt{\left(F^0_{6Px}\right)^2 + \left(F^0_{6Py}\right)^2} + \frac{F^0_{6Px}\delta F_{6Px} + F^0_{6Py}\delta F_{6Py}}{\sqrt{\left(F^0_{6Px}\right)^2 + \left(F^0_{6Py}\right)^2}} \right) = 0
\end{aligned} \tag{2.71}$$

Then, the equilibrium equations of links 4, 5, 6 connected to the platform are established as follows:

$$F^0_{14x} + F^0_{P4x} + \delta F_{14x} + \delta F_{P4x} = -F_{4x} \tag{2.72}$$

$$F^0_{14y} + F^0_{P4y} + \delta F_{14y} + \delta F_{P4y} = -F_{4y} \tag{2.73}$$

$$\begin{aligned} & M_4 - F_{4x} r_4 \sin\theta_4 + F_{4y} r_4 \cos\theta_4 - F_{P4x} l_4 \sin\theta_4 + F_{P4y} l_4 \cos\theta_4 \\ & - \mu_{P4} e_{P4} \operatorname{sign}(\mathbf{v}_{4\mathrm{P}}) \left(\sqrt{\left(F^0_{P4x}\right)^2 + \left(F^0_{P4y}\right)^2} + \frac{F^0_{P4x}\delta F_{P4x} + F^0_{P4y}\delta F_{P4y}}{\sqrt{\left(F^0_{P4x}\right)^2 + \left(F^0_{P4y}\right)^2}} \right) \\ & - \mu_{14} e_{14} \operatorname{sign}(\mathbf{v}_{41}) \left(\sqrt{\left(F^0_{14x}\right)^2 + \left(F^0_{14y}\right)^2} + \frac{F^0_{14x}\delta F_{14x} + F^0_{14y}\delta F_{14y}}{\sqrt{\left(F^0_{14x}\right)^2 + \left(F^0_{14y}\right)^2}} \right) = 0 \end{aligned} \tag{2.74}$$

$$F^0_{25x} + F^0_{P5x} + \delta F_{25x} + \delta F_{P5x} = -F_{5x} \tag{2.75}$$

$$F^0_{25y} + F^0_{P5y} + \delta F_{25y} + \delta F_{P5y} = -F_{5y} \tag{2.76}$$

$$\begin{aligned} & M_5 - F_{5x} r_5 \sin\theta_5 + F_{5y} r_5 \cos\theta_5 - F_{P5x} l_5 \sin\theta_5 + F_{P5y} l_5 \cos\theta_5 \\ & - \mu_{P5} e_{P5} \operatorname{sign}(\mathbf{v}_{5\mathrm{P}}) \left(\sqrt{\left(F^0_{P5x}\right)^2 + \left(F^0_{P5y}\right)^2} + \frac{F^0_{P5x}\delta F_{P5x} + F^0_{P5y}\delta F_{P5y}}{\sqrt{\left(F^0_{P5x}\right)^2 + \left(F^0_{P5y}\right)^2}} \right) \\ & - \mu_{25} e_{25} \operatorname{sign}(\mathbf{v}_{52}) \left(\sqrt{\left(F^0_{25x}\right)^2 + \left(F^0_{25y}\right)^2} + \frac{F^0_{25x}\delta F_{25x} + F^0_{25y}\delta F_{25y}}{\sqrt{\left(F^0_{25x}\right)^2 + \left(F^0_{25y}\right)^2}} \right) = 0 \end{aligned} \tag{2.77}$$

$$F^0_{36x} + F^0_{P6x} + \delta F_{36x} + \delta F_{P6x} = -F_{6x} \tag{2.78}$$

$$F^0_{36y} + F^0_{P6y} + \delta F_{36y} + \delta F_{P6y} = -F_{6y} \tag{2.79}$$

$$
\begin{aligned}
&M_6 - F_{6x} r_6 \sin\theta_6 + F_{6y} r_6 \cos\theta_6 - F_{P6x} l_6 \sin\theta_6 + F_{P6y} l_6 \cos\theta_6 \\
&- \mu_{P6} e_{P6} \operatorname{sign}(\mathbf{v}_{6\mathrm{P}}) \left(\sqrt{\left(F^0_{P6x}\right)^2 + \left(F^0_{P6y}\right)^2} + \frac{F^0_{P6x}\delta F_{P6x} + F^0_{P6y}\delta F_{P6y}}{\sqrt{\left(F^0_{P6x}\right)^2 + \left(F^0_{P6y}\right)^2}} \right) \\
&- \mu_{36} e_{36} \operatorname{sign}(\mathbf{v}_{63}) \left(\sqrt{\left(F^0_{36x}\right)^2 + \left(F^0_{36y}\right)^2} + \frac{F^0_{36x}\delta F_{36x} + F^0_{36y}\delta F_{36y}}{\sqrt{\left(F^0_{36x}\right)^2 + \left(F^0_{36y}\right)^2}} \right) = 0 \qquad (2.80)
\end{aligned}
$$

From the obtained linear equation system (2.69)-(2.80), the 12 unknown reaction forces due to friction δF_{iPx} and δF_{iPy} (for $i = 4,\ 5,\ 6$), as well as δF_{14x}, δF_{14y}, δF_{25x}, δF_{25y}, δF_{36x}, and δF_{36y} are determined.

After solving the system of equations for the first structural group, the forces due to friction acting on the joints of input links 1, 2, and 3 are then determined using their respective equilibrium equations:

$$\delta F_{01x} = -F_{1x} - F^0_{01x} + F^0_{14x} + \delta F_{14x} \qquad (2.81)$$

$$\delta F_{01y} = -F_{1y} - F^0_{01y} + F^0_{14y} + \delta F_{14y} \qquad (2.82)$$

$$\delta F_{02x} = -F_{2x} - F^0_{02x} + F^0_{25x} + \delta F_{25x} \qquad (2.83)$$

$$\delta F_{02y} = -F_{2y} - F^0_{02y} + F^0_{25y} + \delta F_{25y} \qquad (2.84)$$

$$\delta F_{03x} = -F_{3x} - F^0_{03x} + F^0_{36x} + \delta F_{36x} \qquad (2.85)$$

$$\delta F_{03y} = -F_{3y} - F^0_{03y} + F^0_{36y} + \delta F_{36y} \qquad (2.86)$$

After determining the forces due to friction, the reaction forces in all the 3RRR parallel manipulator joints can then be calculated with Eqs. (2.17)-(2.18), and the input torques are expressed as follows:

$$\begin{aligned}\tau_1 &= -F_{14x}l_1\sin\theta_1 + F_{14y}l_1\cos\theta_1 + F_{1x}r_1\sin\theta_1 - F_{1y}r_1\cos\theta_1\\ &- \mu_{14}e_{14}\,\mathrm{sign}(\mathbf{v}_{41})\sqrt{F_{14x}^2+F_{14y}^2} + \mu_{01}e_{01}\,\mathrm{sign}(\mathbf{v}_{10})\sqrt{F_{01x}^2+F_{01y}^2} - M_1\end{aligned} \tag{2.87}$$

$$\begin{aligned}\tau_2 &= -F_{25x}l_2\sin\theta_2 + F_{25y}l_2\cos\theta_2 + F_{2x}r_2\sin\theta_2 - F_{2y}r_2\cos\theta_2\\ &- \mu_{25}e_{25}\,\mathrm{sign}(\mathbf{v}_{52})\sqrt{F_{25x}^2+F_{25y}^2} + \mu_{02}e_{02}\,\mathrm{sign}(\mathbf{v}_{20})\sqrt{F_{02x}^2+F_{02y}^2} - M_2\end{aligned} \tag{2.88}$$

$$\begin{aligned}\tau_3 &= -F_{36x}l_3\sin\theta_3 + F_{36y}l_3\cos\theta_3 + F_{3x}r_3\sin\theta_3 - F_{3y}r_3\cos\theta_3\\ &- \mu_{36}e_{36}\,\mathrm{sign}(\mathbf{v}_{63})\sqrt{F_{36x}^2+F_{36y}^2} + \mu_{03}e_{03}\,\mathrm{sign}(\mathbf{v}_{30})\sqrt{F_{03x}^2+F_{03y}^2} - M_3\end{aligned} \tag{2.89}$$

The following manipulator parameters were selected in numerical simulations: the lengths of linkage: $l_1 = l_2 = l_3 = l_4 = l_5 = l_6 = 0.18\,\mathrm{m}$; the masses of linkage: $m_1 = m_2 = m_3 = 2.6\,\mathrm{kg}$; $m_4 = m_5 = m_6 = 7.2\,\mathrm{kg}$; the axial moments of inertial: $I_{S_i} = 0.02\,\mathrm{kgm}^2$ (for $i = 1, 2, 3, 4, 5, 6$); $I_{S_P} = 0.01\,\mathrm{kgm}^2$; the parameters of the platform: $d_1 = d_2 = 0.1\,\mathrm{m}$ and $\psi_d = 60°$; the locations of the centers of mass of the links: $r_1 = r_2 = r_3 = r_4 = r_5 = r_6 = 0.09\,\mathrm{m}$; the location of the platform mass center: $r_P = 0.05\,\mathrm{m}$; $\psi_P = 30°$; the radius of bearings: $e_{ij} = 0.02\,\mathrm{m}$; the coefficient of friction in mechanism joints: $\mu_{ij} = 0.2$.

The motion of input links was defined as follows:

$$\theta(t) = \begin{cases} \theta_1(t) = \dfrac{\pi}{90}t + \dfrac{\pi}{3} \\ \theta_2(t) = -\dfrac{\pi}{90}t + \dfrac{4}{3}\pi & ,\ 0 \le t \le 10\,\mathrm{s} \\ \theta_3(t) = \dfrac{\pi}{540}t + 1.68\pi \end{cases} \tag{2.90}$$

The forces due to friction in six joints were first determined with linear system (2.69)-(2.80), see Fig. 2.14.

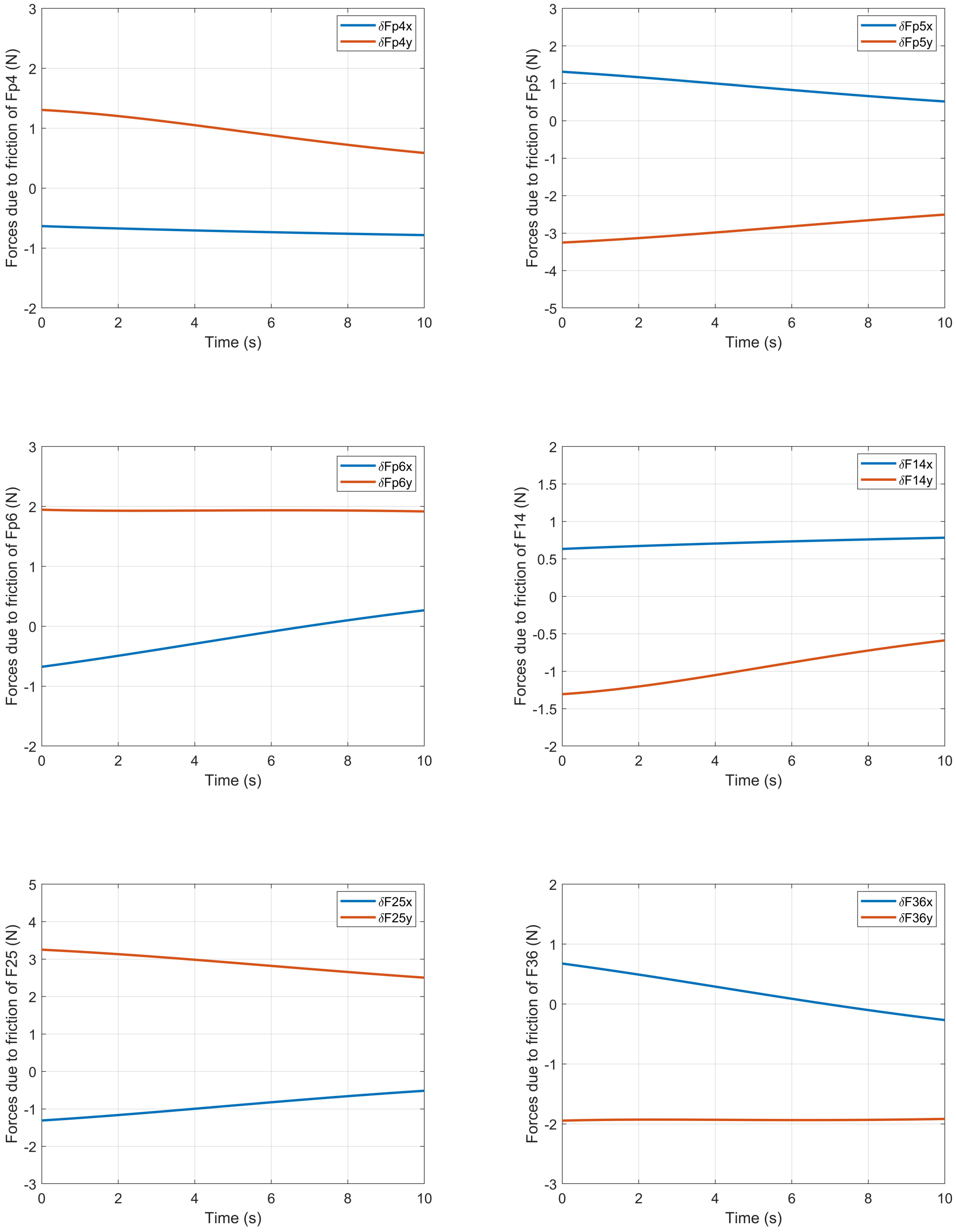

Figure 2.14 – Forces due to the friction determined from linear equations (2.69)-(2.80).

The forces due to friction in the remaining joints and input torques were then similarly calculated using linear systems (2.81)-(2.89).

Then, let us verify the approximation stability using the criterion (2.53). It can be observed from the Fig. 2.15 that the derivative $|f'(a)| < 1$ and the magnitude is less than 6×10^{-2}, which implies that the Babylonian method can produce a result close to the exact reaction force.

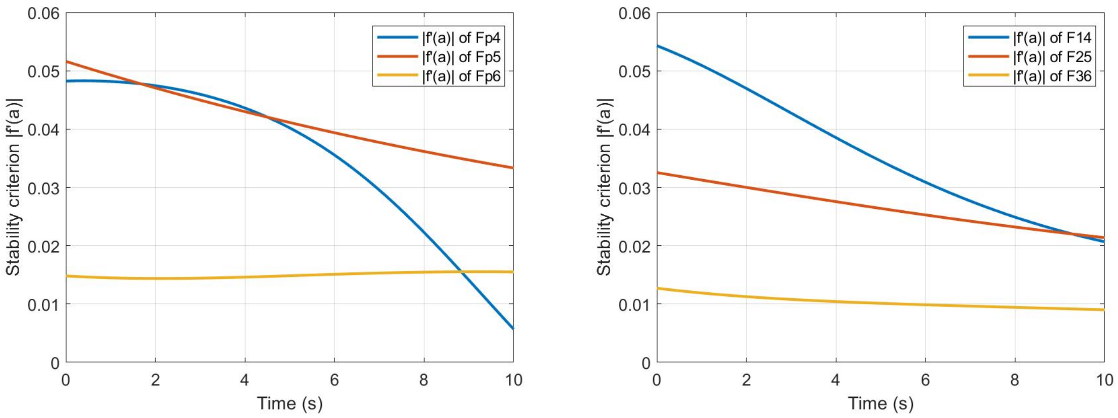

Figure 2.15 – Stability criterion verification for the 3RRR parallel manipulator.

After checking the approximation stability, a comparative analysis was carried out between the reactions, determined using the exact calculation method, and those using the proposed approximation method. Note that the reaction forces applied by the frame at the actuating joints are more important than the other revolute joints, as the frictional forces cumulatively multiply throughout the Assur groups. The comparative analysis was therefore carried out for these joints. Fig. 2.16 shows the exact and approximated solutions for the reaction forces with friction at the actuating joints. The reaction force was also considered, with no accounting for friction. It is evident that the reaction forces differ significantly depending on whether friction is present or not.

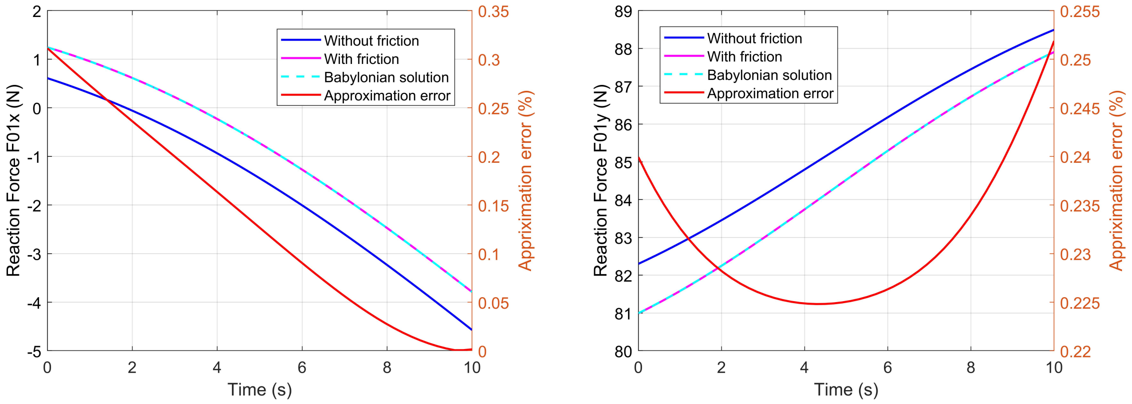

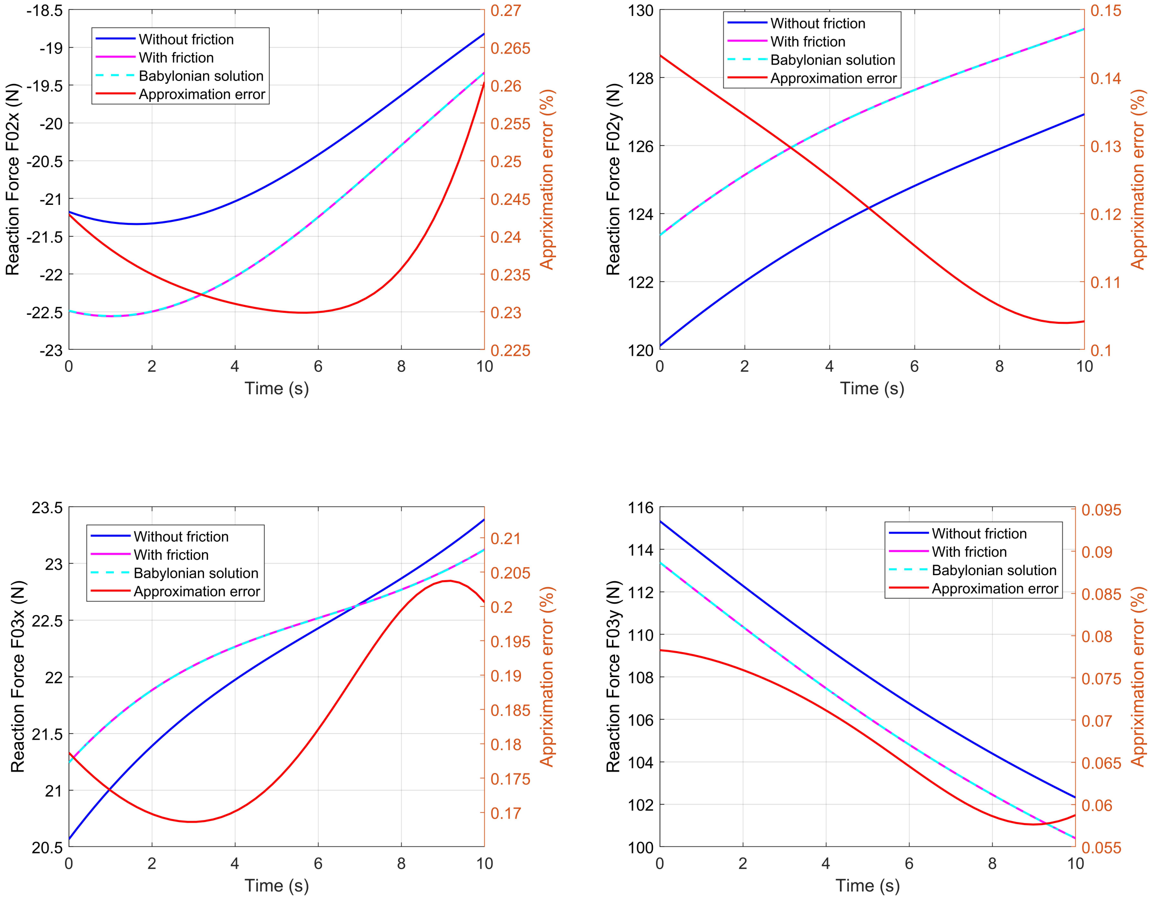

Figure 2.16 – Reaction forces at the actuating joints of the 3RRR parallel manipulator.

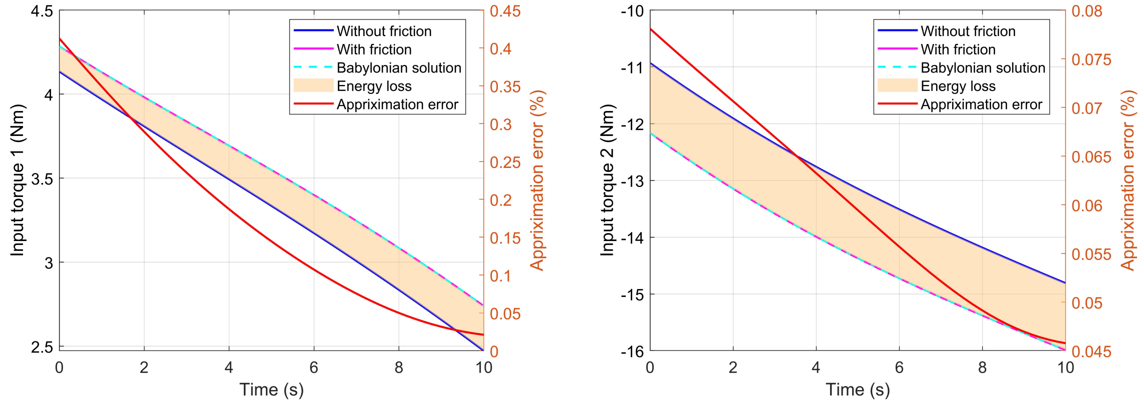

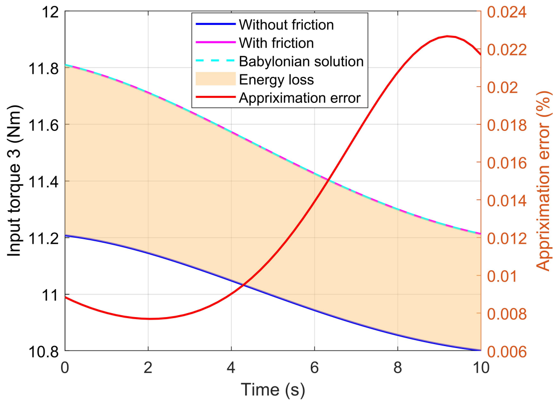

Figure 2.17 – Input torques of the 3RRR parallel manipulator.

It can be observed from Fig. 2.16 that the reaction forces in the presence of friction are obviously deviated from the frictionless case. Furthermore, the approximated solution obtained by the Babylonian method aligns with the exact solution very closely in the 3RRR parallel manipulator. Among all the reaction forces solved from the equilibrium equations, the maximum approximation error between the Babylonian solution and the exact solution is below 0.31%, indicating a high level of precision. Then, the input torques of the mechanism were solved through Eqs. (2.87)-(2.89) and shown in Fig. 2.17, in which the maximum error is below 0.41%. Fig. 2.17 also illustrates how the friction in 3RRR joints results in elevated input torque and increased energy consumption.

A comparative analysis of energy loss was carried out using these numerical simulation results, as shown in Tab. 2.4. In the 3RRR parallel manipulator, there is an observed increase of energy consumption due to joint friction. The approximation error for the energy loss could be neglected.

Table 2.4 – Energy loss due to friction in the 3RRR parallel manipulator.

	Motor 1	Motor 2	Motor 3
Energy consumption of motors (J)	1.23	4.98	0.67
Energy loss due to friction (J)	0.074	0.42	0.029
Energy loss due to friction (%)	6.02	8.43	4.33
Approximation error for energy loss (%)	0.15	0.06	0.01

The numerical simulations have revealed that the proposed method closely approximates the exact solution, with negligible errors that can be disregarded.

2.4 Summary

Friction occurs wherever two interconnected links of a mechanism are in relative motion, at the joint connecting them. The nature and amount of friction are contingent on the choice of bearing. For high-speed and high-load machinery, low-friction bearings are often incorporated into the design. Nevertheless, in numerous scenarios, direct physical contact does sometimes take place between mechanism links. This form of friction is known as dry or Coulomb friction, and is the focus of investigation for this study. Coulomb friction amplifies the forces within mechanical system bearings and leads to energy dissipation, and if the mechanical system comprises a series of interconnected linkages, this can escalate into a major problem as the friction forces multiply through the chain of links.

This chapter has introduced a novel method proposing an analytically tractable approximate solution involving Coulomb friction for force analysis in mechanism joints. The method is based on traditional friction circle concepts and is exceptionally well-suited for calculating and streamlining the solution process for mechanical systems by eliminating the necessity for iterative steps at each stage of the dynamic analysis. Note that modifications to the manipulator parameters can lead to increased discrepancies between the calculated exact and maximum solutions, but given the results obtained and various observations, it is still considered that the technique is clearer and simpler than previous approaches.

The method was tested by applying it to a planar four-bar linkage, 5R and 3RRR parallel manipulators. The simulation results indicated a discrepancy of not more than 0.64% between the exact calculations and the approximate calculations, demonstrating the effectiveness of the method. Similar findings were observed when assessing calculations for increased input torque and energy consumption, where the difference between the exact and approximate calculations did not exceed 0.41%. The study demonstrates that this new method is a valuable asset in machine design and has potential for application in various other mechanisms. The use of this approximation-based approach in calculations can yield substantial time and cost savings.

CHAPTER 3

TORQUE MINIMIZATION AND CONTROL PERFORMANCE IMPROVEMENT OF DYNAMICALLY DECOUPLED SPATIAL SERIAL MANIPULATORS

3.5 Decoupled dynamics of the spatial serial manipulators 92
3.6 Optimal motion generation in dynamically decoupled manipulators 98
3.7 Error sensitivity analysis in dynamically decoupled manipulators 103
3.8 Control performance improvement in dynamically decoupled manipulators 108
3.9 Summary 125

In this chapter, a novel dynamic decoupling technique is introduced, combining the redistribution of masses and the relocation of actuators in the design of spatial serial manipulators. The obtained decoupled system not only enables efficient motion generation to achieve torque minimization but also facilitates the controller design. In the decoupled system, the use of controllers with simple structures leads to an improvement in tracking accuracy and energy consumption in control process.

The chapter is organized as follows: Firstly, the dynamic decoupling technique is applied to the spatial serial manipulators. Next, an optimal motion generation approach for torque minimization in dynamically decoupled manipulators is presented. Then, an analysis of error sensitivity in the presence of parameter uncertainty is conducted. Subsequently, the control performance of tracking the desired motion is analyzed in dynamically decoupled manipulators. Finally, the conclusions drawn from this research are discussed.

3.1 Decoupled dynamics of the spatial serial manipulators

As reviewed in Chapter 1, the dynamics of robot manipulator is known to be highly nonlinear and coupled, leading to poorer control performance at high speeds [47], [48]. The complex dynamics is the result of varying inertia and interactions between the different joints, and the nonlinear coupled dynamics of robot manipulator increases the computational burden or even the energy consumption in control process [47].

Since it is challenging to find a simple and effective strategy for controlling robot manipulators due to the presence of model nonlinearities and errors, dynamic decoupling is adopted for simplifying the dynamics of spatial serial manipulators through mechanical modifications. In a linear and decoupled system, an efficient motion generation technique can then be employed for torque minimization. Moreover, the decoupling technique offers benefits in controller design. A range of straightforward controllers are employed to track the desired motion, with the objective of improving controller performance and enhancing energy efficiency.

Before addressing the torque minimization and control performance improvement, dynamic decoupling is considered being implemented in the spatial serial manipulators with revolute joints. Let us review the Lagrangian dynamics. The equations of motion can be written as follows:

$$\tau_i = \frac{\mathrm{d}}{\mathrm{d}t}\left(\frac{\partial L}{\partial \dot{\theta}_i}\right) - \frac{\partial L}{\partial \theta_i}, i = 1, \cdots, n \tag{3.1}$$

where, n is the number of degrees of freedom; τ_i are the actuating torques; θ_i are the generalized coordinates; $L = K_e - P_t$ is the Lagrangian; K_e is the kinetic energy and P_t is the potential energy. K_e can be expressed as:

$$K_e = \frac{1}{2}\left(\sum_{i=1}^{n} m_i \mathbf{v}_{c_i}^{\top}\mathbf{v}_{c_i} + \omega_i^{\top}\mathbf{I}_i\omega_i\right) \tag{3.2}$$

where $\mathbf{I}_i$ is the inertia matrix of the body i with respect to a frame that the origin is its center of mass C_i, $\mathbf{v}_{c_i}$ is the absolute velocity of C_i, ω_i is the rotational speed of the body i. P_t can be expressed as:

$$P_t = -\sum_{i=1}^{n} m_i \mathbf{g}^{\top}(\mathbf{h}_{0,i} + \mathbf{O}_i\mathbf{C}_i) \tag{3.3}$$

where $\mathbf{g}$ is the gravitational acceleration; $\mathbf{h}_{0,i}$ is the position vector from origin O_0 of frame R_0 to origin O_i of frame R_i; $\mathbf{O}_i\mathbf{C}_i$ is the vector of the center of mass coordinates of link i.

In order to achieve torque minimization and control performance improvement, the decoupling conditions of the spatial serial manipulators 2R and 3R will be studied in this chapter.

3.1.1 Decoupled dynamics of 2R spatial serial manipulator

The dynamic decoupling conditions of the 2R spatial serial manipulator (Fig. 3.1) are addressed below.

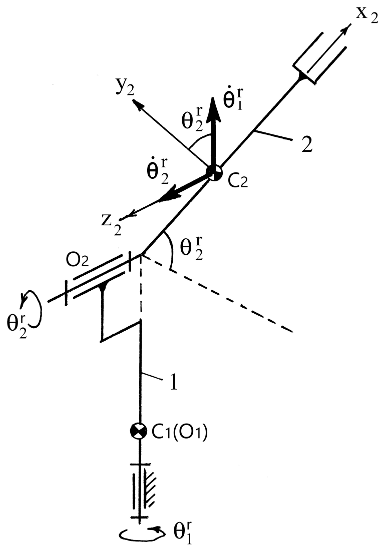

Figure 3.1 – 2R spatial serial manipulator.

The manipulator consists of two orthogonal links, 1 and 2, with revolute joint angles θ_1 and θ_2. We will distinguish the vectors of the joint angular velocities $\dot{\boldsymbol{\theta}}_\mathbf{1}^r$ and $\dot{\boldsymbol{\theta}}_\mathbf{2}^r$ with $\dot{\boldsymbol{\theta}}_\mathbf{1}^r = \mathbf{d}\boldsymbol{\theta}_\mathbf{1}^r/\mathrm{d}t$, $\dot{\boldsymbol{\theta}}_\mathbf{2}^r = \mathbf{d}\boldsymbol{\theta}_\mathbf{2}^r/\mathrm{d}t$, and the vectors of the absolute angular velocities $\dot{\boldsymbol{\theta}}_\mathbf{1}$ and $\dot{\boldsymbol{\theta}}_\mathbf{2}$ with $\dot{\boldsymbol{\theta}}_\mathbf{1} = \dot{\boldsymbol{\theta}}_\mathbf{1}^r$ and $\dot{\boldsymbol{\theta}}_\mathbf{2} = \dot{\boldsymbol{\theta}}_\mathbf{1}^r + \dot{\boldsymbol{\theta}}_\mathbf{2}^r$.

One of the requirements for dynamic decoupling of robot manipulators [115] is the static balance of the manipulator. Therefore, the centre of mass of link 1 should be on the vertical rotation axis of the manipulator (Fig. 3.1) and the centre of mass of link 2 should be at the intersection of the vertical and horizontal rotation axes of the manipulator. In these conditions, the common centre of mass of the manipulator becomes motionless and

$P_t = 0$.

With regard to the kinetic energy of the manipulator, taking into account the conditions of the mentioned static balancing, the following expression is given:

$$K_e = K_{e_1} + K_{e_2} = \frac{1}{2}[I_{z_1}\dot{\theta}_1^2 + I_{x2}\dot{\theta}_{x_2}^2 + I_{y2}\dot{\theta}_{y_2}^2 + I_{z_2}\dot{\theta}_{z_2}^2] \tag{3.4}$$

where, I_{z_1} is the axial moment of inertia of link 1; I_{x_2}, I_{y_2} and I_{z_2} are the axial moments of inertia of link 2 relative to the corresponding coordinate axes of the system associated with link 2; $\dot{\theta}_{x_2}$, $\dot{\theta}_{y_2}$ and $\dot{\theta}_{z_2}$ are the components of the angular velocity $\dot{\theta}_2$ about the same axes, i.e. $\dot{\theta}_2 = (\dot{\theta}_{x_2} + \dot{\theta}_{y_2} + \dot{\theta}_{z_2})^{\frac{1}{2}}$.

Fig. 3.1 shows that:

$$\dot{\theta}_{x_2}^2 = \dot{\theta}_1^r \sin\theta_2 \tag{3.5}$$

$$\dot{\theta}_{y_2}^2 = \dot{\theta}_1^r \cos\theta_2 \tag{3.6}$$

$$\dot{\theta}_{z_2}^2 = \dot{\theta}_2^r \tag{3.7}$$

Thus, the Lagrangian of the manipulator can be rewritten as:

$$L = K_e = K_{e_1} + K_{e_2} = \frac{1}{2}[I_{z_1}\dot{\theta}_1^2 + I_{x2}(\dot{\theta}_1^r \mathrm{sin}\theta_2)^2 + I_{y2}(\dot{\theta}_1^r \mathrm{cos}\theta_2)^2 + I_{z_2}(\dot{\theta}_2^r)^2] \tag{3.8}$$

As it follows from the obtained relationship, the dynamic decoupling of the manipulator can be achieved if $I_{x_2} = I_{y_2} = I^*$, since in this case:

$$L = K_e = K_{e_1} + K_{e_2} = \frac{1}{2}[(I_{z_1} + I^*)(\dot{\theta}_1^r)^2 + I_{z_2}(\dot{\theta}_2^r)^2] \tag{3.9}$$

and as a consequence,

$$\tau_1 = (I_{z_1} + I^*)\ddot{\theta}_1^r \tag{3.10}$$

$$\tau_2 = I_{z_2}\ddot{\theta}_2^r \tag{3.11}$$

The nonlinear dynamic system has been now transformed into a double integrator model and the state space equation of each link can be defined as:

$$\dot{\mathbf{x}} = \mathbf{A}\mathbf{x} + \mathbf{B}\mathbf{u} \tag{3.12}$$

$$\mathbf{y} = \mathbf{C}\mathbf{x} \tag{3.13}$$

with

$$\mathbf{A} = \begin{bmatrix} 0 & 1 \\ 0 & 0 \end{bmatrix}, \ \mathbf{B} = \begin{bmatrix} 0 \\ 1/I \end{bmatrix}, \ \mathbf{C} = \begin{bmatrix} 1 & 0 \end{bmatrix} \tag{3.14}$$

where, I is calculated with inertia moment of each link in Eqs. (3.10) and (3.11). $I = (I_{z_1} + I^*)$ for the first link and $I = I_{z_2}$ for the second link.

3.1.2 Decoupled dynamics of 3R spatial serial manipulator

As mentioned above, the dynamic decoupling technique has been successfully implemented in the 2R spatial serial manipulators with mass redistribution. However, for the robots with more than 3-DOF, actuator relocation technique is required in the decoupling process. The supporting structure of the KUKA industrial robot KR 16R1610, representing a 3R spatial serial manipulator, is considered as an illustrative example.

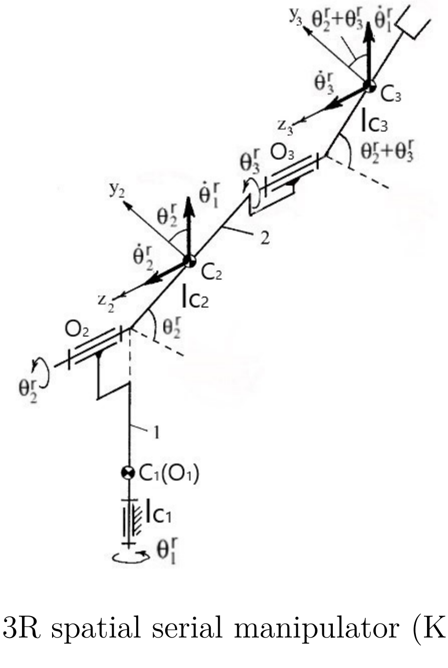

Figure 3.2 – 3R spatial serial manipulator (KR 16R1610).

The KR 16R1610 consists of three orthogonal links, 1, 2 and 3, with revolute joint angles θ_1, θ_2, and θ_3. We will distinguish the vectors of the joint angular velocities

$\boldsymbol{\dot\theta^r_1}$, $\boldsymbol{\dot\theta^r_2}$ and $\boldsymbol{\dot\theta^r_3}$ with $\boldsymbol{\dot\theta^r_1} = \mathbf{d}\boldsymbol{\theta^r_1}/\mathrm{d}t$, $\boldsymbol{\dot\theta^r_2} = \mathbf{d}\boldsymbol{\theta^r_2}/\mathrm{d}t$, $\boldsymbol{\dot\theta^r_3} = \mathbf{d}\boldsymbol{\theta^r_3}/\mathrm{d}t$, and the vectors of the absolute angular velocities $\boldsymbol{\dot\theta_1}$, $\boldsymbol{\dot\theta_2}$, and $\boldsymbol{\dot\theta_3}$ with $\boldsymbol{\dot\theta_1} = \boldsymbol{\dot\theta^r_1}$ and $\boldsymbol{\dot\theta_2} = \boldsymbol{\dot\theta^r_1} + \boldsymbol{\dot\theta^r_2}$ and $\boldsymbol{\dot\theta_3} = \boldsymbol{\dot\theta^r_1} + \boldsymbol{\dot\theta^r_2} + \boldsymbol{\dot\theta^r_3}$. Compared to the R-R spatial serial manipulators, the conditions are similar in the 3R spatial manipulators but little more complex. With regard to potential energy, the following expression is given as:

$$P_t = P_{t_1} + P_{t_2} + P_{t_3} \tag{3.15}$$

with $P_{t_1} = 0$; $P_{t_2} = l_{O_2C_1} + l_{c_2}\sin(\theta^{\mathrm{r}}_2)$; $P_{t_3} = l_{O_2C_1} + l_2\sin(\theta^{\mathrm{r}}_2) + l_{c_3}\sin(\theta^{\mathrm{r}}_2 + \theta^{\mathrm{r}}_3)$, where $l_{O_2C_1}$ is the distance of the center of mass of link 1 from the joint axis O_2; l_2 is the length of link 2; l_{c_2} is the distance of the center of mass of link 2 from the joint axis O_2; l_{c_3} is the distance of the center of mass of link 3 from the joint axis O_3. Now, let us consider that the gravity balancing should be achieved in the manipulator, i.e. $P_t = const$. It can be reached if $l_{c_3} = 0$ and $l_{c_2} = m_3 l_2/m_2$, considering the location of the center of mass outside O_2O_3.

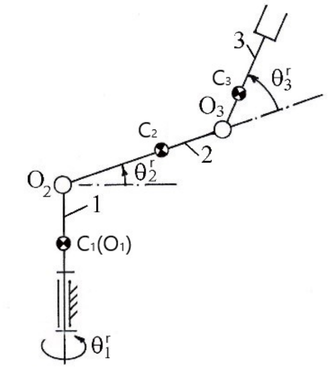

Figure 3.3 – Initial structure.

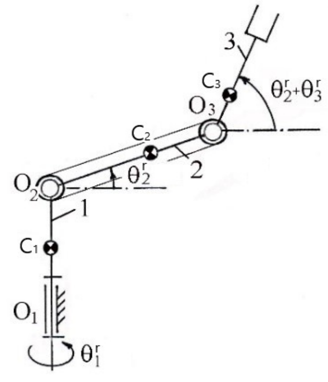

Figure 3.4 – With relocated actuators.

The kinetic energy of the initial structure (Fig. 3.3) can be written as:

$$K_e = \frac{1}{2}(I_{z_1}\dot\theta_1^2 + m_2 {V_{c_2}}^2 + I_{x2}\dot\theta_{x_2}^2 + I_{y2}\dot\theta_{y_2}^2 + I_{z_2}\dot\theta_{z_2}^2 + m_3 V_{c3}^2 + I_{x3}\dot\theta_{x_3}^2 + I_{y3}\dot\theta_{y3}^2 + I_{z_3}\dot\theta_{z_3}^2). \tag{3.16}$$

where the vectors of the absolute velocities are expressed as $\boldsymbol{V_{c_2}} = \boldsymbol{r_2} \times (\boldsymbol{\dot\theta^r_1} + \boldsymbol{\dot\theta^r_2})$ and $\boldsymbol{V_{c_3}} = \boldsymbol{l_2} \times (\boldsymbol{\dot\theta^r_1} + \boldsymbol{\dot\theta^r_2})$; the mass center vector of the second link $\boldsymbol{r_2} = [-l_{c_2},\ 0,\ 0]$; the angles relative to the corresponding coordinate axes of the system are defined as: $\dot\theta_{x_2} = \dot\theta^r_1\sin(\theta^r_2)$; $\dot\theta_{y_2} = \dot\theta^r_1\cos(\theta^r_2)$; $\dot\theta_{z_2} = \dot\theta^r_2$; $\dot\theta_{x_3} = \dot\theta^r_1\sin(\theta^r_1 + \theta^r_2)$; $\dot\theta_{y_3} = \dot\theta^r_1\cos(\theta^r_1 + \theta^r_2)$; $\dot\theta_{z_3} = \dot\theta^r_2 + \dot\theta^r_3$.

Let us consider the dynamic decoupling of the manipulator by combining two different approaches: the mass redistribution and the actuator relocation [115]. For this purpose, let us modify the design of the manipulator by placing the third actuator on the axis O_2 and coupling it with link 3 by a transmission (Figs. 3.3-3.4). This transmission can be a parallelogram, a belt transmission, a gear transmission or other type of motion generation. In this case, the kinetic energy can be expressed as follows:

$$K_e = \frac{1}{2}(I_{z_1}\dot{\varphi}_{z_1}^2 + m_2V_{c_2}^2 + I_{x_2}\dot{\varphi}_{x_2}^2 + I_{y_2}\dot{\varphi}_{y_2}^2 + I_{z_2}\dot{\varphi}_{z_2}^2 + m_3V_{c_3}^2 + I_{x_3}\dot{\varphi}_{x_3}^2 + I_{y_3}\dot{\varphi}_{y_3}^2 + I_{z_3}\dot{\varphi}_{z_3}^2). \quad (3.17)$$

where $\boldsymbol{\varphi_i}$ (where $i = 1$, 2 and 3) is the generalized angles defined as: $\boldsymbol{\varphi_1 = \theta_1^r}$; $\boldsymbol{\varphi_2 = \theta_1^r + \theta_2^r}$; $\boldsymbol{\varphi_3 = \theta_1^r + \theta_2^r + \theta_3^r}$. Then, the components of the angles relative to the corresponding coordinate axes of the system are defined as follows: $\dot{\varphi}_{x_1} = \dot{\varphi}_{y_1} = 0$, $\dot{\varphi}_{z_1} = \dot{\theta}_1^r$; $\dot{\varphi}_{x_2} = \dot{\theta}_1^r\sin(\theta_2^r)$, $\dot{\varphi}_{y_2} = \dot{\theta}_1^r\cos(\theta_2^r)$ and $\dot{\varphi}_{z_2} = \dot{\theta}_2^r$; $\dot{\varphi}_{x_3} = \dot{\theta}_1^r\sin(\theta_2^r+\theta_3^r)$, $\dot{\varphi}_{y_3} = \dot{\theta}_1^r\cos(\theta_2^r+\theta_3^r)$ and $\dot{\varphi}_{z_3} = \dot{\theta}_2^r + \dot{\theta}_3^r$; $\dot{\varphi}_{z_1}$, $\dot{\varphi}_{z_2}$ and $\dot{\varphi}_{z_3}$ are the angular velocities of the actuators.

To achieve the dynamic decoupling, the following mass property conditions of the links should be ensured:

$$I_{x_2} = I_{y_2} + m_3l_2^2 + m_2r_2^2 = I_2^* \quad (3.18)$$

$$I_{x_3} = I_{y_3} = I_3^* \quad (3.19)$$

Thus, the Lagrangian can be represented as follows:

$$L = \frac{1}{2}[I_{z_1}(\dot{\varphi}_{z_1})^2 + I_2^*(\dot{\varphi}_{z_1})^2 + (I_{z_2} + m_3l_2^2 + m_2r_2^2)(\dot{\varphi}_{z_2})^2 + I_3^*(\dot{\varphi}_1)^2 + I_{z_3}(\dot{\varphi}_{z_3})^2] \quad (3.20)$$

As a consequence of such a redistribution of moving masses, the motion equations become linear and decoupled:

$$\tau_1 = (I_{z_1} + I_2^* + I_3^*)\ddot{\varphi}_{z_1} \quad (3.21)$$

$$\tau_2 = (I_{z_2} + m_3l_2^2 + m_2r_2^2)\ddot{\varphi}_{z_2} \quad (3.22)$$

$$\tau_3 = I_{z_3}\ddot{\varphi}_{z_3} \quad (3.23)$$

The nonlinear dynamic system is thus transformed into a double integrator model (3.21)-(3.23) as obtained in the 2R spatial serial manipulator (3.12)-(3.14).

3.2 Optimal motion generation in dynamically decoupled manipulators

3.2.1 Bang-bang motion profile for input torque minimization

By implementing the dynamic decoupling through mass redistribution and actuator relocation, the resultant equations become both linear and decoupled. Referring to the obtained equations ((3.10)-(3.11) and (3.21)-(3.23)), it is evident that decreasing the maximum values of angular accelerations leads to a corresponding reduction in input torques. To ensure this outcome, the subsequent step involves considering the motion generation of links.

With regard to torque minimization in robot manipulators, there are two different approaches. In static mode, it is easily solved by gravity compensation [116]. However, in dynamic mode, solving this problem by means of mechanical modifications is quite difficult [117], therefore the efficient motion generation is applied. The solutions result in torque saturation. Several offline planning algorithms have been proposed for the minimum time trajectory, considering manipulator dynamics with torque limits of the actuators [118]–[123]. However, in this section, based on simplified motion equations due to the dynamic decoupling, the torque minimization will be carried out by diminishing the maximum angular accelerations of robot links. For this purpose, the "bang-bang" law will be applied.

It is obvious that the maximal values of the angular accelerations change following the motion profile: for quintic polynomial profile $\left|\ddot{\theta}_{max}\right| = 10\theta/\sqrt{3}t^2$ and for bang-bang profile $\left|\ddot{\theta}_{max}\right| = 4\theta/t^2$. For generation of motion, it is proposed to apply the bang-bang profile (Fig. 3.5), which allows one to reduce the maximal values of input torques. The motion profile can be expressed as follows:

$$\theta_d(t) = \begin{cases} \theta_d(t_0) + 2(\frac{t}{t_f})^2\theta_d(t_f), & t_0 \leq t \leq t_f/2 \\ \theta_d(t_0) + \left[-1 + 4(\frac{t}{t_f}) - 2(\frac{t}{t_f})^2\right]\theta_d(t_f), & t_f/2 < t \leq t_f \end{cases} \tag{3.24}$$

The application of bang-bang law theoretically brings about a reduction of 30% of the maximal value of the angular acceleration. Thus, by reducing the angular accelerations of the manipulator's links, a decrease in their actuating torques can be achieved. To demonstrate the effectiveness of the proposed method, numerical simulations are carried out in the following sections.

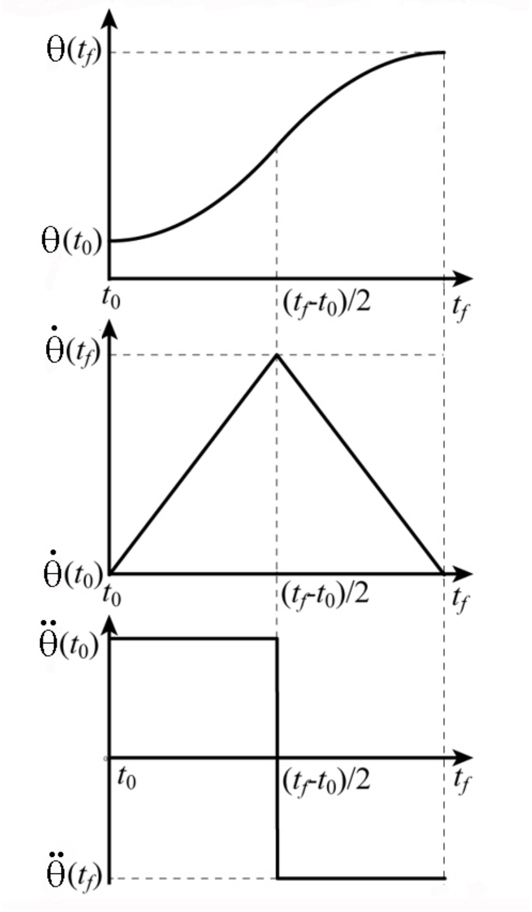

Figure 3.5 – “Bang-bang” profile used for motion generation in dynamically decoupled spatial serial manipulators.

3.2.2 Numerical simulations of 2R spatial serial manipulator

To create a CAD model and carry out simulations via ADAMS software, a decoupled 2R spatial serial manipulator with $I_{z_1} = 0.3$ kgm^2; $I^* = 0.1$ kgm^2; $I_{z_2} = 0.14$ kgm^2 is considered. The mass and length of two links were defined as: $m_1 = 5.98$ kg; $m_2 = 10.34$ kg; $l_1 = 0.25$ m; $l_2 = 0.3$ m. The mass property conditions in Section 3.1.1 were applied for determining the mass-center positions of two links. The initial and final values of the rotating angles θ_1 and θ_2 were defined as the following: $\theta_{1i} = \theta_{2i} = 0°$; $\theta_{1f} = 90°$ and $\theta_{2f} = 60°$. Two types of motions for $t_f = 1$ s were simulated: 1) with fifth order polynomial profile; 2) "bang-bang" profile.

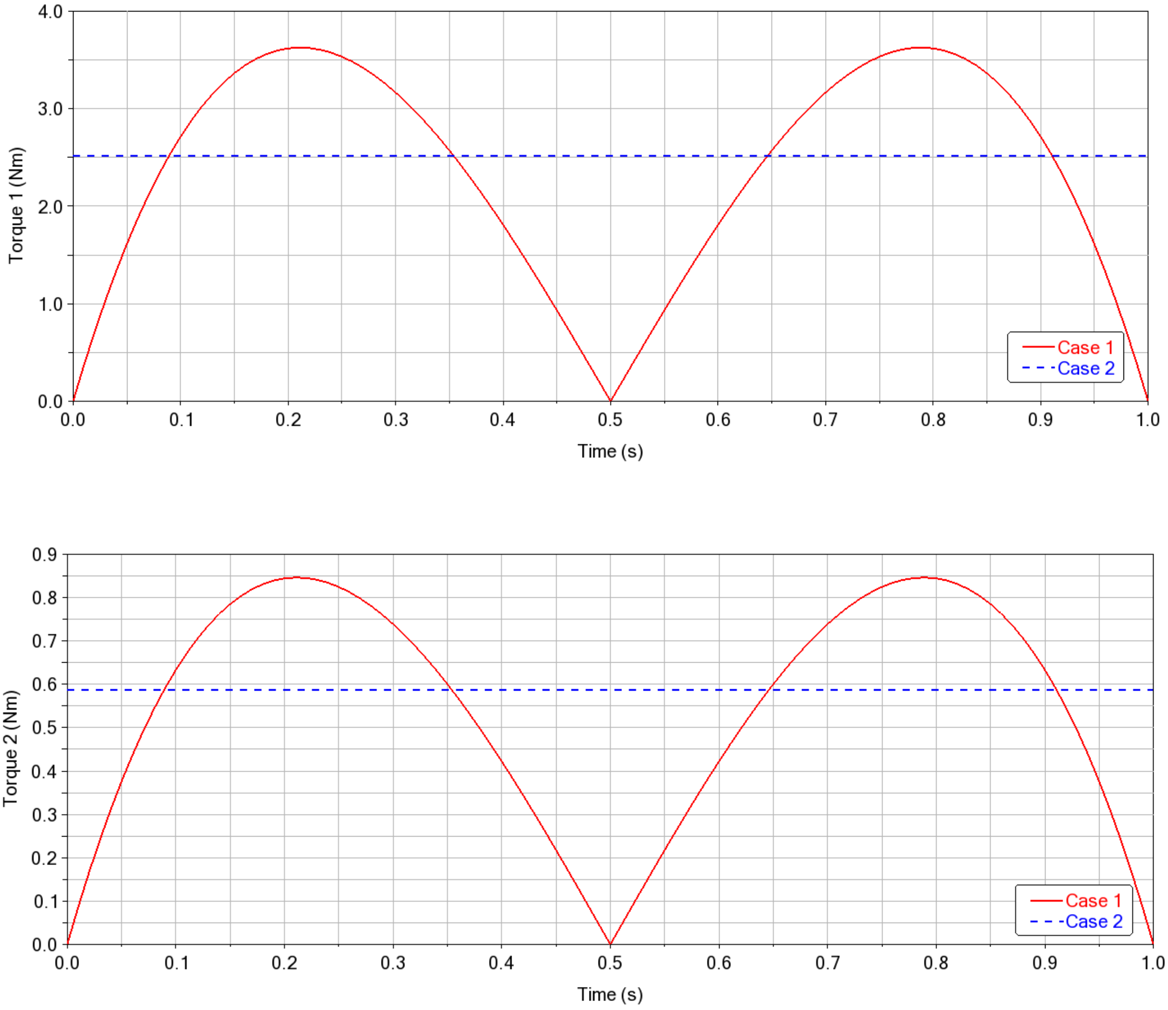

Figure 3.6 – Decoupled 2R manipulator's input torque magnitude for two studied cases (Case 1: fifth order polynomial profile; Case 2: bang-bang profile).

As illustrated in Fig. 3.6, compared to the fifth order polynomial profile, bang-bang motion profile has brought out a reduction of up to 30.7% in the maximum input torques of the decoupled 2R manipulator.

3.2.3 Numerical simulations of 3R spatial serial manipulator

To demonstrate the effectiveness of dynamic decoupling in 3R spatial serial manipulator, a CAD model was created with the parameters in Tab. 3.1 and numerical simulations were conducted via MATLAB®. The parameters of KR 16R1610 in Tab. 3.1 are approximate and round.

Table 3.1 – Length and mass parameters of the industrial robot KR 16R1610 [124].

Length of Link 1	l_1	0.52 m
Length of Link 2	l_2	0.89 m
Length of Link 3	l_3	0.81 m
Mass of Link 1	m_1	122 kg
Mass of Link 2	m_2	83 kg
Mass of Link 3	m_3	40 kg
Mass Center of Link 1	l_{c_1}	0.26 m
Mass Center of Link 2	l_{c_2}	0.465 m
Mass Center of Link 3	l_{c_3}	0.405 m
Axial moment of inertia of Link 1	I_{x_1}	3.52 kgm^2
Axial moment of inertia of Link 1	I_{y_1}	3.52 kgm^2
Axial moment of inertia of Link 1	I_{z_1}	1.56 kgm^2
Axial moment of inertia of Link 2	I_{x_2}	0.82 kgm^2
Axial moment of inertia of Link 2	I_{y_2}	6.43 kgm^2
Axial moment of inertia of Link 2	I_{z_2}	6.43 kgm^2
Axial moment of inertia of Link 3	I_{x_3}	0.13 kgm^2
Axial moment of inertia of Link 3	I_{y_3}	2.25 kgm^2
Axial moment of inertia of Link 3	I_{z_3}	2.25 kgm^2

To achieve the dynamics decoupling, several manipulator parameters were modified by using Eqs. (3.18)-(3.19) and the mass-center conditions in Section 3.1.2. The initial and final values of the rotating angles θ_1, θ_2 and θ_3 were defined as the following: $\theta_{1i} = \theta_{2i} = \theta_{3i} = 0$; $\theta_{1f} = 90°$, $\theta_{2f} = 80°$ and $\theta_{3f} = 60°$. Two types of motions for $t_f = 1$ s were simulated: 1) with fifth order polynomial profile; 2) “bang-bang” profile.

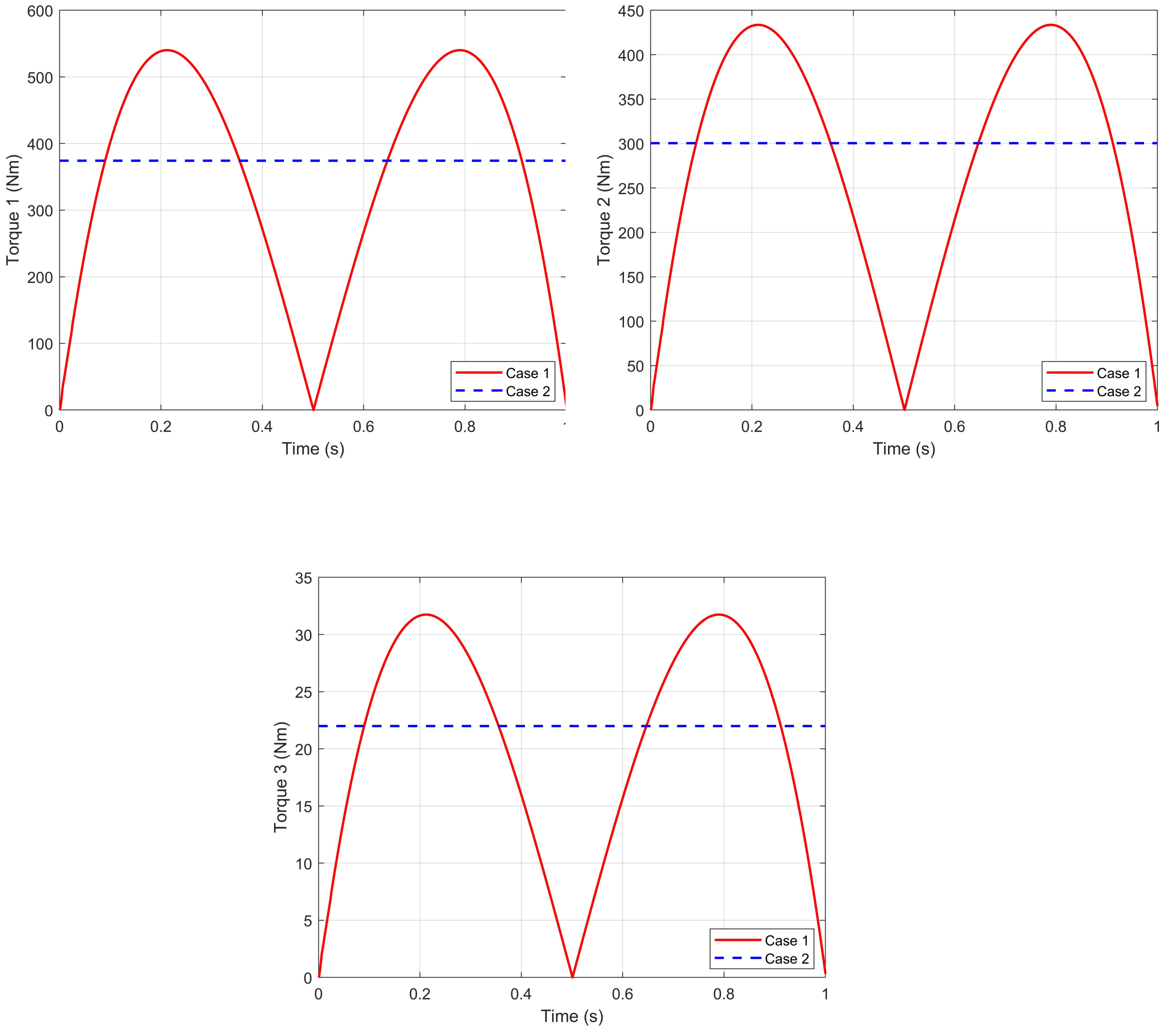

Figure 3.7 – Decoupled 3R manipulator's input torque magnitude for two studied cases (Case 1: fifth order polynomial profile; Case 2: bang-bang profile).

Fig. 3.7 illustrates torque variations for two examined cases. The results demonstrated that the implementation of a bang-bang motion profile in the decoupled 3R manipulator led to a reduction of up to 30.72 % in maximum input torques. Thus, torque minimization has been successfully achieved through the suggested motion profile in the dynamically decoupled manipulators, without adding additional masses.

3.3 Error sensitivity analysis in dynamically decoupled manipulators

3.3.1 Sensitivity analysis criterion

In the previous section, the torque minimization has been achieved in dynamically decoupled manipulator via optimal motion generation. Through the dynamic decoupling approaches like mass redistribution and actuator relocation, a highly nonlinear dynamic model of manipulator is simplified as a double integrator system for each actuator. However, some unpredictable errors could not be avoided in fabrication or assembling process, leading to incomplete dynamic decoupling. An interesting question is: how much is the influence of parameter errors on torque minimization in spatial serial manipulator? Is it possible to find the most influential parameters to the input torques when tracking the bang-bang profile? The sensitivity analysis methods, aiming at exploring the impact of varying input assumptions, is usually considered as a solution to this kind of problem.

As shown in Figs. 3.6-3.7, while tracking the bang-bang motion profile, the absolute values of input torque remain constant in the dynamically decoupled manipulators. However, owing to the incomplete decoupling, input torques may deviate from the reference values, resulting in additional energy consumption. For a clearer illustration, Fig. 3.8 presents the input torques of the 2R spatial serial manipulator with incomplete dynamic decoupling, where there exists 5 % error in I_{x_2}. The incomplete dynamic decoupling due to this parameter error leads to the increased maximum input torques and also the energy consumption. Thus, to quantify the input torque deviation when tracking the bang-bang motion profile, the Root Mean Square (RMS) method is used:

$$\mathrm{RMS} = \sqrt{\frac{1}{N}\sum_{i=1}^{N}(\tau_i - \tau_d)^2} \tag{3.25}$$

where N represents the total number of sampling points in the desired motion trajectory and τ_i denotes the input torques in dynamically decoupled manipulator. τ_d denotes the reference input torque when applying bang-bang motion profile (blue dash lines in Figs. 3.6-3.7).

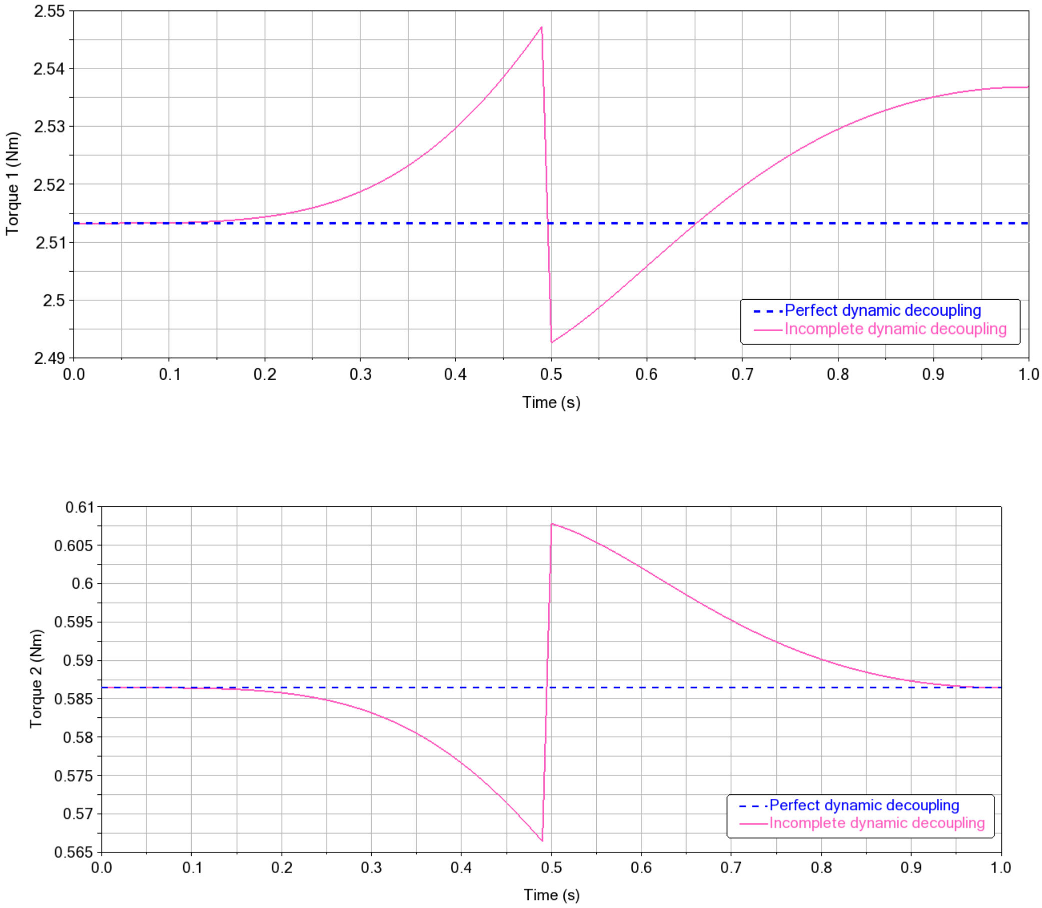

Figure 3.8 – Input torques of 2R spatial serial manipulator with incomplete dynamic decoupling (5 % error in I_{x_2}).

3.3.2 Local and global sensitivity analysis method

Regarding the sensitivity analysis methods, they can be divided into two groups: local sensitivity analysis and global sensitivity analysis. Local sensitivity analysis investigates how a small perturbation near an input space value $x = (x_1, ..., x_n)$ influences the output value y, which is achieved by the partial derivative [125].

$$S_i = \frac{\partial y}{\partial x_i}(x_1^0, ..., x_n^0) \tag{3.26}$$

where $x_1^0, ..., x_n^0$ are the nominal input values. The partial derivative in Eq. (3.26) characterizes the impact of perturbing input values near a nominal value on the random output value. However, due to the presence of nonlinear effects and interactions, accurately estimating the sensitivity of parameters becomes challenging with the local sensitivity analysis. The dynamics of spatial manipulators is also nonlinear and coupled, leading to interaction effects caused by parameter errors. Therefore, for increased accuracy in parameter sensitivity analysis, it is recommended to utilize global sensitivity analysis instead of local sensitivity analysis. In contrast to local sensitivity analysis, global sensitivity analysis investigates the variability of the model output $\mathbf{Y}$ and examines how the variability in input parameters influences the output variance. Sobol indices, known as a global sensitivity analysis method, are employed to assess the sensitivity of input parameters, taking into account the interaction effects [126]. The first-order Sobol indice is stated as follows:

$$S_i = \frac{\mathrm{Var}_{\mathbf{X}_i}(\mathrm{E}_{\mathbf{X}_{\sim i}}(\mathbf{Y}|\mathbf{X}_i))}{\mathrm{Var}(\mathbf{Y})} \tag{3.27}$$

and total order indice is given as:

$$S_{T_i} = \frac{\mathrm{E}_{\mathbf{X}_{\sim i}}(\mathrm{Var}_{\mathbf{X}_i}(\mathbf{Y}|\mathbf{X}_{\sim i}))}{\mathrm{Var}(\mathbf{Y})} = 1 - \frac{\mathrm{Var}_{\mathbf{X}_{\sim i}}(\mathrm{E}_{\mathbf{X}_{\sim i}}(\mathbf{Y}|\mathbf{X}_{\sim i}))}{\mathrm{Var}(\mathbf{Y})} \tag{3.28}$$

where S_i measures the contribution of the parameter $\mathbf{X}_i$ to the total variance of the response. Total order indice S_{T_i} represents the total contribution (including interactions) of a parameter $\mathbf{X}_i$ to the total variance of the response. However, the computational burden linked to the computation of these indices grows significantly, especially in scenarios with numerous parameters. To alleviate this computational load, the Monte Carlo estimators are adopted in this context [127].

$$\mathrm{Var}_{\mathbf{X}_i}(\mathrm{E}_{\mathbf{X}_{\sim i}}(\mathbf{Y}\,|\mathbf{X}_i)) \;\approx \frac{1}{N}\sum_{j=1}^{N} f\,(\mathcal{B})_j\,(f\left(\mathcal{A}_{\mathcal{B}}^{i}\right)_j - f(\mathcal{A})_j) \tag{3.29}$$

$$\mathrm{E}_{\mathbf{X}\sim i}(\mathrm{Var}_{\mathbf{X}_i}(\mathbf{Y}|\mathbf{X}_{\sim i})) \approx \frac{1}{2N}\sum_{j=1}^{N}(f(\mathcal{A})_j) - f\left(\mathcal{A}_{\mathcal{B}}^{i}\right)_j)^2 \tag{3.30}$$

where, $\mathcal{A}$ and $\mathcal{B}$ are the matrix of all the parameters generated by the Sobol sequence, based on a uniform sampling method. $\mathcal{A}_{\mathcal{B}}$ is the combination of the columns of matrix $\mathcal{A}$ and $\mathcal{B}$ (see detail in [127]). The precision of Monte Carlo estimators relies on the density of sampling points within each parameter interval; greater point density results in the increased accuracy of parameter sensitivity analysis.

3.3.3 Sensitivity analysis of 2R spatial serial manipulator

In the 2R spatial serial manipulator, the investigation focuses on the sensitivity of parameters to meet the decoupling condition for both input torques τ_1 and τ_2. The numerical simulation has been carried out via MATLAB® and the results are presented in Tab. 3.2. The Sobol sequence was used for uniform sampling in each parameter interval, with an allowable error of ±5%. Specifically, 1000 sampling points were distributed in each parameter interval.

Table 3.2 – Sobol indices of the decoupled 2R spatial serial manipulator.

Design parameters	τ_1 (S)	τ_1 (S_T)	τ_2 (S)	τ_2 (S_T)
x_{r_1}	0	0	0	0
y_{r_1}	0	0	0	0
z_{r_1}	0	0	0	0
I_{z_1}	0.8950	0.9685	0	0
x_{r_2}	0	0	0.6121	0.6437
y_{r_2}	0	0	0.3487	0.3805
z_{r_2}	0.0057	0	0	0
I_{x_2}	0.0266	0.0329	0	0
I_{y_2}	0.0120	0.0215	0	0
I_{z_2}	0	0	0.0016	0.0018

From the results in Tab. 3.2, it is evident that I_{z_1} is the most influential parameter to the deviation of τ_1, quantified by Eq. 3.25. However, its variation does not significantly impact the decoupling condition (3.10). Regarding τ_2, both x_{r_2} and y_{r_2} are identified as influential parameters to the input torque deviation. Uncertainty of these parameters has a substantial effect on τ_2 and leads to incomplete decoupling in the 2R spatial serial manipulator. To achieve effective torque minimization, it is necessary to ensure high precision in controlling these influential parameters.

3.3.4 Sensitivity analysis of 3R spatial serial manipulator

During the decoupling process of 3R spatial serial manipulator, the sensitivity of 19 parameters to the input torque deviation was studied. The Sobol sequence was applied for the uniform sampling in every interval of parameters, which had ±5% error, wherein 1000 points were distributed in every interval of parameters for the sampling. The numerical simulation results are presented in Tab. 3.3.

Table 3.3 – Sobol indices of the decoupled 3R spatial serial manipulator.

Design parameters	τ_1 (S)	τ_1 (S_T)	τ_2 (S)	τ_2 (S_T)	τ_3 (S)	τ_3 (S_T)
x_{r_1}	0	0	0	0	0	0
y_{r_1}	0	0	0	0	0	0
z_{r_1}	0	0	0	0	0	0
I_{z_1}	0.005	0.0073	0	0	0	0
m_2	0.0479	0.0490	0	0.0021	0	0
x_{r_2}	0.1896	0.1945	0.0167	0.0222	0	0
y_{r_2}	0.0065	0.0073	0.002	0.0022	0	0
z_{r_2}	0.0035	0.0025	0	0	0	0
I_{x_2}	0.2890	0.2901	0	0	0	0
I_{y_2}	0.0075	0.0084	0	0	0	0
I_{z_2}	0	0	0.0049	0.0057	0	0
l_2	0.2413	0.2104	0.6473	0.6320	0	0
m_3	0.2111	0.2101	0.3328	0.3341	0	0
x_{r_3}	0	0.0021	0.0043	0.0055	0.7434	0.7558
y_{r_3}	0.0119	0.0156	0	0.0012	0.0118	0.0111
z_{r_3}	0.0052	0.0024	0.0013	0	0	0
I_{x_3}	0.0028	0.0023	0	0	0.0016	0.0017
I_{y_3}	0	0	0	0	0	0.0017
I_{z_3}	0	0	0	0	0.2220	0.2307

From the obtained results, it can be observed that x_{r_2}, I_{x_2}, l_2 and m_3 are the influential parameters to the deviation of τ_1. l_2 and m_3 are the influential parameters to the deviation of τ_2. Regarding τ_3, x_{r_3} results in more deviation of the input torque than the other parameters. The obtained results reveal that the input torques of dynamically decoupled manipulator are sensitive to the lengths and masses of links, corresponding to the results in [71]. Thus, accurate identification of these parameters is crucial in the decoupled 3R spatial serial manipulator, as errors in these parameters increase the maximum input torque and energy consumption.

3.4 Control performance improvement in dynamically decoupled manipulators

3.4.1 Control performance indices

In Section 3.1, decoupling technique was applied in spatial serial manipulators for achieving torque minimization. Additionally, the technique provides another advantage: a decoupled dynamic system has been converted into a double integrator, which facilitates the controller design. Compared to the non-decoupled manipulator system, a linear and decoupled dynamic system is more likely to be stabilized and exhibits faster response speed. To track the bang-bang motion profile and achieve improved control performance, various straightforward control strategies are employed and studied in this section.

Two performance indices are introduced to quantify and evaluate the control system's performance: the integral of the square of the error (ISE) and the maximum input torque (MT). To evaluate the tracking accuracy, the ISE of the ith link in the decoupled manipulator is defined as follows:

$$\mathrm{ISE_i} = \int_{t_0}^{t_f} e_i^2 \mathrm{d}t, \ i = 1, \cdots, n \tag{3.31}$$

where $e_i = \theta_i - \theta_{id}$ is the tracking error of the first link. The ISE discriminates between excessively over-damped and excessively under-damped systems. Another criterion introduced was the maximum input torque, representing the input energy. The actuator capacity requirement also depends on the maximum input torque.

Besides, the energy efficiency is affected by Joule effect, which describes the process where the energy of an electric current is converted into heat as it flows through a resistance. In electric motors, neglecting the friction, most part of the energy consumption is due to the loss by Joule effect. To evaluate the loss, a criterion is introduced as follows for the ith link in the decoupled manipulator:

$$E_i = const_i \int_{t_0}^{t_f} \tau_i^2 \mathrm{d}t, \ i = 1, \cdots, n \tag{3.32}$$

where τ_i is the actuator torque for the ith link. $const_i$ is the ratio between the resistance of the inductive circuit R of the DC motor and the the square of the torque constant. In this chapter, this $const_i$ will be set equal to 1. For a DC motor, considering that the torque supplied by motor is proportional to the armature current, the criterion (3.32) is proportional to the energy consumption produced by Joule effect. It characterizes the energy that must be produced by the battery to allow the desired motion. Besides, the heat generated by Joule effect degrades the reliability of electrical systems components. For example, the results obtained in [128] have revealed that the useful lifetimes of solder joints have been significantly decreased due to the Joule heating effect at high current densities. Therefore, the effect is undesirable and must be taken into account in controller design. Various straightforward control techniques are applied to track the bang-bang profile and the influence on these criteria will be investigated.

3.4.2 Lead compensation performance

The primary function of the lead compensator is to reshape the frequency-response curve to provide a phase lead angle sufficient to offset the excessive lag phase associated with the components of the fixed system. The frequency-domain expression of the decoupled system is presented as follows:

$$G(\mathrm{s}) = \frac{1}{I\mathrm{s}^2} \tag{3.33}$$

where the letter s, a complex variable, defines the Laplace transform operator; as mentioned above, I can be obtained by the dynamic decoupling. For example, to each linear system (3.21)-(3.23) in the decoupled 3R manipulator, $I = (I_{z_1} + I_2^* + I_3^*)$ for the first link, $I = I_{z_2} + m_3 l_2^2 + m_2 r_2^2$ for the second link and $I = I_{z_3}$ for the third link. As all the dynamic systems are transformed into the similar structure (3.12)-(3.14) of double integrators, the control performance about the first link will be studied, which has the biggest inertial moment and the lowest dynamic respond speed. $I = 0.4$ kgm^2 for the first link in the decoupled 2R manipulator, and $I = 57.60$ kgm^2 for the first link in the decoupled 3R manipulator. Since the obtained linear and decoupled system was a double integrator model, a lead compensator could be employed to stabilize the system by increasing its phase margin. The expression of lead compensator is given as follows:

$$G_c(\mathrm{s}) = K_c \frac{\alpha T\mathrm{s} + 1}{T\mathrm{s} + 1} \tag{3.34}$$

where K_c, T and α are the coefficients determined based on the maximum phase lead angle and the cut-off frequency. However, it's essential to note that modifying the system's dynamic characteristics by increasing the cut-off frequency enhances the dynamic response speed to track the bang-bang profile. The gain crossover frequency of the decoupled system is consequently raised to 89.44 rad/s for the first link, resulting in an improved speed of response. Then, assuming the required maximum phase lead angle ϕ_m is 70°, the coefficients of the lead compensator can be determined. The Bode plot of the compensated system is illustrated as follows (Fig. 3.9).

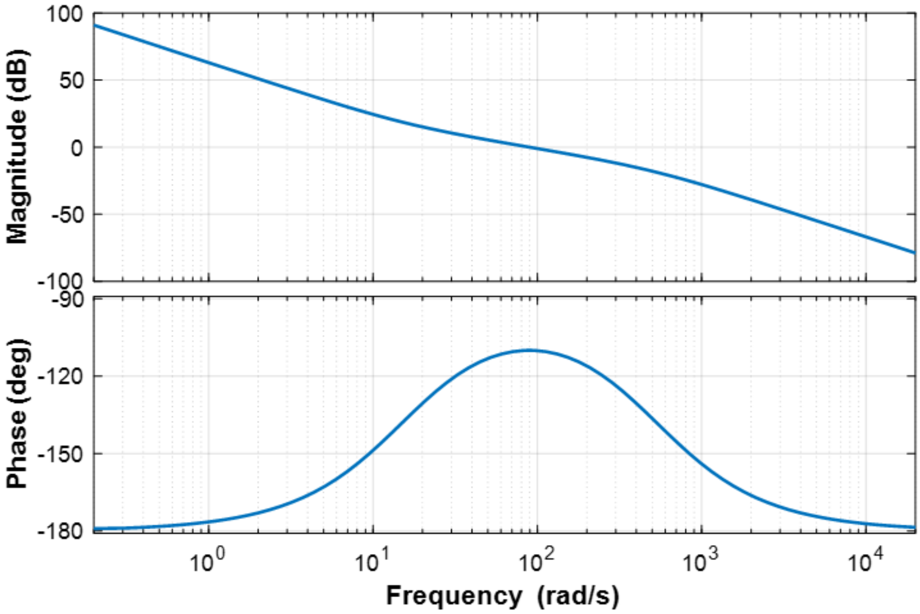

Figure 3.9 – Frequency domain response with 70° phase lead compensator.

As depicted in the Bode plot, the maximum phase lead margin is raised to 70° at the modified gain crossover frequency of 89.44 rad/s, resulting in improved asymptotic stability. For an analysis of tracking performance and input torque, numerical simulations were carried out in Matlab with a time step of 1×10^{-5} s. The initial and final values for the rotating angles were defined as $\theta_i = 0°$ and $\theta_f = 90°$.

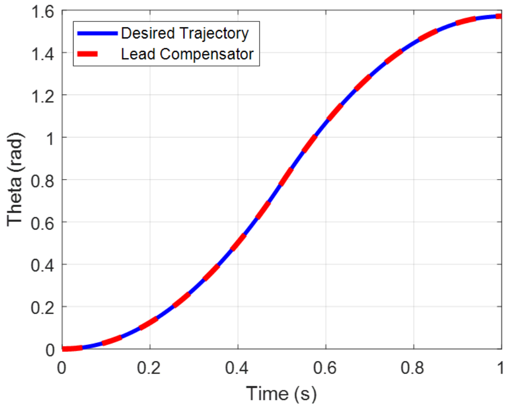

Figure 3.10 – Trajectory tracking of lead compensator in the decoupled 2R spatial serial manipulator.

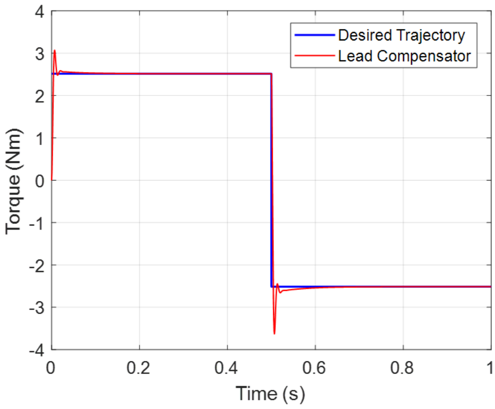

Figure 3.11 – Torque generation of lead compensator in the decoupled 2R spatial serial manipulator.

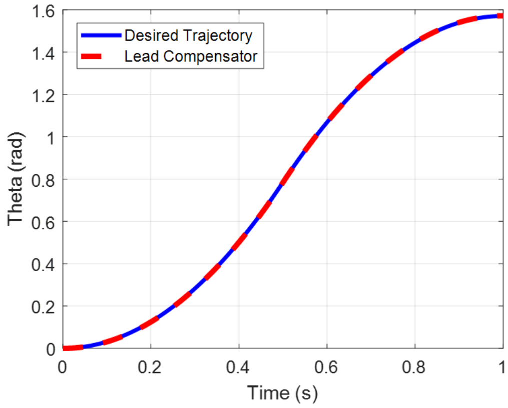

Figure 3.12 – Trajectory tracking of lead compensator in the decoupled 3R spatial serial manipulator.

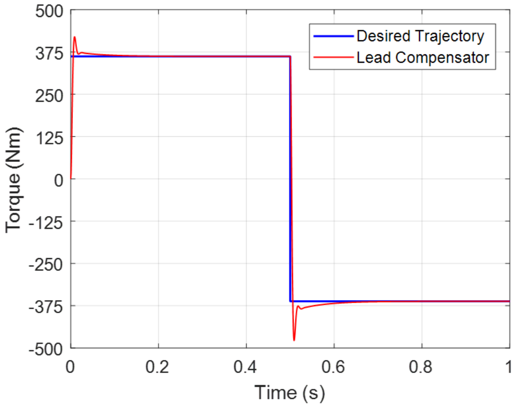

Figure 3.13 – Torque generation of lead compensator in the decoupled 3R spatial serial manipulator.

It is obvious that the decoupled systems (2R and 3R) with the modified gain crossover frequency and 70° phase lead angle are capable of tracking the desired bang-bang profile trajectory. For example, in the decoupled 3R manipulator, the ISE value is 8.29×10^{-2} rad^2s and the maximum torque 4.78×10^2 Nm. The energy consumption produced by Joule effect is 1.33×10^5 J. In addition, a table with a variety of phase lead angles was created to investigate the influence of different phase lead angles on three criteria in both 2R and 3R decoupled manipulators:

Table 3.4 – Results of different phase lead angles in the decoupled 2R spatial serial manipulator.

Tracking Performance	**ISE** (rad^{2}s)	**Joule effect** (J)	**MT** (Nm)
6° **Phase Lead Angle**	2.10×10^{-3}	7.3192	7.1808
10° **Phase Lead Angle**	2.30×10^{-3}	6.9122	6.8946
20° **Phase Lead Angle**	3.20×10^{-3}	6.6145	6.3160
30° **Phase Lead Angle**	4.50×10^{-3}	6.5118	5.7791
40° **Phase Lead Angle**	6.80×10^{-3}	6.4578	5.2676
50° **Phase Lead Angle**	1.08×10^{-2}	6.4232	4.7606
60° **Phase Lead Angle**	1.90×10^{-2}	6.3980	4.2307
70° **Phase Lead Angle**	3.99×10^{-2}	6.3778	3.6289
80° **Phase Lead Angle**	1.18×10^{-1}	6.3589	2.8687

Table 3.5 – Results of different phase lead angles in the decoupled 3R spatial serial manipulator.

Tracking Performance	**ISE** (rad^{2}s)	**Joule effect** (J)	**MT** (Nm)
6° **Phase Lead Angle**	4.48×10^{-3}	1.5298×10^5	1.03×10^3
10° **Phase Lead Angle**	4.84×10^{-3}	1.4422×10^5	9.84×10^2
20° **Phase Lead Angle**	6.57×10^{-3}	1.3766×10^5	8.91×10^2
30° **Phase Lead Angle**	9.39×10^{-3}	1.3542×10^5	8.06×10^2
40° **Phase Lead Angle**	1.41×10^{-2}	1.3424×10^5	7.25×10^2
50° **Phase Lead Angle**	2.24×10^{-2}	1.3349×10^5	6.46×10^2
60° **Phase Lead Angle**	3.94×10^{-2}	1.3295×10^5	5.65×10^2
70° **Phase Lead Angle**	8.29×10^{-2}	1.3252×10^5	4.78×10^2
80° **Phase Lead Angle**	2.46×10^{-1}	1.3210×10^5	3.85×10^2

It could be observed from the tables that the ISE value increases and the maximum torque is diminished when the phase lead angle is increased. In application, a large phase lead angle is required to lower the actuator capacity and energy consumption. However, for a system requiring high tracking accuracy, a small phase lead angle is needed. Obviously, there exists a trade-off between the tracking accuracy and input energy efficiency. This implies that the desired control performance can be attained by adjusting the phase lead angle, thereby facilitating the design of the robot manipulator controller. To achieve a more satisfactory control performance, full-state feedback method is considered in the following parts.

3.4.3 Linear quadratic regulator performance

Since the double integrator model system is unstable, the control technique should aim to improve the stability of the system. Therefore, the speed of response and tracking error requirement should be improved to track the bang-bang profile. Linear quadratic regulator (LQR) is a powerful control technique, which stabilizes and operates a linear dynamic system by minimizing a given cost function. In order to implement a LQR controller, a linear time invariant (LTI) dynamic system must be available, which has already been obtained by the dynamic decoupling, and the system must be completely controllable. It is assumed that all state variables are measurable and also available for feedback in our system. The controllability matrix is given by:

$$\mathbf{C} = \begin{bmatrix}\mathbf{B} & \mathbf{AB} & \mathbf{A^2B} & ... & \mathbf{A^{n-1}B}\end{bmatrix} = \begin{bmatrix} 0 & 1/I \\ 1/I & 0 \end{bmatrix} \tag{3.35}$$

Since the control matrix $\mathbf{C}$ of the state space equation obtained has full row rank 2, this decoupled dynamic system is controllable. LQR algorithme aims to minimize the quadratic cost function as follows:

$$\int_0^\infty (\mathbf{x}^\top \mathbf{Q} \mathbf{x} + \mathbf{u}^\top \mathbf{R} \mathbf{u}) \mathrm{d}\mathbf{x} \tag{3.36}$$

where $\mathbf{Q}$ and $\mathbf{R}$ are the weights related to the system state error (angle and angular velocity) and the control input (motor torque) respectively. The appropriate selection of $\mathbf{Q}$ and $\mathbf{R}$ determines the control performance. The optimal control law to minimize the quadratic cost function is given by:

$$\mathbf{u} = -\mathbf{K}\mathbf{x} \tag{3.37}$$

where,

$$\mathbf{K} = \mathbf{R^{-1}B^\top P} \tag{3.38}$$

and $\mathbf{P}$ is found by solving the continuous time algebraic Riccati equation:

$$\mathbf{A^\top P} + \mathbf{PA} - \mathbf{PBR^{-1}B^\top P} + \mathbf{Q} = \mathbf{0} \tag{3.39}$$

The design steps could be stated as follows:

1. Solve the reduced Riccati equation (3.39), for the matrix $\mathbf{P}$

2. Substitute this matrix **P** into the equation (3.38). The resulting matrix **K** is the optimal one.

The simulation was carried out in Matlab software with $I = 0.4$ kgm^2 (the first link with lower frequency) and the time step set at 1×10^{-5} s. By using the steps mentioned above, the optimal control gains K_1 and K_2 were calculated as $K_1 = 3464.10$ and $K_2 = 634.64$. The values of **Q** and **R** were initialized as follows for the control of the first link:

$$\mathbf{Q} = \begin{bmatrix} 600000 & 0 \\ 0 & 20000 \end{bmatrix}, \mathbf{R} = \begin{bmatrix} 0.05 & 0 \\ 0 & 0.05 \end{bmatrix} \tag{3.40}$$

The tracking performance and input torque were obtained as follows:

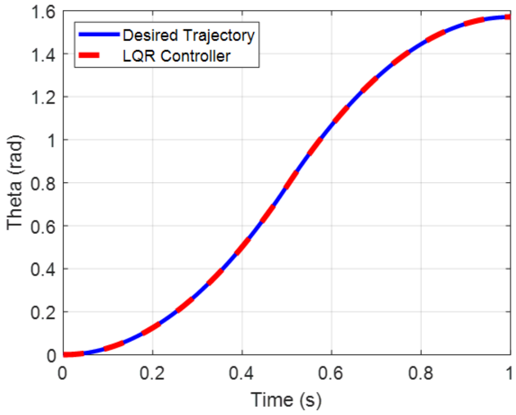

Figure 3.14 – Trajectory tracking of LQR in the decoupled 2R manipulator.

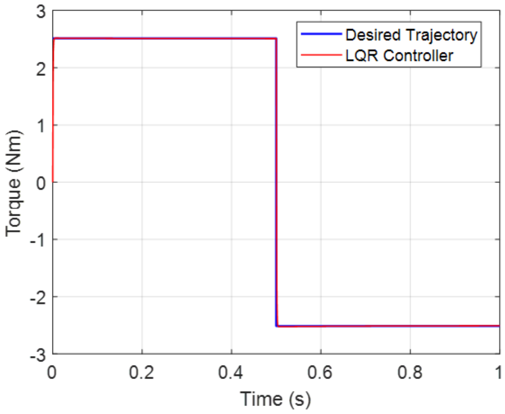

Figure 3.15 – Torque generation of LQR in the decoupled 2R manipulator.

The simulation has also been carried out in the decoupled 3R manipulator ($I = 57.60$ kgm^2) with $K_1 = 109540$ and $K_2 = 40160$. The result was obtained as follows:

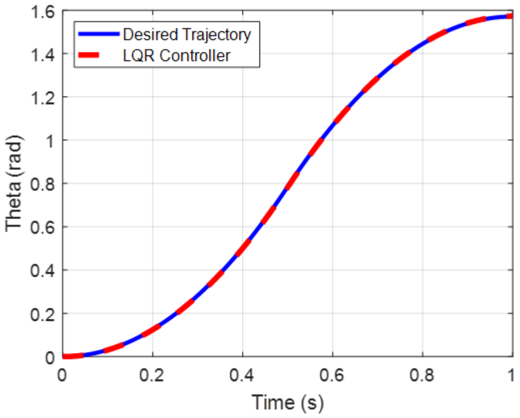

Figure 3.16 – Trajectory tracking of LQR in the decoupled 3R manipulator.

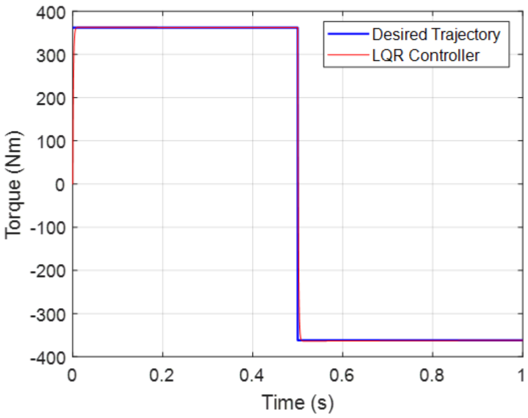

Figure 3.17 – Torque generation of LQR in the decoupled 3R manipulator.

From the simulation results, it can be observed that in the decoupled dynamic system, LQR results in excellent control performance by the bang-bang profile. For exemple, in the 3R decoupled manipulator, the ISE value is 0.21 rad^{2}s and the maximum torque 3.64×10^5 Nm. The energy consumption produced by Joule effect is 1.3109×10^5 J. Based on the obtained results, it is evident that LQR controller performs better than lead compensator in terms of energy consumption. However, these linear controllers do not take the parameter uncertainty and external unknown disturbances into account in the control process, which could destabilize the decoupled dynamic system.

3.4.4 Parameter uncertainty and external disturbance

Generally, not every dynamic system is exactly the same as what we considered in the design process. Parameter uncertainty and unknown external disturbances take place in many practical problems, resulting in poor stability, accuracy, energy consumption etc. These factors should be taken into account in the design of controller.

For the decoupled manipulators designed in Section 3.1, it is assumed that a variation of inertial value I may exist in the dynamic model. Linear control techniques used previously cannot attain perfect control performance. Furthermore, the unknown external disturbances are another thing taken into account when designing controllers for the spatial serial manipulators, which degrades the stability or tracking accuracy of the control system.

As mentioned in Chapter 1, friction is the nemesis of precision control [4]. A lot of friction models have been proposed in the literature. They are mainly classified into two groups: dynamic friction models and static friction models. The dynamic models, like Dahl model or LuGre model [129], can capture more friction characteristics but it is not easy to apply due to the model complexity. To model the friction disturbance, the static friction model considering Stribeck effect and viscous friction (Eq. 1.4) is adopted in our case because of its simple implementation and acceptable accuracy [130]. Considering the nonlinear friction, the plant is represented as follows:

$$I\ddot{\theta} = u + \tau_f(\dot{\theta}) \tag{3.41}$$

where the joint friction $\tau_f(\dot{\theta})$ can be defined as follows:

$$\tau_f(\dot{\theta}) = (F_C + (F_S - F_C)\mathrm{e}^{-\left|\frac{\dot{\theta}}{\dot{\theta}_S}\right|^{\delta_\sigma}})\mathrm{sign}(\dot{\theta}) + F_v\dot{\theta} \tag{3.42}$$

where F_C and F_S are the magnitude of Coulomb friction and static friction respectively; $\dot{\theta}_S$ denotes the Stribeck velocity and δ_σ is the exponent of the Stribeck nonlinearity. F_v represents the magnitude of viscous friction. The curve of the joint friction $\tau_f(\dot{\theta})$ is presented as follows with the parameters used in [130]: $F_C = 3.40 \times 10^{-2}$ Nm; $F_S = 4.60 \times 10^{-2}$ Nm; $F_v = 3.68 \times 10^{-4}$ Nm/(rad/s); $\dot{\theta}_S = 10.68$ rad/s; $\delta_\sigma = 1.93$.

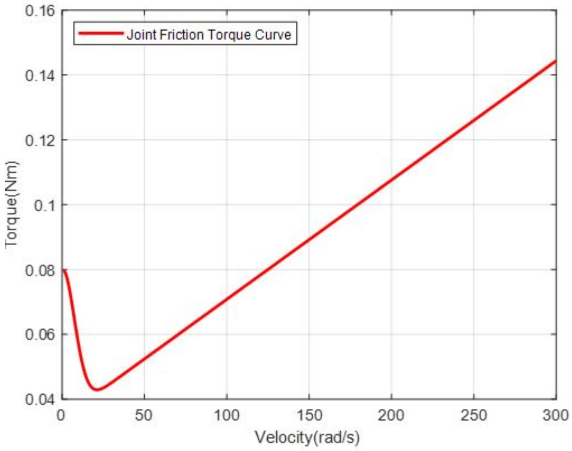

Figure 3.18 – Joint friction curve.

In the following sections, different control techniques are presented and used to stabilize the decoupled dynamic system in the presence of parameter uncertainty and external disturbances.

3.4.5 Model-reference adaptive control performance

The parameter uncertainty or variation occurs in many practical problems. For instance, robot manipulators carry out their tasks such as 'pick and place' with inaccurate inertial parameters. It may cause inaccuracy or instability in control systems. In our case, thanks to the dynamic decoupling, the 2R and 3R spatial manipulator models have been simplified as a double integrator. However, it is very strict to assume that the inertial parameters of the dynamically decoupled manipulator are the exactly same as we know in the design process. To resolve the problem, model-reference adaptive control (MARC) has been proposed in [131], which can be adopted for the decoupled dynamic system. An adaptation mechanism in MARC aims to adjust the parameters in the control law so that the perfect tracking performance can be achieved [131]. The MRAC law is presented as follows:

$$u = \hat{I}(\ddot{\theta}_d - 2\lambda\dot{\hat{\theta}} - \lambda^2\hat{\theta}) \tag{3.43}$$

where the tracking error $\hat{\theta} = \theta - \theta_d$; λ is the positive constant chosen to reflect the performance specification. $\hat{I}$ is defined as the estimate of inertial. The following update law is used to adjust it:

$$\dot{\hat{I}} = -\gamma v s \tag{3.44}$$

where γ is a position constant called the adaptation gain; $v = \ddot{\theta}_d - 2\lambda\dot{\hat{\theta}} - \lambda^2\hat{\theta}$. The combined tracking error s is defined as:

$$s = \dot{\hat{\theta}} + \lambda\hat{\theta} \tag{3.45}$$

The equations above present an adaptation mechanism based on system signals. The proof of the global asymptotic stability is demonstrated in [131] with the Lyapunov theory. The interested reader may refer to [131] for further details. The simulation was carried out in MATLAB® with the following parameter. For the decoupled 2R manipulator: $\gamma_1 = 2$; $\lambda_1 = 50$; $\hat{I}_1(0) = 0.40$ kgm^2. The real inertial value was 0.50 kgm^2. For the decoupled 3R manipulator: $\gamma_2 = 200$; $\lambda_2 = 50$; $\hat{I}_2(0) = 57.60$ kgm^2. The real inertial value was 72 kgm^2. The time step was set as 1×10^{-5} s.

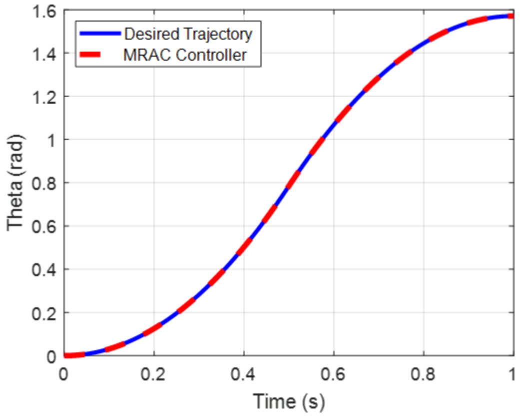

Figure 3.19 – Trajectory tracking of MRAC in the decoupled 2R manipulator.

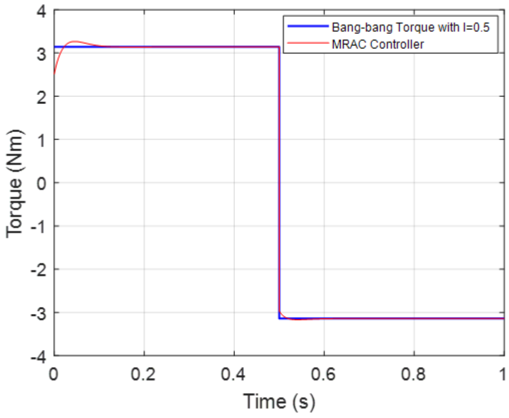

Figure 3.20 – Torque generation of MRAC in the decoupled 2R manipulator.

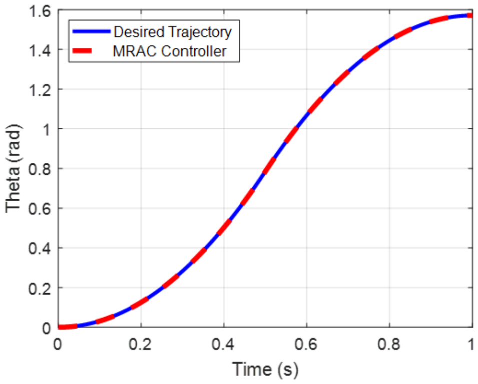

Figure 3.21 – Trajectory tracking of MRAC in the decoupled 3R manipulator.

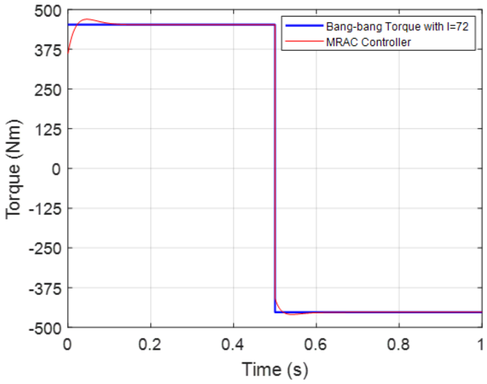

Figure 3.22 – Torque generation of MRAC in the decoupled 3R manipulator.

Observed from the figures above, there is no significant difference between the desired trajectory and the trajectory generated by the MRAC. At the beginning of the control process, an increasing torque is generated due to the wrong inertial information but then the torque generation becomes almost the same as the bang-bang profile by adjusting the inertial value during the control process. The control performance criteria were calculated in Tab. 3.6:

Table 3.6 – Results of two controllers in the presence of parameter uncertainty.

Tracking Performance	**ISE** ($\mathrm{rad}^2\mathrm{s}$)	**Joule effect** (J)	**MT** (Nm)
MRAC(2R)	3.8040×10^{-4}	9.8745	3.2649
LQR(2R)	0.0356	9.8852	3.1613
MRAC(3R)	5.4962×10^{-4}	2.0478×10^5	469.1474
LQR(3R)	0.3349	2.0487×10^5	455.7446

As can be seen from the table above, MRAC consumes less energy than LQR controller in the decoupled dynamic system but the maximum torque is increased a little. Besides, the tracking accuracy of MRAC is much better than LQR controller. It should be noted that MARC could maintain a high tracking accuracy in the presence of parameter uncertainty, which is attractive for the controller design.

3.4.6 Modified twisting controller performance

A lot of nonlinear controllers have been proposed in the literature to overcome the external disturbances [131]. In the joint friction model (3.42), it could be noticed that there always exist the discontinuous terms $\mathrm{sign}(\dot{\theta})$. Attributed to these discontinuous terms of friction, the continuous control algorithms are unable to stabilize the dynamic system.

The discontinuous controllers are brought into sight to resolve the stability problem. Among them, the twisting algorithms are well-recognized for the robustness properties and finite time stability. The controllers, which have switching terms, are capable of forcing the dynamic system to the zero dynamics of error in spite of the external disturbances. However, in the application of twisting controllers, the chattering occurs in the dynamic system due to the important switching gain and degrades the reliability of mechanical systems. Yury Orlov has proposed a modification of the twisting controller to resolve the problem, which aims to avoid the undesirable chattering phenomenon appearing in the closed-loop system when driven by an important switching input. The main advantages of this control is to ensure a convergence in finite time and to be continuous. The effectiveness of the proposed method was demonstrated for a double integrator model [132]. The feedback law is stated as follows:

$$u = -\mu \left|e_2\right|^{\epsilon} \mathrm{sign}(e_2) - v \left|e_1\right|^{\frac{\epsilon}{2-\epsilon}} \mathrm{sign}(e_1) \tag{3.46}$$

where $e_1 = \hat{\theta}$ and $e_2 = \dot{\hat{\theta}}$ in our case. Parameters $v > \mu > 0$ and $\epsilon \in [0, 1)$ is proposed to globally stabilize the double integrator. Suppose that the external disturbance friction satisfies the growth condition:

$$\left|\tau_f(\dot{\theta})\right| \leq \mu_0 \left|e_2\right|^{\epsilon} \tag{3.47}$$

where μ_0 is the upper bound of the external disturbance. According to [132, Theorem 1], for any disturbance satisfying the growing condition, the continuous closed-loop system is globally asymptotically stable if $\mu_0 \leq \mu$. The proof is given in [132] by applying the Lyapunov function and invariance principle. The simulation was carried out in MATLAB® with the following parameters of controller: $\mu_1 = 1000$; $\upsilon_1 = 1500$; $\epsilon_1 = 0.8$ for the decoupled 2R manipulator. $\mu_2 = 140000$; $\upsilon_2 = 230000$; $\epsilon_2 = 0.8$ for the decoupled 3R manipulator. In terms of friction, the parameters in the decoupled 2R manipulator were set to be: $F_C = 3.40 \times 10^{-2}$ Nm; $F_S = 4.60 \times 10^{-2}$ Nm; $F_v = 3.68 \times 10^{-4}$ Nm/(rad/s); $\dot{\theta}_S = 10.68$ rad/s; $\delta_\sigma = 1.93$. In the decoupled 3R manipulators, the friction was supposed to be 30 times of the friction in the decoupled 2R manipulator. The errors of the moment of inertia in the previous section were also considered in the decoupled manipulators. In the simulation, the time step was set as 1×10^{-5} s.

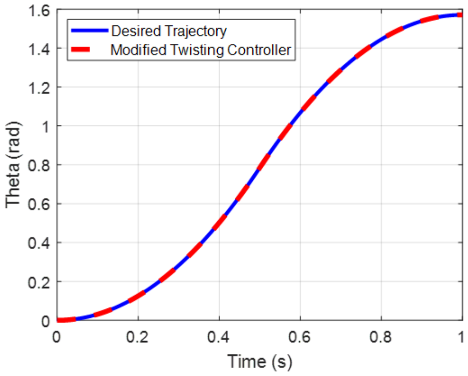

Figure 3.23 – Trajectory tracking of modified twisting controller in the decoupled 2R manipulator.

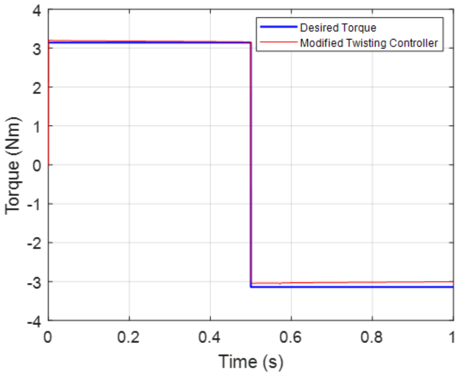

Figure 3.24 – Torque generation of modified twisting controller in the decoupled 2R manipulator.

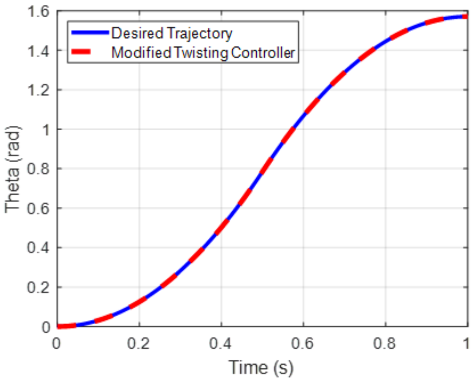

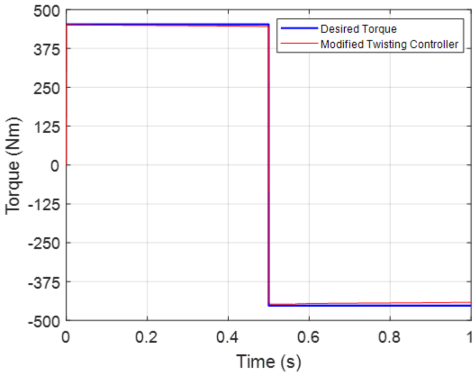

Figure 3.25 – Trajectory tracking of modified twisting controller in the decoupled 3R manipulator.

Figure 3.26 – Torque generation of modified twisting controller in the decoupled 3R manipulator.

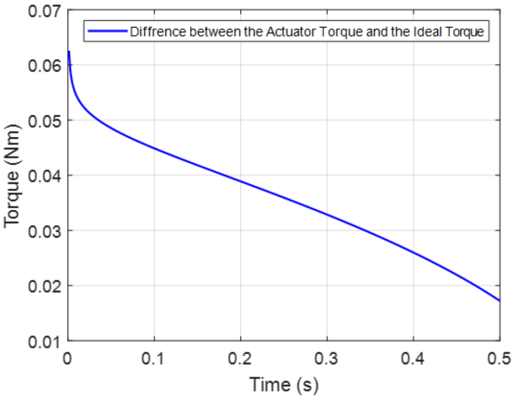

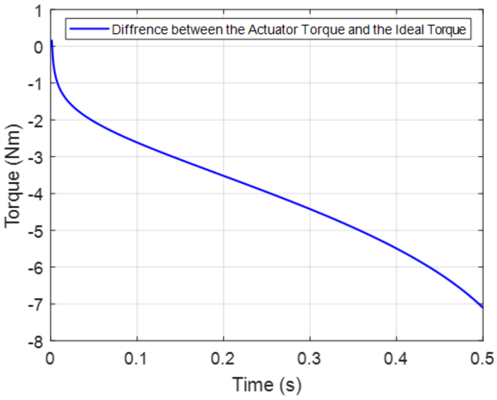

Figure 3.27 – Difference between the actuator torque and the ideal torque in the decoupled 2R manipulator.

Figure 3.28 – Difference between the actuator torque and the ideal torque in the decoupled 3R manipulator.

As shown in the figures above, no significant tacking differences are found after the rise time between the desired trajectory and the trajectory with the modified twisting controller. Even if there exists the discontinuous terms in the friction model (described by sign functions without any approximation in the simulation), it could be observed from Figs. 3.27-3.28 that the torque generated by the modified twisting controller is close to the ideal bang-bang motion profile except the discontinuous points. The maximum differences after the rise time between the actuator torque and the ideal torque are 0.0626 Nm and 7.1040 Nm (both below 2% of the ideal torques) for the decoupled 2R and 3R spatial serial manipulators. The result shows that an appropriate choice of ε in the modified twisting controller attenuates the chattering effects. Then, the control performance criteria were calculated from the simulation results:

Table 3.7 – Results of different controllers in the presence of joint friction.

Tracking Performance	**ISE** (rad^2s)	**Joule effect** (J)	**MT** (Nm)
Modified Twisting(2R)	4.0777×10^{-4}	9.8794	3.2042
LQR(2R)	0.0360	9.8925	3.2296
MRAC(2R)	4.6570×10^{-4}	9.8813	3.3620
Modified Twisting(3R)	3.7061×10^{-4}	2.0474×10^5	452.5666
LQR(3R)	0.3366	2.0488×10^5	456.5749
MRAC(3R)	5.6469×10^{-4}	2.0479×10^5	472.0219

As can be seen from the table above, the best control performance is attained with the modified twisting controller, which consumes less energy and maintains high tracking accuracy. The simulation results demonstrated that the modified twisting controller was effective to stabilize the decoupled dynamic systems in the presence of parameter uncertainty and external disturbances.

3.4.7 Modified twisting observer performance

Previously, it has been demonstrated that the modified twisting controller performs better for the double integrator than the other linear controllers in the presence of friction disturbances. However, sometimes it seems difficult for a system to measure the velocity state. Not all state variables are directly measurable. This can be due to various reasons, including the need to minimize costs by reducing the number of sensors, physical limitations, or the absence of specific sensors. In such cases, an estimation algorithm becomes essential. It processes the incomplete and imperfect information supplied by the available sensors, allowing the reconstruction of a dependable estimate of the entire system state.

The purpose of an observer is to estimate the unmeasurable states of a system based only on the measured outputs and inputs. It is essentially a mathematical replica of the system. A well-known linear observer is Luenberger observer, in which the difference between the output of the plant and the estimated value is fed back linearly into the observer. However, with the presence of disturbance and uncertainty, the performance of Luenberger observer is degraded as it can not force the output estimation error to zero.

The twisting and super-twisting algorithms, generating important classes of second order sliding modes (SOSM), are well-recognized for their finite time stability and robustness properties. In fact, a modified twisting algorithm has been applied in the previous section. The advantage of this type of controller is avoiding using discontinuous or high-gain feedback and reducing chattering effects. Besides, the finite time stabilization is also ensured. However, in the design of observers, observer switching is not as serious as controller switching because does not drive an actuator directly and hence it does not come at the expense of controller switching. For a double integrator system, Orlov *et al.* has proposed a modified super-twisting observer with the modified twisting controller, which presents a finite time stability and robustness with respect to uncertainty and disturbances. The observer form is given as follows [132]:

$$\dot{\hat{x}} = \hat{y} + k_1 \left| x - \hat{x} \right|^{\varepsilon} \operatorname{sign}(x - \hat{x}) + k_2(x - \hat{x}) \tag{3.48}$$

$$\dot{\hat{y}} = u + k_3 \operatorname{sign}(x - \hat{x}) + k_4(x - \hat{x}) \tag{3.49}$$

where x is the measured output. $\hat{x}$ and $\hat{y}$ are the estimates. ε, k_1, k_2, k_3 and k_4 are the constants. As mentioned in [132], the Theorem 3: Given positive k_1, k_2, k_3, k_4 and $\varepsilon \in [\frac{1}{2}, 1)$, the estimated error converges to 0 in finite time. Considering system under the growth condition (3.47), the system is globally finite time stable if the following conditions are met:

$$\epsilon = 1 - \varepsilon \tag{3.50}$$

$$k_1 \geq 0, k_2 \geq 1, k_3 \geq \max\left\{\frac{\mu_0 k_1}{k_2}, \frac{\mu_0(\mu_0 + k_2)}{k_1}\right\}, k_4 \geq \frac{\mu_0(\mu_0 + k_2)}{k_2} \tag{3.51}$$

The numerical simulations were carried out with the following parameters: $\varepsilon = 0.8$, $k_1 = k_2 = k_3 = k_4 = 5$ for the decoupled 2R manipulator and $\varepsilon = 0.7$, $k_1 = k_2 = k_3 = k_4 = 600$ for the decoupled 3R manipulator. The control performance is presented as follows:

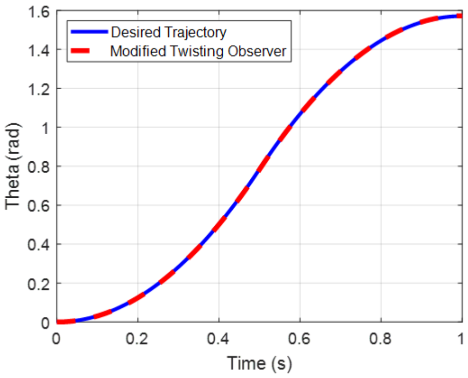

Figure 3.29 – Trajectory tracking with modified twisting observer in the decoupled 2R manipulator.

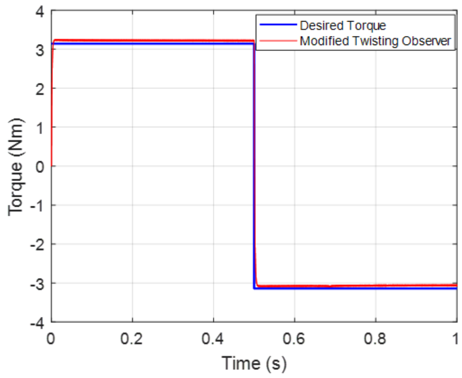

Figure 3.30 – Torque generation with modified twisting observer in the decoupled 2R manipulator.

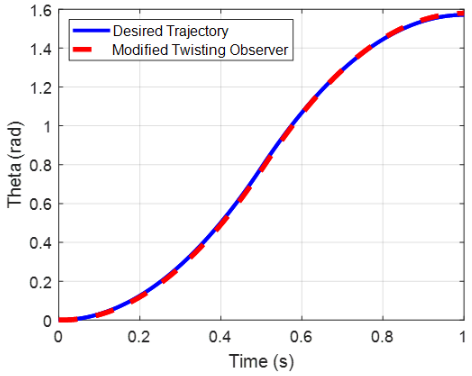

Figure 3.31 – Trajectory tracking with modified twisting observer in the decoupled 3R manipulator.

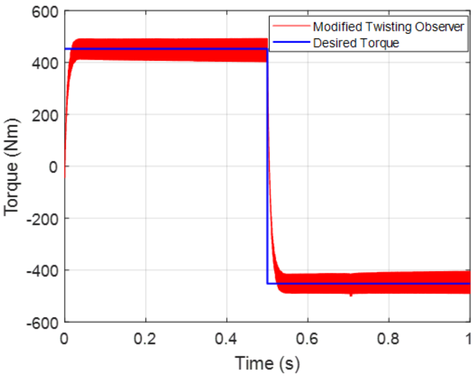

Figure 3.32 – Torque generation with modified twisting observer in the decoupled 3R manipulator.

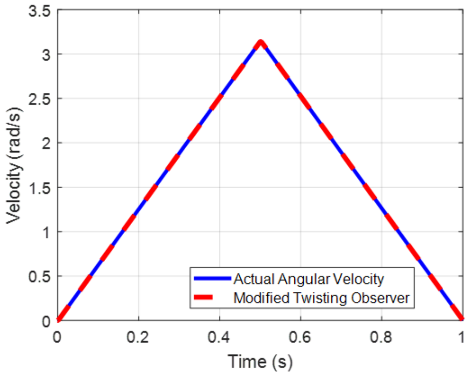

Figure 3.33 – Joint velocity estimation in the decoupled 2R manipulator.

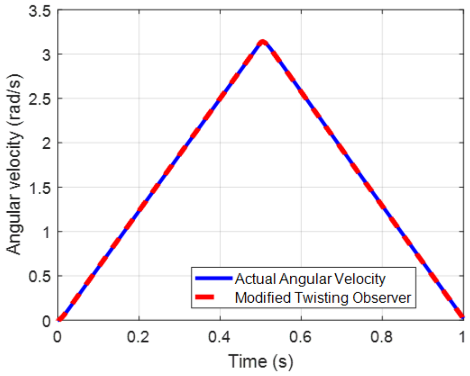

Figure 3.34 – Joint velocity estimation in the decoupled 3R manipulator.

As observed in Figs. 3.29 and 3.31, there are small tracking differences between the desired trajectory and the actual trajectory when using the modified twisting observer. The ISE values are 0.14 rad^{2}s and 4.89 rad^{2}s for the 2R and 3R decoupled system respectively.

Besides, the ISE values of joint velocity estimation are 5.14×10^{-5} rad^2/s and 1.14 rad^2/s for the decoupled 2R and 3R system respectively in Figs. 3.33-3.34. However, it is worth noting that, despite the observer providing reliable estimates for unmeasurable states, the chattering effects (shown in Fig. 3.32) become more prominent in the decoupled 3R manipulator. This aspect needs to be taken into consideration when applying the observer in applications.

3.5 Summary

The control of robot manipulators for demanding high-performance and high-speed tasks has always presented challenges for control engineers. Nonlinear control methods usually face difficulties, including tracking inaccuracies at high speeds and a significant computational burden in robot manipulators with complex structures. Obtaining satisfactory control performance in a highly complex dynamic system remains difficult. To address this, a novel mechatronic approach is proposed to meet the demand for control performance. Rather than focusing on designing control algorithms, this approach prioritizes the redesign of mechanical structure of spatial serial manipulators to achieve a linear and decoupled dynamic system. This offers greater convenience for torque minimization and controller design.

Firstly, the dynamic decoupling has been carried out in spatial serial manipulators. The arrangement of centers of mass and inertia redistribution for the links were described to obtain the decoupled and linear dynamic equations for the manipulators. It was demonstrated that the input torques of the 2R and 3R dynamically decoupled manipulators obtained were directly proportional to the angular accelerations. Then, for motion generation, it was proposed to adopt the "bang-bang" motion profile, which allowed one to reduce the maximum input torques.

The linear and decoupled system also facilitates the controller design and it is easier to stabilize asymptotically a linear dynamic system. To track the desired motion profile, various controllers with simple structure were used for controlling the decoupled system. The classical linear control techniques linear quadratic regulator and lead compensation were adopted to track the desired bang-bang profile trajectory. Then, in the presence of parameter uncertainty and external disturbances, adaptive control MRAC and modified twisting control were adopted to stabilize the decoupled system asymptotically. In the presence of parameter uncertainty and external disturbances, the MRAC and the modified twisting controller performed well in tracking the desired motion profile. Furthermore, in the situations where direct measurements of all state variables were not feasible, a modified twisting observer was implemented in the control system. This implementation ensured finite-time stability and provided reliable estimates.

The results of the simulations demonstrated that the proposed dynamic decoupling method reduced the computational burden and provided an improved control performance in tracking accuracy, energy consumption and maximum input torque.

Chapter 4

OPTIMAL DESIGN OF AN EXOSUIT FOR LOAD CARRIAGE BASED ON HUMAN COMFORT CONDITIONS AND ENERGY EFFICIENCY PERFORMANCE

4.1 Design concept of robotic suit for load carriage 128
4.2 Cable-driving wearable robot modeling 130
4.3 Multi-objective optimization algorithm and development 140
4.4 Numerical simulations and sensitivity analysis 144
4.5 Summary 156

As discussed in Chapter 1, exoskeleton robots have emerged as promising solutions for assisting patients with locomotor disabilities and enhancing the physical capabilities of industrial workers. Among them, the flexible exoskeletons, known as the "exosuits", have attracted a great deal of interest from researchers. They are usually made up of flexible components such as cables and pieces of fabric. However, limited attention has been devoted to the excessive pressure exerted by cables on soft tissues and skeleton of the human, leading to discomfort or even injuries. Additionally, it is also required to consider energy efficiency during the exosuit design phase.

This chapter presents an upper-limb exosuit design for load-carriage assistance. A cable transmission system is incorporated into the exosuit system for gravitational compensation. In comparison to existing studies, more exosuit performance criteria are considered in this work. Additionally, an advanced optimization framework is proposed, which enables that efficient optimization processes by distinguishing and prioritizing different objectives in nonlinear exosuit model. Another important contribution of this work is the identification of design parameters that have the strongest influence on optimization criteria and constraints, providing valuable insights during the design phase.

4.1 Design concept of robotic suit for load carriage

Although rigid exoskeleton robots exhibit a high performance in providing substantial forces and torques, they come with several drawbacks, such as important weight, inertia, and misalignment. Faced with these design challenges, exosuits consisting of soft materials like fabrics and cables offer certain advantages over rigid ones, including lower inertia and less misalignment problems.

In this study, a soft robotic suit to assist users for carrying heavy loads is proposed. This soft robotic suit is planned to have three features: 1) mechanical transparency: the mass of the suit introduces little additional inertia, ensuring that the user's movement remains unimpeded when wearing the robotic suit. 2) human comfort: the forces exerted on human body are reduced. 3) energy efficiency: the energy efficiency of exosuit is taken into account during the design phase.

4.1.1 Functionality of cables in exosuit

When humans move their limbs, the long and short head of bicep brachii contract for generating tension forces, then the forces are transmitted to the skeletons through tendons hence moments will be generated on the articulations for moving their limbs. When human's limbs stay in a certain position, muscles can generate high tension force while keeping in the same length. As illustrated in Fig 4.1, OpenSim model: Arm 26 has shown that the long bicep and short bicep muscles contract to maintain the arm configuration.

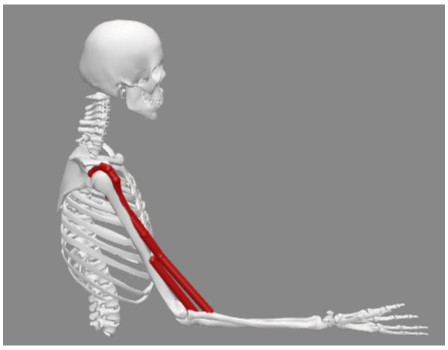

Figure 4.1 – OpenSim model: Arm26 [133] .

In the proposed design, cables are employed to replicate the functionality of human muscles, with cable tension acting as the equivalent of muscle contraction force. These cables can transmit forces to the user's arm through arm bracelets. By precisely controlling the tension forces of these cables, users can achieve the desired posture during load-carriage assistance, as shown in Fig. 4.2.

Fig. 4.2 depicts a 3D model of a user wearing the proposed robotic suit, with cables connected to rigid cuffs. For each of the user's arms, four cables originate from anchors on the forearm or upper arm, respectively. They pass through attachment points on the upper limb and shoulder and finally terminate at the spool on the motor mounted on the back. The anchor point is fixed on the user's body and the attachment point acts like pulley where the cable passes through.

The cables used in the robotic suit are polyethylene braid-style cables, originally designed for fishing [134]. These cables have a diameter of only 0.4 mm and are extremely lightweight. Despite their small size, they can tolerate loads of up to 34 kg with minimal deformation.

Figure 4.2 – A human body wearing the proposed exosuit for load carriage.

4.1.2 Robotic suit operation

In the proposed design, four DC motors are equipped with cable spools, delivering active forces to the corresponding cables. The lifting process, when a person intends to raise an object, typically comprises two phases. The initial phase involves bringing the hands closer to the object and grasp it. In this stage, the DC motors exert forces on the cables, steadily lifting the person's arm to the desired position. Subsequently, in the second phase, the DC motors maintain constant forces to counteract gravitational effects at the desired posture. It is important to note that the cable tension forces generate interaction forces on the human body, necessitating consideration during the design phase.

4.2 Cable-driving wearable robot modeling

In general, the structure of the hand is quite complex. However, in the case of a person wishing to lift and hold a load, it is possible to limit the study to a 3-DOF structure, with 2-DOF at the shoulder (flexion-extension and horizontal abduction) and 1-DOF at the elbow joint (flexion-extension), as illustrated in Fig. 4.3.

The proposed exosuit can be represented by four cables, which are routed through four cuffs supporting attachment points. They run from the anchors on upper limb and terminate at the cable winding system on the back A_i $(i = 1, 2, 3, 4)$, which are attached to the shoulder and upper limb for transmitting forces. The attachment points B_i $(i = 1, 2, 3)$ on the right shoulder and B_i $(i = 4, 5, 6)$ on the left shoulder remain fixed. Their positions do not change with shoulder movement or rotation. Due to the constraints of space on the right shoulder, one cable has been placed on the left shoulder. It is also advantageous due to the resulting increase in the moment arm concerning the axis of the right shoulder revolute joint when assuming postures in front of the body. Cable 1 runs from the winch point A_1 and passes through the anchor and attachment points on point B_i $(i = 1, 2, 3)$ and C_i $(i = 1, 2)$. Cable 2 runs from the winch point A_2 and passes through the anchor and attachment points on point B_i $(i = 1, 2, 3)$ and D_i $(i = 1, 2)$. Cable 3 runs from the winch point A_3 and passes through the anchor and attachment points on point B_i $(i = 1, 2, 3)$ and E_i $(i = 1, 2, 3)$. Cable 4 runs from the winch point A_4 and passes through the anchor and attachment points on point B_i $(i = 4, 5, 6)$ and K_i $(i = 1, 2)$. The anchor points C_2, D_2, E_3, and K_2 are rigidly fixed on the upper-limb and the other attachment points acts like pulley system through which the cables pass. Q is considered as the end effector and mass center of the load.

Table 4.1 – Modified Denavit Hartenberg parameters of human arm

Link	α_i	d_i	θ_i	r_i
1	0	0	q_1	0
2	$\pi/2$	0	$\pi/2 + q_2$	0
3	0	$-l_a$	q_3	0
4	0	$-l_f$	0	0

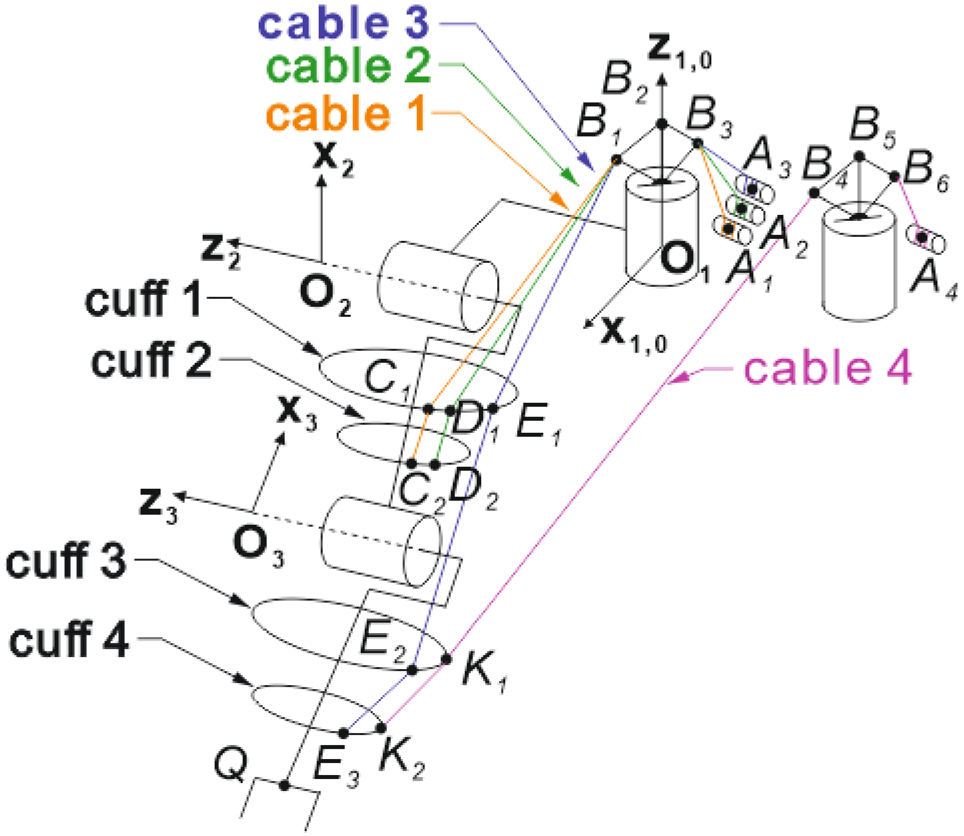

Figure 4.3 – Modeling of an exosuit with four cables.

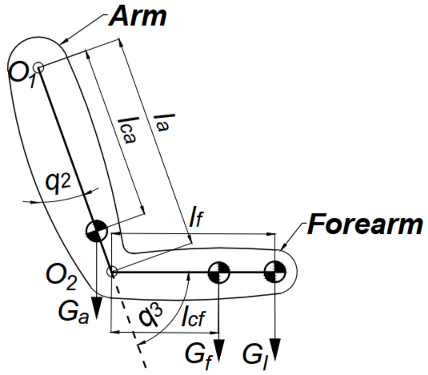

Figure 4.4 – Human upper-limb carrying load in the sagittal plane.

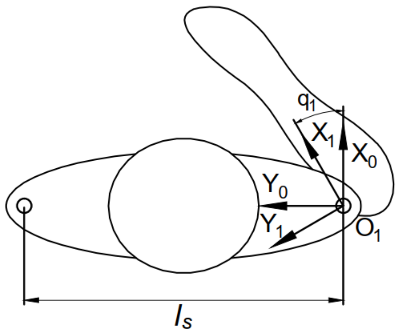

Figure 4.5 – Human upper-limb carrying load in the transversal plane.

The sketch of the exosuit with four cables is shown in Fig. 4.3. The modified Denavit Hartenberg parameters are listed in Tab. 4.1 [135].

4.2.1 Cable-tension force analysis

In contrast to rigid exoskeletons, the proposed exosuit is characterized by the absence of rigid elements except the four cuffs, resulting in reduced inertial forces. The inertial forces of the exosuit depend mainly on its motion profile. As an assistive device for load carriage, the gravitational force plays a key role and high-velocity motion profiles are not currently a priority in our applications. This study focuses on studying the right upper limb in static equilibrium, aiming to reduce forces exerted on human body and energy consumption. It is also believed that the dynamic analysis could also be studied during the exosuit design phase with the proposed method in this chapter.

As illustrated in Figs. 4.4-4.5, to maintain certain arm configurations, the moments on the shoulder and elbow joints due to the gravitational force can be calculated as:

$$\begin{aligned}\tau_{O_1} &= \tau_{O_2} + [(m_f + m_l) g l_a + m_a g l_{ca}] \sin(q_1) && (4.1)\\ \tau_{O_2} &= (m_f g l_{cf} + m_l g l_f) \sin(q_1 + q_2) && (4.2)\end{aligned}$$

where m_a, m_f, and m_l are the masses of the arm, forearm, and load respectively; g is the gravitational acceleration; l_a and l_f are the lengths of arm and forearm; l_{ca} and l_{cf} denote the locations of mass center in arm and forearm; q_1 and q_2 are the shoulder and the forearm flexion angle; q_3 is the horizontal shoulder flexion angle. So that the user does not exert any strain on the shoulder and elbow joints, a cable transmission system driven by motors is introduced to compensate the gravitational forces. Let R_j $(j = 1, 2, 3)$ be the three frames attached to the two joints of the right shoulder and to the elbow joint respectively, Fig. 4.3. Let us recall the (4×4) homogeneous transformation matrix ${}^i\mathbf{T}_j$ representing the transformation from frame R_i to frame R_j:

$$ {}^i\mathbf{T}_j = \begin{bmatrix} & {}^i\mathbf{R}_j & & {}^i\mathbf{P}_j \\ 0 & 0 & 0 & 1 \end{bmatrix} \qquad (4.3)$$

The matrix ${}^i\mathbf{R}_j$ is (3×3) orientation matrix as follows:

$$ {}^i\mathbf{R}_j = \begin{bmatrix} {}^i\mathbf{s}_j & {}^i\mathbf{n}_j & {}^i\mathbf{a}_j \end{bmatrix} \qquad (4.4)$$

where ${}^i\mathbf{s}_j$, ${}^i\mathbf{n}_j$, and ${}^i\mathbf{a}_j$ indicate the unit vectors along the axes $\mathbf{x_j}$, $\mathbf{y_j}$, and $\mathbf{z_j}$ of the frame R_j expressed in the frame R_i. The column vector ${}^i\mathbf{P}_j$ is a column vector expressing the origin of the frame R_j in the frame R_i.

In Fig. 4.3, starting from the shoulder to the forearm, $M_{|O_2}$, a point defined in frame R_2 whose origin is O_2, and located on the first or the second cuff can be expressed in the reference frame R_0, whose origin O coincides with the origin O_1 of R_1 in the arm studied, as follows:

$$M =^0 \mathbf{T}_1{}^1\mathbf{T}_2 M_{|O_2} \tag{4.5}$$

Similarly a point $M_{|O_3}$ defined in frame R_3 whose origin is O_3, and located on the third or the fourth cuff can be expressed in the reference frame R_0 as follows:

$$M =^0 \mathbf{T}_1{}^1\mathbf{T}_2{}^2\mathbf{T}_3 M_{|O_3} \tag{4.6}$$

From Eqs. (4.5) or (4.6) the virtual displacement $\delta\mathbf{O_1M}$ of the point M can be defined in frame R_0 such as:

$$\delta\mathbf{O_1M} \quad = \quad \mathbf{J_M}\begin{bmatrix}\delta q_1\\ \delta q_2\\ \delta q_3\end{bmatrix} \tag{4.7}$$

where $\mathbf{J_M}$ is the (3×3) Jacobian matrix. Considering that this virtual displacement (4.7) is due to the application of a cable tension force F that is directed with a unit vector $\mathbf{u}^*$, the principle of virtual power can be deduced:

$$\begin{aligned}\delta\omega &= (F\mathbf{u}^*)^\top\cdot\delta\mathbf{O_1M}\\ &= (F\mathbf{u}^*)^\top\cdot\mathbf{J_M}\begin{bmatrix}\delta q_1\\ \delta q_2\\ \delta q_3\end{bmatrix}\\ &= (\mathbf{\Gamma}^{cable})^\top\cdot\begin{bmatrix}\delta q_1\\ \delta q_2\\ \delta q_3\end{bmatrix}\end{aligned} \tag{4.8}$$

where $\mathbf{\Gamma}^{cable} = \mathbf{J}_\mathbf{M}^\top F\mathbf{u}^*$ is the (3×1) vector moment applied in the shoulder or elbow joint by the cable tension force F. The joints 1 and 2 are actuated by all cables, whereas the joint 3 is only actuated by cables 3 and 4.

The principle of virtual works and the expression of the moment applied by the tension of a cable to a joint enable us to assess the joint forces provided by the four cables at shoulder and elbow level.

In each cuff, due to the motor actions each cable tension force F_i $(i = 1, 2, 3, 4)$ exerts effort moments $\mathbf{\Gamma}^{cable.i}$ (Fig. 4.3).

— The cable 1 through cuffs 1 and 2 applies effort moments to the joints 1 and 2 while exerting no effort on joint 3:

$$\begin{pmatrix} \tau_{z_1}^{cable.1} \\ \tau_{z_2}^{cable.1} \\ 0 \end{pmatrix} = \left[\mathbf{J}_{\mathbf{C_1}}^{\top}(\mathbf{u}_{\mathbf{C_1B_1}}^{*} + \mathbf{u}_{\mathbf{C_1C_2}}^{*}) + \mathbf{J}_{\mathbf{C_2}}^{\top}\mathbf{u}_{\mathbf{C_2C_1}}^{*}\right] F_1 \tag{4.9}$$

— The cable 2 through cuffs 1 and 2 applies effort moments to the joints 1 and 2 while exerting no effort on joint 3:

$$\begin{pmatrix} \tau_{z_1}^{cable.2} \\ \tau_{z_2}^{cable.2} \\ 0 \end{pmatrix} = \left[\mathbf{J}_{\mathbf{D_1}}^{\top}(\mathbf{u}_{\mathbf{D_1B_1}}^{*} + \mathbf{u}_{\mathbf{D_1D_2}}^{*}) + \mathbf{J}_{\mathbf{D_2}}^{\top}\mathbf{u}_{\mathbf{D_2D_1}}^{*}\right] F_2 \tag{4.10}$$

— The cable 3 through cuffs 1, 3, and 4 applies effort moments to the joints 1, 2, and 3:

$$\begin{pmatrix} \tau_{z_1}^{cable.3} \\ \tau_{z_2}^{cable.3} \\ \tau_{z_3}^{cable.3} \end{pmatrix} = [\ \mathbf{J}_{\mathbf{E_1}}^{\top}(\mathbf{u}_{\mathbf{E_1B_1}}^{*} + \mathbf{u}_{\mathbf{E_1E_2}}^{*}) + \mathbf{J}_{\mathbf{E_2}}^{\top}(\mathbf{u}_{\mathbf{E_2E_1}}^{*} + \mathbf{u}_{\mathbf{E_2E_3}}^{*}) + \mathbf{J}_{\mathbf{E_3}}^{\top}\mathbf{u}_{\mathbf{E_3E_2}}^{*}\ ] F_3 \tag{4.11}$$

— The cable 4 through cuffs 3 and 4 applies effort moments to the joints 1, 2, and 3:

$$\begin{pmatrix} \tau_{z_1}^{cable.4} \\ \tau_{z_2}^{cable.4} \\ \tau_{z_3}^{cable.4} \end{pmatrix} = [\ \mathbf{J}_{\mathbf{K_1}}^{\top}(\mathbf{u}_{\mathbf{K_1B_4}}^{*} + \mathbf{u}_{\mathbf{K_1K_2}}^{*}) + \mathbf{J}_{\mathbf{K_2}}^{\top}\mathbf{u}_{\mathbf{K_2K_1}}^{*}\ ] F_4 \tag{4.12}$$

where $\mathbf{u}_{\mathbf{ij}}^{*}$ denotes a unit vector between two points i and j, originating at i and pointing towards j; F_i $(i = 1, 2, 3, 4)$ is the ith cable tension force. Then, the moments induced by the four cables could be expressed under a concatenate form as:

$$\mathbf{\Gamma}^{cable} = \begin{bmatrix} \tau_{z_1}^{cable.1} + \tau_{z_1}^{cable.2} + \tau_{z_1}^{cable.3} + \tau_{z_1}^{cable.4} \\ \tau_{z_2}^{cable.1} + \tau_{z_2}^{cable.2} + \tau_{z_2}^{cable.3} + \tau_{z_2}^{cable.4} \\ \tau_{z_3}^{cable.3} + \tau_{z_3}^{cable.4} \end{bmatrix} = \mathbf{J}^{\top} \begin{bmatrix} F_1 \\ F_2 \\ F_3 \\ F_4 \end{bmatrix} \tag{4.13}$$

Let Eq. (4.13) take the following concatenated form:

$$\mathbf{\Gamma}^{cable} = \mathbf{J}^{\top}\mathbf{F} \tag{4.14}$$

where $\mathbf{F} = \begin{bmatrix} F_1 & F_2 & F_3 & F_4 \end{bmatrix}^{\top}$ is the 4×1 vector of cable tension force; $\mathbf{J}$ is denoted as a 4×3 Jacobian matrix relating the anchor and attachment point positions. When wearing the exosuit, the moments produced by the gravitational force $\mathbf{G} = [0\ \tau_{O_1}\ \tau_{O_2}]^{\top}$ can be compensated by the moments generated by cables. In statics, the general form can be written as:

$$\mathbf{G} = \mathbf{J}^{\top}\mathbf{F} \tag{4.15}$$

It can be noted that Eq. (4.15) is an under-determined system. The solution of cable tension forces is not unique if $\mathbf{J}^{\top}\mathbf{J}$ is invertible. The general solution can be written as

$$\mathbf{F} = \overline{\mathbf{F}} + \mathbf{N}(\mathbf{J}^{\top})\zeta \tag{4.16}$$

where, $\overline{\mathbf{F}}$ is the minimum norm solution, which is given by:

$$\overline{\mathbf{F}} = \mathbf{J}(\mathbf{J}^{\top}\mathbf{J})^{-\mathbf{1}}\mathbf{G} \tag{4.17}$$

$\mathbf{N}(\mathbf{J}^{\top})$ is a 4×1 null space vector and ζ is an arbitrary value, assuming $\mathbf{J}^{\top}$ is a row full-rank matrix. Considering the cable tension force vector $\mathbf{F} \in [\mathbf{F_{min}}, \mathbf{F_{max}}]$, the equivalent condition is given as:

$$\begin{bmatrix} \mathbf{N}(\mathbf{J}^{\top}) \\ -\mathbf{N}(\mathbf{J}^{\top}) \end{bmatrix} \zeta \geq \begin{bmatrix} \mathbf{F_{min}} - \overline{\mathbf{F}} \\ -\mathbf{F_{max}} + \overline{\mathbf{F}} \end{bmatrix} \tag{4.18}$$

The feasible solution of ζ is characterized by a convex region bounded by eight linear inequalities on parameter ζ. If there exists no feasible numerical value of ζ, the cable tension force constraint could not be met. According [136], linear programming was employed for optimizing the sum of cable tension forces. ζ could take any value to minimize the sum of cable tension forces in linear programming technique, which must satisfy the constraint (4.18). Although it provides a high computational efficiency, the continuity of cable tension forces is very poor in the planned trajectory. To resolve the problem, quadratic programming (QP) is adopted, which brings fewer abrupt changes between nearby configurations. Step-less adjustment of cable tension forces is desirable in workspace to smoothly switch between different tension levels to reduce the energy consumption in control process [137]. Thus, the reference cable-tension force vector is introduced in QP and the cable-tension distribution problem can be formulated as :

$$\min \quad \mathbf{f(F)} = \frac{\mathbf{1}}{\mathbf{2}}(\mathbf{F}-\mathbf{F_r})^\top(\mathbf{F}-\mathbf{F_r}) \tag{4.19}$$

$$\textbf{s.t.} \quad \mathbf{F_{min}} \leq \mathbf{F} + \mathbf{N}(\mathbf{J}^\top)\zeta \leq \mathbf{F_{max}} \tag{4.20}$$

where $\mathbf{F_r}$ is a 4×1 vector of reference cable tension force and should fall in $[\mathbf{F_{min}}, \mathbf{F_{max}}]$. The vector elements of $\mathbf{F_r}$ are the estimated average values of cable tension forces in workspace, and they can be further fine-tuned to enhance force continuity within the workspace. ζ is the decision variable to minimize the QP objective function (4.19). It could take any value to minimize the objective function but must satisfy the constraint defined in the inequality (4.20), ensuring available cable tension forces in workspace.

4.2.2 Optimization goals and design constraints

The design parameters of exosuit are denoted as: s_i $(i = 1, ..., 4)$, h_i $(i = 1, ..., 4)$, ψ_i $(i = 1, ..., 9)$, φ, β, and b, which describe the arrangement of anchor and attachment points (see Figs. 4.6, 4.7, and 4.8). It is assumed that when users carry load, their back is always upright and cable winch systems are attached to the body, ie. all the vectors to the winch $\mathbf{v_{B_3A_i}}$ $(i = 1, 2, 3)$ and $\mathbf{v_{B_6A_4}}$ are opposed to the axis $\mathbf{z_0}$ $(\beta = 0°)$. The mentioned 19 design parameters are chosen as unknown variables of the considered optimization problem.

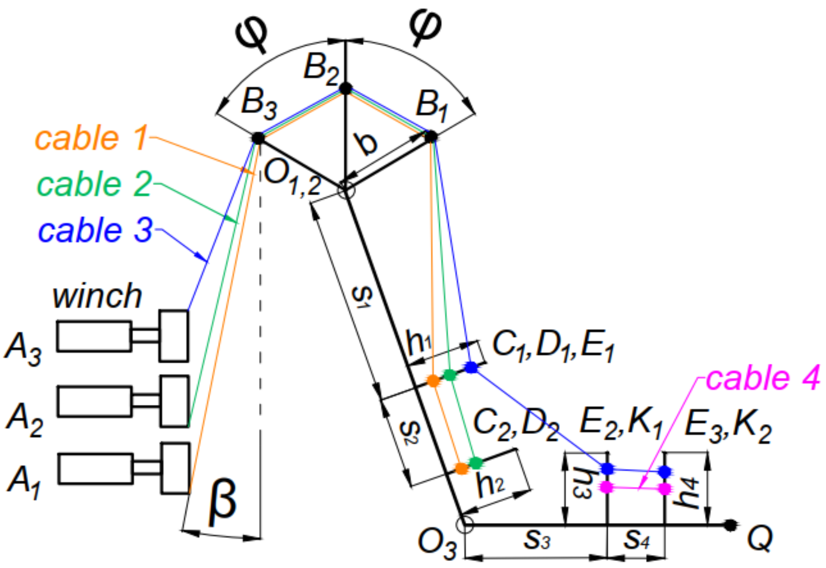

Figure 4.6 – Sagittal plane, the assisted arm with the exosuit (cable 4 passes through the attachment points on the right shoulder, see Fig 4.3).

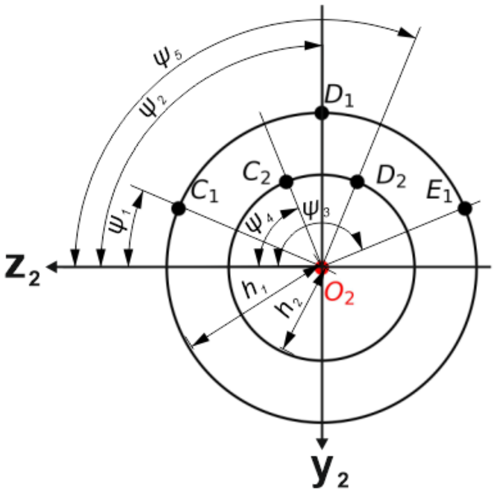

Figure 4.7 – Attachment points of cuffs at arm.

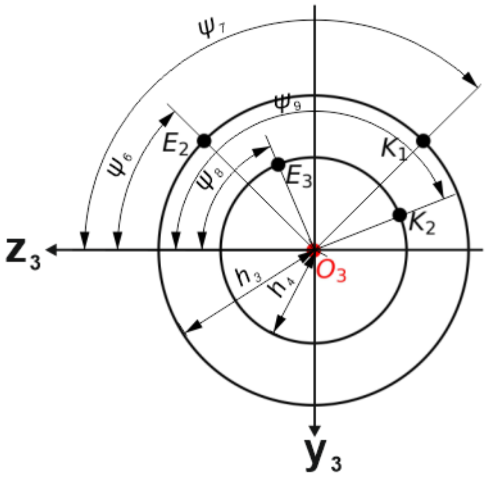

Figure 4.8 – Attachment points of cuffs at forearm.

It can be observed from Eq. (4.13) that the relation between the cable tension forces and the moments induced by cables on joints are determined by these design variables. As the same situation in cable-driven robot, the attachment points on the frame should be identified precisely for high transmission efficiency. Since exoskeleton robots are quite different from traditional robots, which have a contact area with human body, safety and comfort are considered as two critical criteria in the design process. Rocon et al. [93]

have concluded that kinematic compatibility and application of loads to human are the two influencing factors for the safety and comfort. As the cables are used for transmitting loads in the exosuit system, the kinematic structure is compatible with the human body and thereby no significant misalignment exists in the joints, which contributes a lot to the user safety and comfort. However, the application of loads to human raises two main concerns in the exosuit design: excessive pressure on the shoulder and incompatible force on the soft tissues of upper limb, which will probably cause injuries and discomfort. The sum of the forces exerted on the left and right shoulder is given by:

$$\begin{aligned} \|\mathbf{F}^{\mathbf{cable}}_{\mathbf{shoulder}}\| = \|\Big(\mathbf{u}^*_{\mathbf{B_1C_1}} + \mathbf{u}^*_{\mathbf{B_3A_1}}\Big)F_1 + \Big(\mathbf{u}^*_{\mathbf{B_1D_1}} + \mathbf{u}^*_{\mathbf{B_3A_2}}\Big)F_2 + \\ \Big(\mathbf{u}^*_{\mathbf{B_1E_1}} + \mathbf{u}^*_{\mathbf{B_3A_3}}\Big)F_3 + \Big(\mathbf{u}^*_{\mathbf{B_4K_1}} + \mathbf{u}^*_{\mathbf{B_6A_4}}\Big)F_4\| \end{aligned} \tag{4.21}$$

Besides, it is known that the load transmission to the human skeletal system from the wearable robot is mediated by soft tissues like skin, fat, and muscle. In the exosuit design, the tangential force induced by cables could lead to friction between mechanical components and skin, which causes pain or at least discomfort [101]. In the exosuit model (see Fig. 4.6), the sum of the tangential forces exerted on upper-limb skin are induced from the cables, which could be expressed as the following equation:

$$\|\mathbf{F}^{\mathbf{cable}}_{\mathbf{upper\ limb}}\| = \|\mathbf{F}^{\mathbf{cable}}_{\mathbf{arm}}\| + \|\mathbf{F}^{\mathbf{cable}}_{\mathbf{forearm}}\| \tag{4.22}$$

where,

$$\mathbf{F}^{\mathbf{cable}}_{\mathbf{arm}} = \Big[\mathbf{u}^*_{\mathbf{C_1B_1}}F_1 + \mathbf{u}^*_{\mathbf{D_1B_1}}F_2 + \Big(\mathbf{u}^*_{\mathbf{E_1B_1}} + \mathbf{u}^*_{\mathbf{E_1E_2}}\Big)F_3\Big] \cdot \mathbf{u}^*_{\mathbf{O_3O_2}} \tag{4.23}$$

$$\mathbf{F}^{\mathbf{cable}}_{\mathbf{forearm}} = \Big(\mathbf{u}^*_{\mathbf{E_2E_1}}F_3 + \mathbf{u}^*_{\mathbf{K_1B_4}}F_4\Big) \cdot \mathbf{u}^*_{\mathbf{QO_3}} \tag{4.24}$$

Another objective to be considered is the energy efficiency because sometimes exosuit should be worn by user over long time for industrial needs. Particularly when upper limb remains static for holding a load, energy efficiency is mainly affected by Joule effect, which describes the process where the energy of an electric current I is converted into heat as it flows through a resistance R. In electric motors, neglecting the friction, most part of the dissipated energy is due to the loss by Joule effect. To evaluate the energy loss power P, a criterion is introduced as follows:

$$P = I^2R \tag{4.25}$$

For a DC motor, considering that the torque supplied by motor is proportional to the armature current, the energy-loss criterion could be similarly evaluated as follows:

$$P' = \sum_{i=1} const_i \ \tau_i^2 \tag{4.26}$$

$$\tau_i^2 = (F_i r_w)^2 \tag{4.27}$$

where τ_i $(i = 1, 2)$ is the ith actuator torque, which could be expressed by cable tension force F_i and r_w is the ratio of the output shaft of the DC motor; $const_i$ is the ratio between the resistance of the inductive circuit R of the DC motor and the square of the torque constant. In this chapter, this $const_i$ will be set equal to 1. It characterizes the energy that must be produced by the battery to allow the desired motion. The heat generated by Joule effect also degrades the reliability of electrical systems components [128], which should be minimized in the design process. Although energy efficiency needs to be taken into account in the design of exosuit, the first priority must be given to the user safety and comfort. Besides, in the optimization process, three constraints need to be taken into account:

- Cables must be always in tension, *i.e.* The cable tension forces are always positive and do not exceed the limit of cable.
- The space constraints of the positions of anchors and attachment points.
- The vulnerable parts of upper limb should be avoided in the optimization (medial, lateral epicondyle and radial, ulnar styloid process).

Based on these considerations, the multi-objective optimization problem is defined as follows:

$$\mathcal{O}_1 : \frac{1}{N}\sum_{q_1}\sum_{q_2}\sum_{q_3}\left(\|\mathbf{F}^{\mathbf{cable}}_{\mathbf{shoulder}}\| + \rho\right) \longrightarrow \min_{s_1, s_2, \ldots, b} \tag{4.28}$$

$$\mathcal{O}_2 : \frac{1}{N}\sum_{q_1}\sum_{q_2}\sum_{q_3}\left(\|\mathbf{F}^{\mathbf{cable}}_{\mathbf{upper\ limb}}\| + \rho\right) \longrightarrow \min_{s_1, s_2, \ldots, b} \tag{4.29}$$

$$\mathcal{O}_3 : P'_{max} \longrightarrow \min_{1,2,\ldots,n} \tag{4.30}$$

where,

$$\rho = \begin{cases} 0, & \text{if } F_{min} \le F_i \le F_{max} \\ 10000, & \text{if } F_i < F_{min} \text{ or } F_i > F_{max} \end{cases}, \ (i = 1, 2, 3, 4) \tag{4.31}$$

ρ is a very large value to penalize the objective function when the cable tension force

F_i is outside the available range $[F_{min},\ F_{max}]$ at certain configuration. The value of ρ in Eq. (4.31) is selected to be ten times greater than the magnitude of cable tension force. N is the number of points discretizing the joint space and n is the number of non-dominated solutions found by multi-objective optimization. If the cable tension forces across the entire workspace are feasible, $\mathcal{O}_1$ and $\mathcal{O}_2$ denote average forces for all postures in workspace. $\mathcal{O}_3$ denotes the maximum Joule effect power in feasible workspace.

An optimization strategy is formulated: a multi-objective optimization will be first carried out to minimize $\mathcal{O}_1$ and $\mathcal{O}_2$. Then, an optimal solution, which minimizes Joule effect power, will then be selected among all the non-dominated solutions found by multi-objective optimization. Non-dominated solutions for multi-objective optimization means that there exists no feasible solution which would decrease some criterion without causing a simultaneous increase in at least one other criterion. To obtain non-dominated solutions in a constrained domain, a multi-objective optimization algorithm is presented in the next section.

4.3 Multi-objective optimization algorithm and development

In this section, a novel swarm intelligence-based optimization framework is proposed to enhance the human comfort conditions and energy efficiency performance of exosuit. This framework identifies the optimal design parameters in high-dimensional and nonlinear exosuit system. Additionally, prioritization is given to the minimization of interaction forces over energy efficiency during the optimization process, ensuring the exosuit provide improved comfort and safety for users.

4.3.1 Inverse-PageRank-PSO

According [96], [136], [138], [139], pattern search and *fmincon* functions via MATLAB ® software are adopted as optimization algorithm to improve the tension values and feasible workspace of exosuit. However, these popular nonlinear programming (NLP) methods may fall into the local optimum in some highly nonlinear cases. The quality of optimal solution obtained mainly depends on its initial input value. Given the highly nonlinear nature of the exosuit system described by Eq. (4.15), a meta-heuristic algorithm is considered as a more suitable approach. In particular, particle swarm optimization

(PSO) is well-suited for multi-objective optimization mainly because of the high speed of global convergence that the algorithm presents for single-objective optimization [140], [141].

PSO is a population-based meta-heuristic optimization inspired by the choreography of a bird flock, which has been found to be successful in a wide variety of optimization task. To identify the design parameters of exosuit, a more efficient PSO variant, named Inverse-PageRank-PSO (I-PR-PSO), has been used [142]. I-PR-PSO is based both on the standard PSO [143]–[145] and PageRank algorithm [146], [147]. By ranking the particles in a smart way, defined by an inverse PageRank strategy [142], [148], this algorithm is strongly decreasing the number of iterations, and so the number of fitness calculation calls needed to obtain an optimized solution. At each iteration $k+1$ of the optimization process, the speed $\mathbf{V_i^{k+1}}$ and position $\mathbf{X_i^{k+1}}$ of every particle i has to be updated, by using the following equations:

$$\begin{cases} \mathbf{V_i^{k+1}} = w\mathbf{V_i^k} + c_1\mathcal{R}_1(\mathbf{P_{i,best}^{k+1}} - \mathbf{X_i^k}) + c_2\mathcal{R}_2\sum_{j=1}^{n}\mathcal{C}_{ij}[\mathbf{P_{j,best}^{k+1}} - \mathbf{X_i^k}] \\ \mathbf{X_i^{k+1}} = \mathbf{X_i^k} + \mathbf{V_i^{k+1}} \end{cases} \tag{4.32}$$

where w is weighing the influence of the previous speed on the new one, *i.e.* is representing the inertia of particles during their movement in the research domain, c_1 and c_2 denote acceleration constants, $\mathcal{R}_1$ and $\mathcal{R}_2$ are random numbers in interval [0, 1] bestowing the heuristic characteristics of the algorithm, $\mathbf{P_{i,best}^{k+1}}$ represents the best personal position of particle i found so far. $\mathcal{C}$ is the probability transition matrix containing the coefficients weighing the influence of all the particles on the others, based on their relative success among the swarm (for more details, see [142]).

The advantage of this algorithm has been mentioned in [142]: I-PR-PSO achieves a better balance between the exploration and exploitation phases needed by the particles to find the global optimum in large dimensions. Compared to the classical PSO, the social behavior is enhanced and I-PR-PSO is more likely to find the global optimum of the considered objective function. Regarding the exosuit optimization, consisting of the identification of the attachment point positions, each particle's position $\mathbf{X_i}$ is a vector containing values of design parameters that are going to be tested among the fitness calculation.

However, it should be noticed that there are two optimization goals $\mathcal{O}_1$ and $\mathcal{O}_2$ first to be minimized in the optimization strategy formulated, which is a multi-objective optimization problem. Di Cesare et al. [142] do not provide a solution to this kind of problem.

4.3.2 Development for multi-objective optimization

To resolve a multi-objective optimization problem, Pareto-based approaches have been considered as one of solutions [149]. They aim to find the non-dominated solutions, which constitutes a Pareto front. For example, multi-objective particle swarm optimization (MOPSO) has been proposed in [140]. In MOPSO, a repository is created and contains all the non-dominated solutions found, which may be updated in each iteration. The speed of each particle can be computed using the following expression:

$$\mathbf{V_i^{k+1}} = w\mathbf{V_i^k} + c_1\mathcal{R}_1(\mathbf{P_{i,best}^{k+1}} - \mathbf{X_i^k}) + c_2\mathcal{R}_2[\mathbf{REP_h^{k+1}} - \mathbf{X_i^k}] \tag{4.33}$$

where $\mathbf{REP_h}$ is a non-dominated solution vector taken from the repository through the roulette wheel selection method [140]. Instead of $\mathbf{G_{best}}$ in PSO, MOPSO selects a non-dominated vector $\mathbf{REP_h}$ from the repository to guide all the particles towards the Pareto front. $\mathbf{P_{i,best}}$ is the non-dominated solution found in the searching history of the i-th particle, and it may be updated during each iteration. Inspired from MOPSO, let us consider extending functionality of I-PR-PSO for resolving a multi-objective optimization problem. The vectors taken from repository are used to calculate the stochastic matrix $\mathcal{C}$. Since there are more than one optimization goals, several matrices $\mathcal{C}_\lambda$, are calculated with Markov chain technique. A new stochastic matrix $\mathcal{C}'$ taking all the objective functions into account, which is given by:

$$\begin{aligned} &\mathcal{C}' = \sum_{\lambda}^{n_{\mathcal{O}}} w_\lambda^* \mathcal{C}_\lambda,\ \ \lambda = 1, ..., n_{\mathcal{O}} \\ &\sum_{\lambda}^{n_{\mathcal{O}}} w_\lambda^* = 1,\ \ \lambda = 1, ..., n_{\mathcal{O}} \end{aligned} \tag{4.34}$$

where w_λ^* denotes the weight of each probability matrix $\mathcal{C}_\lambda$ and $n_{\mathcal{O}}$ denotes the number of objective functions. Hence, to compute the velocity and displacement, a new expression is given as follows:

$$\begin{cases} \mathbf{V_i^{k+1}} = w\mathbf{V_i^k} + c_1\mathcal{R}_1\ (\mathbf{P_{i,best}^{k+1}} - \mathbf{X_i^k}) + c_2\mathcal{R}_2 \sum_{j=1}^{n} \mathcal{C}'_{ij}[\mathbf{P_{j,best}^{k+1}} - \mathbf{X_i^k}] \\ \mathbf{X_i^{k+1}} = \mathbf{X_i^k} + \mathbf{V_i^{k+1}} \end{cases} \tag{4.35}$$

Through the extension inspired from MOPSO, I-PR-PSO is capable of resolving multi-objective problems and will be then used for identifying optimal exosuit design parameters. Fig. 4.9 illustrates the entire optimization process. The initial positions of particles are randomly selected in a constrained domain $[\mathbf{X_{min}}, \mathbf{X_{max}}]$, which is designed to avoid the vulnerable parts of upper limb. For each particle, its fitness values are calculated using Eqs. (4.28)-(4.29) respectively. If the cable tension force condition is satisfied (Eq. (4.20)), no penalty value will be added on objective functions. Otherwise, penalties are applied to the objective functions. In each iteration, the algorithm compares the objective values of each particle and selects the non-dominated particles to be stored in the repository **REP**. Subsequently, the positions and velocities of all particles are updated using Eq. (4.35). Upon reaching the maximum number of iterations, the position of one of the solutions stored in the repository is returned as the optimal variables, aiming to minimize the Joule effect power (4.30). In the following section, numerical simulations were conducted to demonstrate the effectiveness of the proposed optimization algorithm for enhancing the exosuit performance. The Inverse-PageRank-PSO has been coded in MATLAB®, in which the *Optimization Toolbox* is employed to compute the cable tension forces using quadratic programming.

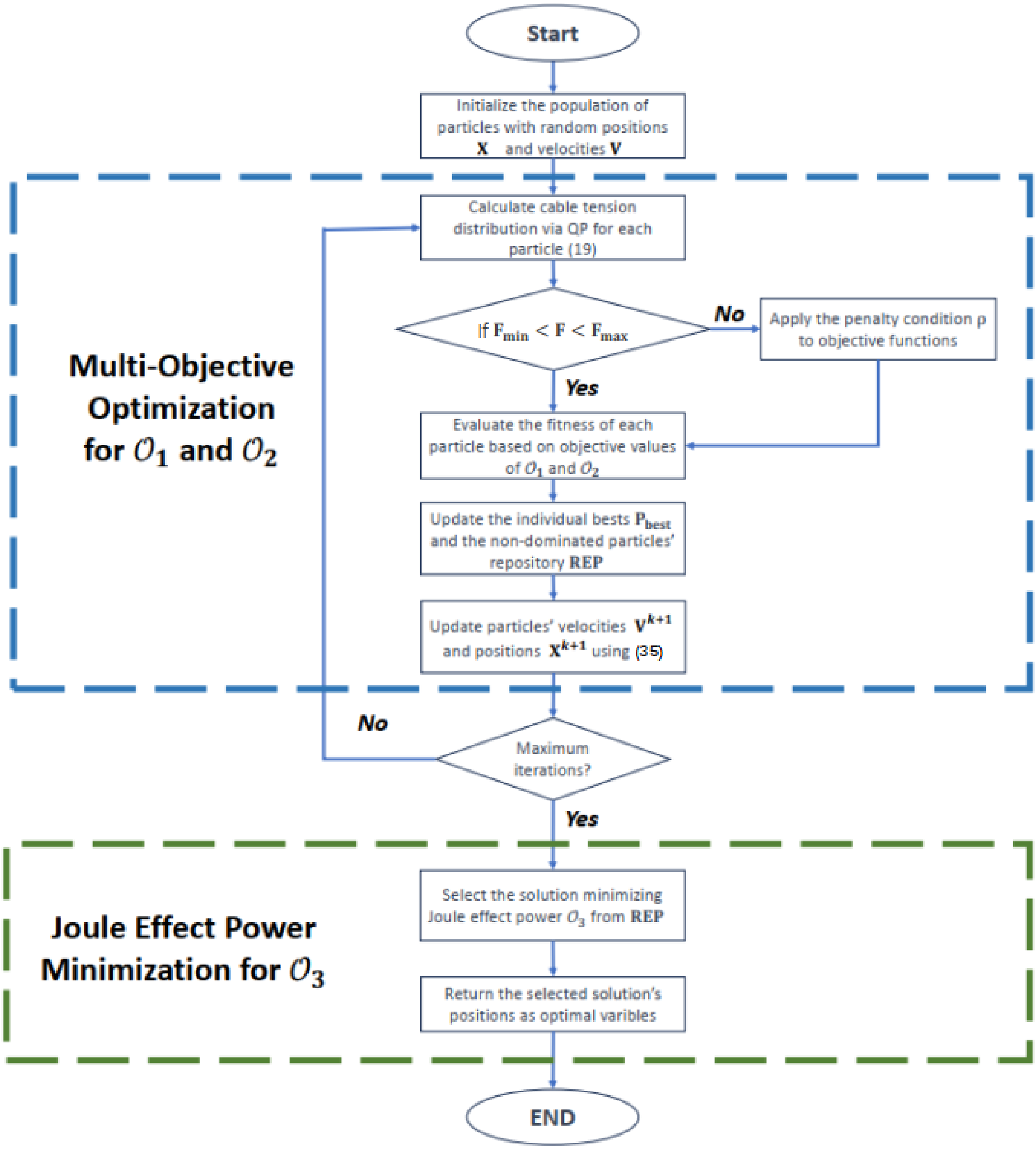

Figure 4.9 – Diagram of multi-objective optimization process.

4.4 Numerical simulations and sensitivity analysis

4.4.1 Optimization results and analysis

From [150], we got the average body segment parameters (shown in Figs. 4.4-4.5) of an adult male with 172.68 cm height and 63.97 kg weight as following: $l_a = 0.364$ m;

$l_f = 0.299$ m; $l_{ca} = 0.182$ m; $l_{cf} = 0.149$ m; $m_a = 2.07$ kg; $m_f = 1.70$ kg. The shoulder width l_s is 0.400 m and the right shoulder joint is assumed to be located at the origin $[0, 0, 0]^\top$ of the base frame. Radius of the winch of the DC motor shafts r_w is 0.030 m. Firstly, let us consider a scenario in which the exosuit is designed for assisting the users with upper-limb impairment in carrying a small load, such as holding a few apples in their hands. The load mass m_l is 0.50 kg.

Since the exosuit is used for assisting users in carrying load with their upper limb, the range of arm configurations are specified as $q_1 \in [-30°, 30°]$, $q_2 \in [10°, 70°]$ and $q_3 \in [10°, 70°]$. The range of each joint angle is discretized into 10 configurations, representing an evenly spaced sequence. It should be noted that some extreme postures are not considered in this chapter because they probably result in a more infeasible workspace and increased force levels. The postures in front of the human body for load carriage are mainly considered. Hence, the entire exosuit workspace is discretized into $N = 1000$ points. The use of a polyethylene braid-style cable is considered, which can bear load up to 34 kg while having little deformation [134], the limit of cable tension force is set to be: $F_{min} = 1$ N and $F_{max} = 150$ N. Cable tension vector is calculated through QP (4.19), in which the reference force vector is defined as $\mathbf{F_r} = [30\ 30\ 15\ 10]^\top$ N. With respect to the cable tension force constraint (4.20), $\mathcal{O}_1$ and $\mathcal{O}_2$ will be minimized during the optimization process. The ranges of optimization variables are defined in the following table:

Table 4.2 – Range of the exosuit design parameters.

Design Parameter Inequality Bounds			
Unit: m			
$0.120 \leq s_1 \leq 0.254$	$0.040 \leq s_2 \leq 0.060$	$0.120 \leq s_3 \leq 0.190$	$0.040 \leq s_4 \leq 0.060$
$0.080 \leq h_1 \leq 0.120$	$0.040 \leq h_2 \leq 0.080$	$0.080 \leq h_3 \leq 0.120$	$0.040 \leq h_4 \leq 0.080$
$0.100 \leq b \leq 0.150$			
Unit: degree			
$0 \leq \psi_1 \leq 90$	$0 \leq \psi_2 \leq 180$	$90 \leq \psi_3 \leq 180$	$0 \leq \psi_4 \leq 90$
$0 \leq \psi_5 \leq 180$	$90 \leq \psi_6 \leq 270$	$90 \leq \psi_7 \leq 270$	$90 \leq \psi_8 \leq 270$
$90 \leq \psi_9 \leq 270$	$0 \leq \varphi \leq 90$		

Before optimization, the initial parameters with respect to the positions of anchors and attachment points are given as following: $\varphi = 60°$; $b = 0.125$ m; $s_1 = 0.200$ m; $s_2 = 0.050$ m; $s_3 = 0.150$ m; $s_4 = 0.050$ m; $h_1 = 0.100$ m; $h_2 = 0.060$ m; $h_3 = 0.100$ m; $h_4 = 0.060$ m; $\psi_1 = 0°$; $\psi_2 = 0°$; $\psi_3 = 90°$; $\psi_4 = 0°$; $\psi_5 = 90°$; $\psi_6 = 90°$; $\psi_7 = 90°$; $\psi_8 = 90°$; $\psi_9 = 90°$. The initial solution is characterized by a very limited workspace with important forces exerted on the human body, which allows for evaluating the enhancement brought by the proposed optimization framework.

As shown in Fig. 4.10, with the initial parameters, 95.3 % of the workspace is infeasible, in which the cable tension forces are not permissible. Another thing to be concerned with is the force exerted on the shoulder and arms by cables. Regarding the rest feasible configurations in workspace, simulation results show that a large portion of force is redistributed on the shoulder and upper limb. In these configurations, the average forces exerted on shoulder and upper limb $\mathcal{O}_1$ and $\mathcal{O}_2$ are 300.41 N and 121.04 N respectively. These values indicate substantial stresses for users. Therefore, it is crucial to identify appropriate design parameters during the exosuit conception phase.

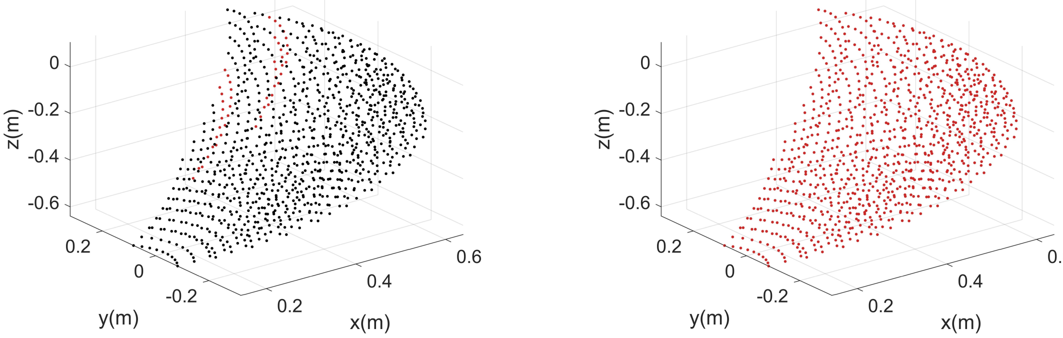

Figure 4.10 – End-effector positions before (left) and after (right) optimization. Brown dots are feasible, while black dots are infeasible.

Therefore, the multi-objective optimization process (Fig. 4.9) has been carried out in MATLAB®. I-PR-PSO calculation parameters were chosen from [142]: inertial weight of particles $w = 0.8$; acceleration constants $c_1 = c_2 = 2$; number of particles $N_p = 20$; repository capacity $N_r = 20$; maximum number of I-PR-PSO iterations $r_{max} = 120$; weight of probability matrix $w_1^* = w_2^* = 0.5$. The observations showed that two fitness values of the particles, representing different design parameter combinations, converged to the Pareto front in the searching process (Fig. 4.11). Sixteen non-dominated solutions, minimizing $\mathcal{O}_1$ or $\mathcal{O}_2$, exist on the Pareto front (Fig. 4.12)).

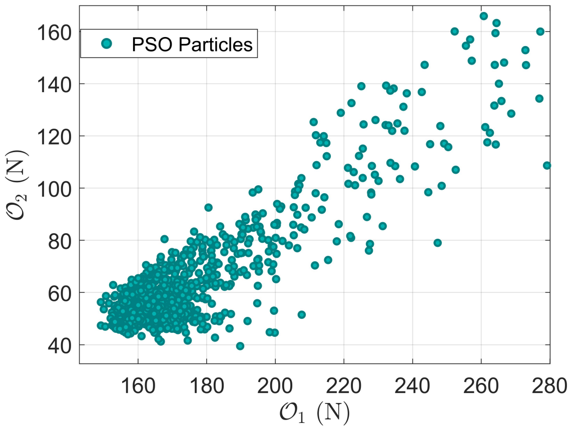

Figure 4.11 – Movement of particles during the searching process.

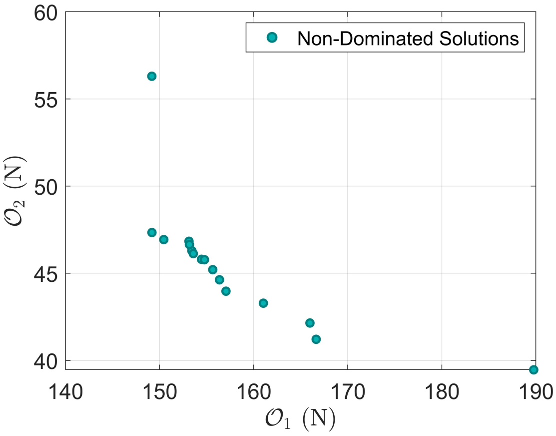

Figure 4.12 – Non-dominated solutions found by multi-objective I-PR-PSO.

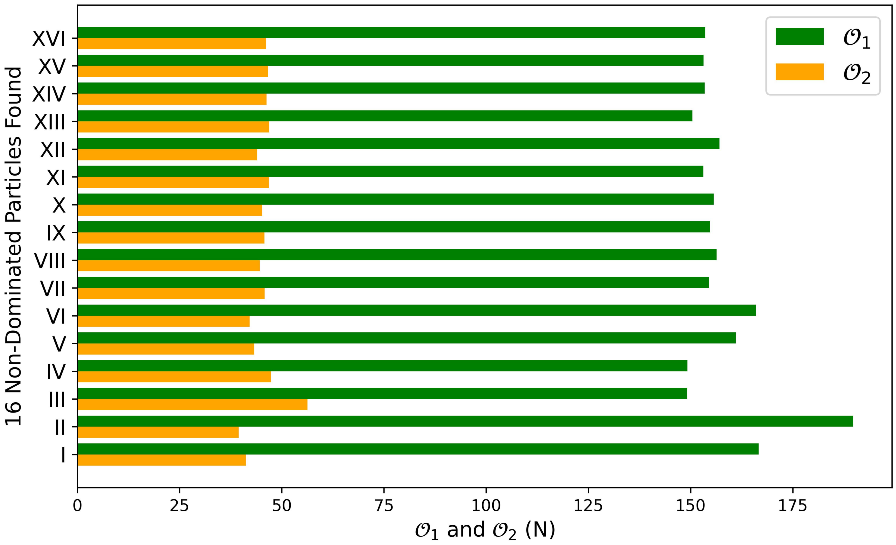

Figure 4.13 – $\mathcal{O}_1$ and $\mathcal{O}_2$ of sixteen non-dominated solutions found by multi-objective I-PR-PSO.

Table 4.3 – Sixteen non-dominated solutions found by multi-objective I-PR-PSO.

Solutions	$\mathcal{O}_1$ (N)	$\mathcal{O}_2$ (N)	$\mathcal{O}_3$ (W)
I	166.65	41.21	13.50
II	189.77	39.46	19.06
III	149.19	56.30	7.62
IV	149.20	47.34	7.02
V	161.04	43.29	7.95
VI	165.99	42.15	8.90
VII	154.46	45.80	7.36
VIII	156.37	44.63	7.59
IX	154.78	45.78	7.65
X	155.66	45.21	7.51
XI	153.13	46.84	7.73
XII	157.04	43.97	7.66
XIII	150.46	46.93	7.45
XIV	153.44	46.29	7.67
XV	153.18	46.65	7.81
XVI	153.59	46.13	7.43

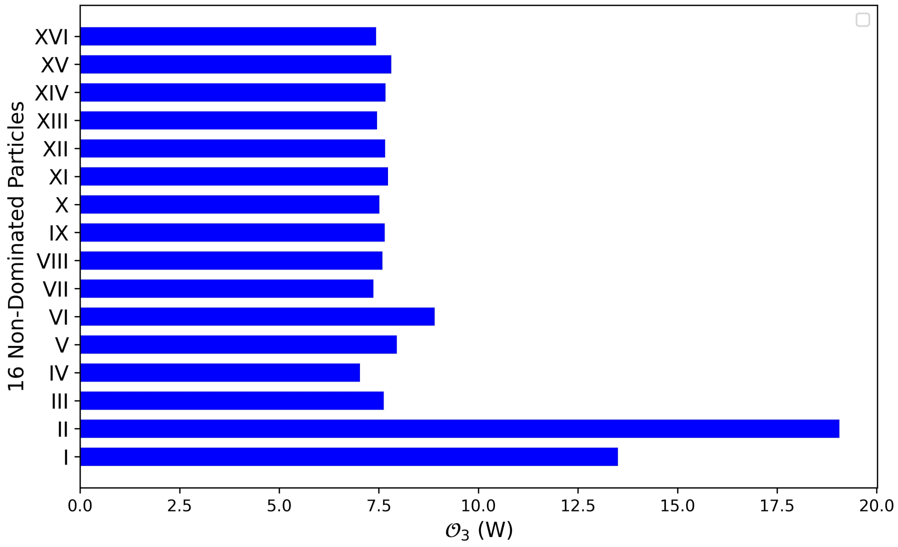

Figure 4.14 – $\mathcal{O}_3$ of sixteen non-dominated solutions found by multi-objective I-PR-PSO.

The objective values of the sixteen non-dominated solutions are presented in Figs. 4.13-

4.14 and Tab. 4.3. They are labeled with Roman numerals. In Tab. 4.3, it could be observed that solutions VII to XVI exhibit similar objective values. The optimization process might be influenced by some insensitive parameters, leading to the generation of several close non-dominated solutions (Fig. 4.12). The identification of these parameters will be addressed in Section 4.4.2.

As solution IV owns the minimal $\mathcal{O}_3$, it has been selected as optimal variables (see Fig. 4.14): $\varphi = 71.91°$; $b = 0.150$ m; $s_1 = 0.138$ m; $s_2 = 0.052$ m; $s_3 = 0.150$ m; $s_4 = 0.049$ m; $h_1 = 0.090$ m; $h_2 = 0.062$ m; $h_3 = 0.104$ m; $h_4 = 0.058$ m; $\psi_1 = 11.48°$; $\psi_2 = 180°$; $\psi_3 = 151.07°$; $\psi_4 = 62.66°$; $\psi_5 = 113.29°$; $\psi_6 = 138.46°$; $\psi_7 = 119.59°$; $\psi_8 = 178.92°$; $\psi_9 = 222.03°$. $\mathcal{O}_3$, the maximum Joule effect power P'_{max} for all postures is 7.02 W. Figs. 4.15-4.16 illustrate the attachment point positions in exosuit with solution IV.

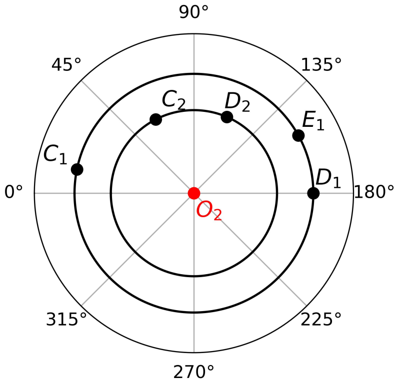

Figure 4.15 – Cuffs at arm with solution IV.

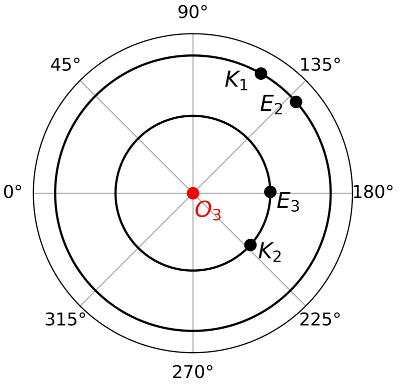

Figure 4.16 – Cuffs at forearm with solution IV.

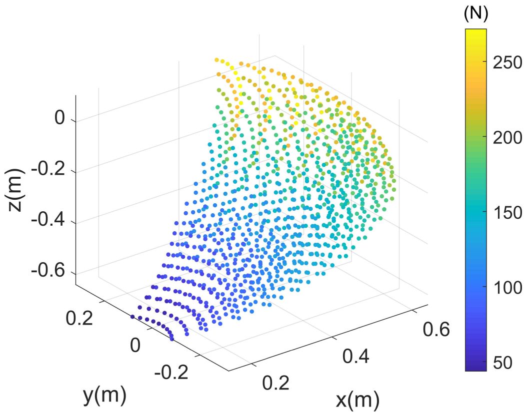

Figure 4.17 – Forces exerted on the shoulder by 4 cables with solution IV.

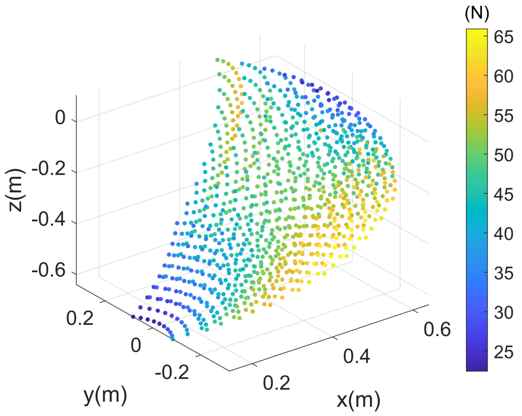

Figure 4.18 – Forces exerted on the upper limb by 4 cables with solution IV.

Regarding the workspace, it can be observed from Fig. 4.10 that the feasible workspace of exosuit has been enlarged with solution IV. Due to the penalty condition set in optimization (4.28), the number of infeasible configurations has been reduced to zero, which means that 4 cables are always in tension for all postures. Besides, the tension forces of 4 cables always fall in range $[F_{min}, F_{max}]$.

The average forces exerted on user $\mathcal{O}_1$ and $\mathcal{O}_2$ throughout the entire workspace are 149.20 N and 47.34 N respectively, which are more tolerable compared to the forces endured by the user before optimization. The optimized design has achieved a reduction of 50.34% and 60.89% in $\mathcal{O}_1$ and $\mathcal{O}_2$, resulting in a substantial improvement in user comfort and safety.

The forces exerted on human, with respect to different postures in workspace, are presented in Figs. 4.17-4.18. It could be observed from the figures that the force exerted by exosuit on shoulder and upper limb also depends on user's posture. For instance, the points where $\mathbf{F}^{\mathbf{cable}}_{\mathbf{shoulder}} > 200$ N or $\mathbf{F}^{\mathbf{cable}}_{\mathbf{upper\ limb}} > 55$ N occupy 36.40 % of the workspace in Fig. 4.19. Therefore, it is highly recommended for users to avoid performing their tasks in the postures with important forces.

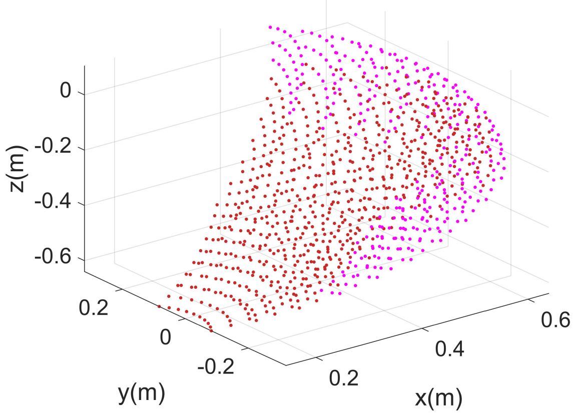

Figure 4.19 – Important forces exerted on shoulder and upper limb (magenta dots).

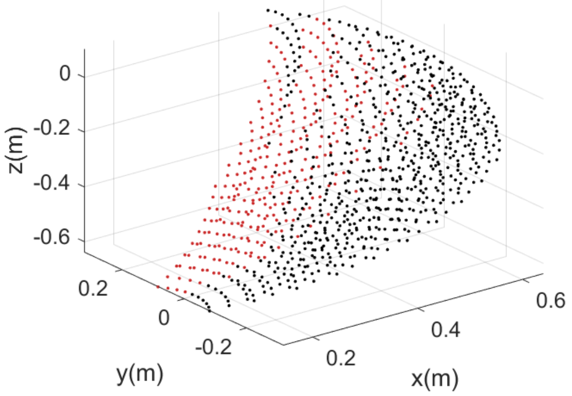

Figure 4.20 – Feasible workspace of the solution obtained by *fmincon* (brown dots).

Regarding the tension force of four cables, it is necessary to verify the continuity of forces. Poor continuity of cable tension forces in the workspace can have adverse effects on the controller performance, leading to increased energy consumption and vibrations. To verify this, the exosuit workspace is discretized into 8000 points. The range of each joint angle is discretized into 20 configurations. Figs. 4.21-4.24 show the tension force of four cables in workspace. The yellow zone in Figs. 4.21-4.24 indicates high cable tension forces, while the blue zone indicates low cable tension forces. Since the color variation is continuous, it can be deduced that the tension induced by four cables is step-less in the workspace. This continuity of cable tension force provides an advantage in controller design, ensuring smoother operation and improved stability.

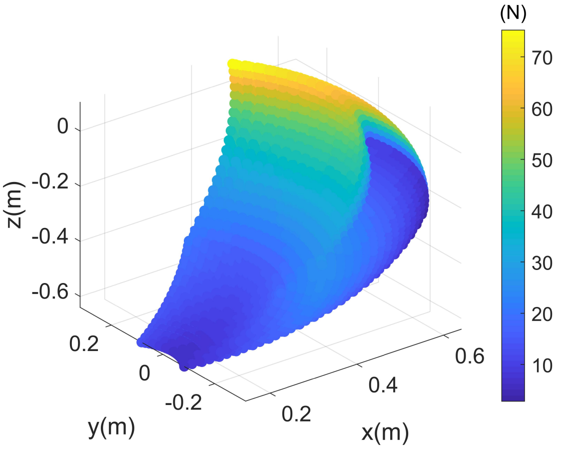

Figure 4.21 – F_1 in workspace.

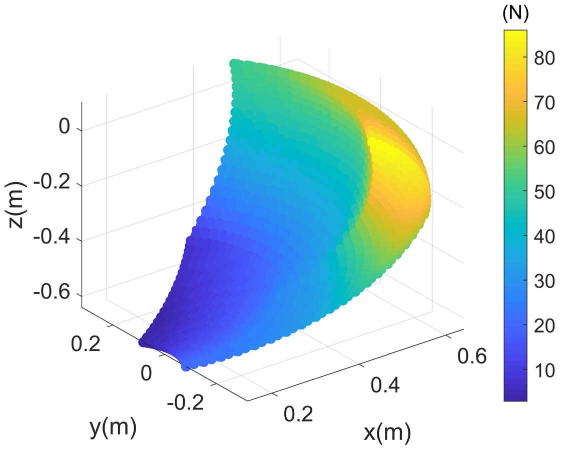

Figure 4.22 – F_2 in workspace.

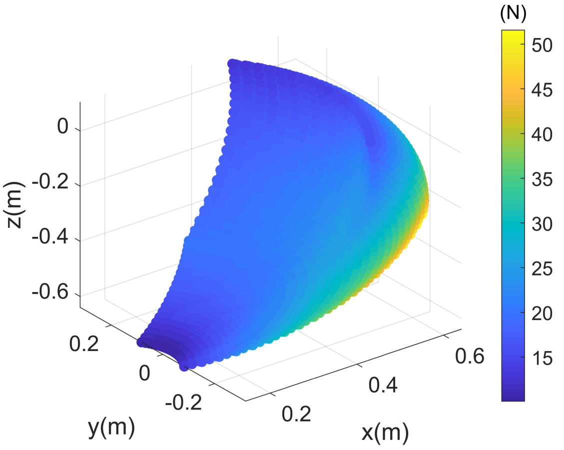

Figure 4.23 – F_3 in workspace.

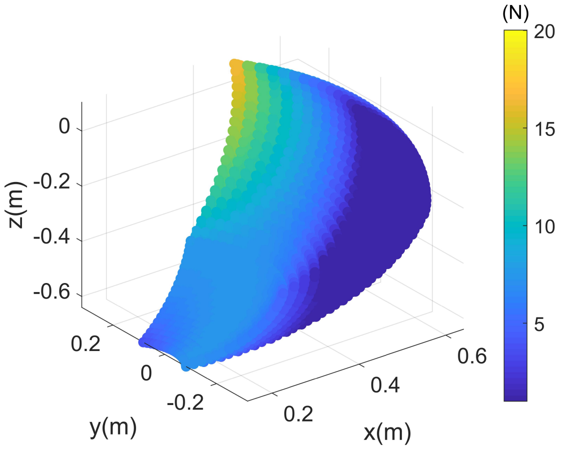

Figure 4.24 – F_4 in workspace.

To compare the I-PR-PSO with other popular NLP method, an optimization with *fmincon* (the interior-point method) was carried out. The obtained solution shows that 69 % of the workspace is infeasible with *fmincon* (Fig. 4.20). Among the feasible points, the average forces exerted on shoulder and upper limb are 218.32 N and 52.75 N respectively.

These values are 1.5 and 1.1 times larger than those of the selected optimal solution IV. It could be asserted that the optimization with *fmincon* converged to a local optimum.

Regarding the industrial applications, the exosuit is also capable of assisting the workers to carry or hold a heavy load, such as the drilling machines [151]. Another numerical simulation with $m_l = 5$ kg was conducted. The number of infeasible configurations has been reduced to zero and the continuity of cable tension forces in workspace is also ensured. The forces exerted on shoulder and upper limb are shown in Figs. 4.25-4.26.

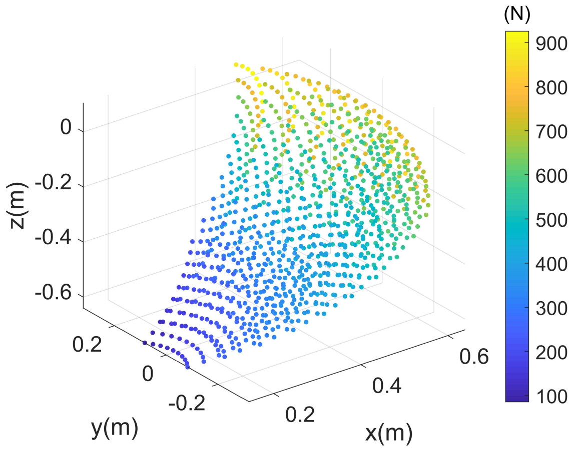

Figure 4.25 – Forces exerted on the shoulder with a 5 kg load.

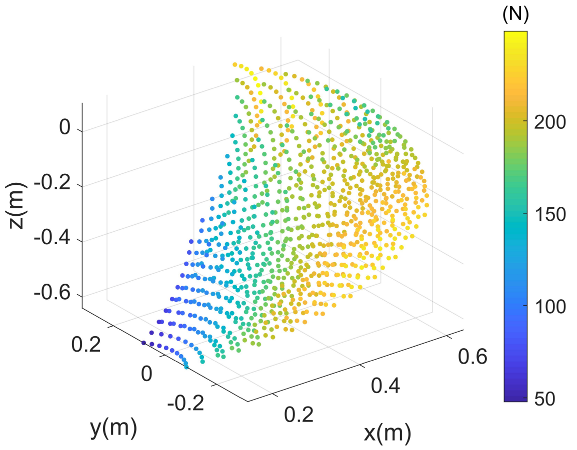

Figure 4.26 – Forces exerted on the upper limb with a 5 kg load.

With a 5 kg load, the average forces exerted on shoulder and upper-limb in workspace have been reduced up to 36.56 % and 34.09 % respectively in comparison with the initial parameters. It can be observed that they are still important and are about three times greater than those with a 0.5 kg load.

4.4.2 Sensitivity analysis of design parameters

In the previous section, it has been demonstrated via numerical simulations that the proposed optimization methodology is capable of improving human comfort conditions and energy efficiency performance in exosuit. However, it is also necessary to identify the design parameters more affecting the human comfort, which helps us enhance the understanding of exosuit model and provide valuable insights for future improvements. Taking into consideration the safety and comfort of the exosuit, obtaining information about the most influential parameter to $\mathcal{O}_1$ and $\mathcal{O}_2$ is significant during the design phase.

Global sensitivity analysis methods, like Sobol indices [126], are attractive in dealing with non linear systems and measuring the effect of interactions in non-additive systems. It should be admitted that these methods are capable of identifying the influential model parameters with high accuracy, but they need a large number of sampling for each model parameter. In addition, a nonlinear model with high dimension may also lead to a high computational burden.

Given the presence of 19 design parameters in the nonlinear exosuit model, a more efficient method for conducting sensitivity analysis is required. Random forest (RF), known as a stable and robust machine learning algorithm, combines the performance of numerous decision tree algorithms to classify or predict the value of a variable in a highly nonlinear model [152]. Due to the interpretability, RF is capable of providing an assessment of the relative importance of different evidential features [153], which could be applied for sensitivity analysis of design parameters. Nineteen design parameters in exosuit model are considered as features in RF. The sensitivity analysis stages are shown in Fig. 4.27:

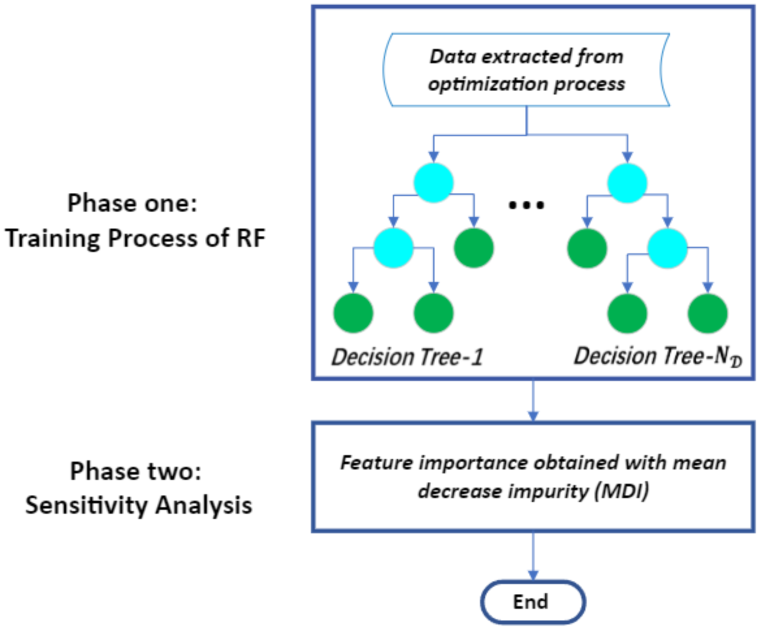

Figure 4.27 – Sensitivity analysis stages.

A total of 985 design parameter combinations, which are available solutions throughout the entire workspace, have been extracted from the previous multi-objective optimization process. They have been split into training and testing data set (4:1). In phase one, RF is fed with training data set and a trained RF is grown. RF is made up with numerous decision trees. The decision tree algorithm operates on the principle of selecting features in the splitting node (blue nodes in Fig. 4.27) that result in the maximum reduction in variance. Based on the selected features in all decision trees, the trained RF model is capable of predicting the objective function values of the testing dataset. This is done by calculating the average value of the leaf nodes (green nodes in Fig. 4.27). However, in our study, the trained RF is used for feature importance analysis rather than prediction of unknown dataset, which is the same application described in [154].

In phase two, the importance of a feature in RF is assessed using mean decrease impurity (MDI). MDI calculates the average variance reduction $\mathcal{S}_i$ brought by that feature i in each decision tree.

$$\mathcal{S}_i = \frac{1}{N_{\mathcal{D}}} \sum_{j=1}^{N_{\mathcal{D}}} \Delta\sigma_{i,j}, \ j = 1, ..., N_{\mathcal{D}} \tag{4.36}$$

where $N_{\mathcal{D}}$ denotes the number of decision trees; $\Delta\sigma_{i,j}$ denotes the variance reduction brought by the ith feature in the jth decision tree. Training process of RF has been carried out with a Python module: scikit-learn random forest regressor. Two hundred decision trees were created in RF. Then, the fitting performance of trained RF was verified with the testing data using R^2 criteria. The R^2 value are 0.80 and 0.81 for $\mathcal{O}_1$ and $\mathcal{O}_2$ respectively. In other words, the trained RF has explained about 80% variance of training data set. Thus, it is asserted that the trained random forest is capable of representing the forces exerted on shoulder and upper limb with various design parameter combinations. Feature importance could then be calculated using mean decrease impurity (MDI) to evaluate its sensitivity to interaction forces (Eqs. (4.21)-(4.22)).

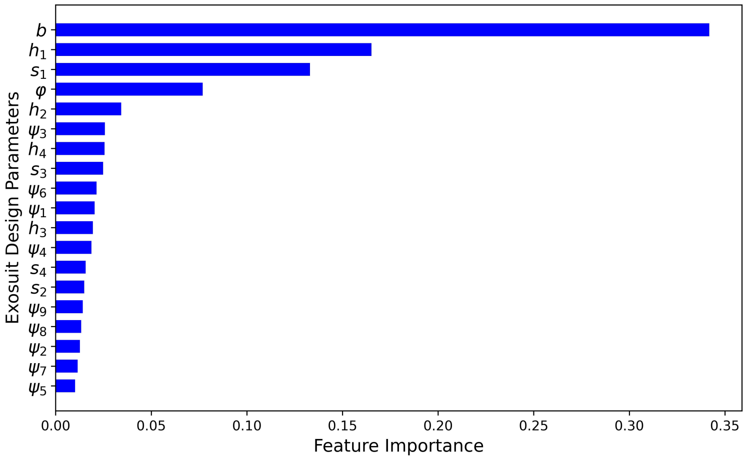

Figure 4.28 – Feature importance to $\mathcal{O}_1$.

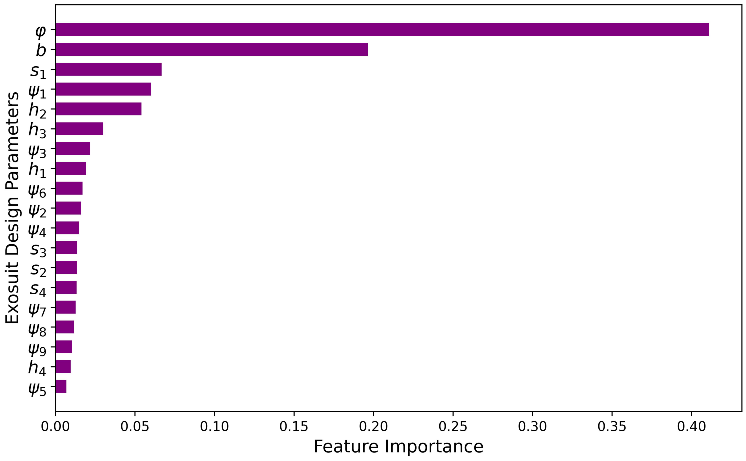

Figure 4.29 – Feature importance to $\mathcal{O}_2$.

Observed from Figs. 4.28-4.29, design parameters b and φ own the most feature importance (34 % and 41 %) to $\mathcal{O}_1$ and $\mathcal{O}_2$ in RF respectively. In other words, the variations of b and φ contributes to most variations of objective function values respectively. They are the most sensible factors to the forces exerted on users.

During the usage of exosuit in any working condition, the anchor points should remain the position on the shoulder, with respect to b and φ, so that the forces exerted on user do not increase. It could also observed from Figs. 4.28-4.29 that the trained RF has also identified design parameters with less feature importance. Because they have low sensitivity to interaction forces, they can be slightly adjusted to accommodate the upper limb size of different users. Furthermore, insensitive parameters impact the optimization process. Regarding the similar non-dominated solutions VII to XVI, the most notable variations are observed in the parameters ψ_6, ψ_7, and ψ_9, exhibiting magnitudes at least ten times greater than the others. They are the less sensitive parameters, as shown in Figs. 4.28-4.29. Their occupations of feature importance are all less than 5 %, leading to the emergence of close non-dominated solutions VII to XVI, as shown in Fig. 4.12. In the future, it is also worth considering the possibility of reducing the dimensionality of the optimization problem by fixing parameters that have less sensitivity. By doing so, the optimization algorithm can focus on exploring the more influential parameters, increasing the possibility of discovering additional non-dominated solutions on the Pareto front within the constrained domain.

4.5 Summary

Excessive forces exerted on the human body has always been a challenge in the exosuit design. Although exosuits provide lower inertia and they have better kinematic compatibility than rigid ones, application of external loads to human body, including pressure distribution and pressure force magnitude, may reduce the level of user safety and comfort. Besides, as assist devices, exosuits are required to be manipulated by users for long time and thereby the energy efficiency of exosuits needs to be improved. Since there are more than one criteria to be considered in the exosuit design, a multi-objective optimization framework has been proposed to improve the performance of an upper-limb exosuit for assistance, which is based on Particle Swarm Optimization. Inverse Page-Rank Particle Swarm Optimization is a powerful PSO variant, which has been proved that it has a better global optimum searching ability than the peers. In this chapter, to resolve a multi-criteria problem, the functionality of I-PR-PSO has been extended by taking the effects of all the fitness values into account. The application of the suggested optimization on the exosuit resulted in a reduction of forces exerted on human body more than 50 % and 34 % with 0.5 kg and 5 kg load respectively. The infeasible workspace of exosuit has been reduced to zero and the cable tension forces are also continuous in workspace, which benefits the controller design.

In comparison to the local optimum achieved through the widely used NLP method, the obtained exosuit system applies less forces on shoulder and upper limb. Additionally, two design parameters of exosuit were identified as the most influential parameters to human comfort conditions, providing valuable insights during the design phase.

Chapter 5

VALIDATION THROUGH EXPERIMENTATION OF THE OPTIMIZED EXOSUIT DESIGN WITH REDUCED ENERGY CONSUMPTION

5.6 Numerical simulation with demonstrator-mannequin upper-limb 158
5.7 Experimental equipements 161
5.8 Experimentation and results 169
5.9 Summary 172

In Chapter 4, an exosuit design for upper-limb assistance has been introduced, using a multi-objective optimization framework to enhance the human comfort conditions and energy efficiency. Despite promising results from the numerical simulations, the validation of these improvements through real-world experiments is essential.

This chapter focuses on an experimental step, aiming to validate the exosuit design with reduced energy consumption. A demonstrator-mannequin upper-limb was fabricated in the laboratory LS2N. It is known that the Joule heating in DC motors increases the energy consumption. Hence, the main objective is to measure the current in DC motors during the experimentation and demonstrate the reduced energy consumption brought out by the optimal numerical solution.

This chapter is structured as follows: we begin by conducting multi-objective optimization for the demonstrator-mannequin upper-limb. Next, the selection and functionality of the experimental equipment will be presented. Finally, the obtained results from the experimentation will be discussed and analyzed.

5.1 Numerical simulation with demonstrator-mannequin upper-limb

In Chapter 4, an advanced optimization framework was developed with the aim of improving the human comfort conditions and energy efficiency. Despite promising results from the numerical simulations in Section 4.4, the validation of these improvements through real-world experiments is necessary. Thus, in this chapter, an experimentation step has been designed for validating the exsuit design with reduced energy consumption, comprising three main steps:

1. **Optimization for the demonstrator-mannequin upper-limb:** The proposed optimization framework in Chapter 4 is conducted to identify the design parameters (arrangement of the anchor and attachment points) of the demonstrator-mannequin upper-limb for higher energy efficiency in DC motors.
2. **Selection of electronic components in experimentation:** The necessary electronic components are selected for experimentation.
3. **Experimentation and results:** The experimentation results are obtained and analyzed.

5.1.1 Parameters of the demonstrator-mannequin upper-limb

Figure 5.1 – Demonstrator-mannequin fabricated in LS2N.

As shown in Fig. 5.1, a demonstrator-mannequin was fabricated in the laboratory LS2N and its upper limb is considered as a 2-DOF manipulator (shown in Fig. 5.1). The parameters of demonstrator-mannequin upper-limb are listed in Tab. 5.1. The detailed system modeling of the demonstrator-mannequin's upper limb is similar to the content in Section 4.2.1, as shown in Appendix A.

Table 5.1 – Parameters of mannequin upper-limb.

Body Part	Mass (kg)	Length (m)	Center of Mass (m)	Radius (m)
Forearm and hand	0.87	0.48	0.24	0.05
Upper Arm	0.9	0.31	0.12	0.05

5.1.2 Numerical simulation results and analysis

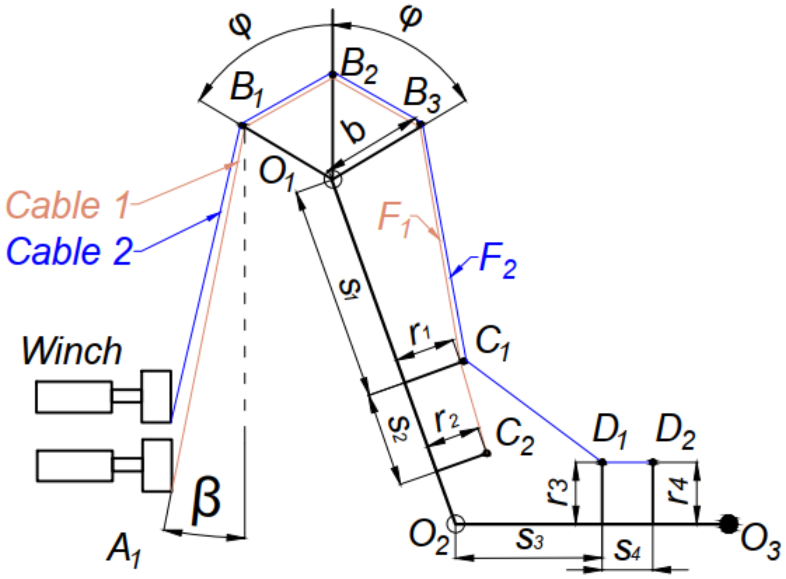

Figure 5.2 – Demonstrator-mannequin upper-limb with cable transmission system.

The proposed multi-objective optimization framework in Chapter 4 has been carried out for identifying the optimal anchor and attachment point positions of the demonstrator-mannequin, which improved the human comfort conditions and energy efficiency performance. The optimization domain was defined as follows (Fig. 5.2): 0.06 m $\leq r_1 \leq$ 0.1 m; 0.06 m $\leq r_2 \leq$ 0.1 m; 0.06 m $\leq r_3 \leq$ 0.1 m; 0.06 m $\leq r_4 \leq$ 0.1 m; 0.05 m $\leq s_1 \leq$

0.15 m; 0.04 m $\leq s_2 \leq$ 0.06 m; 0.1 m $\leq s_3 \leq$ 0.15 m; 0.04 m $\leq s_4 \leq$ 0.06 m; 0.06 m $\leq b \leq$ 0.15 m; $0° \leq \varphi \leq 60°; 0° \leq \beta \leq 70°$.

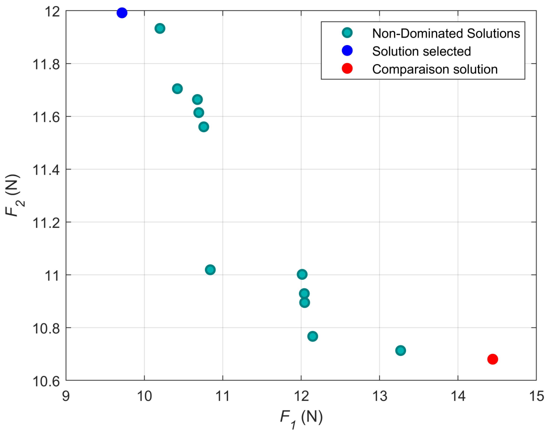

Figure 5.3 – Non-dominated solutions found by multi-objective I-PR-PSO.

As shown in Fig. 5.3, 13 non-dominated solutions were found. The blue point is the selected solution which produces less Joule effects among all the configurations while the red point is the non-dominated solution which produces the most Joule effects. Tab. 5.2 shows the performance of all the non-dominated solutions:

Table 5.2 – Performance of the non-dominated solutions found.

Solutions	F_1 (N)	F_2 (N)	Joule effect power (W)
I	10.84	11.02	253.89
II	10.42	11.70	260.45
III	12.04	10.93	281.60
IV	12.04	10.90	280.29
V	12.15	10.77	281.41
VI	10.68	11.66	265.29
VII	14.44	10.68	347.79
VIII	10.20	11.93	260.98
IX	9.72	12.00	252.36
X	13.27	10.71	311.17
XI	10.76	11.56	264.13
XII	10.69	11.61	264.16
XIII	12.01	11.00	282.24

Observed from the Tab. 5.2, the solutions IX and VII are selected for the experimental validation, representing the optimal solution (blue point) and the non-dominated solution with the lowest enery efficiency (red point). To actuate the demonstrator-mannequin upper-limb and achieve the experimental goal, various electronic components are selected and employed in the experimentation.

5.2 Experimental equipements

5.2.1 DC Gear motor selection

Figure 5.4 – Couzet DC gear motor.

The experimental validation goal is to verify the energy consumption of the proposed optimal exosuit design, especially the Joule effect produced by DC motor. During the DC gear motor selection, the motor capacity is the priority to be considered: output torque and rotation velocity. The motor capacity should cover the maximum torque required among all the exosuit postures. Couzet Gear motor 828690 has been selected, as shown in Figs. 5.4-5.5. The parameters of the selected DC motor are listed in Tab. 5.3.

Table 5.3 – Parameters of Couzet gear motor 828690 [155].

Parameter	**Value**
Motor	Couzet Brushed DC motor 828690
Nominal power	3 W
Nominal voltage	12 V
Nominal output speed	27 rpm
Resistance	8 Ω
Gearbox ratio	160
Maximum permitted torque	2 Nm
Axial load static	1 daN
Radial load static	10 daN
Maximum output power	3.9 W
Gearbox case temperature rise	50 °C
Weight	240 g

The maximum permitted torque is 2 Nm, which is sufficiently large and covers all the upper-limb postures in the optimization, with the radius of winch $r_w = 0.03$ m. Furthermore, the previous optimization framework focused on the static case, without consideration of inertial forces. In experimentation, we maintain a low output rotational velocity and the nominal output speed of the gear motor 27 rpm is adequate. Fig. 5.6 presents the torque-speed relationship of the selected motor.

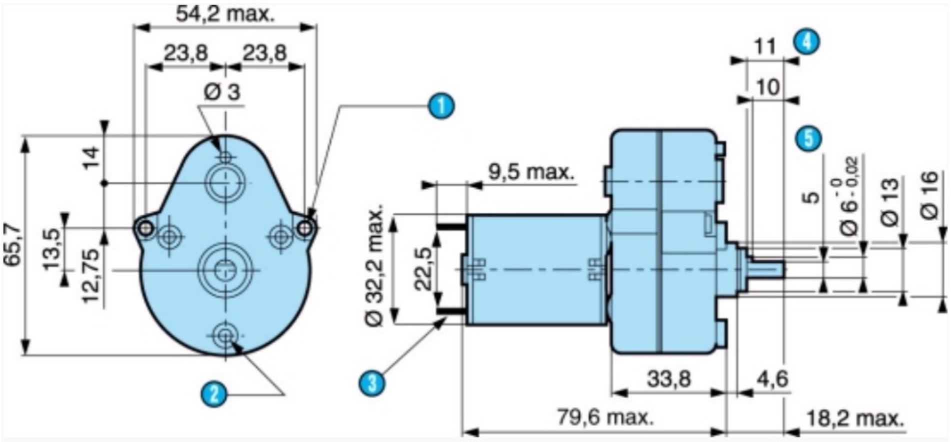

Figure 5.5 – Couzet DC gear motor [155].

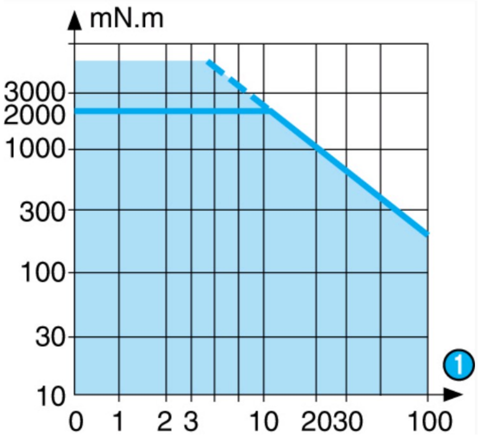

Figure 5.6 – Torque-speed relationship [155].

5.2.2 Arduino Mega controller

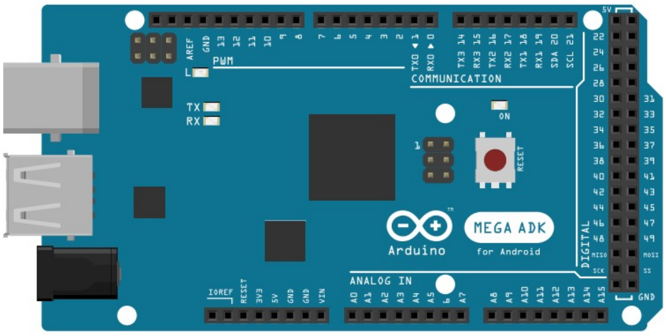

Figure 5.7 – Arduino Mega controller [156].

The Arduino Mega is used as controller in the experimentation. The Arduino board is an open-source microcontroller platform built around the ATmega2560 microcontroller. Its user-friendly environment enables individuals with minimal technical background to quickly acquire essential programming skills and operate the Arduino board, making it a significant player in the automation industry.

The Arduino Mega provides ample connectivity for a wide range of sensors, actuators, and other peripherals, making it suitable for complex and multifaceted projects. The Mega also boasts a larger flash memory and RAM compared to other Arduino boards, enabling the implementation of more intricate programs and handling larger datasets.

5.2.3 L298N motor driver

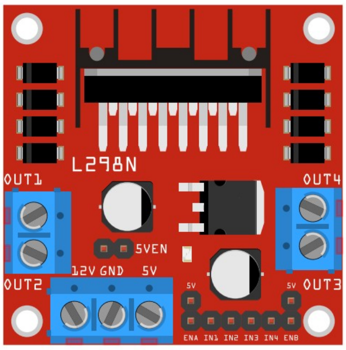

Figure 5.8 – L298N motor driver [156].

Microcontrollers operate on low-level voltage/current signals. As an example, the Arduino Mega has a maximum voltage of 5 V and a maximum current of 40 mA. However, the nominal voltage and current of the selected DC motors is 12 V and 325 mA. Thus, the output of Arduino Mega is not sufficient to power up the selected DC motors. To overcome this challenge, L298N motor driver module is used in experimentation. The motor driver module acts as an intermediary between microcontroller and motor. The output voltage range is 5 V-35 V and the maximum current is 2 A. It allows the microcontroller to control the motor's direction and speed by providing higher voltage and current.

The L298N motor driver is designed based on the H-bridge circuit (Fig. 5.9), which is a simple circuit enabling precise control of DC motor rotation direction. An H-bridge allows us to switch the motor's polarity, determining whether it rotates in the forward or backward direction.

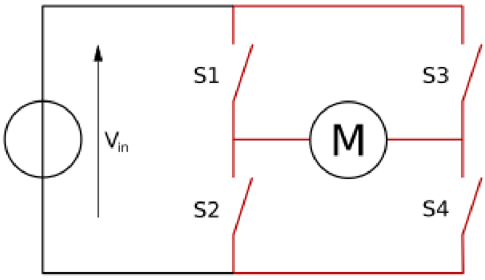

Figure 5.9 – H-bridge circuit [157].

The direction of motor rotation is determined by the positions of the switches. When S1 and S4 are turned ON and S2 and S3 are turned OFF, the left side of the motor terminal becomes more positive than the other terminal. This results in the motor rotating clockwise. Conversely, when S2 and S3 are turned ON and S1 and S4 are turned OFF, the right side of the motor terminal becomes more positive than the left terminal. This causes the motor to rotate counterclockwise. Additionally, the motor can also be commanded to stop rotation by turning ON the S1 and S3 while turning OFF the S2 and S4. This action effectively applies the same voltage to both motor terminals, causing it to come to an immediate stop. The table below summarizes the actions, with S1-S4 corresponding to the diagram above:

Table 5.4 – Switch control in the H-bridge.

S1	S2	S3	S4	Motor direction
1	0	0	1	Clockwise
0	1	1	0	Counter clockwise
1	0	1	0	Brakes
0	1	0	1	Brakes

In the experimental validation, the L298N is also utilized to control the angular velocities of DC motors. Firstly, the Arduino Mega delivers a pulse-width modulation (PWM) signal to the L298N, which then controls the switching frequency in the H-bridge to apply a desired voltage across the motor terminals. In other words, the switching frequency of L298N could be controlled by Arduino Mega, which allows the upper arm and forearm of the demonstrator-mannequin to be lifted up at low or high speed during the experimentation.

5.2.4 INA219 current sensor

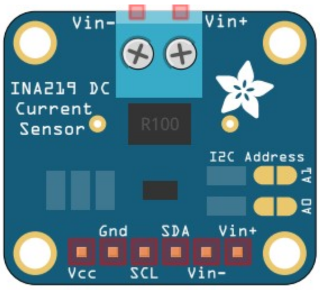

Figure 5.10 – INA219 current sensor [156].

In experimentation, to obtain the energy efficiency, INA219s are employed for measuring the current in DC motors. The INA219 is a high-side current shunt and power monitor with an I2C (Inter-Integrated Circuit) interface. It is designed to monitor both the shunt voltage drop and supply voltage. By using a programmable calibration value in conjunction with an internal multiplier, the INA219 can provide direct readouts in amperes. Additionally, it includes a multiplying register to calculate power in watts.

The INA219 operates efficiently on a single supply voltage between +3 V to +5.5 V, drawing a maximum of 1 mA of supply current. It has a measured current range of 0 A to 3.2 A and is capable of accurately measuring currents in the milliampere (mA) range. The nominal current of the selected DC motors is 325 mA. This level of precision is sufficient for measuring the DC motor current during the operation of the demonstrator-mannequin upper-limb. In the experimentation, it should be noted that it is required to measure the current of two DC motors. To achieve this, the A0 pin on the INA219 board is utilized for obtaining different I2C addresses to measure the currents of two motors. The SCL (Serial Clock) and SDA (Serial Data) pins on the INA219s are used for I2C communication. This communication protocol is widely used for connecting microcontrollers, sensors, and other devices, allowing them to exchange data over a two-wire interface.

5.2.5 MPU6050 IMU sensor

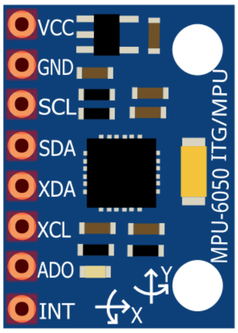

Figure 5.11 – MPU6050 [156].

Furthermore, MPU6050s are employed for measuring the upper-limb positions in the experimentation. The MPU6050 sensor (Fig 5.11) is a versatile 6-axis motion tracking device. It combines a 3-axis gyroscope and a 3-axis accelerometer into a compact package. It connects easily to microcontrollers via an I2C bus interface and also provides an auxiliary I2C bus for communicating with other sensor devices like a 3-axis magnetometer or a pressure sensor.

It operates within a voltage range of 2.375 V to 3.46 V for the MPU6050. Despite its small size, it has low power consumption, drawing only 3.9 mA during full operation. This module is not only compact but also highly accurate, with excellent repeatability and shock tolerance. Inside the MPU6050, a 3-axis accelerometer is used to determine the angle of tilt or inclination along the X, Y, and Z axes, as shown in Fig. 5.12. The accelerometer detects acceleration along these axes by displacing a movable mass. Its displacement creates an imbalance in the differential capacitor, resulting in a sensor output. The amplitude of the output is directly proportional to the acceleration and is measured

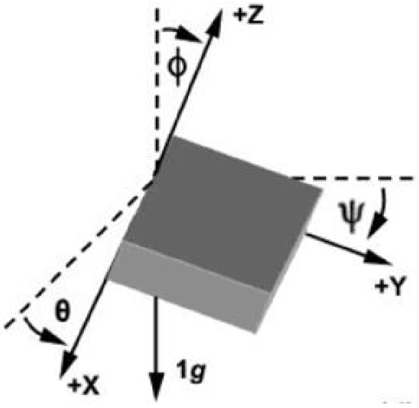

Figure 5.12 – Yaw, roll and pitch angles of MPU6050.

in units of "g" (gravity force). When the device is placed on a flat surface, it will register 0 g on the X and Y axes and +1 g on the Z axis. This information is obtained through a 16-bit Analog-to-Digital Converter (ADC) for precise digital output.

As shown in Fig 5.12, θ, ψ and ϕ denote the yaw, roll and pitch angles of MPU6050. Among them, the roll and pitch angles could be calculated with the following expressions:

$$\psi = \arccos(\frac{\sqrt{a_x^2 + a_z^2}}{\sqrt{a_x^2 + a_y^2 + a_z^2}}) \tag{5.1}$$

$$\phi = \arccos(\frac{\sqrt{a_y^2 + a_z^2}}{\sqrt{a_x^2 + a_y^2 + a_z^2}}) \tag{5.2}$$

where a_x, a_y and a_z are the magnitudes of gravity accelerations along the three axes. In our case, MPU6050 accelerator is used for measuring the upper-limb position in the experimentation.

5.3 Electronic diagram

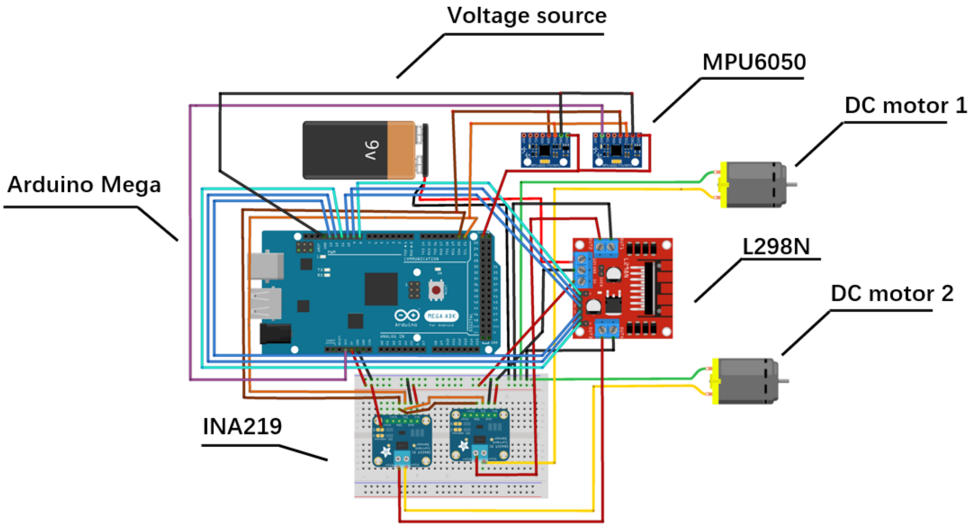

Figure 5.13 – Electronic diagram and components in the experimentation [156].

Fig. 5.13 presents the electronic diagram of experimentation. Arduino Mega is connected to the laptop for uploading the program created in the Arduino Integrated Development Environment (IDE). Arduino IDE is an open source IDE that allows users to write code and upload it to any Arduino board.

Two DC motors are connected to the L298N motor drivers, which are powered by a 9 V source. The Arduino Mega sends two types of signals to the L298N: analog signals and digital signals. The blue wires transmitting digital signals are connected to the pins on the L298N, maintaining a high tension level. Subsequently, through the cyan wires connected to the ENA and ENB pins, the Arduino Mega could send PWM analog signals to the L298N for controlling the rotational velocity of the DC motors.

The INA219s and MPU6050s are both powered by the Arduino Mega using the 5 V output pin. Their wires are also connected to the SCL and SDA pins on the Arduino Mega for I2C communication. Thus, INA219s and MPU6050s are capable of transmitting the measured data to Arduino Mega. Then, the laptop records all the measured data from the Arduino Mega.

5.4 Experimentation and results

During the experimentation phase, the performances of optimal solution and non-dominated solution are compared. Fig. 5.14 shows the optimal arrangement of anchor and attachment points, while Fig. 5.15 illustrates the non-dominated solution's arrangement. A noticeable difference is observed in the parameter s_1 (Fig. 5.21).

Two cable winches, one motor support and four cuff supports have been designed and fabricated with 3D impression technique at INSA Rennes. The radius of the winch r_w is 0.03 m. The cables in exosuit system pass through the cuff supports with different anchor and attachment point positions. A polyethylene braid-style cable was adopted in the exosuit system, which could bear load up to 34 kg while having little deformation [134].

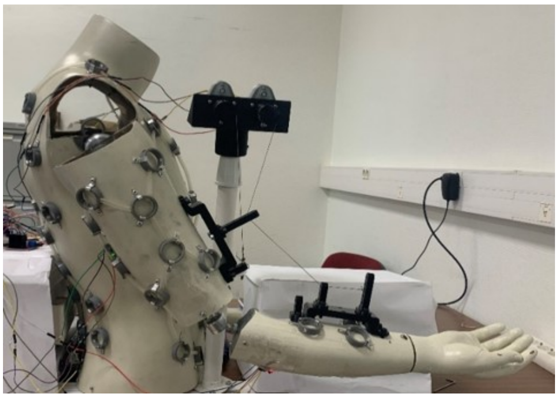

Figure 5.14 – Optimal solution IX.

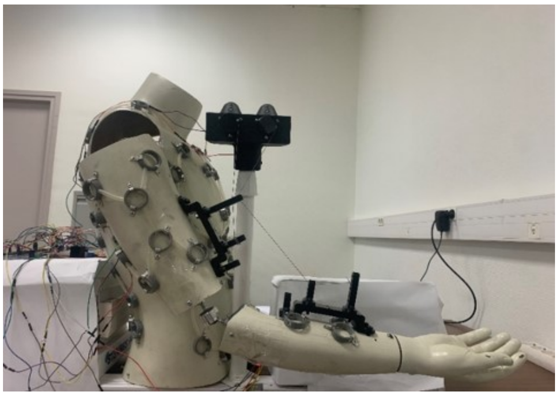

Figure 5.15 – Non-dominated solution VII.

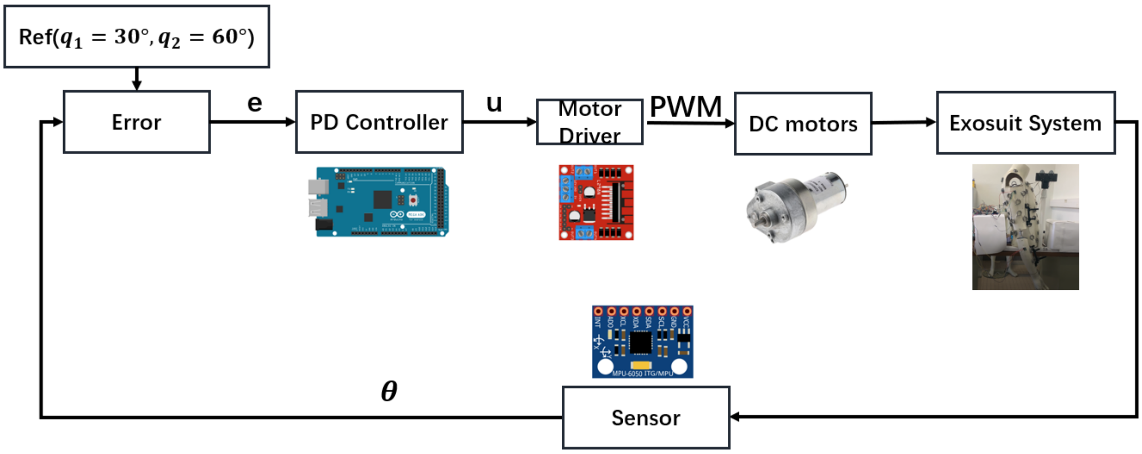

Figure 5.16 – Control loop in experimentation.

With the introduced electronic components and diagram (Fig. 5.13), the experimentation has been carried out. A control loop was defined in Fig 5.16. To achieve the reference trajectory ($q_1 = 30°$ and $q_2 = 60°$), PD controller was implemented in the Arduino Mega board for adjusting the PWM signals sent to L298N. The PD controller parameters were defined as: $K_p = 70$; $K_d = 5$. Additionally, the Arduino MPU6050 module was also implemented in the Arduino Mega board for measuring the upper-limb positions through Eqs. (5.1)-(5.2). Figs. 5.17-5.18 show the positions of upper arm and forearm in the control process. It has been demonstrated that the upper limb of the demonstrator-mannequin was capable of achieving the desired position.

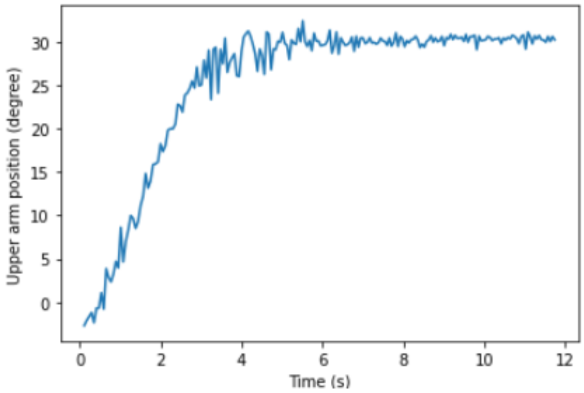

Figure 5.17 – Upper-arm position measured by MPU6050 in the control process.

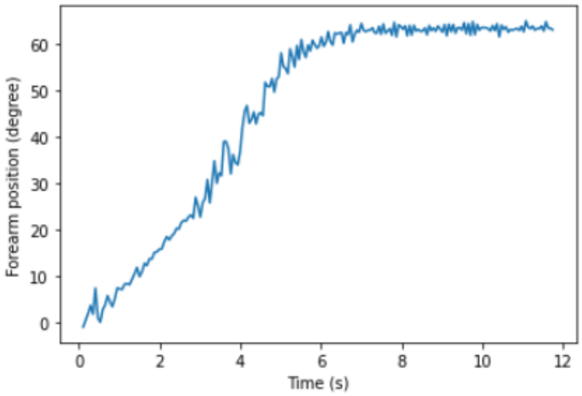

Figure 5.18 – Forearm position measured by MPU6050 in the control process.

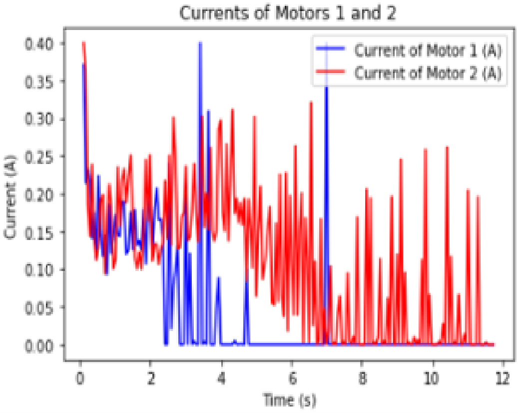

Figure 5.19 – Current measured with optimal solution IX in the control process.

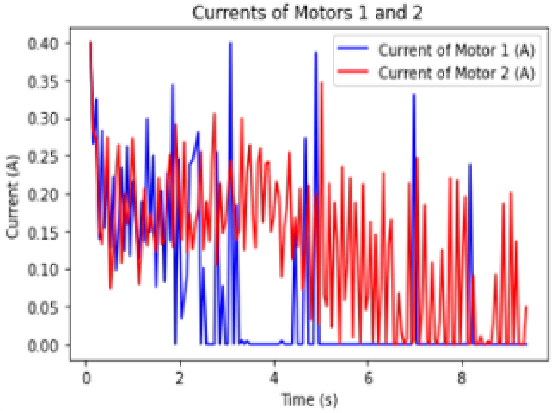

Figure 5.20 – Current measured with solution VII in the control process.

Table 5.5 – Average energy loss power.

Experimentation	Average Joule effect power (W) in the control process
Optimal solution	0.434
Non-dominated solution	0.600

Figs. 5.19-5.20 show the current measured by INA219s for the optimal solution and non-dominated solution in the control process. Then, the average Joule effect power in two cases was calculated in Tab. 5.5. Compared to the non-dominated solution VII, the optimal solution IX brought out a reduction about 28%, demonstrating its high energy efficiency.

5.5 Summary

In this chapter, an experimentation step has been carried out to validate the optimized exosuit design with reduced energy consumption. The optimization framework proposed in Chapter 4 was applied to the demonstrator-mannequin fabricated in LS2N for identifying the design parameters, which improved the human comfort conditions and energy efficiency. To achieve the experimentation goal, various electronic components were employed for driving the motors, measuring the current, and recording the upper-limb positions. A PD control loop was implemented in the microcontroller. In the experimentation, the upper limb of the demonstrator-mannequin was capable of attaining the desired position. The results of experimentation revealed that the optimal numerical solution resulted in a 28% reduction in energy loss power in comparison with the other design solution. Regarding the future work, an additional cable will be incorporated on the left shoulder of the demonstrator-mannequin to achieve shoulder internal rotation. Subsequently, another prototype will be fabricated and worn by a human for load-carriage assistance, with force sensors incorporated into the exosuit system to measure the forces exerted on the human body.

CONCLUSION AND FUTURE WORKS

Conclusion

The work presented in this thesis deals with the methods for design and control of robotic systems considering energy consumption and improving their behavior. Four main parts are considered in the thesis:

- Estimation of energy loss in mechanical systems due to the friction: a new solution to force analysis including Coulomb friction.
- Torque minimization and control performance improvement of dynamically decoupled spatial serial manipulators.
- Optimal exosuit design for upper-limb assistance based on human comfort conditions and energy efficiency.
- Validation through experimentation of the optimized exosuit design with reduced energy consumption.

In the thesis, a novel method has been developed for approximating the reactions and energy consumption involving Coulomb friction in mechanism joints. Coulomb friction amplifies the forces within mechanical system bearings and leads to energy dissipation, and if the mechanical system comprises a series of interconnected linkages, this can escalate into a major problem as the friction forces multiply through the chain of links. The proposed method is based on traditional friction circle concepts and the Babylonian method, which is exceptionally well-suited for calculating and streamlining the solution process for mechanical systems by eliminating the necessity for iterative steps at each stage of the dynamic analysis. The stability of the approximation method was verified and proved in applications. The numerical simulation results showed that the discrepancy between the exact and approximation calculations did not exceed 0.64 % and could be disregarded in most of the time. The proposed method was also applied in a mechanism with complex structure, such as 3RRR parallel manipulator, indicating a high approximation accuracy. Additionally, another advantage of the Babylonian method lies in its ability to provide insights into the reaction forces due to friction. The proposed method is also capable of providing a reliable approximation of energy loss due to friction, which should be taken into account during the design phase. It should be noted that the modifications to the manipulator parameters can lead to increased discrepancies between the calculated exact and maximum solutions, but given the results obtained and various observations, it is still considered that the technique is clearer and simpler than previous approaches.

Dynamic decoupling technique has also been introduced in the thesis for achieving the torque minimization and control performance improvement in spatial serial manipulators. Nonlinear coupled dynamics of robot manipulator increases the computational burden or even the energy consumption in control process. Instead of developing complicated control laws, the dynamic decoupling technique is employed to simplify the dynamics of spatial serial manipulators through mechanical modifications. In the decoupling process, the mass redistribution and actuator relocation were applied for eliminating the nonlinearities in the dynamics of 2R and 3R spatial serial manipulator. Their dynamics was simplified as a double integrator system, which was linear and decoupled. Next, bang-bang motion profile could be applied for reducing the maximum torque. The numerical simulation results showed that the implementation of the proposed motion profile has brought out a reduction of up to 30 % in maximum input torques of the decoupled manipulators.

As the obtained decoupled system was a double integrator model, various straightforward control strategies were employed for improving the control performance, such as stability, tracking accuracy and energy consumption. The classical linear control techniques linear quadratic regulator and lead compensation were adopted to track the desired bang-bang profile trajectory. Then, in the presence of parameter uncertainty and external disturbances, adaptive control MRAC and modified twisting control were adopted to stabilize the decoupled system asymptotically. In the presence of parameter uncertainty and external disturbances, the MRAC and the modified twisting controller performed well for the double integrator model. In the case that the joint velocity was not directly measurable, modified twisting observer was applied and provided reliable estimates. The simulation results illustrated that these controllers effectively reduced computational burden while enhancing the control performance in terms of tracking accuracy, energy consumption, and maximum input torque in the decoupled systems.

In Chapter 3, the proposed exosuit design for load-carriage assistance improves human comfort conditions and energy efficiency. A cable transmission system driven by motors was incorporated in exosuit system to compensate the gravitational forces. The principal of virtual works was applied for modelling the exosuit system. As the obtained exosuit system was an under-actuated system, quadratic programming technique was then adopted for determining the cable tension forces, reducing the abrupt changes of cable tension force between nearby configurations.

It could also be noticed that the arrangement of anchors and attachment points affects the exosuit performance, such as human comfort conditions and energy efficiency. Thus, various optimization goals and constraints were defined in the exosuit design. The excessive pressure on the shoulder and incompatible force on the soft tissues of upper limb should be minimized. Another objective to be considered is the energy consumption because sometimes exosuit should be worn by user over long time for industrial needs. Moreover, due to the nature of cable, the cable tension force is always positive and do not exceed the limit of cable. Since there are more than one criteria to be considered in the exosuit design, a multi-objective optimization framework has been proposed to improve the performance of an upper-limb exosuit for assistance, based on Inverse PageRank Particle Swarm Optimization. The proposed optimization framework distinguished and prioritized different objectives in a nonlinear exosuit model. The application of the suggested optimization on the exosuit has brought out a reduction of forces exerted on human body more than 50 % and 34 % with 0.5 kg and 5 kg load respectively. The energy efficiency was also improved during the optimization process. Additionally, global sensitivity analysis based on Random Forest was carried out for identifying the most influential design parameters to human comfort conditions, offering valuable information during the design phase.

The last chapter of the thesis presented an experimentation step for validating the exosuit design with reduced energy consumption. A demonstrator-mannequin upper-limb was fabricated in the laboratory LS2N. The proposed optimization framework was then applied for identifying the optimal arrangement of anchor and attachment points, resulting in high energy efficiency of DC motors during load carriage. The objective of the experimentation was to measure the average energy loss power of DC motors. Necessary electronic components were employed for driving the DC motors, measuring current and recording upper-limb position in the experimentation. A comparison between the optimal solution and non-dominated solution was conducted. The experimentation demonstrated that the upper limb of demonstrator-mannequin was capable of lifting the load to the desired position. Furthermore, the experimental results revealed a 28 % reduction of average energy loss power with the optimal solution compared to the non-dominated solution.

Future works

This thesis generally focuses on the design and control of robotic systems based on energy efficiency and various criteria. In the last part of this manuscript, I would like to indicate some points which may be promising in the future work.

Firstly, for the proposed approximation method based on the Babylonian algorithm, it could be valuable to applicate it in more complex mechanism, such as special parallel manipulators, walking robotic systems.... Furthermore, this method will also be considered being implemented in control system for achieving friction compensation, leading to enhanced stability and accuracy of control loop.

Secondly, for the torque minimization and control performance improvement in spatial serial manipulators, an experimentation step will be designed to validate the proposed approach. Besides, the possibility of applying the proposed approach will be explored in the parallel robots for improving its energy consumption and control performance. The dynamics of parallel robot is quite complex and it is advantageous to simplify it through mechanical modifications.

Thirdly, with respect to the optimal exosuit design for load-carriage assistance, a dimension-reduced optimization will be carried out for discovering additional non-dominated solutions on the Pareto front within the constrained domain, which leads to enhanced human comfort conditions and energy efficiency. Additionally, various strategies to further reduce forces on users carrying heavy loads will be explored, including the introduction of more cables and elastic units in the exosuit system.

Finally, for the experimentation of the exosuit design, the fabricated demonstrator-mannequin upper-limb has only 2-DOF, which is limited in the real application. In future, a 3-DOF demonstrator-mannequin upper-limb will be fabricated and an additional cable will be incorporated on the left shoulder of the demonstrator-mannequin to achieve shoulder internal rotation. Its energy efficiency performance will then be evaluated and analyzed. Subsequently, another prototype will be fabricated and worn by a human for load-carriage assistance, with force sensors incorporated into the exosuit system to measure the forces exerted on human body.

BIBLIOGRAPHY

[1] Z. A. Khan, V. Chacko, and H. Nazir, « A review of friction models in interacting joints for durability design », *Friction*, vol. 5, pp. 1–22, 2017.

[2] J.-L. Ligier and B. Noel, « Friction reduction and reliability for engines bearings », *Lubricants*, vol. 3, *3*, pp. 569–596, 2015.

[3] M. R. Kermani, M. Wong, R. V. Patel, M. Moallem, and M. Ostojic, « Friction compensation in low and high-reversal-velocity manipulators », *in IEEE International Conference on Robotics and Automation, 2004. Proceedings. ICRA'04. 2004*, IEEE, vol. 5, 2004, pp. 4320–4325.

[4] J. Haessig D. A. and B. Friedland, « On the Modeling and Simulation of Friction », *Journal of Dynamic Systems, Measurement, and Control*, vol. 113, *3*, pp. 354–362, Sep. 1991.

[5] C. Canudas de Wit, P. Noel, A. Aubin, and B. Brogliato, « Adaptive friction compensation in robot manipulators: low velocities », *The International journal of robotics research*, vol. 10, *3*, pp. 189–199, 1991.

[6] B. Bona and M. Indri, « Friction compensation and robustness issues in force/position controlled manipulators », *IEE Proceedings-Control Theory and Applications*, vol. 142, *6*, pp. 569–574, 1995.

[7] B. Armstrong-Helouvry, *Control of machines with friction.* Springer Science & Business Media, 2012, vol. 128.

[8] J. Moreno, R. Kelly, and R. Campa, « Manipulator velocity control using friction compensation », *IEE Proceedings-Control Theory and Applications*, vol. 150, *2*, pp. 119–126, 2003.

[9] V. Arakelian, S. Sargsyan, and M. Harutyunyan, « Friction torque compensation in the balanced leg orthosis for robotic rehabilitation », *in Proceedings of the 8th European Solid Mechanics Conference (ESMC 2012)*, 2012, pp. 23–25.

[10] S. Grami and Y. Gharbia, « Gms friction compensation in robot manipulator », *in IECON 2013-39th Annual Conference of the IEEE Industrial Electronics Society*, IEEE, 2013, pp. 3555–3560.

[11] *Lubrication (tribology) education and research : a report on the present position and industry's needs*, eng. London: HMSO, 1966.

[12] K. Holmberg, P. Andersson, and A. Erdemir, « Global energy consumption due to friction in passenger cars », *Tribology international*, vol. 47, pp. 221–234, 2012.

[13] J. Awrejcewicz and P. Olejnik, « Analysis of dynamic systems with various friction laws », *Applied Mechanics Reviews*, vol. 58, *6*, pp. 389–411, 2005.

[14] F. Marques, P. Flores, J. P. Claro, and H. M. Lankarani, « A survey and comparison of several friction force models for dynamic analysis of multibody mechanical systems », *Nonlinear Dynamics*, vol. 86, *3*, pp. 1407–1443, 2016.

[15] H. Olsson, K. J. Åström, C. C. De Wit, M. Gäfvert, and P. Lischinsky, « Friction models and friction compensation », *Eur. J. Control*, vol. 4, *3*, pp. 176–195, 1998.

[16] F. Marques, P. Flores, and H. M. Lankarani, « On the frictional contacts in multibody system dynamics », *in Multibody Dynamics*, Springer, 2016, pp. 67–91.

[17] E. Pennestrì, V. Rossi, P. Salvini, and P. P. Valentini, « Review and comparison of dry friction force models », *Nonlinear dynamics*, vol. 83, *4*, pp. 1785–1801, 2016.

[18] C. A. Coulomb, *Théorie des machines simples en ayant égard au frottement de leurs parties et à la roideur des cordages*. Bachelier, 1821.

[19] F. Marques, P. Flores, J. P. Claro, and H. M. Lankarani, « Modeling and analysis of friction including rolling effects in multibody dynamics: a review », *Multibody System Dynamics*, vol. 45, *2*, pp. 223–244, 2019.

[20] S. Andersson, A. Söderberg, and S. Björklund, « Friction models for dry, boundary and mixed lubricated contacts », *in 11th Nordic Symposium on Tribology Nordtrib 2004, 4-7 June, Tromsö-Harstad-Hurtigrutten, Norway.*, 2004.

[21] D. Threlfall, « The inclusion of coulomb friction in mechanisms programs with particular reference to dram au programme dram », *Mechanism and Machine Theory*, vol. 13, *4*, pp. 475–483, 1978.

[22] J. Ambrósio, « Impact of rigid and flexible multibody systems: deformation description and contact models », *in Virtual nonlinear multibody systems*, Springer, 2003, pp. 57–81.

[23] A. Tustin, « The effects of backlash and of speed-dependent friction on the stability of closed-cycle control systems », *Journal of the Institution of Electrical Engineers-Part IIA: Automatic Regulators and Servo Mechanisms*, vol. 94, *1*, pp. 143–151, 1947.

[24] D. P. Hess and A. Soom, « Friction at a Lubricated Line Contact Operating at Oscillating Sliding Velocities », *Journal of Tribology*, vol. 112, *1*, pp. 147–152, Jan. 1990.

[25] K. Popp and P. Stelter, « Nonlinear oscillations of structures induced by dry friction », *in Nonlinear Dynamics in Engineering Systems: IUTAM Symposium, Stuttgart, Germany, August 21–25, 1989*, Springer, 1990, pp. 233–240.

[26] C. Makkar, W. Dixon, W. Sawyer, and G. Hu, « A new continuously differentiable friction model for control systems design », *in Proceedings, 2005 IEEE/ASME International Conference on Advanced Intelligent Mechatronics.*, IEEE, 2005, pp. 600–605.

[27] L. C. Bo and D. Pavelescu, « The friction-speed relation and its influence on the critical velocity of stick-slip motion », *Wear*, vol. 82, *3*, pp. 277–289, 1982.

[28] T. Specker, M. Buchholz, and K. Dietmayer, « A new approach of dynamic friction modelling for simulation and observation », *IFAC Proceedings Volumes*, vol. 47, *3*, pp. 4523–4528, 2014.

[29] P. Brown and J. McPhee, « A continuous velocity-based friction model for dynamics and control with physically meaningful parameters », *Journal of Computational and Nonlinear Dynamics*, vol. 11, *5*, p. 054 502, 2016.

[30] S. Andersson, A. Söderberg, and S. Björklund, « Friction models for sliding dry, boundary and mixed lubricated contacts », *Tribology international*, vol. 40, *4*, pp. 580–587, 2007.

[31] H. Dankowicz, « On the modeling of dynamic friction phenomena », *ZAMM-Journal of Applied Mathematics and Mechanics/Zeitschrift für Angewandte Mathematik und Mechanik: Applied Mathematics and Mechanics*, vol. 79, *6*, pp. 399–409, 1999.

[32] J. Liang, S. Fillmore, and O. Ma, « An extended bristle friction force model with experimental validation », *Mechanism and Machine Theory*, vol. 56, pp. 123–137, 2012.

[33] A. Aghdasi and M. Khonsari, « Friction behavior of radial shaft sealing ring subjected to unsteady motion », *Mechanism and Machine Theory*, vol. 156, p. 104 171, 2021.

[34] F. Marques, Ł. Woliński, M. Wojtyra, P. Flores, and H. M. Lankarani, « An investigation of a novel lugre-based friction force model », *Mechanism and Machine Theory*, vol. 166, p. 104 493, 2021.

[35] P. R. Dahl, « A solid friction model », *The Aerospace Corporation*, vol. 18, *1*, pp. 1–24, 1968.

[36] P. R. Dahl, « Solid friction damping of mechanical vibrations », *AIAA journal*, vol. 14, *12*, pp. 1675–1682, 1976.

[37] C. C. De Wit, H. Olsson, K. J. Astrom, and P. Lischinsky, « A new model for control of systems with friction », *IEEE Transactions on automatic control*, vol. 40, *3*, pp. 419–425, 1995.

[38] T. Brogårdh, « Present and future robot control development—an industrial perspective », *Annual Reviews in Control*, vol. 31, *1*, pp. 69–79, 2007.

[39] J. Luh, W. Fisher, and R. Paul, « Joint torque control by a direct feedback for industrial robots », *IEEE Trans. on Automatic Control*, vol. 28, *2*, pp. 153–161, 1983.

[40] J. Luh, « Conventional controller design for industrial robots—a tutorial », *IEEE Trans. on Systems, Man, and Cybernetics*, *3*, pp. 298–316, 1983.

[41] J. A. Meda-Campaña, J. O. Escobedo-Alva, J. d. J. Rubio, C. Aguilar-Ibañez, J. H. Perez-Cruz, G. Obregon-Pulido, R. Tapia-Herrera, E. Orozco, D. A. Cordova, and M. A. Islas, « On the rejection of random perturbations and the tracking of random references in a quadrotor », *Complexity*, vol. 2022, pp. 1–16, Jan. 2022.

[42] J. de Jesús Rubio, E. Orozco, D. A. Cordova, M. A. Islas, J. Pacheco, G. J. Gutierrez, A. Zacarias, L. A. Soriano, J. A. Meda-Campaña, and D. Mujica-Vargas, « Modified linear technique for the controllability and observability of robotic arms », *IEEE Access*, vol. 10, pp. 3366–3377, 2022.

[43] C. Aguilar-Ibanez, J. Moreno-Valenzuela, O. Garcıía-Alarcón, M. Martinez-Lopez, J. Á. Acosta, and M. S. Suarez-Castanon, « Pi-type controllers and Σ–Δ modulation for saturated dc-dc buck power converters », *IEEE Access*, vol. 9, pp. 20 346–20 357, 2021.

[44] L. A. Soriano, J. d. J. Rubio, E. Orozco, D. A. Cordova, G. Ochoa, R. Balcazar, D. R. Cruz, J. A. Meda-Campaña, A. Zacarias, and G. J. Gutierrez, « Optimization of sliding mode control to save energy in a scara robot », *Mathematics*, vol. 9, *24*, p. 3160, 2021.

[45] L. A. Soriano, E. Zamora, J. Vazquez-Nicolas, G. Hernandez, J. A. Barraza Madrigal, and D. Balderas, « Pd control compensation based on a cascade neural network applied to a robot manipulator », *Frontiers in Neurorobotics*, p. 78, 2020.

[46] R. Silva-Ortigoza, E. Hernández-Márquez, A. Roldán-Caballero, S. Tavera-Mosqueda, M. Marciano-Melchor, J. R. Garcıía-Sánchez, V. M. Hernández-Guzmán, and G. Silva-Ortigoza, « Sensorless tracking control for a "full-bridge buck inverter–dc motor" system: passivity and flatness-based design », *IEEE Access*, vol. 9, pp. 132 191–132 204, 2021.

[47] C. Y. Kuo and S.-P. T. Wang, « Nonlinear Robust Industrial Robot Control », *Journal of Dynamic Systems, Measurement, and Control*, vol. 111, *1*, pp. 24–30, Mar. 1989.

[48] E. Freund, « Fast nonlinear control with arbitrary pole-placement for industrial robots and manipulators », *The Int.J. of Robotics Research*, vol. 1, *1*, pp. 65–78, 1982.

[49] P. Poignet and M. Gautier, « Nonlinear model predictive control of a robot manipulator », *in 6th International workshop on advanced motion control. Proceedings (Cat. No. 00TH8494)*, IEEE, 2000, pp. 401–406.

[50] D. Wang and M. Vidyasagar, « Control of a Class of Manipulators With a Single Flexible Link: Part I—Feedback Linearization », *Journal of Dynamic Systems, Measurement, and Control*, vol. 113, *4*, pp. 655–661, Dec. 1991.

[51] F. Lewis, C. Abdallah, and D. Dawson, « Control of robot », *Manipulators, Editorial Maxwell McMillan, Canada*, pp. 25–36, 1993.

[52] M. Spong and M. Vidyasagar, « Robust linear compensator design for nonlinear robotic control », *IEEE J. on Robotics and Automation*, vol. 3, *4*, pp. 345–351, 1987.

[53] J.-J. E. Slotine, « The robust control of robot manipulators », *The Int.J. of Robotics Research*, vol. 4, *2*, pp. 49–64, 1985.

[54] T.-J. Tarn, A. K. Bejczy, A. Isidori, and Y. Chen, « Nonlinear feedback in robot arm control », *in The 23rd IEEE Conf. on Decision and Control*, IEEE, 1984, pp. 736–751.

[55] W. Shang and S. Cong, « Nonlinear computed torque control for a high-speed planar parallel manipulator », *Mechatronics*, vol. 19, *6*, pp. 987–992, 2009.

[56] D. Nguyen-Tuong, M. Seeger, and J. Peters, « Computed torque control with non-parametric regression models », *in 2008 American Control Conf.*, IEEE, 2008, pp. 212–217.

[57] H. Sage, M. De Mathelin, and E. Ostertag, « Robust control of robot manipulators: a survey », *Int.J. of control*, vol. 72, *16*, pp. 1498–1522, 1999.

[58] E. S. Barjuei, P. Boscariol, A. Gasparetto, M. Giovagnoni, and R. Vidoni, « Control design for 3d flexible link mechanisms using linearized models », *in Advances on Theory and Practice of Robots and Manipulators*, M. Ceccarelli and V. A. Glazunov, Eds., Cham: Springer International Publishing, 2014, pp. 181–188.

[59] Q. Li and F. Wu, « Control performance improvement of a parallel robot via the design for control approach », *Mechatronics*, vol. 14, *8*, pp. 947–964, 2004.

[60] W. Zhang, Q. Li, and L. Guo, « Integrated design of mechanical structure and control algorithm for a programmable four-bar linkage », *IEEE/ASME Trans. on mechatronics*, vol. 4, *4*, pp. 354–362, 1999.

[61] K. Youcef-Toumi and H. Asada, « The design of open-loop manipulator arms with decoupled and configuration-invariant inertia tensors », *in Proceedings. 1986 IEEE International Conference on Robotics and Automation*, vol. 3, 1986, pp. 2018–2026.

[62] H. Asada and K. Youcef-Toumi, « Analysis and Design of a Direct-Drive Arm With a Five-Bar-Link Parallel Drive Mechanism », *Journal of Dynamic Systems, Measurement, and Control*, vol. 106, *3*, pp. 225–230, Sep. 1984.

[63] P. N. Belyanin, « Mechanical arm », Apr. 1981.

[64] V. Arakelian, *Dynamic Decoupling of Robot Manipulators.* Springer, 2018.

[65] M. Vukobratović and D. Stokić, « Contribution to the decoupled control of large-scale mechanical systems », *Automatica*, vol. 16, *1*, pp. 9–21, 1980.

[66] T. A. Coelho, L. Yong, and V. F. Alves, « Decoupling of dynamic equations by means of adaptive balancing of 2-dof open-loop mechanisms », *Mechanism and Machine Theory*, vol. 39, *8*, pp. 871–881, 2004.

[67] V. Arakelian and S. Sargsyan, « On the design of serial manipulators with decoupled dynamics », *Mechatronics*, vol. 22, *6*, pp. 904–909, 2012.

[68] V. Arakelian, J. Xu, and J.-P. Le Baron, « Mechatronic design of adjustable serial manipulators with decoupled dynamics taking into account the changing payload », *J. of Engineering Design*, vol. 27, *11*, pp. 768–784, 2016.

[69] J. Xu, V. Arakelian, and J.-P. Le Baron, « Dynamic decoupling of adjustable serial manipulators taking into account the changing payload », *in Robotics and Mechatronics: Proceedings of the 4th IFToMM International Symposium on Robotics and Mechatronics*, Springer, 2016, pp. 313–320.

[70] W. Freemantle, « Straight-line linkage », *British Patent*, vol. 2741, p. 17, 1803.

[71] J. Xu, J.-P. Le Baron, and V. Arakelian, « Tolerance analysis of planar serial manipulators with decoupled and non-decoupled dynamics », *in New Trends in Mechanism and Machine Science: Theory and Industrial Applications*, Springer, 2017, pp. 29–37.

[72] M. P. De Looze, T. Bosch, F. Krause, K. S. Stadler, and L. W. O'sullivan, « Exoskeletons for industrial application and their potential effects on physical work load », *Ergonomics*, vol. 59, *5*, pp. 671–681, 2016.

[73] M. A. Gull, S. Bai, and T. Bak, « A review on design of upper limb exoskeletons », en, *Robotics*, vol. 9, *1*, p. 16, Mar. 2020, number: 1 publisher: Multidisciplinary Digital Publishing Institute.

[74] S. Mendis, « Stroke disability and rehabilitation of stroke: world health organization perspective », en, *International Journal of Stroke*, vol. 8, *1*, pp. 3–4, Jan. 2013.

---

[75] Y. Zhang, V. Arakelian, and J. Baron, « Design concepts and functional particularities of wearable walking assist devices and power-assist suits—a review », *in* Proceedings of 58th international conference of machine design departments, 2017, pp. 436–41.

[76] M. M. Janssen, A. Bergsma, A. C. Geurts, and I. J. De Groot, « Patterns of decline in upper limb function of boys and men with dmd: an international survey », *Journal of neurology*, vol. 261, *7*, pp. 1269–1288, 2014.

[77] K. Kiguchi and Y. Hayashi, « An emg-based control for an upper-limb power-assist exoskeleton robot », *IEEE Transactions on Systems, Man, and Cybernetics, Part B (Cybernetics)*, vol. 42, *4*, pp. 1064–1071, 2012.

[78] Y. Muramatsu, H. Kobayashi, Y. Sato, H. Jiaou, T. Hashimoto, and H. Kobayashi, « Quantitative performance analysis of exoskeleton augmenting devices-muscle suit-for manual worker. », *Int. J. Autom. Technol.*, vol. 5, *4*, pp. 559–567, 2011.

[79] G. Franco and L. Fusetti, « Bernardino ramazzini's early observations of the link between musculoskeletal disorders and ergonomic factors », *Applied Ergonomics*, vol. 35, *1*, pp. 67–70, 2004.

[80] M. Antwi-Afari, H. Li, D. Edwards, E. Pärn, J. Seo, and A. Wong, « Biomechanical analysis of risk factors for work-related musculoskeletal disorders during repetitive lifting task in construction workers », *Automation in Construction*, vol. 83, pp. 41–47, 2017.

[81] A. Hoque, S. T. Ahmed, S. Paul, and M. Parvez, « Topsis based ergonomic analysis on work related musculoskeletal disorders of sewing machine operators », *International Journal of Advances in Engineering & Technology*, vol. 8, *5*, p. 728, 2015.

[82] H. M. Alkosha, M. I. Mohammed, and M. M. Amen, « Risk assessment and prevalence of work-related musculoskeletal disorders among cranial and spinal neurosurgeons », *World Neurosurgery*, vol. 176, e151–e161, 2023.

[83] *Lockheed Martin FORTIS*. [Online]. Available: `https://www.robrady.com/venture/fortis` (visited on 12/05/2023).

[84] M. A. Gull, T. Bak, and S. Bai, « Dynamic modeling of an upper limb hybrid exoskeleton for simulations of load-lifting assistance », *Proceedings of the Institution of Mechanical Engineers, Part C: Journal of Mechanical Engineering Science*, vol. 236, *5*, pp. 2147–2160, 2022.

[85] J. C. Perry, J. Rosen, and S. Burns, « Upper-limb powered exoskeleton design », *IEEE/ASME transactions on mechatronics*, vol. 12, *4*, pp. 408–417, 2007.

[86] T. Nef and R. Riener, « Armin-design of a novel arm rehabilitation robot », *in 9th International Conference on Rehabilitation Robotics, 2005. ICORR 2005.*, IEEE, 2005, pp. 57–60.

[87] A. Gupta and M. K. O'Malley, « Design of a haptic arm exoskeleton for training and rehabilitation », *IEEE/ASME Transactions on mechatronics*, vol. 11, *3*, pp. 280–289, 2006.

[88] A. Blanco, J. M. Catalán, J. A. Dıíez, J. V. Garcıía, E. Lobato, and N. Garcıía-Aracil, « Electromyography assessment of the assistance provided by an upper-limb exoskeleton in maintenance tasks », *Sensors*, vol. 19, *15*, p. 3391, 2019.

[89] *EXHAUSS Exosquelettes.* [Online]. Available: `https://www.exhauss.com/` (visited on 12/16/2022).

[90] A. Ebrahimi, « Stuttgart exo-jacket: an exoskeleton for industrial upper body applications », *in 2017 10th International Conference on Human System Interactions (HSI)*, IEEE, 2017, pp. 258–263.

[91] A. Schiele and F. C. Van Der Helm, « Kinematic design to improve ergonomics in human machine interaction », *IEEE Transactions on neural systems and rehabilitation engineering*, vol. 14, *4*, pp. 456–469, 2006.

[92] D. Verdel, S. Bastide, N. Vignais, O. Bruneau, and B. Berret, « An identification-based method improving the transparency of a robotic upper limb exoskeleton », *Robotica*, vol. 39, *9*, pp. 1711–1728, 2021. DOI: `10.1017/S0263574720001459`.

[93] E. Rocon, A. Ruiz, R. Raya, A. Schiele, J. L. Pons, J. Belda-Lois, R. Poveda, M. Vivas, and J. Moreno, « Human-robot physical interaction », *Wearable robots: Biomechatronic exoskeletons*, pp. 127–163, 2008.

[94] D. M. Baechle, E. D. Wetzel, and S. K. Agrawal, « Maxfas: mechatronic arm exoskeleton for firearm aim stabilization », *Journal of Mechanisms and Robotics*, vol. 8, *6*, p. 061 013, 2016.

[95] Y. Zhang and V. Arakelian, *Design of a passive robotic exosuit for carrying heavy loads. in 2018 ieee-ras 18th international conference on humanoid robots (humanoids), 860–865*, 2018.

[96] S. K. Agrawal, V. N. Dubey, J. J. Gangloff, E. Brackbill, Y. Mao, and V. Sangwan, « Design and optimization of a cable driven upper arm exoskeleton », *Journal of Medical Devices*, vol. 3, *3*, 2009.

[97] E. M. Landis, « Micro-injection studies of capillary blood pressure in human skin », *Heart*, vol. 15, pp. 209–228, 1930.

[98] K. Wegmann, K. Burkhart, T. Koslowsky, J. Koebke, W. Neiss, and L. Müller, « Arterial supply of the distal humerus », *Surgical and Radiologic Anatomy*, vol. 36, pp. 705–711, 2014.

[99] R. S. Goonetilleke and T. J. Eng, « Contact area effects on discomfort », *in Proceedings of the Human Factors and Ergonomics Society Annual Meeting*, SAGE Publications Sage CA: Los Angeles, CA, vol. 38, 1994, pp. 688–690.

[100] M. Langard, Y. Aoustin, V. Arakelian, and D. Chablat, « Investigation of the stresses exerted by an exosuit of a human arm », *in Advanced Technologies in Robotics and Intelligent Systems: Proceedings of ITR 2019*, Springer, 2020, pp. 425–435.

[101] N. Jarrassé and G. Morel, « Connecting a human limb to an exoskeleton », *IEEE Transactions on Robotics*, vol. 28, *3*, pp. 697–709, 2011.

[102] E. Pennestri, P. Valentini, and L. Vita, « Multibody dynamics simulation of planar linkages with dahl friction », *Multibody System Dynamics*, vol. 17, *4*, pp. 321–347, 2007.

[103] E. Haug, S.-C. Wu, and S.-M. Yang, « Dynamics of mechanical systems with coulomb friction, stiction, impact and constraint addition-deletion—i theory », *Mechanism and Machine Theory*, vol. 21, pp. 401–406, 1986.

[104] S.-C. Wu, S.-M. Yang, and E. Haug, « Dynamics of mechanical systems with coulomb friction, stiction, impact and constraint addition-deletion—ii planar systems », *Mechanism and Machine Theory*, vol. 21, pp. 407–416, 1986.

[105] J. Frączek and M. Wojtyra, « On the unique solvability of a direct dynamics problem for mechanisms with redundant constraints and coulomb friction in joints », *Mechanism and Machine Theory*, vol. 46, *3*, pp. 312–334, 2011.

[106] T. Piatkowski, « Gms friction model approximation », *Mechanism and Machine Theory*, vol. 75, pp. 1–11, 2014.

[107] C. E. Wilson and J. P. Sadler, *Kinematics and dynamics of machinery.* Pearson Education India, 2003.

[108] J. Sadler, « Dynamic analysis of mechanisms including coulomb friction via equilibrium equations », *in Third Applied Mechanism Conference, Oklahoma State University*, vol. 13, 1973, pp. 1–11.

[109] I. Imam, M. Skreiner, and J. P. Sadler, « A New Solution to Coulomb Friction in Mechanism Bearings: Theory and Application », *Journal of Mechanical Design*, vol. 103, *4*, pp. 764–775, Oct. 1981.

[110] J. Verbeke and R. Cools, « The newton-raphson method », *International Journal of Mathematical Education in Science and Technology*, vol. 26, *2*, pp. 177–193, 1995.

[111] T. L. Heath, *A history of greek mathematics. clarendon*, 1921.

[112] F. J. Dellajustina, L. C. Martins, *et al.*, « The hidden geometry of the babylonian square root method », *Applied Mathematics*, vol. 5, *19*, p. 2982, 2014.

[113] A. M. Lyapunov, « The general problem of the stability of motion », *International journal of control*, vol. 55, *3*, pp. 531–534, 1992.

[114] *Assur group,wikipedia.* [Online]. Available: `https://en.wikipedia.org/wiki/Assur_group`.

[115] V. Arakelian, J. Xu, and J.-P. Le Baron, « Dynamic decoupling of robot manipulators: a review with new examples », *Dynamic Decoupling of Robot Manipulators*, pp. 1–23, 2018.

[116] V. Arakelian, « Gravity compensation in robotics », *Advanced Robotics*, vol. 30, *2*, pp. 79–96, 2016.

[117] V. Arakelian, J.-P. Le Baron, and P. Mottu, « Torque minimisation of the 2-dof serial manipulators based on minimum energy consideration and optimum mass redistribution », *Mechatronics*, vol. 21, *1*, pp. 310–314, 2011.

[118] K. Shin and N. McKay, « Minimum-time control of robotic manipulators with geometric path constraints », *IEEE Transactions on Automatic Control*, vol. 30, *6*, pp. 531–541, 1985.

[119] J. E. Bobrow, S. Dubowsky, and J. S. Gibson, « Time-optimal control of robotic manipulators along specified paths », *The international journal of robotics research*, vol. 4, *3*, pp. 3–17, 1985.

[120] H. Arai, K. Tanie, and S. Tachi, « Path tracking control of a manipulator considering torque saturation », *IEEE Transactions on Industrial Electronics*, vol. 41, *1*, pp. 25–31, 1994.

[121] H. Arai and K. Tanie, « Real-time path tracking with torque limits by using a disturbance observer », *in Proceedings of the 1994 IEEE International Conference on Robotics and Automation*, IEEE, 1994, pp. 1859–1865.

[122] K. Ohishi and T. Someno, « Robust robot manipulator control with autonomous consideration algorithm of torque saturation », *Advanced robotics*, vol. 12, *7-8*, pp. 755–769, 1997.

[123] K. S. Eom, I. H. Suh, and W. K. Chung, « Disturbance observer based path tracking control of robot manipulator considering torque saturation », *Mechatronics*, vol. 11, *3*, pp. 325–343, 2001.

[124] P. S. Vishal and M. S. Mohan, « Simulation and analysis of articulated robot », *in 2021 International Conference on Advancements in Electrical, Electronics, Communication, Computing and Automation (ICAECA)*, 2021, pp. 1–5.

[125] J. Morio, « Global and local sensitivity analysis methods for a physical system », *European journal of physics*, vol. 32, *6*, p. 1577, 2011.

[126] I. M. Sobol, « Global sensitivity indices for nonlinear mathematical models and their monte carlo estimates », *Mathematics and computers in simulation*, vol. 55, *1-3*, pp. 271–280, 2001.

[127] A. Saltelli, P. Annoni, I. Azzini, F. Campolongo, M. Ratto, and S. Tarantola, « Variance based sensitivity analysis of model output. design and estimator for the total sensitivity index », *Computer physics communications*, vol. 181, *2*, pp. 259–270, 2010.

[128] Y. Jiao, K. Jermsittiparsert, A. Y. Krasnopevtsev, Q. A. Yousif, and M. Salmani, « Interaction of thermal cycling and electric current on reliability of solder joints in different solder balls », *Materials Research Express*, vol. 6, *10*, p. 106 302, 2019.

[129] O. Muvengei, J. Kihiu, and B. Ikua, « Dynamic analysis of planar multi-body systems with lugre friction at differently located revolute clearance joints », *Multibody System Dynamics*, vol. 28, *4*, pp. 369–393, 2012.

[130] A. C. Bittencourt and S. Gunnarsson, « Static friction in a robot joint—modeling and identification of load and temperature effects », *Journal of Dynamic Systems, Measurement, and Control*, vol. 134, *5*, 2012.

[131] J.-J. E. Slotine, W. Li, *et al.*, *Applied nonlinear control.* Prentice hall Englewood Cliffs, NJ, 1991, vol. 199.

[132] Y. Orlov, Y. Aoustin, and C. Chevallereau, « Finite time stabilization of a perturbed double integrator—part i: continuous sliding mode-based output feedback synthesis », *IEEE Transactions on Automatic Control*, vol. 56, *3*, pp. 614–618, 2010.

[133] *SimTK OpenSim Documentation Musculoskeletal Models.* [Online]. Available: `https://simtk-confluence.stanford.edu:8443/display/OpenSim/Musculoskeletal+Models` (visited on 12/16/2023).

[134] *Polyethylene braid-style cables.* [Online]. Available: `https://www.amazon.com/JIOUDAO-Fishing-Multicolor-Strength-15LB-200LB/dp/B0BYHHWCLS?th=1&psc=1` (visited on 11/17/2023).

[135] W. Khalil and E. Dombre, *Modeling identification and control of robots.* 2002.

[136] Y. Mao and S. K. Agrawal, « A cable driven upper arm exoskeleton for upper extremity rehabilitation », *in 2011 IEEE International Conference on Robotics and Automation*, IEEE, 2011, pp. 4163–4168.

[137] W. Kraus, *Force control of cable-driven parallel robots.* 2016.

[138] Y. Mao and S. K. Agrawal, « Design of a cable-driven arm exoskeleton (carex) for neural rehabilitation », *IEEE transactions on robotics*, vol. 28, *4*, pp. 922–931, 2012.

[139] Y. Mao, X. Jin, G. G. Dutta, J. P. Scholz, and S. K. Agrawal, « Human movement training with a cable driven arm exoskeleton (carex) », *IEEE Transactions on Neural Systems and Rehabilitation Engineering*, vol. 23, *1*, pp. 84–92, 2014.

[140] C. A. C. Coello, G. T. Pulido, and M. S. Lechuga, « Handling multiple objectives with particle swarm optimization », *IEEE Transactions on evolutionary computation*, vol. 8, *3*, pp. 256–279, 2004.

[141] « Preface », *in Swarm Intelligence*, ser. The Morgan Kaufmann Series in Artificial Intelligence, J. Kennedy, R. C. Eberhart, and Y. Shi, Eds., San Francisco: Morgan Kaufmann, 2001, pp. xiii–xxvii.

[142] N. Di Cesare, D. Chamoret, and M. Domaszewski, « A new hybrid pso algorithm based on a stochastic markov chain model », *Advances in engineering software*, vol. 90, pp. 127–137, 2015.

[143] M. Clerc and J. Kennedy, « The particle swarm-explosion, stability, and convergence in a multidimensional complex space », *IEEE transactions on Evolutionary Computation*, vol. 6, *1*, pp. 58–73, 2002.

[144] J. Kennedy and R. Mendes, « Population structure and particle swarm performance », *in Proceedings of the 2002 Congress on Evolutionary Computation. CEC'02 (Cat. No. 02TH8600)*, IEEE, vol. 2, 2002, pp. 1671–1676.

[145] C. W. Reynolds, « Flocks, herds and schools: a distributed behavioral model », *in Proceedings of the 14th annual conference on Computer graphics and interactive techniques*, 1987, pp. 25–34.

[146] S. Brin and L. Page, « The anatomy of a large-scale hypertextual web search engine », *Computer networks and ISDN systems*, vol. 30, *1-7*, pp. 107–117, 1998.

[147] A. N. Langville and C. D. Meyer, « Deeper inside pagerank », *Internet Mathematics*, vol. 1, *3*, pp. 335–380, 2004.

[148] P. K. Newton, J. Mason, K. Bethel, L. A. Bazhenova, J. Nieva, and P. Kuhn, « A stochastic markov chain model to describe lung cancer growth and metastasis », *PloS one*, vol. 7, *4*, e34637, 2012.

[149] C. M. Fonseca and P. J. Fleming, « An overview of evolutionary algorithms in multiobjective optimization », *Evolutionary computation*, vol. 3, *1*, pp. 1–16, 1995.

[150] R. Drillis and R. Contini, « Body segment parameters, new york university », NY, Technical Report, Tech. Rep., 1966.

[151] *BOSCH Drills.* [Online]. Available: `https://www.bosch-professional.com/sa/en/drills-213949-ocs-c/` (visited on 11/10/2023).

[152] L. Breiman, « Random forests », *Machine learning*, vol. 45, pp. 5–32, 2001.

[153] V. Rodriguez-Galiano, M. Sanchez-Castillo, M. Chica-Olmo, and M. Chica-Rivas, « Machine learning predictive models for mineral prospectivity: an evaluation of neural networks, random forest, regression trees and support vector machines », *Ore Geology Reviews*, vol. 71, pp. 804–818, 2015.

[154] A. Antoniadis, S. Lambert-Lacroix, and J.-M. Poggi, « Random forests for global sensitivity analysis: a selective review », *Reliability Engineering & System Safety*, vol. 206, p. 107 312, 2021.

[155] *Couzet gear motor 828690.* [Online]. Available: `https://fr.rs-online.com/web/p/moteurs-a-courant-continu/1784945` (visited on 11/17/2023).

[156] *Fritzing.* [Online]. Available: `https://fritzing.org/` (visited on 11/17/2023).

[157] *H-bridge.* [Online]. Available: `https://en.wikipedia.org/wiki/H-bridge` (visited on 11/17/2023).

APPENDIX A

This appendix shows the detailed system modelling of the mannequin upper-limb in Section 5.1.

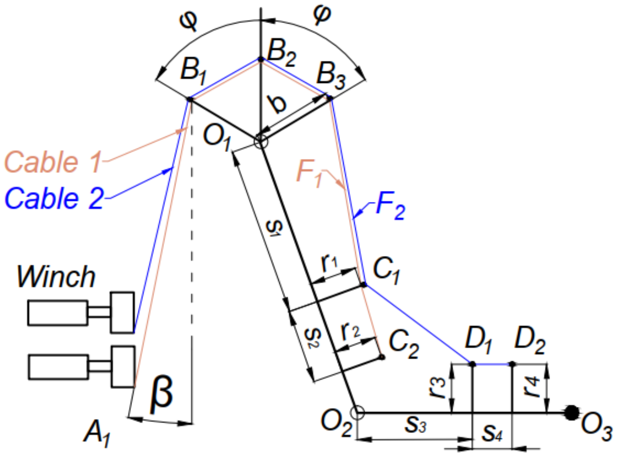

Figure 5.21 – Mannequin upper-limb with cable transmission system.

The proposed exosuit can be represented by two cables. Assuming two motors are positioned closely to each other, both cables originate from the winch point A_1 (Fig. 5.21). As shown in Fig. 5.21, Cable 1 passes through the anchor and attachment points on point B_i $(i = 1, 2, 3)$ and C_i $(i = 1, 2)$. Cable 2 passes through the anchor and attachment points on point B_i $(i = 1, 2, 3)$, C_1, and D_i $(i = 1, 2)$.

The design parameters of exosuit are denoted as: β, φ, b, s_1, s_2, s_3, s_4, r_1, r_2, r_3, r_4, representing the arrangement of anchor and attachment points. The moment induced by cables on shoulder and elbow joints could be calculated as:

$$\begin{bmatrix} \tau_{shoulder}^{cable} \\ \\ \\ \tau_{elbow}^{cable} \end{bmatrix} = \begin{bmatrix} \tau_{shoulder}^{cable\ 1} + \tau_{shoulder}^{cable\ 2} \\ \\ \\ \tau_{elbow}^{cable\ 2} \end{bmatrix} = \mathbf{J} \begin{bmatrix} F_1 \\ \\ \\ F_2 \end{bmatrix} \tag{5.3}$$

The vector of the moment induced by cables could be expressed as:

$$\tau_{\mathbf{shoulder}}^{\mathbf{cable\ 1}} = \left(\mathbf{O_1C_1} \times \left(\frac{\mathbf{C_1B_3}}{\|\mathbf{C_1B_3}\|} + \frac{\mathbf{C_1C_2}}{\|\mathbf{C_1C_2}\|} \right) \right) F_1 \tag{5.4}$$

$$\begin{aligned}\tau^{\textbf{cable 2}}_{\textbf{shoulder}} = &\left(\mathbf{O_1C_1} \times \left(\frac{\mathbf{C_1B_3}}{\|\mathbf{C_1B_3}\|} + \frac{\mathbf{C_1D_1}}{\|\mathbf{C_1D_1}\|}\right) + \mathbf{O_1D_1} \times \left(\frac{\mathbf{D_1C_1}}{\|\mathbf{D_1C_1}\|} + \frac{\mathbf{D_1D_2}}{\|\mathbf{D_1D_2}\|}\right)\right. \\ &\left. + \mathbf{O_1D_2} \times \frac{\mathbf{D_2D_1}}{\|\mathbf{D_2D_1}\|}\right) F_2\end{aligned} \tag{5.5}$$

$$\tau^{\textbf{cable 2}}_{\textbf{elbow}} = \left(\mathbf{O_2D_1} \times \left(\frac{\mathbf{D_1C_1}}{\|\mathbf{D_1C_1}\|} + \frac{\mathbf{D_1D_2}}{\|\mathbf{D_1D_2}\|}\right) + \mathbf{O_2D_2} \times \frac{\mathbf{D_2D_1}}{\|\mathbf{D_2D_1}\|}\right) F_2 \tag{5.6}$$

where, **J** is the Jacobian matrix. When wearing the exosuit, the moments induced by the gravitational force can be compensated by the moments generated by cables. Therefore, the cable tension forces F_1 and F_2 can be calculated by:

$$\begin{bmatrix} F_1 \\ \\ F_2 \end{bmatrix} = \mathbf{J}^{-1} \begin{bmatrix} \tau_{\mathbf{O_1}} \\ \\ \tau_{\mathbf{O_2}} \end{bmatrix} \tag{5.7}$$

The total shoulder force can be given as the following form:

$$\|\mathbf{F}^{\textbf{cable}}_{\textbf{shoulder}}\| = \left\|\left(\frac{\mathbf{B_1A_1}}{\|\mathbf{B_1A_1}\|} + \frac{\mathbf{B_3C_1}}{\|\mathbf{B_3C_1}\|}\right)(F_1 + F_2)\right\| \tag{5.8}$$

The total tangential force exerted on upper-limb as the following equation:

$$\|\mathbf{F}^{\textbf{cable}}_{\textbf{upper limb}}\| = \|\mathbf{F}^{\textbf{cable}}_{\textbf{arm}}\| + \|\mathbf{F}^{\textbf{cable}}_{\textbf{forearm}}\| \tag{5.9}$$

where,

$$\mathbf{F}^{\textbf{cable}}_{\textbf{arm}} = \left(\frac{\mathbf{C_1B_3}}{\|\mathbf{C_1B_3}\|}(F_1 + F_2) + \frac{\mathbf{C_1D_1}}{\|\mathbf{C_1D_1}\|}F_2\right) \cdot \frac{\mathbf{O_2O_1}}{\|\mathbf{O_2O_1}\|} \tag{5.10}$$

$$\mathbf{F}^{\textbf{cable}}_{\textbf{forearm}} = \frac{\mathbf{D_1C_1}}{\|\mathbf{D_1C_1}\|}F_2 \cdot \frac{\mathbf{O_3O_2}}{\|\mathbf{O_3O_2}\|} \tag{5.11}$$

To validate an enhanced exosuit performance in human comfort conditions and energy efficiency, the cable tension forces F_1 and F_2 are considered as two objectives in the optimization process because they mainly affect the forces exerted on the human body and are also proportional to the currents in DC motors, related to energy efficiency of the exosuit system.

LIST OF PUBLICATIONS

Journal articles

[1] **Lu, Y**., Aoustin, Y., Arakelian, V.: Mechatronic design of dynamically decoupled manipulators based on the control performance improvement. Robotica, 41(2) 609-631 (2023)

[2] **Lu, Y**., Arakelian, V.: A New Solution to Force Analysis Including Coulomb Friction in Mechanism Joints. Mechanisme and Machine Theory (peer review).

[3] **Lu, Y**., Aoustin, Y., Arakelian, V.: Design of an Exosuit for assistance considering the physical human-robot interaction performance improvement. Multibody System Dynamics (peer review)

Conference proceedings

[1] Arakelian, V., Geng, J., **Lu, Y**.: Torque Minimization of Dynamically Decoupled R-R Spatial Serial Manipulators via Optimal Motion Control. In: Zeghloul, S. et al. (eds) Mechanism Design for Robotics. MEDER 2021. Mechanisms and Machine Science, vol 103. Springer, 20–27 (2021)

[2] **Lu, Y**., Arakelian, V.: Une nouvelle solution approximative au frottement de Coulomb dans les systèmes mécaniques. 25ème Congrès Français de Mécanique (2021)

[3] **Lu, Y**., Aoustin, Y., Arakelian, V.: Control performance improvement in dynamically decoupled manipulators. In: Kecskeméthy, A., Parenti-Castelli, V. (eds) ROMANSY 24 - Robot Design, Dynamics and Control. ROMANSY 2022. CISM International Centre for Mechanical Sciences, vol 606. Springer, Cham., 606 199-209 (2022).

[4] Arakelian, V., **Lu, Y**., Geng, J.: Application of the «bang-bang» law in robot manipulators for the reduction of inertial forces and input torques. The 16th IFToMM World Congress, November 5 – 10, Tokyo, Japan.

[5] **Lu, Y**., Aoustin, Y., Arakelian, V.: Physical Human-Robot Interaction Performance Optimization of an Exosuit for Assistance The 16th IFToMM World Congress, November 5 – 10, Tokyo, Japan.

COLLEGE
DOCTORAL SCIENCES
BRETAGNE POUR L'INGENIEUR

INSA INSTITUT NATIONAL
DES SCIENCES
APPLIQUÉES
RENNES

Titre : Méthodes de conception et de commande de systèmes robotiques prenant en compte la consommation d'énergie et améliorant leur comportement

Mot clés : Consommation d'énergie, Performance de commande, Frottement, Découplage dynamique, Exosquelette

Résumé : Cette thèse traite de méthodes de conception et de commande des systèmes robotiques. Divers critères et méthodes sont employés pour évaluer et améliorer leurs performances, notamment la consommation d'énergie. Une solution approximative novatrice a été développée pour déterminer les réactions dans les liaisons et les pertes d'énergie dans les systèmes mécaniques, en tenant compte de l'impact du frottement de Coulomb. Il s'agit d'une des solutions analytiques les plus simples parmi les méthodologies existantes. Elle repose sur la méthode babylonienne d'approximation des racines carrées, conduisant à la résolution d'un système d'équations linéaires. Afin de démontrer l'efficacité de la méthode proposée, des simulations numériques ont été réalisées pour des manipulateurs parallèles 5R et 3RRR. La dynamique des manipulateurs est connue pour sa non-linéarité intrinsèque élevée et son couplage, pouvant entraîner une diminution des performances de contrôle, notamment à des vitesses élevées. Dans la thèse, des techniques innovantes de découplage intégrant la redistribution de masse et le déplacement d'actionneurs sont introduites pour les manipulateurs sériels spatiaux. L'objectif est d'établir un système dynamique linéaire et découplé pour répondre à ces défis. Par la suite, une loi de mouvement efficace est appliquée pour réduire les couples d'entrée des manipulateurs découplés. La thèse explore également un exosquelette pour l'assistance du membre supérieur. Ensuite, une approche d'optimisation multi-objectifs, utilisant «l'intelligence collective», est développée et appliquée pour minimiser les inconforts ressentis par l'utilisateur dans la conception de l'exosquelette. Une étude expérimentale est menée pour valider la conception de l'exosquelette avec une consommation d'énergie minimale.

Title: Methods for design and control of robotic systems considering energy consumption and improving their behavior

Keywords: Energy consumption, Control performance, Friction, Dynamic decoupling, Exoskeleton

Abstract: This thesis deals with the methods for design and control of robotic systems. Various criteria and methods are employed to evaluate and enhance their performance, including energy consumption. An innovative approximate solution has been developed to determine joint reactions and energy loss in mechanical systems, taking into account the impact of Coulomb friction. It is one of the simplest analytically tractable solutions among existing methodologies. It relies on the Babylonian method for approximating square roots, leading to the resolution of a system of linear equations. To demonstrate the effectiveness of the proposed method, numerical simulations were conducted for 5R and 3RRR parallel manipulators. The dynamics of robot manipulators are known for their inherent high nonlinearity and coupling, which can result in diminished control performance, particularly at high speeds. In the thesis, innovative decoupling techniques that integrate mass redistribution and actuator relocation are introduced for spatial serial manipulators. The objective is to establish a linear and decoupled dynamic system to address these challenges. Following this, an efficient motion profile is applied to reduce the input torques of the decoupled manipulators. The thesis also explores an exosuit for upper-limb power assistance. Subsequently, a multi-criteria optimization approach, utilizing "swarm intelligence", is developed and applied to minimize the discomfort forces experienced by the user in the exosuit design. An experimental study is conducted to validate the exosuit design with minimized energy consumption.